1986

Fresnoite ceramics and thin films.

Robert J. White
University of Windsor

Recommended Citation

White, Robert J., "Fresnoite ceramics and thin films." (1986). *Electronic Theses and Dissertations.* Paper 2160.

National Library of Canada
Canadian Theses Service
Ottawa, Canada
K1A 0N4

Bibliothèque nationale du Canada
Services des thèses canadiennes

CANADIAN THESES

THÈSES CANADIENNES

NOTICE

The quality of this microfiche is heavily dependent upon the quality of the original thesis submitted for microfilming. Every effort has been made to ensure the highest quality of reproduction possible.

If pages are missing, contact the university which granted the degree.

Some pages may have indistinct print especially if the original pages were typed with a poor typewriter ribbon or if the university sent us an inferior photocopy.

Previously copyrighted materials (journal articles, published tests, etc.) are not filmed.

Reproduction in full or in part of this film is governed by the Canadian Copyright Act, R.S.C. 1970, c. C-30.

AVIS

La qualité de cette microfiche dépend grandement de la qualité de la thèse soumise au microfilmage. Nous avons tout fait pour assurer une qualité supérieure de reproduction.

S'il manque des pages, veuillez communiquer avec l'université qui a conféré le grade.

La qualité d'impression de certaines pages peut laisser à désirer, surtout si les pages originales ont été dactylographiées à l'aide d'un ruban usé ou si l'université nous a fait parvenir une photocopie de qualité inférieure.

Les documents qui font déjà l'objet d'un droit d'auteur (articles de revue, examens publiés, etc.) ne sont pas microfilmés.

La reproduction, même partielle, de ce microfilm est soumise à la Loi canadienne sur le droit d'auteur, SRC 1970, c. C-30.

THIS DISSERTATION
HAS BEEN MICROFILMED
EXACTLY AS RECEIVED

LA THÈSE A ÉTÉ
MICROFILMÉE TELLE QUE
NOUS L'AVONS REÇUE

NL-339 (r. 86/06)

Canada

FRESNOITE CERAMICS AND THIN FILMS

by

© ROBERT J. WHITE

A Thesis
Submitted to the Faculty of Graduate Studies and Research
Through the Department of Engineering Materials
in Partial Fulfillment of the Requirements for
the Degree of Master of Applied Science
at the University of Windsor

Windsor, Ontario

1986

ISBN 0-315-29298-9

852327

To My Parents

ABSTRACT

Piezoelectric fresnoite ($Ba_2Si_2TiO_8$) thin films have been proposed to have the potential to be used for electro-acoustic devices such as surface-acoustic-wave devices.

As the first step in the formation of fresnoite thin films, ceramic sputtering targets of two different compositions were fabricated: a ceramic which was produced from a raw powder mixed according to the stoichiometric formula of fresnoite, and a ceramic which was enriched in barium. The dielectric constant of the fresnoite-based ceramics was determined to be comparable to the single crystal values.

The ceramic targets were found to crystallize into at least three distinct phases - $Ba_2Si_2TiO_8$, $BaTiSiO_5$, and Ba_2SiO_4. The composition of the fresnoite-based ceramics was analyzed by means of both wavelength-dispersive-x-ray spectroscopy and electron spectroscopy for chemical analysis (ESCA). Correction factors for each element - Ba, Si, Ti, and O were determined and subsequently applied to ESCA analyses of the compositions of the thin films.

The compositions of the films r.f.-sputtered from both types of ceramics were discovered to have shifted from their target compositions. In general, the thin films were deficient in barium and had a slight excess of titanium. The only film which gave any indication of being partially crystallized in the as-deposited condition was deposited on (100)Si heated to 650°C.

A temperature of 700°C was sufficient to crystallize the thin films formed on (100)Si. When annealed, the thin

films sputtered from both types of ceramics crystallized into four different types of barium titanium silicates: $Ba_2Si_2TiO_8$, $BaTiSiO_5$, $BaTiSi_2O_7$ and $BaTiSi_3O_9$. The $Ba_2Si_2TiO_8$ and $BaTiSiO_5$ phases of a film deposited on (100)Si at 650°C showed some indication of c-axis orientation (which is necessary for the film to be piezoelectric) when annealed.

ACKNOWLEDGEMENTS

The author wishes to express his sincere gratitude to Dr. Hisao Yamauchi for his supervision and guidance throughout the course of this work.

The author would also like to acknowledge the assistance of various individuals and institutions which contributed in some way to this work. In particular, the contributions of: Mr. Chris Marushima and Valenite Modco Co. for the use of the press machine; Mr. John Robinson of the University of Windsor for his assistance in the maintenance of the sputter-deposition system and in the electron microscopy analysis; Dr. M. Sayer of Queen's University for the RBS analysis; Mr. John Tyler, Mr. Greg DeMaggio, and Dr. B. Chao of Energy Conversion Devices Inc. of Troy, Michigan for their very excellent compositional analyses; Dr. G.R. Raju of the University of Windsor for his assistance with the dielectric measurements; Mrs. X. Meng and Dr. D.O. Northwood for their helpful discussions regarding the electron diffraction results, and Mr. G. Vazsonyi for his photographic expertise.

Finally, I would like to thank my friends and members of my family who encouraged me throughout this study.

TABLE OF CONTENTS

Page

LIST OF TABLES

LIST OF FIGURES

CHAPTER 1

INTRODUCTION

The field of piezoelectric devices has expanded rapidly, due to the development and discovery of new piezoelectric materials. One such material is the mineral, "fresnoite", which was recently discovered. This material is piezoelectric but not ferroelectric, and it is very stable under normal environments (unlike ZnO). Thus, fresnoite has the potential to be used as a piezoelectric component for various device applications. The surface-acoustic-wave (SAW) characteristics of synthetic fresnoite single crystals were determined and it was concluded that fresnoite single crystals could be used as a piezoelectric material for SAW devices, but they possess no significant advantages over the materials presently used. The SAW characteristics of a fresnoite thin film fabricated on a fused quartz substrate were also calculated, and some interesting SAW features were predicted. However, in order to be piezoelectric, these films have to be crystalline, with the grains oriented so that their c-axis is perpendicular to the substrate. To this author's knowledge, no actual fabrication of piezoelectric fresnoite thin films has been reported.

While thin films can be formed by a variety of methods, the most common method utilized for the production of high quality thin films is the sputter-deposition technique, and thus this was the method chosen as the means to produce fresnoite thin films. Since fresnoite is a "new" material, a procedure for the fabrication of high quality fresnoite ceramic sputtering targets had to be developed and refined. Also, the fact that fresnoite is an electrical insulator necessitated that the sputtering operation be performed in an r.f. mode.

In this study, the characterization of sputter-deposited thin films from fresnoite ceramic targets is reported. Emphasis is placed on the compositional and structural analyses of the ceramic targets and thin films, since a prerequisite for the attainment of c-axis oriented fresnoite thin films is that the films possess the stoichiometric fresnoite composition. Quantitative compositional analyses were performed by a variety of techniques, including: wavelength dispersive x-ray spectroscopy, electron spectroscopy for chemical analysis, and Rutherford backscattering spectroscopy. The structure of the ceramic targets was determined by x-ray diffraction, and the structure of the thin films in the as-deposited and annealed states was characterized by both x-ray and electron diffraction techniques.

CHAPTER 2

LITERATURE REVIEW

2.1 Fresnoite

Fresnoite was one of seven minerals that were discovered during a geological study of the sanbornite deposits in eastern Fresno County, California. The chemical formula of fresnoite was determined to be $Ba_2Si_2TiO_8$ [1,(1965)]. Previous investigations of the $BaTiO_3$-SiO_2 system did not reveal the existence of fresnoite [2,(1955)]. Since its initial discovery, fresnoite has been found to be very widespread in occurrence. It is found in gneissic sanbornite-quartz rock and in quartzite that is deficient in sanbornite.

The crystal structure, interatomic distances, and bond angles were investigated by Louisnathan and Moore [3,(1967)], and by Calvert and Trotter [4,(1967)]. These groups found that fresnoite has a body-centred tetragonal structure and belongs in the point group 4mm. This is a non-centro-symmetric point group and one consequence of this structure is that fresnoite exhibits both piezo- and pyro-electric behaviour.

Kimura et al [5,(1976)] and Haussuhl et al [6,(1977)] successfully grew single crystals of fresnoite by means of the Czochralski technique. These groups measured the elastic, dielectric, piezoelectric, optical, and thermal properties of fresnoite. Both groups concluded that this material's strong piezoelectric and elastic properties warranted further investigation for technical applications. Kimura [7,(1977)] measured all of the elastic constants, temperature coefficients of the elastic constants, and thermal expansion coefficients of fresnoite.

Melngailis et al [8,(1978)] used bulk material parameters to calculate the properties of surface acoustic waves (SAW) on single crystal fresnoite. Measured values were found to be in good agreement with the calculations. Yamauchi [9,(1978)] independently calculated the SAW characteristics of single crystal fresnoite. Yamauchi's calculations took into account the temperature coefficients of the piezoelectric constants while the calculations of Melngailis et al did not. Thus, the results of Yamauchi were more precise. Yamauchi, Yamashita and Takeuchi [10,(1979)] calculated the temperature coefficients of delay (TCD's) of fresnoite. They found that a layered structure consisting of an oriented fresnoite thin film deposited on a fused quartz substrate should possess excellent SAW characteristics.

Halliyal et al [11,(1981)] prepared $Ba_2TiGe_2O_8$ and $Ba_2TiSi_2O_8$ glass ceramics and studied the piezoelectric, and dielectric properties of them. These glass ceramics possessed pyroelectric responses up to 50% of the values reported for single crystals of them. Halliyal et al [12,(1984)] also measured the electromechanical and hydrostatic piezoelectric properties of both grain-oriented glass fresnoite and single crystal fresnoite. The glass ceramics they prepared showed great promise for various hydrophone and piezoelectric device applications.

Ayukawa [13,(1983)] used both R.F. diode-magnetron and

R.F. triode sputter deposition techniques to prepare thin films of fresnoite. He sputtered at low substrate temperatures and obtained a c-axis oriented thin film on a NaCl substrate which was heated to 170°C. However, the maximum thickness of his thin films was only 4000Å.

Halliyal et al [14,(1985)] and Markgraf et al [15,(1985)] analyzed the dielectric, piezoelectric, and pyroelectric properties of fresnoite single crystal and glass ceramics in the temperature range of -150 to 200°C. The dielectric constant, pyroelectric coefficient, and planar coupling coefficient exhibited maximum values at 160°C; and the frequency constant exhibited a minimum value at this temperature. X-ray intensity data collected at 24 and 300°C failed to identify a phase transition at 160°C. It was postulated that these anomalies could be the result of large oxygen displacements which change some of the elastic constants enough to cause a sign reversal of the pyroelectric coefficients.

The physical and chemical properties of fresnoite are shown in Table 1.

2.2 Properties of Dielectric Materials

Dielectric materials have many unique properties. These properties include: piezoelectricity, pyroelectricity, and ferroelectricity, and they result from the structure of the crystal.

Piezoelectricity is defined in the following manner. The direct piezoelectric effect is the appearance of electric polarization due to an applied stress or strain. The converse

TABLE 1

Physical and Chemical Properties of Fresnoite

Property		Reference
Chemical Formula	$Ba_2Si_2TiO_8$	1
Crystal Structure	Tetragonal	1
Space Group	P4bm	3
Lattice Constants	a = 0.852±0.001 nm c = 0.521±0.0005 nm	3 3
Specific Gravity	4.45±0.02	6
Colour	lemon or canary yellow	1
Vickers Indentation Hardness (20°C)	380 ± 17 kg·cm^{-2}	6
Melting Point	1445±5°C	6
Solvents	1:1 hot HCl and cold glacial acetic acid	1

piezoelectric effect is the appearance of a stress or strain in a crystal due to the application of an electric field. These effects were first discovered by Pierre and Jacques Curie in 1880 [16,(1971)]. In non-pyroelectric materials, what occurs is that the applied stress separates the centre of gravity of the positive charges from the centre of gravity of the negative charges, thus producing a permanent dipole moment. Thus the piezoelectric effect is limited to those crystals which are <u>not</u> centrosymmetric.

Figures 1 and 2 show the structure of fresnoite projected on the x-y and x-z planes respectively. These figures show that the unit cell of fresnoite consists of four silicon centred oxygen tetrahedra which are joined to a compressed titanium centred oxygen square pyramid. Figure 1 shows that fresnoite is centrosymmetric in the x-y plane. However, Figure 2 shows that this is not true for the x-z plane. This is where fresnoite receives its piezoelectric character.

The piezoelectric effect is a first order effect. That is, the electric field produced varies linearly with the applied stress and the field produced reverses sign when the sign (or direction) of the stress is reversed.

Electrostriction is a phenomena exhibited by all dielectrics. It is the production of mechanical strain due to the application of an electric field which displaces molecules or ions. The strain produced is proportional to the square of the applied field and thus a reversal in the sign of the field will not reverse the direction of the strain [17,(1964)].

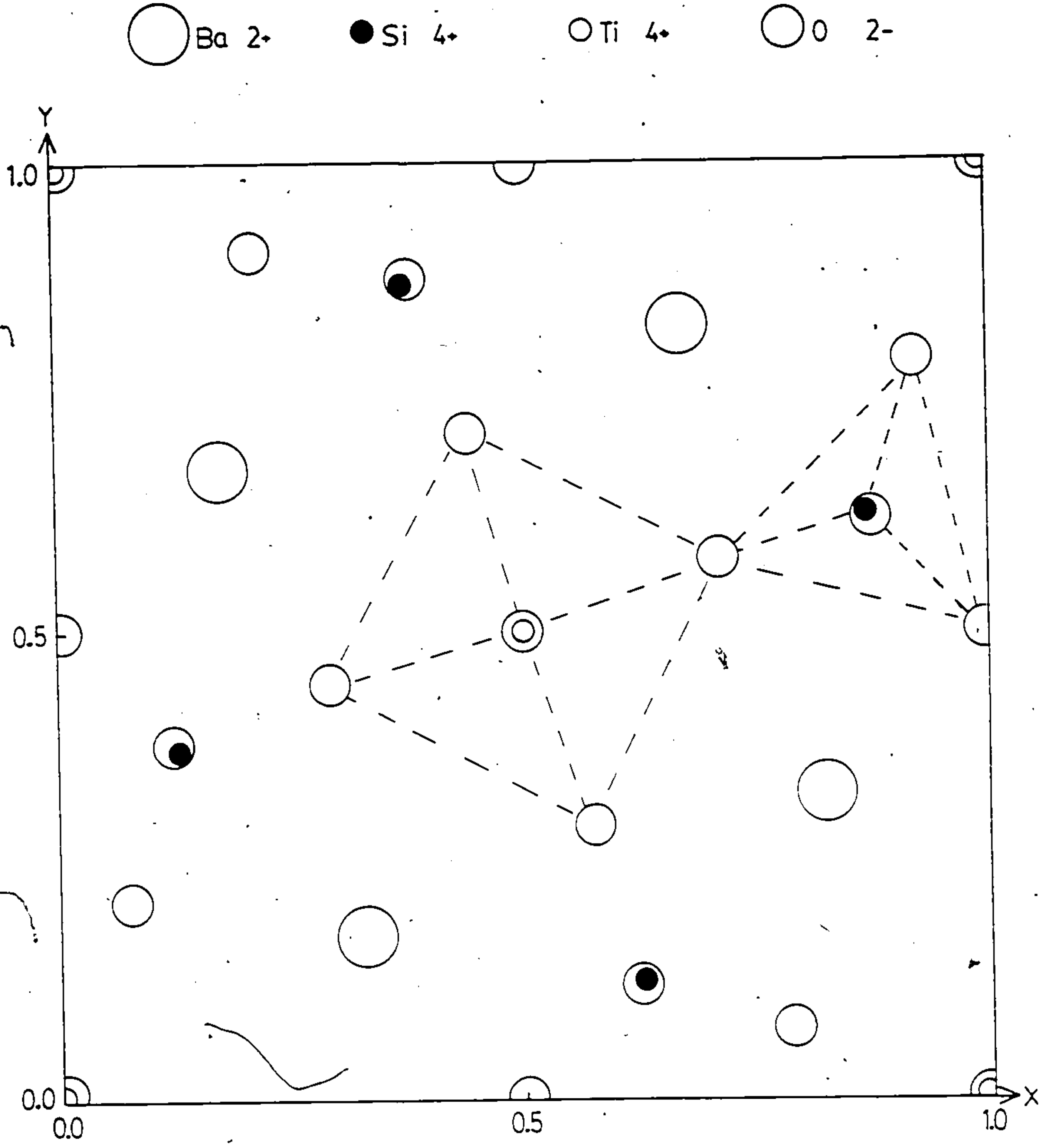

Figure 1 Structure of fresnoite projected on the X-Y plane [4,(1967)]. Fresnoite is symmetrical in this plane.

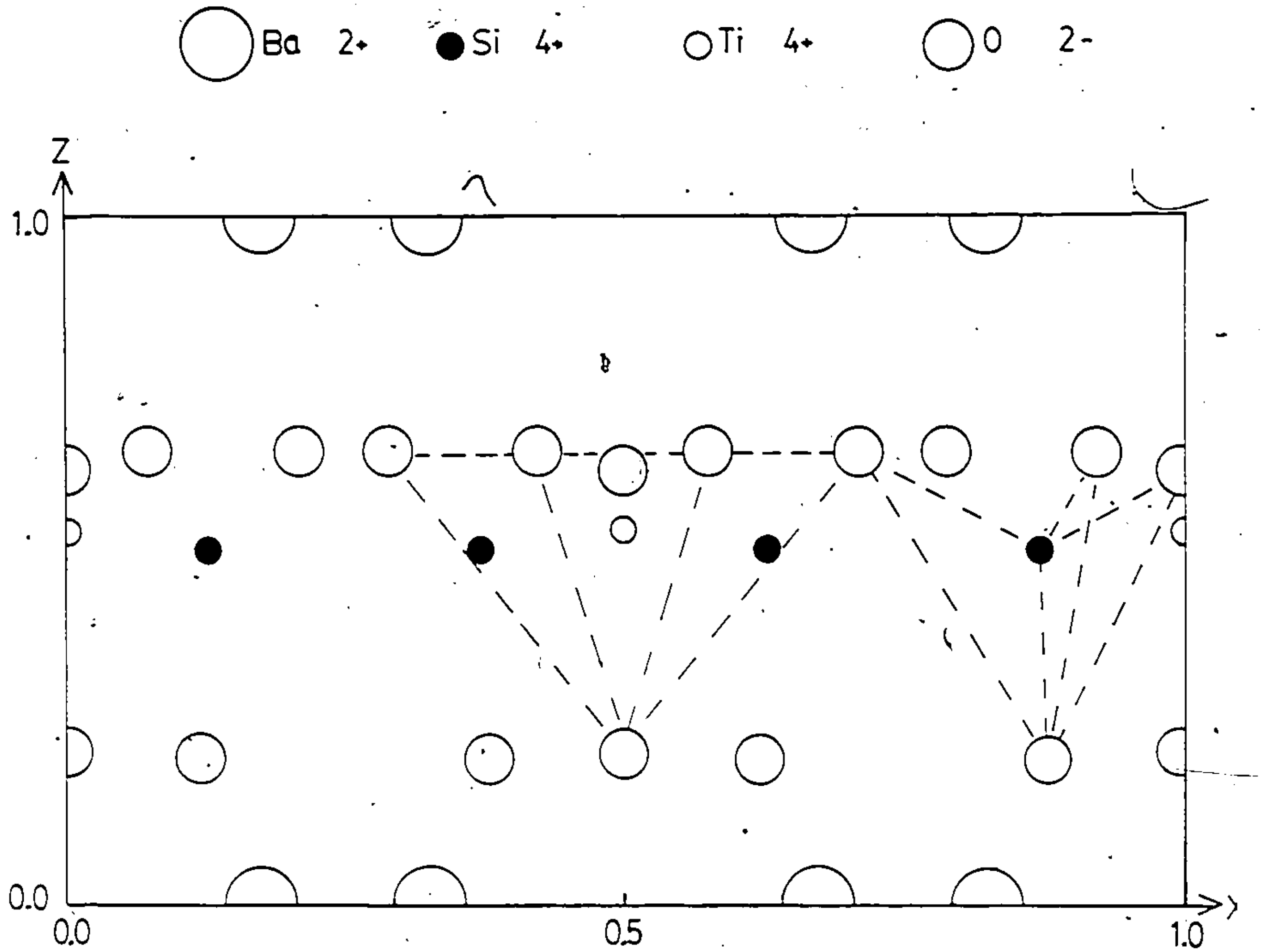

Figure 2 Structure of fresnoite projected on the X-Z plane [4,(1967)]. Fresnoite is not symmetrical in this plane.

Phenomena of this nature are known as second order or quadratic effects.

Some crystals change the magnitude of their spontaneous polarization when heated. These crystals are said to be pyroelectric. The direct pyroelectric effect occurs when there is a change in the positive and negative polarization in certain parts of a crystal due to an increase in temperature. All pyroelectric crystals are piezoelectric. Thus, when a crystal is heated it expands and receives an additional electric charge due to the direct piezoelectric effect. This is called the indirect pyroelectric effect [18,(1979)].

A crystal is ferroelectric if it has two or more orientational states in the absence of an electric field and it can be shifted from one state to another by an electric field [19,(1977)]. Ferroelectric materials are a subset of pyroelectric materials which are in turn a subset of piezoelectric materials. There are 32 crystal classes. Of these, 10 are centrosymmetric and exhibit no piezoelectric character. Piezoelectricity is demonstrated by 21 of the remaining 22 crystal classes, and 10 of these 21 are also pyroelectric. Crystal symmetry considerations cannot be used to predict ferroelectricity; it can only be tested for experimentally.

2.2.1 Piezoelectric Relations

Piezoelectricity is a linear property. For the direct piezoelectric effect, the applied stress σ (a second rank tensor) is related to the polarization P (a first rank tensor) by:

$$P_i = d_{ijk}\sigma_{jk\,(i,j,k\,=\,1\to 3)} \qquad (1)$$

where d_{ijk} are the piezoelectric moduli.

Note that in Eqn. (1), the summation notation is employed, i.e.,

$$d_{ijk}\sigma_{jk} = \sum_{j=1}^{3}\sum_{k=1}^{3} d_{ijk}\sigma_{jk}$$

The piezoelectric moduli form a third rank tensor that has 27 elements. However, symmetry considerations lead to:

$$d_{ijk} = d_{ikj} \qquad (2)$$

which reduces the number of independent moduli to 18.

So far, tensor notation has been used. In practice, matrix notation is usually used. This notation doesn't reduce the number of independent moduli, but it does reduce the number of suffixes. If matrix notation is used, Eqn. (1) becomes:

$$P_i = d_{ij}\sigma_{j\,(i=1\to 3,\ j=1\to 6)} \qquad (3)$$

Similarly, the relationship for the converse piezoelectric effect is:

$$\varepsilon_j = d_{ij}E_{i\,(i=1\to 3,\,j=1\to 6)} \qquad (4)$$

where, ε_j are the components of the strain tensor (2nd rank);

E_i are the components of the electric field intensity intensity tensor (1st rank).

The most important parameter used to characterize piezoelectric materials is the electromechanical coupling factor (k^2). This factor can be defined by the use of thermodynamical relations.

If a constant temperature is assumed, the Gibb's free energy of a crystal can be written as:

$$\Delta G = \Delta U - \varepsilon_i\sigma_i - D_m E_m \quad (i=1\to6, m=1\to3) \tag{5}$$

where, U = internal energy;

ε = strain (2nd rank tensor);

σ = stress (2nd rank tensor);

D = electric displacement (1st rank tensor);

E = electric field intensity (1st rank tensor);

A reversible process is assumed, so that $\Delta U = 0$. If σ and E are taken to be the dependent variables (this is an arbitrary decision), then:

$$dG = -\varepsilon_i d\sigma_i - D_m dE_m \ . \tag{6}$$

Thus,

$$\varepsilon_i = \left(\frac{-\partial G}{\partial \sigma_i}\right)_E \tag{7a}$$

$$D_m = \left(\frac{-\partial G}{\partial E_m}\right)_\sigma \quad (i=1\to6, m=1\to3) \tag{7b}$$

Exact partial derivatives of ε_i and D_m are taken to yield,

$$d\varepsilon_i = \left(\frac{\partial \varepsilon_i}{\partial \sigma_j}\right)_E d\sigma_j + \left(\frac{\partial \varepsilon_i}{\partial E_m}\right)_\sigma dE_m \quad (i,j=1\to6; m=1\to3) \tag{8a}$$

$$dD_m = \left(\frac{\partial D_m}{\partial \sigma_j}\right)_E d\sigma_j + \left(\frac{\partial D_m}{\partial E_k}\right)_\sigma dE_k \quad (j=1\to6; m,k=1\to3) \tag{8b}$$

If Eqns. (7) and (8) are combined, it is seen that,

$$\left(\frac{\partial \varepsilon_i}{\partial E_m}\right)_{\sigma,T} = \left[\frac{\partial}{\partial E_m}\left(-\frac{\partial G}{\partial \sigma_i}\right)_E\right]_T = \left[\frac{\partial}{\partial \sigma_i}\left(\frac{-\partial G}{\partial E_m}\right)_\sigma\right]_{E,T} = \left(\frac{\partial D_m}{\partial \sigma_i}\right)_{E,T} \equiv d^T_{mi} \tag{9a}$$

Similarly,

$$\left(\frac{\partial \varepsilon_i}{\partial \sigma_j}\right)_E \equiv s_{ij}^E \qquad (9b)$$

$$\left(\frac{\partial D_m}{\partial E_k}\right)_\sigma \equiv \varepsilon_{mk}^\sigma \,. \qquad (9c)$$

Eqn. (8) can now be rewritten as:

$$d\varepsilon_i = s_{ij}^E d\sigma_j + d_{mi}^T dE_m$$

$$dD_m = d_{mj}^T d\sigma_j + \varepsilon_{mk}^\sigma dE_k$$

Thus,

$$\varepsilon_i = s_{ij}^E \sigma_j + d_{mi}^T E_m \qquad (10a)$$

$$D_m = d_{mj}^T \sigma_j + \varepsilon_{mk}^\sigma E_k \qquad (10b)$$

$$(i,j=1\rightarrow 6, m,k=1\rightarrow 3)$$

If only small changes in σ_j and E_m are considered, and they are measured from their equilibrium values, then the total energy due to mechanical effects (U_M) can be written as,

$$U_M = \int \varepsilon_i d\sigma_i \,. \qquad (11)$$

Similarly, the total energy due to electrical effects (U_E) can be written as:

$$U_E = \int D_m dE_m \qquad (12)$$

Substitution of Eqn. (10) into Eqn. (11) and Eqn. (12) yields:

$$U_M = \int \varepsilon_i d\sigma_i = \int (s_{ij}^E \sigma_j + d_{mi}^T E_m) d\sigma_i$$

$$= \tfrac{1}{2} s_{ij}^E E \sigma_j \sigma_i + \tfrac{1}{2} d_{mi}^T E_m \sigma_i \qquad (13)$$

$$U_E = \int D\, dE_m = \int (d^T_{mj}\sigma_j + \varepsilon^\sigma_{mk}D_k)\, dE_m$$

$$= \tfrac{1}{2} d^T_{mj}\sigma_j E_m + \tfrac{1}{2}\varepsilon^\sigma_{mk}E_kE_m \qquad (14)$$

The total energy of the piezoelectric system is $U = U_m + U_E$.

$$U = \tfrac{1}{2} s^E_{ij}\sigma_j\sigma_i + d^T_{mi}E_m\sigma_i + \tfrac{1}{2}\varepsilon^T_{mk}E_kE_m \qquad (15)$$

which may be defined as:

$$U \equiv U_{MM} + 2U_{ME} + U_{EE} \qquad (16)$$

The electromechanical coupling factor (k) is now defined by the relation:

$$k = \frac{U_{ME}}{\sqrt{U_{MM}U_{EE}}} \qquad (17)$$

Eqn. (17) is very difficult to evaluate in the most general cases, but it can be simplified considerably by symmetry or when most stresses are zero. For example, a piezoelectric material which has its c-axis aligned to the z direction, and has its a and b axes randomly oriented will behave, on average, as (and consequently can be treated as) a crystal in the 6mm class [20,(1978)]. Table 2 shows the formulae of different coupling factors for the 6mm class, as well as the elastic conditions and the geometry of a typical resonant element.

2.2.2 Applications of Piezoelectric Materials

The first practical piezoelectric devices utilized barium titanate ($BaTiO_3$). This material was independently discovered in the United States, Japan, and the Soviet Union during the latter stages of World War II. Today, piezoelectric materials

TABLE 2

Electromechanical Coupling Factors for 6mm Class Crystals [21,(1964)]

Coupling Factor	Elastic Conditions	Typical Resonant Element	Formula
k_{31}	$\sigma_1\neq 0;\sigma_2=\sigma_3=0$ $\varepsilon_1\neq 0;\varepsilon_2\neq 0;\varepsilon_3\neq 0$	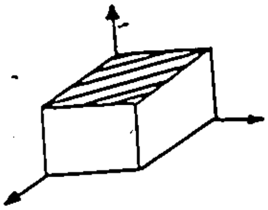	$\frac{d_{31}}{\sqrt{\varepsilon_{33}^{\sigma}s_{11}^{E}}}$
k_{33}	$\sigma_1=\sigma_2=0;\sigma_3\neq 0$ $\varepsilon_1=\varepsilon_2\neq 0;\varepsilon_3\neq 0$	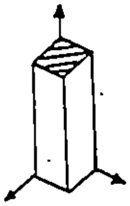	$\frac{d_{33}}{\sqrt{\varepsilon_{33}^{\sigma}s_{33}^{E}}}$
k_p	$\sigma_1=\sigma_2\neq 0;\sigma_3=0$ $\varepsilon_1=\varepsilon_2\neq 0;\varepsilon_3\neq 0$		$k_{31}\sqrt{\frac{2}{1-\sigma^{E}}}$
k_t	$\sigma_1=\sigma_2\neq 0;\sigma_3\neq 0$ $\varepsilon_1=\varepsilon_2=0;\varepsilon_3\neq 0$	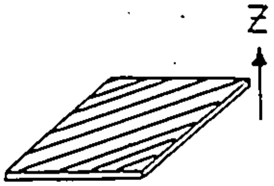	$h_{33}\sqrt{\frac{\varepsilon_{33}^{\varepsilon}}{c_{33}^{D}}} =$ $\frac{k_{33}-Ak_p}{\sqrt{1-A^2}\sqrt{1-k_p^2}}$

where $\sigma^E = \frac{-s_{12}^E}{s_{11}^E}$ (Poisson's ratio)

$$A = \frac{\sqrt{2}\, s_{13}^E}{\sqrt{s_{33}^E(s_{11}^E+s_{12}^E)}} \quad ; \quad h_{33} = (\varepsilon^S)_{3n}^{-1}\, e_{n_3} = d_{mn}c_{n_3}^E$$

(m,n=1→3)

are employed in a wide range of devices. Table 3 shows the applications and piezoelectric components of some of these devices.

SAW devices are among the newest family of piezoelectric devices. These devices have many potential applications [23,(1972); 24,(1972)]. The three different types of materials which can be used for SAW devices are: piezoelectric single crystals, piezoelectric ceramics, and piezoelectric thin films deposited on a non-piezoelectric substrate. There are many parameters used to characterize the suitability of a piezoelectric material for SAW use. The three main parameters are: the electromechanical coupling factor (k^2), the temperature coefficient of SAW delay (TCD), and the power flow angle (PFA).

The electromechanical coupling factor (k^2) will vary depending on the geometry under investigation. For SAW analysis, k^2 can be approximated by [25,(1968); 26,(1972)]:

$$k^2 \approx \frac{2(V_\infty - V_o)}{V_\infty}$$

where, V_∞ is the SAW velocity on a free surface (electrically open surface);

V_o is the SAW velocity in the presence of an infinitesimally thin perfect conductor (electrically shorted surface).

The temperature coefficient of SAW delay (TCD) is defined as [27,(1970)]:

$$\text{TCD} \equiv \alpha - \frac{1}{V_\infty}\frac{dV_\infty}{dT}$$

where, α is the thermal expansion coefficient along the direction of the acoustic wave.

TABLE 3

Applications and Piezoelectric Components of Some Piezoelectric Devices [22,(1982)]

Device	Piezoelectric Materials(s)	Applications
Ultrasonic transducers	$BaTiO_3$, PZT* Ceramics	Fish finders, ultrasonic cleaners; ultrasonic humidifiers, ultrasonic processing machines, burglar alarm systems, T.V. remote controls, ultrasonic diagnosis machines.
Audio transducers	PZT Ceramics, $BaTiO_3$	Piezoelectric buzzers, underwater microphones.
Measurement devices	PZT Ceramics, $BaTiO_3$	Pressure measurement devices, vibration measurement devices.
Quartz filters	Quartz single crystals	Narrow band filters.
Mechanical filters	Piezoelectric ceramics (eg., PZT) combined with an alloy that has a constant elastic modulus.	Low frequency filters.
Ceramic filters	Piezoelectric ceramics	Wide range of consumer electronics.
SAW devices	Quartz, $LiNbO_3$, $LiTaO_3$	High frequency filters, delay lines, oscillators, amplifiers.
High voltage devices	PZT ceramics	Piezoelectric igniters for a wide range of gas apparatuses. Piezoelectric transformers.

* PZT refers to the family of $Pb(Zr,Ti)O_3$ ceramics.

Piezoelectric materials are anisotropic in nature. This leads to the consideration of the power flow angle (PFA), which is the angle between the phase and group velocity vectors. For isotropic materials, the PFA is always zero, but for anisotropic materials, the PFA is zero only for specific crystal directions [28,(1973)].

In general, for SAW device applications, a high k^2, low TCD, and nearly zero PFA are simultaneously required - with the first two criterion being the most important. Table 4 shows the k^2 and TCD values for various piezoelectric materials.

Quartz is the most widely used material for SAW devices. Quartz single crystals are not easy to grow, but the conditions necessary have been well established. These crystals are also inexpensive and possess very stable temperature characteristics (a zero value of TCD). Lithium niobate ($LiNbO_3$) has the highest k^2 value among all the single crystals, but it has a very poor temperature stability. Table 4 shows the fresnoite single crystals have SAW characteristics between those of $LiNbO_3$ and $LiTaO_3$. The piezoelectric ceramics shown in Table 4 have a high k^2 and very good temperature stability. The only drawback associated with these materials is their high acoustic losses, which are due to the many grains in the ceramic, and therefore it is difficult to use them in high-frequency devices.

Present research in SAW device materials involves the fabrication of piezoelectric thin films on non-piezoelectric substrates. The chief advantage of these materials over those shown in Table 4 is a significantly lower material cost due to the fact that the piezoelectric thin film is much smaller in volume than the piezoelectric ceramic or single crystal.

TABLE 4

SAW Characteristics of Piezoelectric Single Crystals and Piezoelectric Ceramics

Piezoelectric Single Crystals

Material	Orientation*	k^2 (%)	TCD (ppm/^{o}C)	Reference
Quartz	ST Cut	0.16	0	[29,(1978)]
$LiNbO_3$	Y Cut Z Direction	4.86	94	[30,(1982)]
$LiTaO_3$	X Cut 119.4^{o} Y Direction	0.77	32	[9,(1978)]
$Ba_2Si_2TiO_8$	Z Cut 45^{o} X Direction	1.5	52	[9,(1978)]
$Pb_2KNb_5O_{15}$	Y-axis Boule 66.6^{o}	1.88	0	[29,(1978)]
$LiIO_3$	Z Cut	0.51	--	[31,(1970)]
Ba_2NaNbO_{15}	Z Cut	0.57	--	[31,(1970)]
CuCl	100 Cut 22^{o}	1.5	60	[32,(1981)]
$Bi_{12}GeO_{20}$	110 Cut 001 Direction	0.85	140	[33,(1973)]
$AlPO_4$	X-axis Boule 80.4^{o}	0.49	0	[34,(1977)]
Tl_3VS_4	110 Cylinder Cut 24^{o}	1.2	0	[35,(1976)]
Tl_3TaSe_4	110 Cylinder Cut 19^{o}	1.7	0	[35,(1976)]
$Li_2B_4O_7$	100 Cut Z Propagating	1.20	0	[36,(1981)]

(cont'd.)

Table 4 (cont'd.)

Piezoelectric Ceramics (z-Cut)

Material	k2 (%)	TCD (ppm/^oC)	Reference
$(Pb_{1-3/2x+\frac{1}{2}z})Nd_x)*Ti_{1-y-z}Mn_yIn_z)O_3^*$	2.6	0	[37,(1978)]
$0.07In(Li_{3/5}W_{2/5})O_3$-$0.49PbTiO_3$-$0.44PbZrO_3$	6.0	-10.7	[38,(1975)]
$Pb(Mn_{1/3}Nb_{2/3})O_3$-$PbTiO_3$-$PbZrO_3$	5.7	17	[39,(1974)]

* where x = 0.1, y - 0.02, z = 0.06.

Piezoelectric thin films of ZnO [41,(1982)], AlN [42,(1983)], and Se [43,(1982)] have been fabricated. All of these films have a fairly high k^2 and a low or zero TCD. In fact, the TCD value of piezoelectric thin films can be modified by the choice of the non-piezoelectric substrate material. The chief requirements of these thin films is that they are: oriented with their c-axis perpendicular to the substrate (so that they are piezoelectric), and that they are easily mass produced.

None of the three thin films previously mentioned are widely used in SAW devices. ZnO films of high orientation and reproducibility have been fabricated, but ZnO absorbs moisture and its performance degrades with time. The reproducibility of zero TCD and AlN and Se thin films are not fully controlled so that these films are not yet available for SAW devices. Yamauchi et al [10,(1979)] calculated that Z cut 45°y fresnoite deposited on a fused quartz substrate would have a zero TCD and k^2 of about 1.6% (for kh ~ 2.0). These values are comparable to ZnO and fresnoite is much more stable than ZnO.

Figure 3 is an equivalent electrical circuit for a piezoelectric crystal vibrator. This circuit consists of a capacitor, C_o, connected in parallel with a series resonant circuit (a series circuit which contains inductance, capacitance, and resistance). The magnitude of these components can be very impressive. For example, the values for an x-cut quartz crystal mounted in air with dimensions of 0.03 m x 0.004 m x 0.0015 m are: $C_o = 3.15 \times 10^{-12}$F, R = 4750Ω, C = 0.0268×10^{-12}F, and L = 457H [44,(1962)]. In IC circuitry

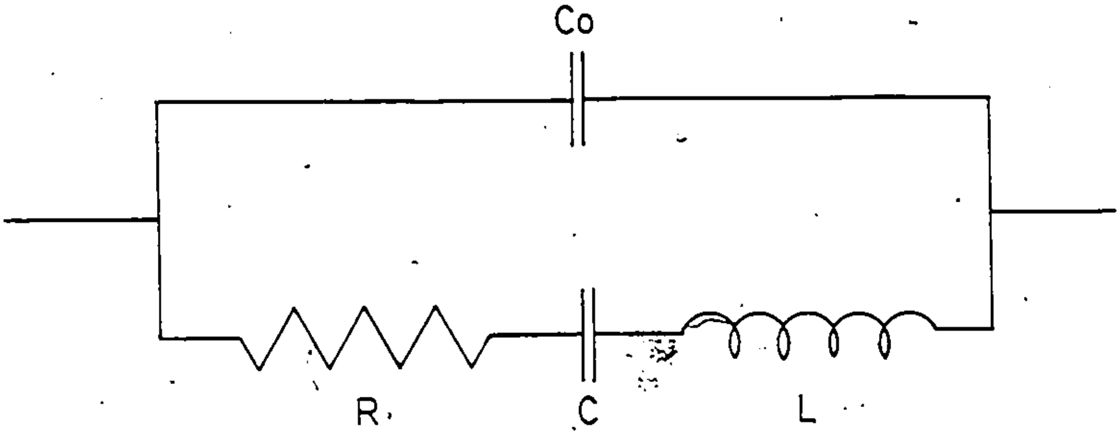

Figure 3 Equivalent electrical circuit for a piezoelectric crystal vibrator.

it is not practical to build in inductance [45,(1971)]. External coils are usually used, and these coils must be manually tuned. However, a coil with the same inductance as the quartz crystal mentioned above would be huge in size and it would also have much higher losses.

Martin et al [46,(1983)] constructed an SAW resonator of ZnO on a silicon substrate. Such a device can be monolithically incorporated in IC circuits and would eliminate the need for off-chip components.

2.3 Sputtering

When a surface is irradiated by energetic particles, surface atoms are eroded and removed. This process is called "sputtering". Although this process was first observed over 125 years ago, it was not extensively studied until about 20 years ago [47,(1982)].

The main advantage of sputtering over other deposition techniques is its versatility. Thin films containing almost every element in the periodic table have been prepared by sputtering. Other advantages provided by sputtering include:

(1) good adhesion between the film and substrate;
(2) thickness and compositional uniformity over large planar areas;
(3) a very high degree of reproducibility.

The principle limitations of sputtering are:

(1) target material must be available in sheet form;
(2) deposition rates are usually less than 2,000 Å/min.

Figure 4 [48,(1974)] is a schematic representation of the sputtering process. The target (source of coating material)

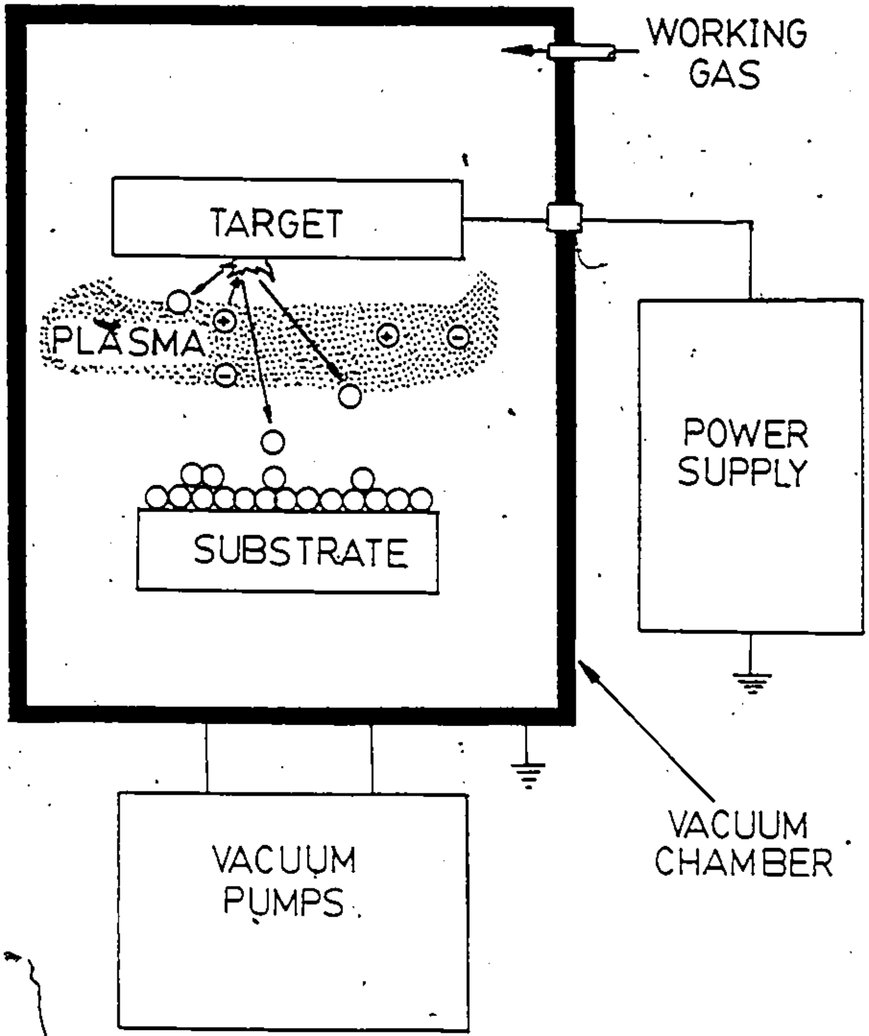

Figure 4 Schematic representation of the sputtering process.

and substrate (object to be coated) are located inside a vacuum chamber. The chamber is evacuated down to a pressure in the range of 1 x 10^{-7} torr and then backfilled with an inert gas (usually argon) to a pressure in the range of 5 x 10^{-4} to 5 x 10^{-2} torr. A high voltage is applied which ionizes the inert gas near the target. An external power supply is used to maintain the target potential negative relative to the plasma. This causes argon ions to be accelerated towards the target, and they strike it with an energy greater than the binding energy of the atoms. Thus, atoms are ejected from the target and strike the substrate which is located to intercept them.

The plasma is an area of ionized gas (ions and electrons) which is confined to the front of the target by a grounded shield and surrounding magnets. Since the walls of the vacuum chamber provide effective surfaces for the recombination of ions and electrons, the only way to maintain a steady-state plasma is to constantly re-ionize the gas.

Various mechanisms are used to sustain the plasma. The simplest and most widely used method is the planar d.c. diode system, which is shown in Figure 5(a). In this system, a d.c. power supply is used to maintain the target as the discharge cathode. The target is fastened by solder or conducting epoxy to a water cooled backing plate. The electrodes are usually separated by about 5 cm., and a voltage (Va) of about 1-6kV is applied between them. This results in the production of an "abnormal glow discharge", which is simply a discharge where the current density increases with Va [49,(1976)].

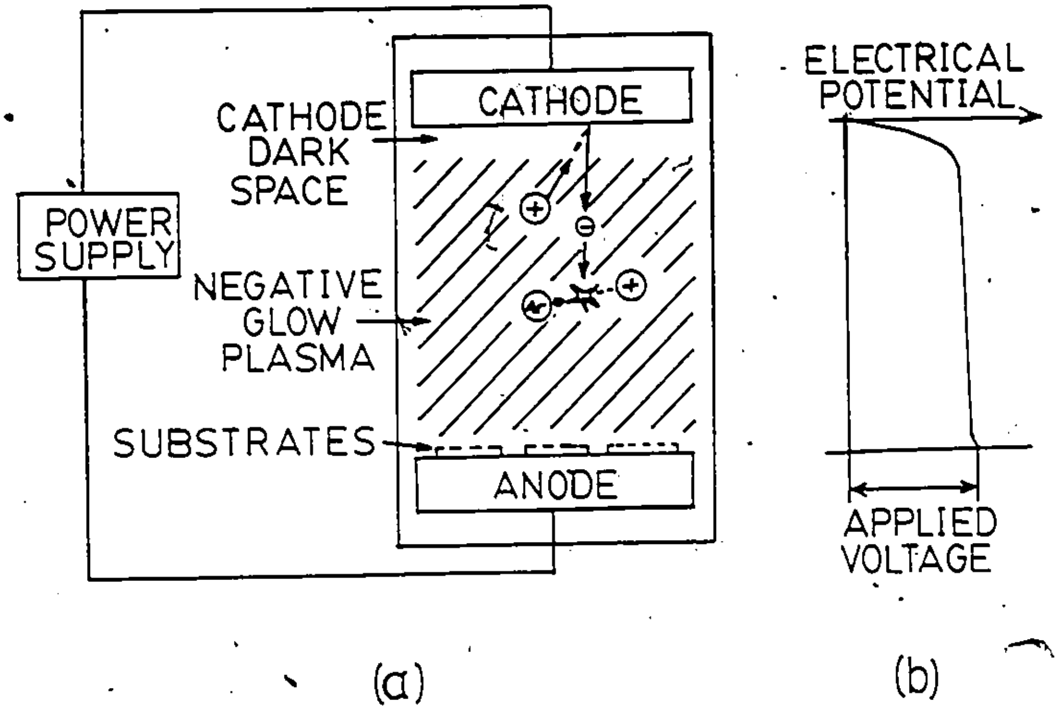

Figure 5(a) Schematic illustration of a planar d.c. diode sputtering system [(48,1974)]. The plasma is sustained if every secondary electron generates enough ions to free one more electron from the cathode.

Figure 5(b) Voltage distribution within the plasma and dark space [48,(1974)]. Most of the applied potential is distributed within the cathode dark space because the plasma is essentially electrically neutral (contains almost an equal amount of ions and electrons).

Figure 5(b) shows the voltage distribution within the plasma and dark space. The plasma contains almost equal amounts of ions and electrons so that most of the applied voltage is distributed in the dark space between the target and the plasma. As the ions go through the plasma and reach the edge of the dark space they are rapidly accelerated towards the target. The ions strike the target and release atoms which traverse the dark space and plasma and are incident on the substrate. The gas ions then pick up electrons from the target and are released from it. Thus it is necessary that the target be an electrical conductor (i.e., be a source of free electrons). If the target was an electrical insulator, it would become coated with inert gas ions and would no longer be sputtered.

In addition to releasing atoms from the target, the inert gas ions also release electrons which are called secondary electrons. These electrons are accelerated in the cathode dark space to energies which approach the applied potential. The electrons then enter the plasma where they collide with argon atoms to create ions and thus sustain the plasma.

The plasma is self-sustaining if each secondary electron generates enough ions to free one more electron from the cathode. The deposition rate is more dependent on the ion density (current) than the ion energy (applied voltage). This is shown in Figure 6, for tantalum films. This means that d.c. planar diode systems must be operated at fairly

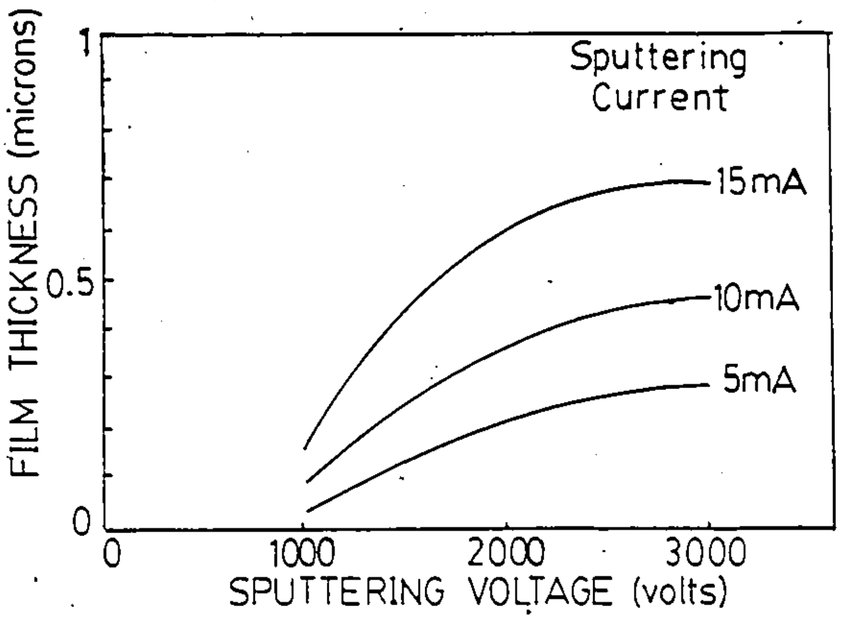

Figure 6 Deposition rate of tantalum films vs. voltage at a constant current [47,(1970)].

high pressures. If the pressure is too low, the secondary electrons will not ionize enough argon ions to maintain the plasma. However, the pressure cannot be too high, because then a significant number of sputtered atoms will undergo elastic collisions with the argon ions within the plasma and they will be deflected away from the substrate.

2.3.1 Triode Sputtering

A triode sputtering system is one that utilizes an external, independent electrode to sustain the plasma. Figure 7 is a schematic illustration of a triode sputtering system. A thermionic emitter (usually W or Ta) is heated by the application of a voltage of about 50V, and electrons are emitted from it and travel across the plasma to the anode. While they travel across the plasma, these electrons make ionizing collisions with argon gas atoms. Thus the maintenance of the plasma is not dependent on the generation of a sufficient number of secondary electrons, and these systems can be operated at pressures substantially below those of d.c. planar diode systems [50(1972)].

The only disadvantage of triode systems is that the thermionic emitter (or filament) is often vulnerable to reactive gases, and care must be taken - especially when sputtering in the presence of oxygen. Also, since it is independent of the power supply, triode sputtering devices can be incorporated into both d.c. and r.f. sputtering systems.

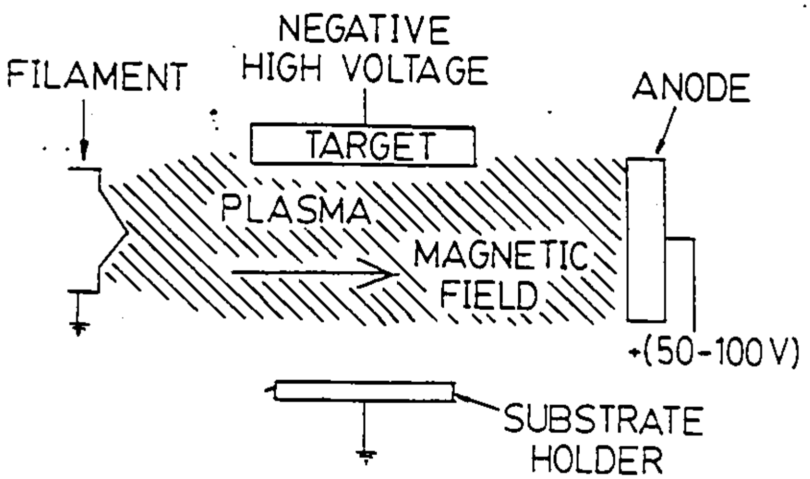

Figure 7 Schematic illustration of a triode sputtering device [52,(1983)]. The magnetic field is used to confine the plasma. A triode sputtering system can be operated at much lower pressures than a conventional planar diode system.

2.3.2 RF Sputtering

RF (or Radio Frequency) sputtering is a technique which was initially outlined by Anderson et al [51,(1962)] to sputter insulating materials. These materials could not be sputtered by conventional (i.e., d.c.) methods because of the charge build-up which occurs on the target surface.

Figure 8 is a schematic illustration of an rf diode sputtering system. This is very similar to the dc diode system shown in Figure 5(a). However, consideration of an rf power supply makes the system shown in Figure 8 much more complex than a d.c. system of a similar size. The variable impedance matching network and the rf power supply combine to form a resonant circuit. The incident and reflected power meters are usually located on the rf generator chassis, and they indicate how well the matching network is adjusted. The matching network is always adjusted so that the reflected power is minimized. The blocking capacitor ensures that the target cannot be shorted to ground through the matching network. An insulator target is usually sufficient for this, but the blocking capacitor provides added insurance by making the system independent of any fluctuations in the target capacitance, and it also enables conductors to be rf sputtered as well as insulators.

A free electron in a vacuum will oscillate in an alternating field and will, on average, absorb no power from the applied field. However, the electron will gain energy when it collides with gas atoms while it is in the field. The

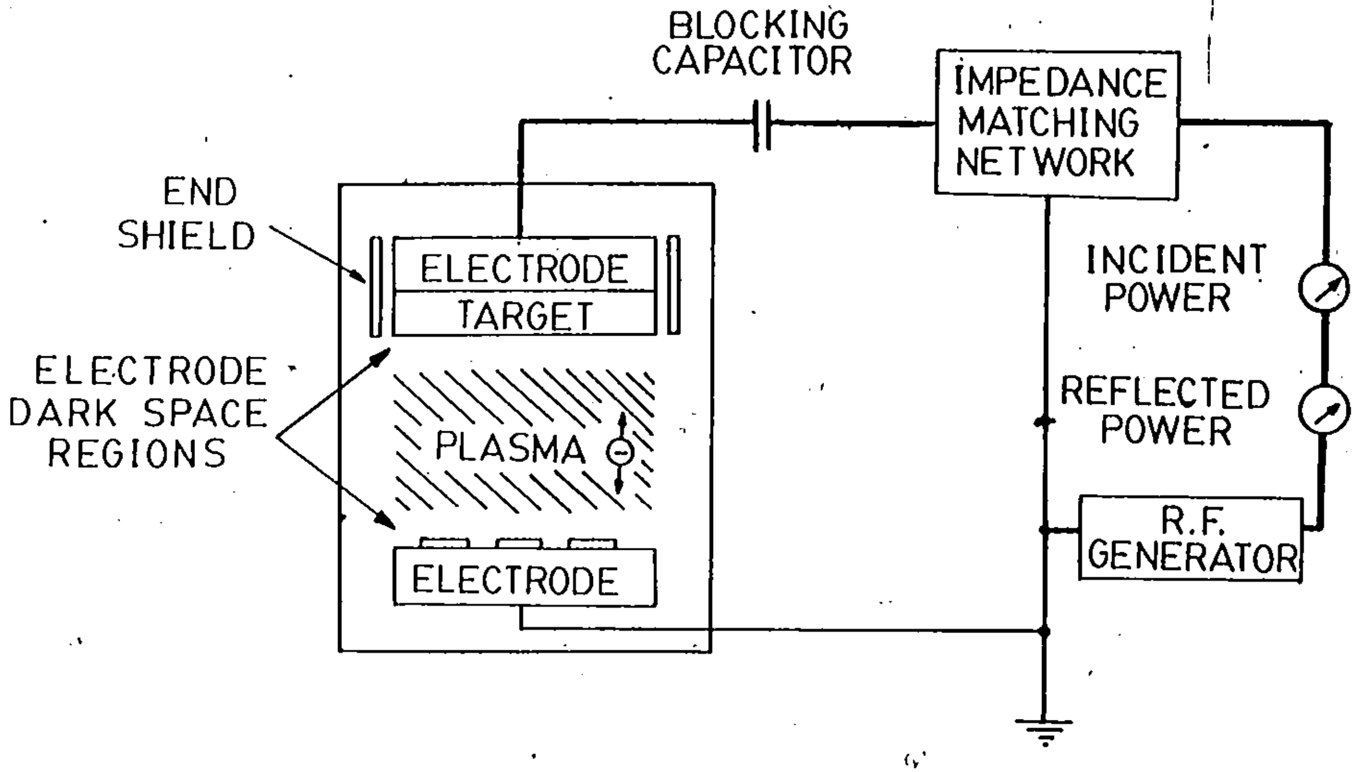

Figure 8 Schematic illustration of the plasma distribution in an r.f. diode sputtering system.

electron will gain energy with each collision until it has enough energy to ionize a gas atom.

At rf frequencies, the electrons are able to oscillate in the field, but the ions which are much heavier cannot. Because of this, relatively few ions strike each electrode during each cycle. Since the ion and electron flow per cycle must balance, the electron cloud has to touch each electrode for only a fraction of a cycle to provide enough electrons to match the total number of incident ions per cycle. Thus the plasma appears as shown in Figure 8, with a dark space in front of each electrode, and the electron cloud, on average, centred between the two electrodes.

When both electrodes are of equal size, material is continuously sputtered from each of them. Usually, the substrate is mounted on an electrode which is much larger than the target electrode. This reduces the current per unit area on the substrate electrode and consequently, the dark space region in front of the substrate is also reduced. Thus argon ions are not accelerated across the dark space with enough velocity to cause sputtering. They do, however, have sufficient energy to cause the desorption of gases when they impinge upon a surface, which results in a much lower level of contaminants in the system, and thus higher quality films. The versatility of rf sputtering (i.e., the fact that both conductors and insulators can be deposited) have led to this technique being very widely used. When a discharge assist device, such as a triode, is used in an rf system, the assist device maintains the plasma, while the rf discharge satisfies the electro-neutrality condition at the insulator target surface.

2.4 Thin Film Analysis

The properties of a thin film are mainly dependent on its chemical composition and structure. The structure of a thin film can usually be determined from both electron and x-ray diffraction techniques. It is more difficult to accurately characterize the composition of a thin film. There are many techniques in use today, and some of the common ones include: Auger electron spectroscopy (AES), electron spectroscopy for chemical analysis (ESCA) (also known as x-ray photoelectron spectroscopy (XPS)), secondary ion mass spectorscopy (SIMS), Rutherford backscattering (RBS), electron probe microanalysis (EPMA), and x-ray fluorescence spectroscopy. These techniques are all surface sensitive; that is, they analyze the thin film surface (or at most a depth of a few microns). Thus the film must be analyzed under a high vacuum to ensure that it remains clean. Each of the techniques discussed herein has its own strengths and is more sensitive to certain elements than others. Consequently, if feasible, more than one technique should be used to characterize a thin film, especially if it is composed of elements that have a wide difference in atomic masses.

2.4.1 Auger Electron Spectroscopy (AES)

Auger electron spectroscopy is a very widely used method of surface analysis. The sample is bombarded by either: a high energy (3-5keV) electron beam, ion beam, or x-rays. At an atomic level, this results in the creation of an electron vacancy in an interior electron shell. The excited atom will return to its ground state when an electron from an outer shell fills the vacancy. Energy is then released as either characteristic x-rays, or it is transferred to another outer level electron which then leaves the atom. These two mechanisms are shown in Figure 9. The energy of the emitted (also known as Auger) electrons can be related to the core atoms. Thus AES is based on the energy analysis of the emitted electrons [53,(1973)].

The Auger process requires three electrons, so AES cannot be used to detect hydrogen or helium. However, AES does provide very good qualitative information on other light elements. Quantitative analysis is only possible with the use of calibration standards. The escape depth of the Auger electrons is only 5-20Å; consequently, depth analysis is only possible if AES is combined with in-situ sputtering.

Auger analysis is usually limited to materials with electrically conductive surfaces. Techniques such as bombarding the surface with an ion beam to neutralize any charge accumulation and the implantation of metal grids have been used to Auger analyze insulator materials, but these methods have not been widely accepted [62,(1978)].

It is standard practice in AES measurements to plot the first derivative of the signal from the detector. This is

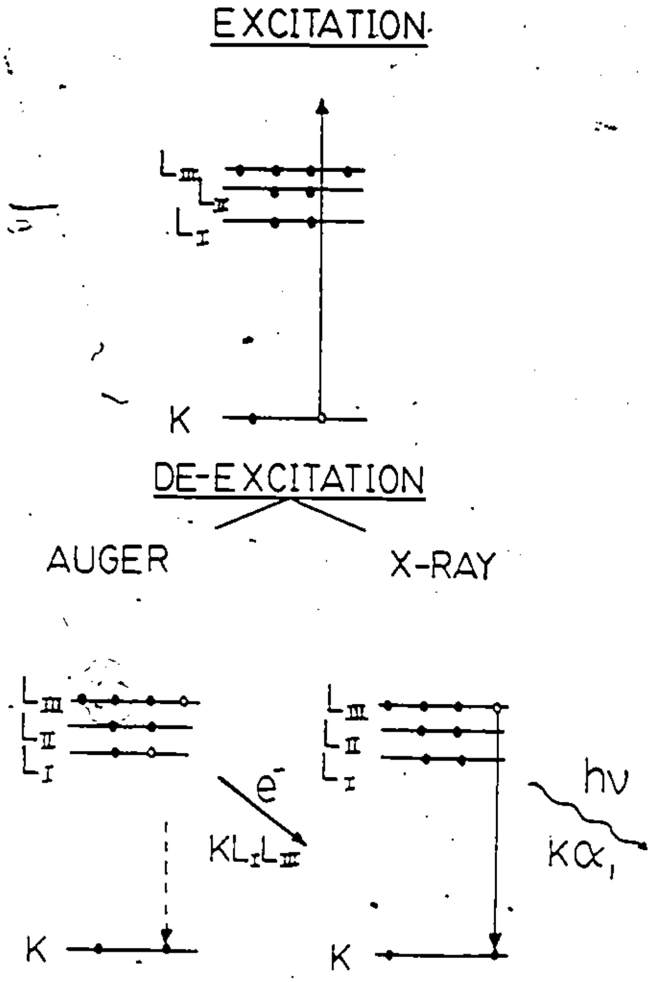

Figure 9 Two modes of atomic de-excitation which follow the creation of an inner shell vacancy. The Auger mode occurs when the L_I electron falls back into the K shell, and energy is given up to the L_{III} electron which is then liberated. The x-ray mode results in the emission of a photon. Auger emission is more probable for lighter elements [54,(1967)].

done to suppress background effects and it was this procedure that helped make AES so popular [63,(1982)].

2.4.2 Electron Spectroscopy for Chemical Analysis (ESCA or XPS)

This surface analysis technique is similar to AES. The sample is irradiated with an x-ray beam, and the ejected photoelectrons are analyzed in a magnetic or electrostatic spectrometer. Figure 10 is a schematic illustration of an ESCA experiment. The kinetic energy (E_{kin}) of the ejected photoelectron is given by [54,(1968)]:

$$E_{kin} = E_{x\text{-ray}} - E_b - E_r$$

where, $E_{x\text{-ray}}$ is the quantum energy of the x-ray photon;

E_b is the binding energy of the electron;

E_r is the recoil energy.

The recoil energy is normally very small ($E_r << 1.0$ eV) and thus it is usually ignored. A correction factor which accounts for an interaction between the source material and spectrometer material is also incorporated into the above relation. The resolution of the spectrometer is very high. This enables bond information to be determined, since the chemical state of an atom will affect the binding energy of its electrons. Standards are needed to perform quantitative analysis, but the results obtained are generally more reliable than those obtained by AES. Sputtering must be used to obtain depth profiles.

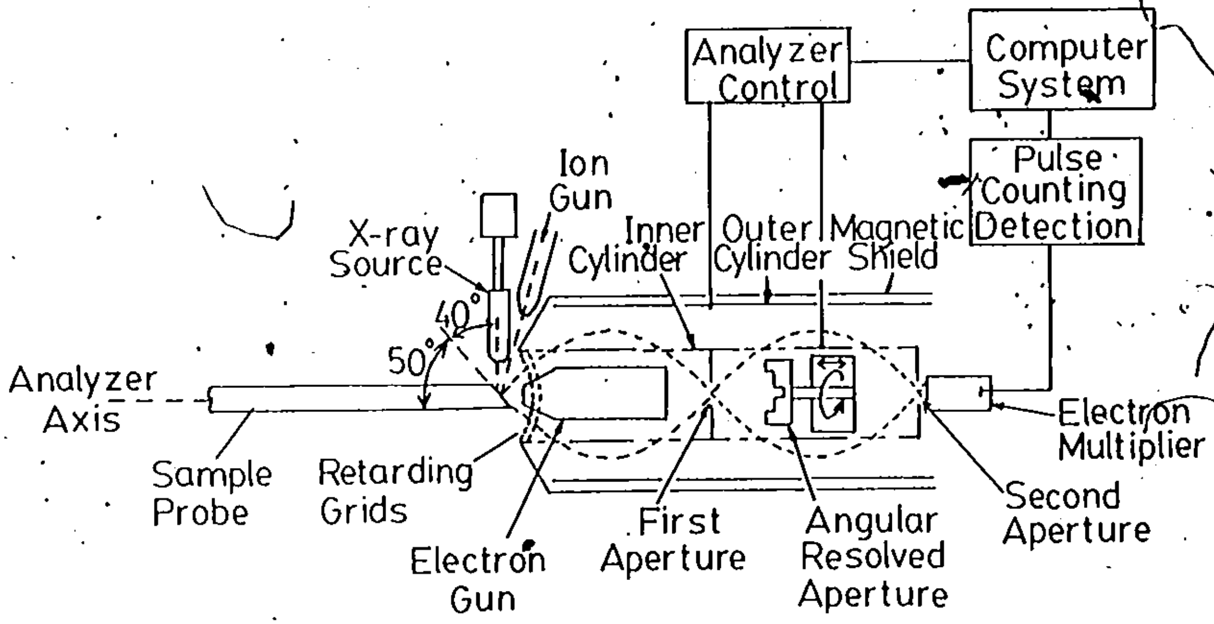

Figure 10 , Schematic illustration of an ESCA experiment [88,(1979)].

2.4.3 Secondary Ion Mass Spectrometry (SIMS)

SIMS is the most widely used ion beam surface analysis technique. It utilizes a high energy (1-25 keV) beam of primary ions to bombard the sample. The sample surface is sputtered, and the sputtered species include: neutral atoms and molecules, secondary electrons, photons, and positive and negative ions. The ejected ions are analyzed by a mass spectrometer.

SIMS is the only method which can detect both hydrogen and helium [55,(1973)]. However, quantitative results are extremely difficult to obtain - even with the use of external standards. Since the ion beam removes surface atoms, depth profiles can be obtained, but the sample is destroyed in the process.

2.4.4 Rutherford Backscattering (RBS)

RBS is a very versatile method of compositional analysis. The sample is bombarded with a beam of mono-energetic ions (hydrogen, helium, or any other light element). These ions are accelerated by a 1-4MV nuclear particle accelerator. A schematic illustration of an RBS experiment is shown in Figure 11.

If the incident ion is backscattered by a surface atom, the energy lost is dependent only on the mass of the target atom, mass of the incident ion, and the backscattering angle. If the incident ion is not scattered by a surface atom, it will also lose energy due to ionization and excitation processes it undergoes as it penetrates the target. The ion will

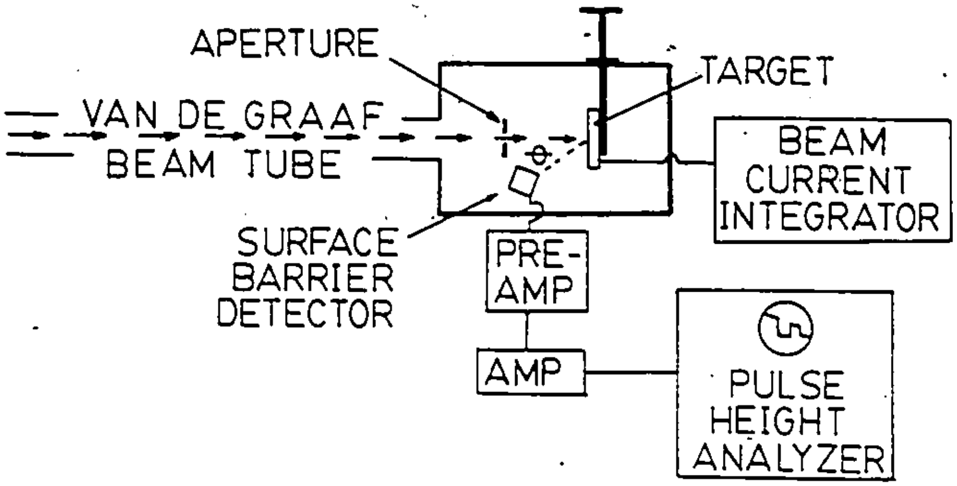

Figure 11 Schematic illustration of an RBS experiment.

also be slowed down on its way back to the surface [56,(1973)]. These mechanisms enable RBS to provide depth profile information as well as compositional information. This is one of the two main advantages of this technique - the ability to provide depth profile information without destructively sputtering the sample. This is very important because sputtering the surface of a sample can give rise to surface roughness and preferential sputtering effects (all elements are not necessarily sputtered at the same rate) and thus the composition analyzed may not be the true one which can lead to interpretational errors [61,(1976)]. Thus it is desirable to obtain depth profiles without sputtering the sample. The other advantage of RBS is the fact that it can provide absolute quantitative information without the use of external standards.

RBS is most sensitive to elements with 30<z<50 (where z is the atomic number), but it can detect all elements with z>10. RBS cannot distinguish between two very heavy elements unless they differ by at least 10 a.m.u. [57,(1972)]. RBS also cannot provide any information on the chemical state of the elements in the sample.

2.4.5 Electron Probe Microanalysis (EPMA)

EPMA is a technique that can be used to determine the chemical composition of a specimen with a volume as small as one cubic micron. The specimen is struck by a beam of electrons which are accelerated by a voltage of 10-30 kV. This causes the emission of the characteristic x-ray spectrum of the sample.

Tradiationally, the emitted x-ray spectrum is analyzed by the wavelength dispersion method. The x-rays are dispersed spatially by crystal diffraction before they reach a detector. Thus the detector receives only one wavelength at a time, and it must be scanned over the whole 2θ range [60,(1978)]. Quantitative analysis is made by comparing the intensity of the emitted x-rays of both the sample and an external standard. Any standards used should be in a form which is similar to that of the sample. Various corrections are made when the relative intensities are compared. These corrections include allowances for: atomic number, x-ray absorption, and x-ray fluorescence [58,(1974)].

2.4.6 X-ray Fluorescence Spectrometry

X-ray fluorescence spectrometry is an analysis technique that is similar in principle to EPMA. The sample is bombarded with photons (whereas in EPMA it is struck by a beam of electrons) which causes it to emit its characteristic x-rays.

The emitted spectrum is usually analyzed by the wavelength dispersion technique. However, it can also be analyzed by the energy dispersion technique. The x-rays are intercepted by a lithium drifted silicon, Si(L), detector. The detector generates a pulse of electric current for each x-ray photon it receives, with the height of the pulse proportional to the energy of the x-ray. The elements present are identified by the energy spectrum obtained from the detector. This method is relatively quick and provides good qualitative results. Quantitative results are obtained only by the use of standards, and the accuracy obtained is limited by the resolution of the detector - which is only about 150 eV [59, (1974)]. Problems can arise from multi-component samples composed of elements which possess overlapping energy spectra. The separation of overlapping energy peaks is very difficult and can lead to very uncertain results.

Many scanning electron microscopes have the capability of performing chemical analysis using a technique known as energy-dispersive x-ray spectrometry (EDS). The incident beam of electrons which is used to generate the image causes the emission of the characteristic x-ray spectrum of the sample. The spectrum is analyzed by the energy dispersion technique described above. EDS is very widely used, but results are influenced by the same factors that affect EPMA and x-ray fluorescence spectrometry.

CHAPTER 3

EXPERIMENTAL PROCEDURE

3.1 Ceramic Sputtering Target Fabrication

The ceramic sputtering targets used throughout this work were fabricated by mixing high purity (>99.95% pure) $BaCO_3$, SiO_2 and TiO_2 oxide powders according to the formula,

$$2BaCO_3 + 2SiO_2 + TiO_2 \rightarrow Ba_2Si_2TiO_8 + 2CO_2 \uparrow$$

The fabrication procedure is outlined below. It was adopted from a procedure developed by the Hitachi Central Research Laboratory and is similar to the method used by M. Ayukawa [13,(1983)] at the University of Windsor.

1. $BaCO_3$(1), SiO_2(2), and TiO_2(3) oxide powders were dried on a hot plate at 150°C for two hours. This removed any moisture absorbed by the powders.
2. Immiediately after they were baked, the powders were weighed in the desired proportions. Table 5 shows the ratios used.
3. The powders were placed in a ball mill(4) and distilled water was added. They were then mixed for 24 hours. The ball mill, jar, and balls are shown in Figure 12.
4. The powder was dried on a hot plate until all the water had evaporated. This took approximately 10 hours.

---

(1) Fisher Scientific Co., cat. no. B-30.
(2) Fisher Scientific Co., cat. no. S-662.
(3) Fisher Scientific Co., cat. no. T-315.
(4) Norton Scientific Co.; Canlab cat. no. C8700-1, C8750-4, C8775-1A.

TABLE 5

Ratio of the Oxide Powders Used in the Fabrication of Ceramic Sputtering Targets

Powder Composition	Weight Ratio of $BaCO_3:SiO_2:TiO_2$	Amounts of $BaCO_3$, SiO_2, TiO_2 Necessary To Yield 100g of Raw Powder
$Ba_2Si_2TiO_8$	4.94:1.504:1.00	66.40g $BaCO_3$ 20.16g SiO_2 13.44g TiO_2
$Ba_{2.99}Si_2Ti_{0.8}O_{8.59}$	9.23:1.88:1.00	76.22g $BaCO_3$ 15.52g SiO_2 8.26g TiO_2

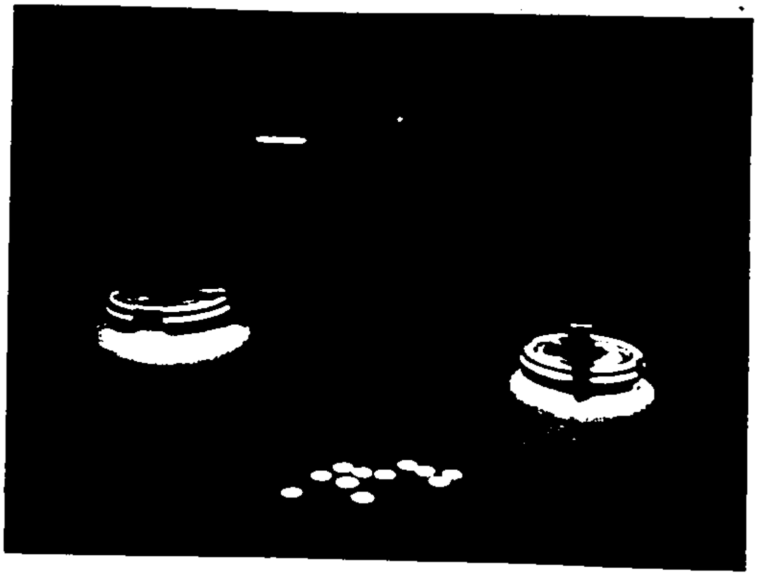

Figure 12 Ball mill used to mix the oxide powders.

(5) The powder was crushed by a mortar and pestle(5) for about 2 hours. The mortar and pestle are shown in Figure 13.

(6) The powder was placed in an alumina crucible and heated for 10 hours at 1000°C in a high temperature furnace(6). The furnace is shown in Figure 14.. At this temperature, the barium carbonate is reduced according to the reaction,

$$BaCO_3 \rightarrow BaO + CO_2$$

(7) The powder was crushed and mixed by the mortar and pestle.

(8) 5wt% of high purity paraffin was dissolved in chlorine-based solvent(7). The liquid was mixed into the powder with the mortar and pestle. The powder was put on a hot plate and baked at 100°C for about 2 hours. This evaporated the chlorothene VG and left the wax, which acted as a binder, behind.

(9) The powder was pressed into discs 2.794 cm. dia. (1.10 in.) and between 0.15 and 0.2 cm. thick. Each disc weighed about 3.0 grams. The pressing pressure was about 3.4 MPa.

(10) The discs were sintered on Al_2O_3 plates in the high temperature furnace. They were held at 400°C

(5) Coors; Canlab Cat. no. M9001-5, M9002-5.

(6) Lindberg 51314-52814 (furnace) and 59246-828074 (controller).

(7) Dow Chemical Co., Chlorothene VG.

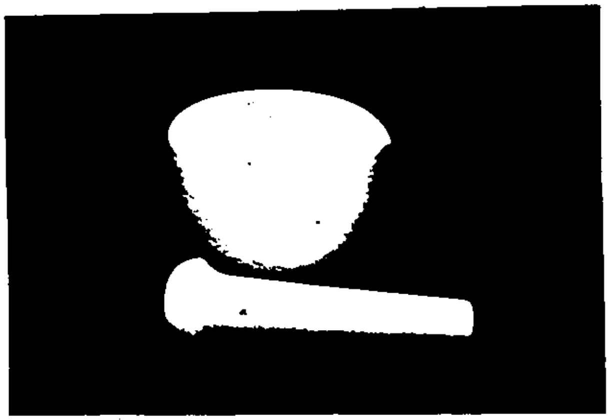

Figure 13 Mortar and pestle used to crush the powders.

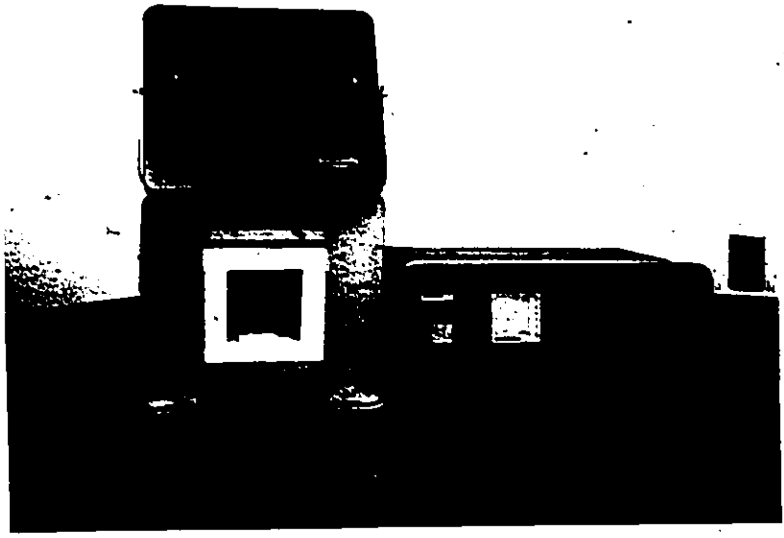

Figure 14 High temperature furnace used to sinter the ceramic targets.

for 10 hours to allow the binder and any adsorbed moisture to evaporate. The furnace temperature was then increased to 1000°C, and the temperature was increased at a rate of 50°C/hr until the sintering temperature (1245→1275°C depending on the composition) was reached. The discs were sintered for five hours. The temperature was decreased at a rate of 50°C/hr. down to 700°C, and then they were allowed to cool more quickly.

A differential temperature analysis (DTA) was performed to roughly determine the sintering temperature for the ceramics. The DTA unit(8) used is shown in Figure 15. It measured the temperature difference between the ceramic powder and a standard (which was high purity Al_2O_3 powder since it is chemically inert) as they were heated from room temperature up to about 1500°C. As the ceramics were heated, they underwent chemical reactions, and while these reactions took place, the temperature of the sample remained constant whereas the temperature of the standard increased. The differential temperature is plotted versus the temperature of the standard, and in general, the curve has a gentle slope. The regions where chemical reactions took place are identified as areas where there is a deviation from the overall gentle curve.

3.2 Thin Film Fabrication

Thin films were sputter-deposited on different substrates. The sputtering deposition system used is shown in Fig. 16(a)-

(8) Harrop Laboratories, DT-716 (Differential Thermal Analyser), TA-700 (Control Console).

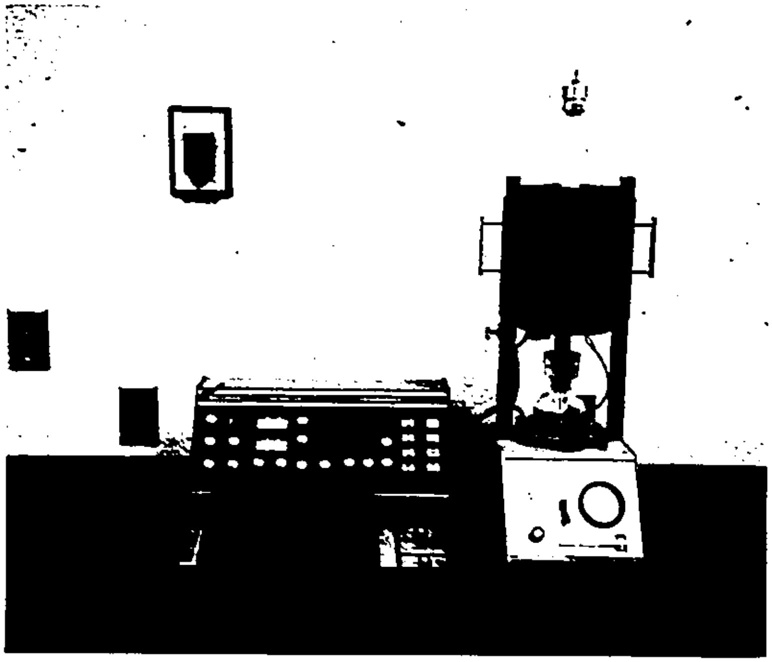

Figure 15 DTA apparatus.

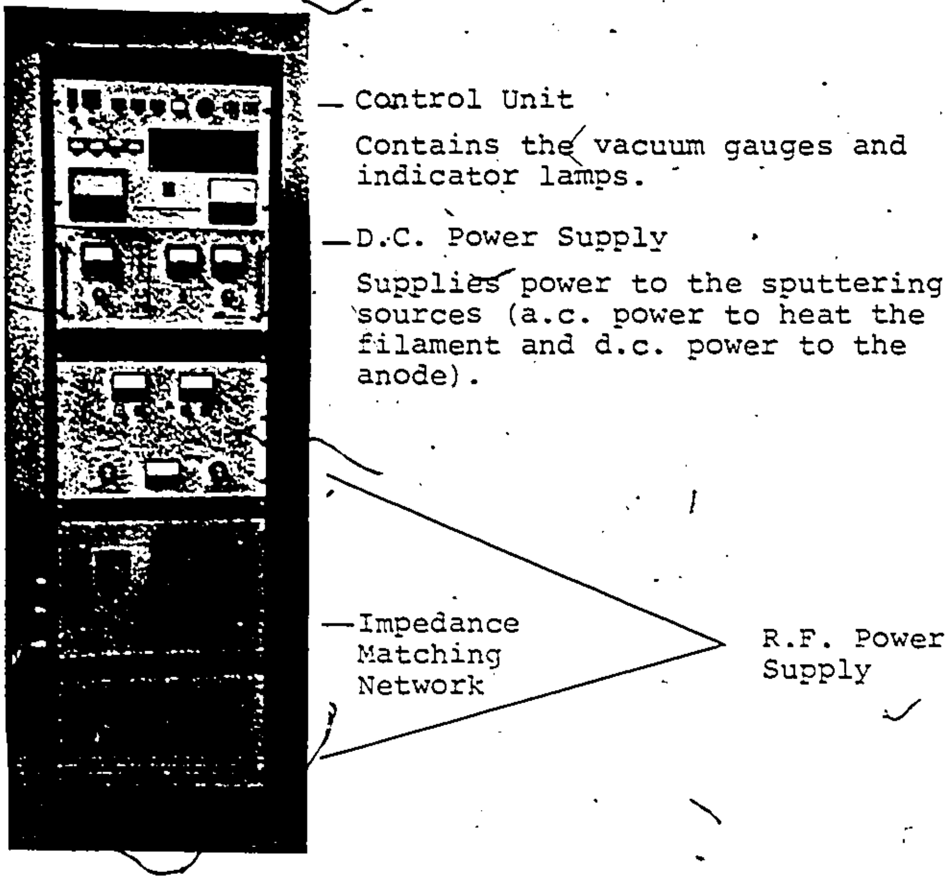

Figure 16(a) Control unit and power supplies for the r.f. sputter-deposition system.

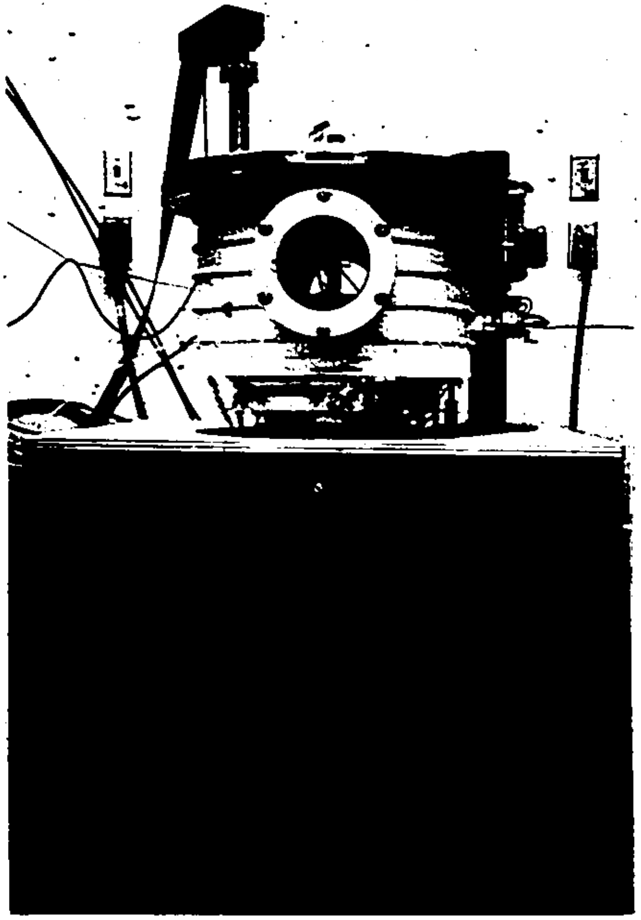

Sputtering Chamber

Main Housing

Contains the diffusion pump, mechanical pump and chamber lid hoist motor. The combination of the diffusion and mechanical pumps can achieve a vacuum of 1 x 10^{-6} torr.

Figure 16(b) Sputtering Chamber.

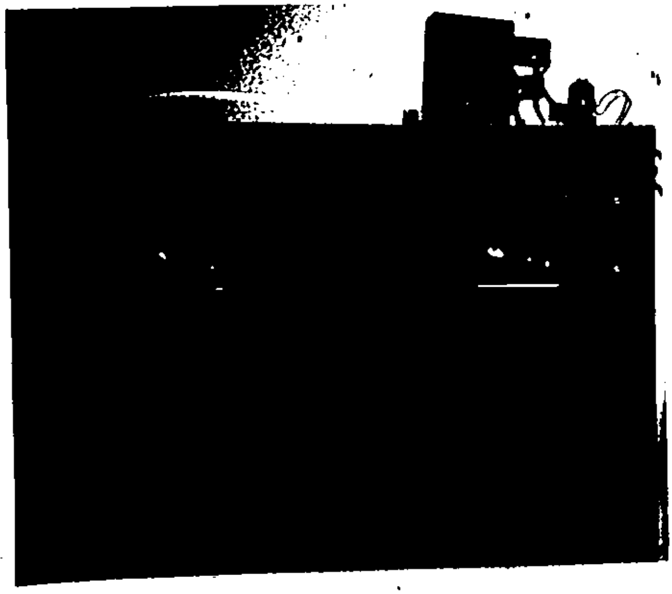

Mass flow controllers provided an accurate steady flow of argon and oxygen.

Residual Gas Analyzer used primarily as a leak detector.

Figure 16(c) Mass flow controllers and residual gas analyzer.

(c). It has an rf triode sputtering source. The rf power supply enabled this system to sputter both electrically insulating and conducting targets, and the triode source allowed the system to be operated at lower pressures than a diode source of a comparable size. The various experimental details which were found to enhance the sputtering process are discussed below.

The filament used in the triode source was made out of 0.762 mm (0.030 in.) diameter tantalum wire. The filament current (a measure of how many electrons are emitted by the filament) was found to decrease with time. This degradation was primarily due to the presence of oxygen, and because of it, a new filament was used for each sputtering run.

To minimize this problem, the oxygen gas was released through a perforated copper ring. The ring was positioned between the target and substrate just above the plasma. It kept the oxygen flow centred in the sputtering area, so that a lower oxygen gas pressure could be used to supply the same amount of oxygen to this area.

The target was joined to a water cooled copper block by a thin continuous layer of silver epoxy. This was very important because if this layer was not thin enough or not continuous, proper cooling (by thermal conduction) was not achieved and the target would crack during the sputtering process. Figure 17 is a schematic illustration of the target area. The target can be of any diameter up to 25.4 mm (1.0 in.). The diameter of the confining ring shown in

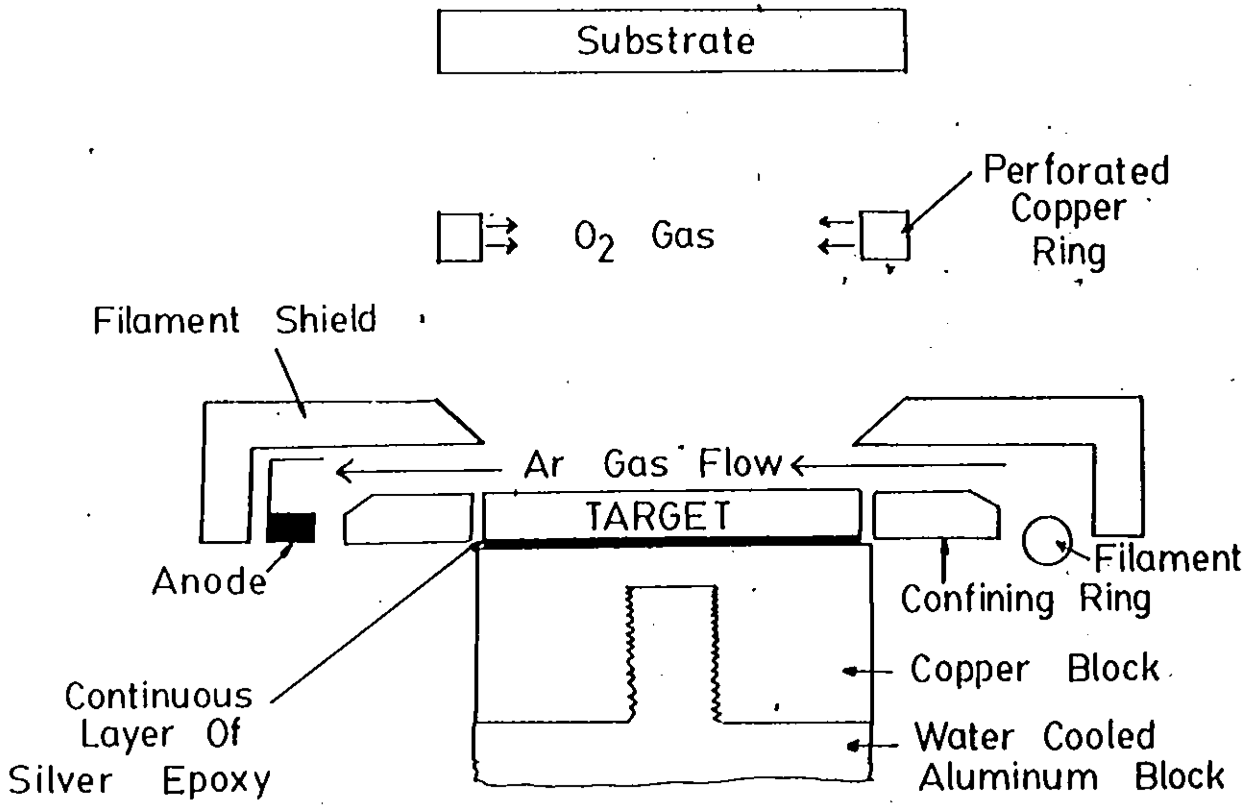

Figure 17 Schematic illustration of the target area.

Figure 17 is always 1.0 mm greater than that of the target. If the spacing is greater than this, there is a good chance that the target assembly will be sputtered along with the target. Figure 18 shows the inside of the sputtering chamber.

3.2.1 Substrate Preparation

Thin films were deposited on various substrates. The procedure used to clean and prepare these substrates is outlined below:

(1) NaCl - Large single crystals of NaCl were cleaved until thin crystals (about 2-3 mm) were obtained. These were immediately placed into the sputtering chamber.

(2) Mica - The mica was originally obtained in the form of thin sheets 3.81 x 3.81 x 0.1 mm thick. These sheets were cut and cleaved so that fresh surfaces were obtained and then they were immediately placed in the vacuum chamber.

(3) Silicon - Highly polished silicon wafers of both (111) and (100) orientations were used. These wafers were cut into sections about 1 cm x 1 cm. with a diamond tipped pencil. They were then etched with a 5% HF solution to remove any SiO_2 and immediately placed in the vacuum chamber.

The substrates were heated by a ceramic heater which was clamped to the substrate material. An isolated d.c. power

Figure 18 The inside of the sputtering chamber. The perforated copper ring provided an even distribution of oxygen gas in the sputtering area. The target diameter is approximately 2.4 cm. The sputtering source is a Simard Tri-Mag Model 3121 and there is another source located opposite to the one shown.

supply was used to provide the power for the heater because of the interaction that would occur between an a.c. power supply and the r.f. power supply in the sputtering system. The heater was clamped to the substrate to ensure that there was good contact between the substrate and heater. A piece of alumina was placed between the clamp and the heater to minimize any heat loss through the metal clamp.

To prevent both the heater from cracking and the film from peeling and cracking due to thermal shock, the substrates were heated and cooled very slowly. An alumel-chromel thermocouple was placed on the substrate and was also clamped down to provide accurately monitor this substrate temperature. This arrangement is shown schematically in Figure 19.

The thickness of the thin films was measured by an Å-Scope interferometer(9), which is shown in Figure 20. This instrument employs a sodium vapour lamp with an effective wavelength of 589.2 nm. The films were coated with an approximately 1,000 Å thick layer of aluminum to improve their reflectivity. A fitted spring loaded fizeau plate (a very flat, smooth optical element with a high reflectivity and low absorption) was placed in contact with the film. Incident light was reflected by the fizeau plate to produce a fringe pattern in the wedged-shaped air-gap between the fizeau plate and the film as shown in Figure 21. This figure also shows that the films require an edge angled at about 95-100° to produce a suitable fringe pattern. With respect to figure 21, the film thickness, t, is determined by the

(9) Varian A-Scope Model 980-4000.

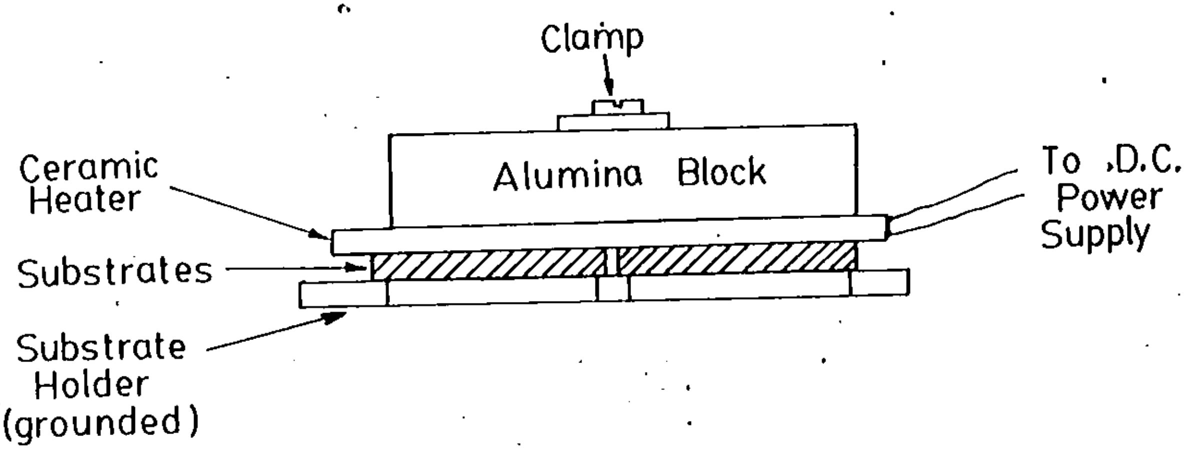

Figure 19 Schematic cross-section of the substrate and heater arrangement.

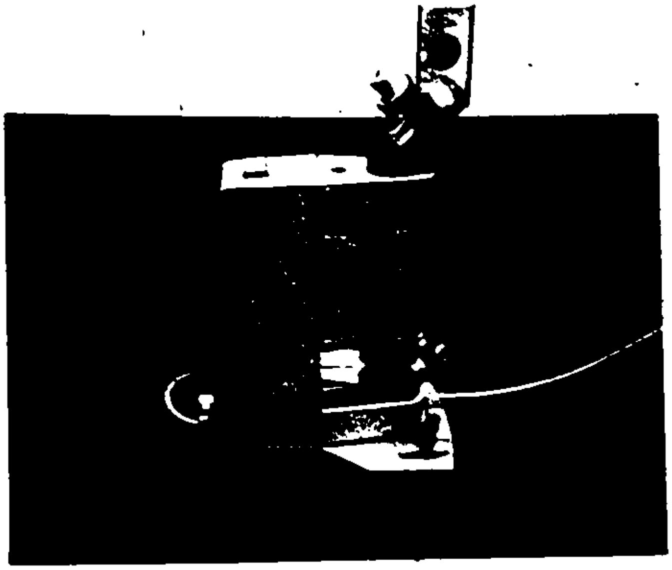

Figure 20 Å-scope interferometer used to measure the film thickness.

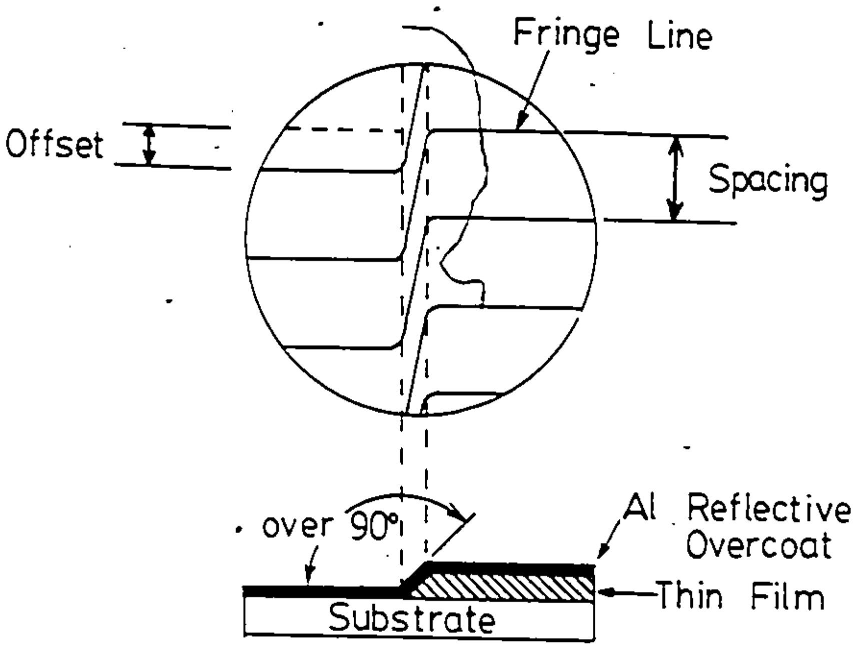

$$\text{Film Thickness (nm)} = \frac{\text{Offset (filar units)}}{\text{Spacing (filar units)}} \times 294.6\ \text{(nm)}$$

Figure 21 Fringe pattern produced from the film.

ratio of the fringe line offset to the fringe line spacing (which is always one-half wavelength or 294.6nm). Thus,

$$t(\mathrm{nm}) = \frac{\text{fringe offset (filar units)}}{\text{fringe spacing (filar units)}} \times 294.6 \text{ nm}$$

The fringe offset and spacing are measured with the filar eyepiece. This type of interferometer is designed to measure surface variations from 3 to 2,000 nm, with an accuracy of ±3nm. The thickness of each film was measured at five different locations, and the average value was calculated and recorded.

3.3 Dielectric Measurements

The dielectric properties of single-crystal fresnoite have been investigated: the most recent and complete investigation is that of Halliyal et al [14,(1985)]. However, the dielectric properties of multigrain fresnoite ceramics have never been reported.

The ceramic discs that were analyzed were prepared as described in section 3.1. A schematic cross-section of the apparatus designed and used to measure the capacitance and dielectric loss of the ceramics is shown in Figure 22. The diameter of the upper inner electrode corresponded exactly to that of the ceramic discs. The teflon ring and grounded brass outer ring ensured that any edge or fringe effects were minimized.

The capacitance and dielectric loss of the ceramics were measured over a frequency range of 10 kHz to 10 MHz and a temperature range of 20°C to 200°C using a capacitance

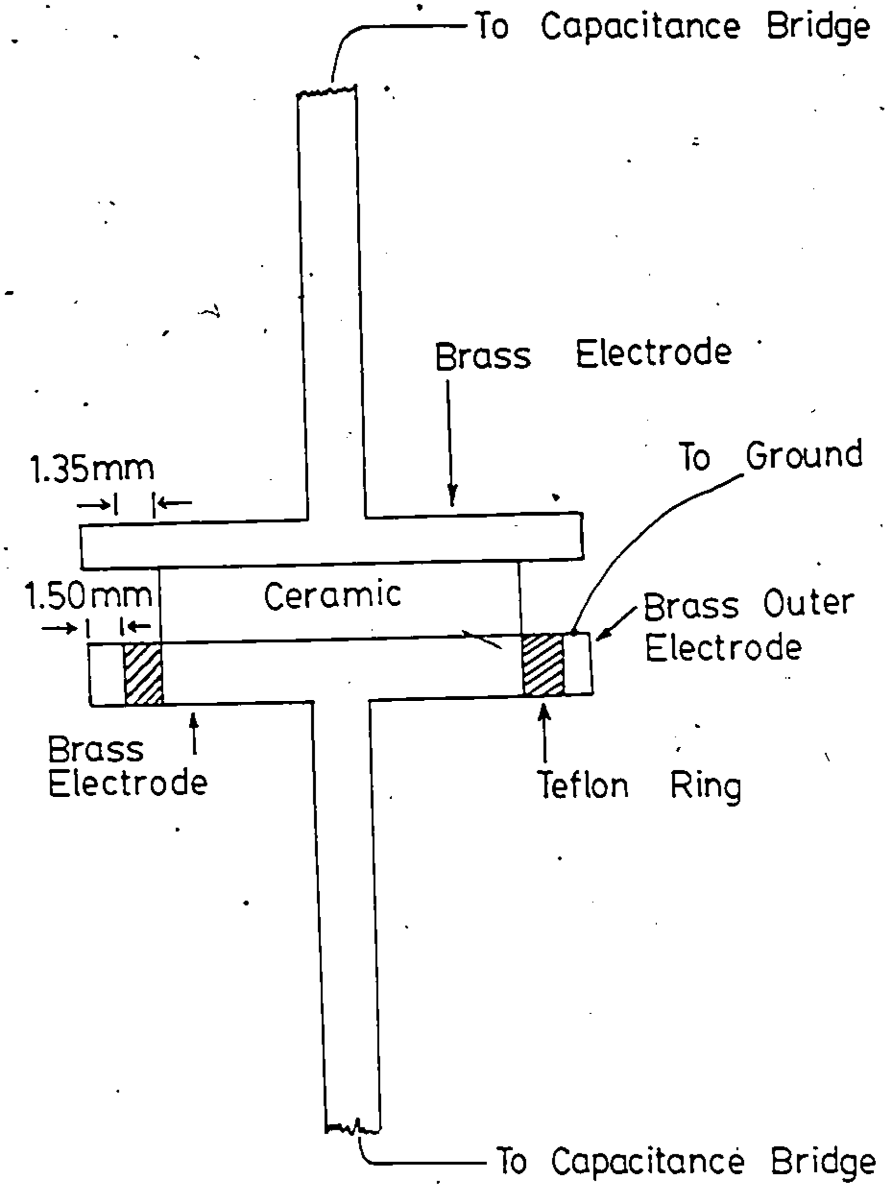

Figure 22 Schematic cross-section of the apparatus used to measure the dielectric properties of the fresnoite ceramics.

bridge(10) and an environmental chamber. The faces of the ceramic discs were polished and then coated with evaporated aluminum to enhance the contact between the ceramics and the electrodes.

---

(10) Hewlett Packard Model 4275A Multi-Frequency LCR Meter.

CHAPTER 4

RESULTS AND DISCUSSION

4.1 Dielectric Measurements

Dielectric measurements were performed on two fresnoite discs. These discs were of the same diameter (2.31 cm) but possessed different thicknesses. Disc 1 was 2.65 mm thick, while Disc 2 was 1.47 mm thick. The measured values for the capacitance and dielectric loss (tan δ) of both discs are summarized in Tables 6 and 7.

The dielectric constant, ε_r, was calculated from the relation:

$$\varepsilon_r = \frac{C}{\varepsilon_o}\frac{d}{A} \qquad (1)$$

where, d is the thickness of the disc;

A is the area of the face of the disc;

ε_o is the permittivity of a vacuum which is 8.854 x 10^{-12} F/m; and

C is the measured value of the capacitance of the disc.

Tables 8 and 9 list the values of ε_r for fresnoite discs 1 and 2 respectively.

When a dielectric is placed in a parallel plate condenser, and an alternating field is applied, an alternating current will flow. This current, i, is given by [17,(1964)]:

$$i = j\omega\varepsilon_r C_o v \qquad (2)$$

where, $j = \sqrt{-1}$;

ω = the frequency of the field, (rad/sec);

v = the magnitude of the field, (volts);

TABLE 6

Values of Capacitance (c) and Dielectric Loss (tan δ) for Fresnoite Disc 1.* Blank Values of tan δ Indicate a Value Less than 0.00001.

T(°C)		10 KHz	20 KHz	40 KHz	100 KHz	200 KHz	400 KHz	1 MHz	2 MHz	4 MHz	10 MHz
20	c(pF) tan δ	19.867 .00019	19.857 .00020	19.872 .0005	19.057	19.816 .00016	19.859	19.[illegible]	19.870	19.649 .006	19:678 .00155
40	c(pF) tan δ	19.867 .00022	19.855 .00019	19.870 .0006	19.855	19.812 .00016	19.853	19.854	19.862	19.694	19.677 .0015
60	c(pF) tan δ	19.894 .00029	19.880 .00027	19.893 .0007	19.878	19.836 .00022	19.875	19.874	19.884	19.719	19.709 .00152
80	c(pF) tan δ	19.930 .00042	19.915 .00040	19.927 .0008	19.911 .00009	19.868 .00030	19.907	19.906	19.915	19.747	19.741 .00145
100	c(pF) tan δ	19.905 .00054	19.889 .00046	19.900 .0009	19.882 .00017	19.840 .00036	19.878	19.876	19.884	19.703	19.712 .00157
120	c(pF) tan δ	19.979 .00075	19.937 .00069	19.947 .0010	19.927 .00024	19.886 .00043	19.923	19.920	19.928	19.745	19.759 .00160
140	c(pF) tan δ	20.006 .00095	19.988 .00081	19.997 .0011	19.976 .00031	19.934 .00050	19.971	19.968	19.976	19.795	19.810 .00163
160	c(pF) tan δ	20.061 .00111	20.041 .00093	20.049 .0012	20.027 .00039	19.986 .00056	20.022	20.019	20.025	19.845	19.864 .00166
180	c(pF) tan δ	20.125 .00134	20.104 .00108	20.110 .0013	20.087 .00044	20.046 .00059	20.082	20.077	20.085	19.903	19.927 .00173
200	c(pF) tan δ	20.177 .00164	20.153 .00135	20.159 .0015	20.133 .00058	20.091 .00070	20.127 .0001	20.123	20.129	19.946	19.978 .00176

* For calculations, three significant digits were used

TABLE 7

Values of Capacitance* (c) and Dielectric Loss (tan δ) for Fresnoite Disc 2. Blank Values of tan δ Indicate a Value Less than 0.00001

T(°C)		10 KHz	20 KHz	[illegible] KHz	100 KHz	200 KHz	400 KHz	1 MHz	2 MHz	4 MHz	10 MHz
20	c(pF) tan δ	31.429	31.418	31.435 .0003	31.401	31.356	31.482 .0046	31.475	31.583	31.773 .0026	32.530 .00151
40	c(pF) tan δ	31.686	31.682	31.711	31.690	31.666	31.720 .006	31.713 .00024	32.815	32.001 .0026	32.622 .00205
60	c(pF) tan δ	31.732	31.731	31.762	31.740	31.712	31.786 .0062	31.763 .00044	31.866	32.041 .0027	32.655 .00201
80	c(pF) tan δ	31.801	31.800	31.828	31.808	31.779	31.863 .0061	31.842 .00043	31.939	32.119 .0027	32.713 .00187
100	c(pF) tan δ	31.870	31.863	31.892	31.870	31.865	31.892 .0061	31.907 .00035	32.007	32.191 .0027	32.794 .00215
120	c(pF) tan δ	31.958	31.946	31.969	31.946	31.922	31.966 .0058	31.968 .00014	32.071	32.258 .0026	32.864 .00214
140	c(pF) tan δ	32.070 .00043	32.058 .00034	32.074 .0006	32.042 .00003	32.019	32.035 .0056	32.048 .00007	32.153	32.340 .0026	32.948 .0021
160	c(pF) tan δ	32.171 .00071	32.150 .00052	32.163 .0007	32.125 .00012	32.100	32.117 .0057	32.130 .00012	32.235	32.422 .0026	33.030 .0021
180	c(pF) tan δ	32.257 .00086	32.234 .00062	32.246 .0008	32.213 .00014	32.187	32.194 .0060	32.211 .00008	32.217	32.506 .0023	33.116 .00143
200	c(pF) tan δ	32.320 .00100	32.295 .00076	32.306 .0009	32.269 .00021	32.244	32.254 .0059	32.268 .00008	32.274	32.564 .0023	33.174 .00136

* For calculations, three significant digits were used

TABLE 8

Dielectric Constant of Fresnoite Disc 1

T(°C)	Frequency									
	10 KHz	20 KHz	40 KHz	100 KHz	200 KHz	400 KHz	1 MHz	2 MHz	4 MHz	10 MHz
20	14.19	14.18	14.19	14.18	14.15	14.18	14.18	14.19	14.03	14.05
40	14.19	14.18	14.19	14.18	14.15	14.18	14.18	14.18	14.06	14.05
60	14.21	14.20	14.21	14.20	14.17	14.19	14.19	14.20	14.08	14.08
80	14.23	14.22	14.23	14.22	14.19	14.22	14.22	14.22	14.10	14.10
100	14.21	14.20	14.21	14.19	14.17	14.19	14.19	14.20	14.07	14.08
120	14.27	14.24	14.25	14.23	14.20	14.23	14.23	14.23	14.10	14.11
140	14.29	14.27	14.28	14.27	14.24	14.26	14.26	14.27	14.14	14.15
160	14.33	14.31	14.32	14,30	14.27	14.30	14.30	14.30	14.17	14.19
180	14.37	14.36	14.36	14.35	14.32	14.34	14.34	14.34	14.21	14.23
200	14.41	14.39	14.40	14.38	14.35	14.37	14.37	14.37	14.24	14.27

TABLE 9

Dielectric Constant of Fresnoite Disc 2

T(°C)	Frequency									
	10 KHz	20 KHz	40 KHz	100 KHz	200 KHz	400 KHz	1 MHz	2 MHz	4 MHz	10 MHz
20	12.45	12.45	12.45	12.44	12.42	12.47	12.47	12.51	12.59	12.89
40	12.55	12.55	12.56	12.55	12.54	12.57	12.56	12.60	12.68	12.92
60	12.57	12.57	12.58	12.57	12.56	12.59	12.59	12.62	12.69	12.94
80	12.60	12.60	12.61	12.60	12.59	12.62	12.61	12.65	12.72	12.96
100	12.63	12.62	12.63	12.63	12.62	12.63	12.64	12.68	12.75	12.99
120	12.66	12.66	12.66	12.66	12.65	12.66	12.66	12.71	12.78	13.02
140	12.70	12.70	12.71	12.69	12.68	12.69	12.70	12.74	12.81	13.05
160	12.74	12.74	12.74	12.73	12.72	12.72	12.73	12.77	12.84	13.08
180	12.78	12.77	12.77	12.76	12.75	12.75	12.76	12.80	12.88	13.12
200	12.80	12.79	12.80	12.78	12.77	12.78	12.78	12.83	12.90	13.14

ε_r = the relative permittivity (or relative dielectric constant) of the dielectric;

C_o = the capacitance of the condenser without the dielectric.

If the dielectric was an ideal one, this current, i, would be 90° out of phase with the voltage. However, in practice, it is often found that there is an in-phase component of the current present in the dielectric. Because of this, the dielectric constant is usually a complex quantity, i.e.,

$$\varepsilon_r = \varepsilon' - j\varepsilon'' , \qquad (3)$$

where ε' and ε'' are both real quantities.

The current that flows in the condenser is then given by:

$$i = \omega\varepsilon'' C_o v + j\omega\varepsilon' C_o v \qquad (4)$$

The magnitude of ε'' depends on the magnitude of the in-phase or "loss" component of the current. When the dielectric is ideal or loss-free, then ε'' will be zero. Equation (3) is a convenient way to define the dielectric constant because it does not require any specific knowledge of the type of loss mechanism which occurs in the dielectric.

The loss tangent, tan δ, is defined by:

$$\tan \delta \equiv \frac{\varepsilon''}{\varepsilon'} \qquad (5)$$

and this parameter is used to evaluate the performance of the dielectric as an insulator. Tables 6 and 7 list the values of tan δ for fresnoite discs 1 and 2 respectively.

4.1.1 Discussion of the Dielectric Constant

The values of the dielectric constant of fresnoite discs

1 and 2 shown in Tables 8 and 9 were plotted vs. temperature (at a constant frequency) and vs. frequency (at a constant temperature). On inspection, it was seen that all of the curves for each constant temperature and frequency were very similar: thus Figure 23 is a plot of ε' vs. temperature at 100 k Hz and Figure 29 is a plot of ε' vs. frequency at 160°C. The other curves are shown in Appendix 1.

The only data available to compare these measurements with is that of Halliyal et al [14,(1985)]. They measured the dielectric constant of: fresnoite single crystals, a fresnoite glass, and a fresnoite glass-ceramic. The single crystals were produced by the Czochralski method. The fresnoite glass was formed by melting 1 excess mole silica (i.e., $2BaO-3SiO_2-TiO_2$) in a platinum crucible. The glass-ceramic samples were prepared by crystallizing the glass in a large temperature gradient normal to the surface of the glass.

Figure 24 is a plot of the dielectric constant of these materials vs. temperature measured at a frequency of 100 k Hz [14,(1985)]. Also shown in this figure are the values of discs 1 and 2. Figure 24 shows that the dielectric constant of a fresnoite single crystal (ε'_{33}) rises with temperature up to 160°C and then it drops off. The reason for this peak is not clear, but it was postulated that it was due to some anomalous behaviour in a few of the elastic constants at 160°C.

Figure 24 shows that the dielectric constant of the

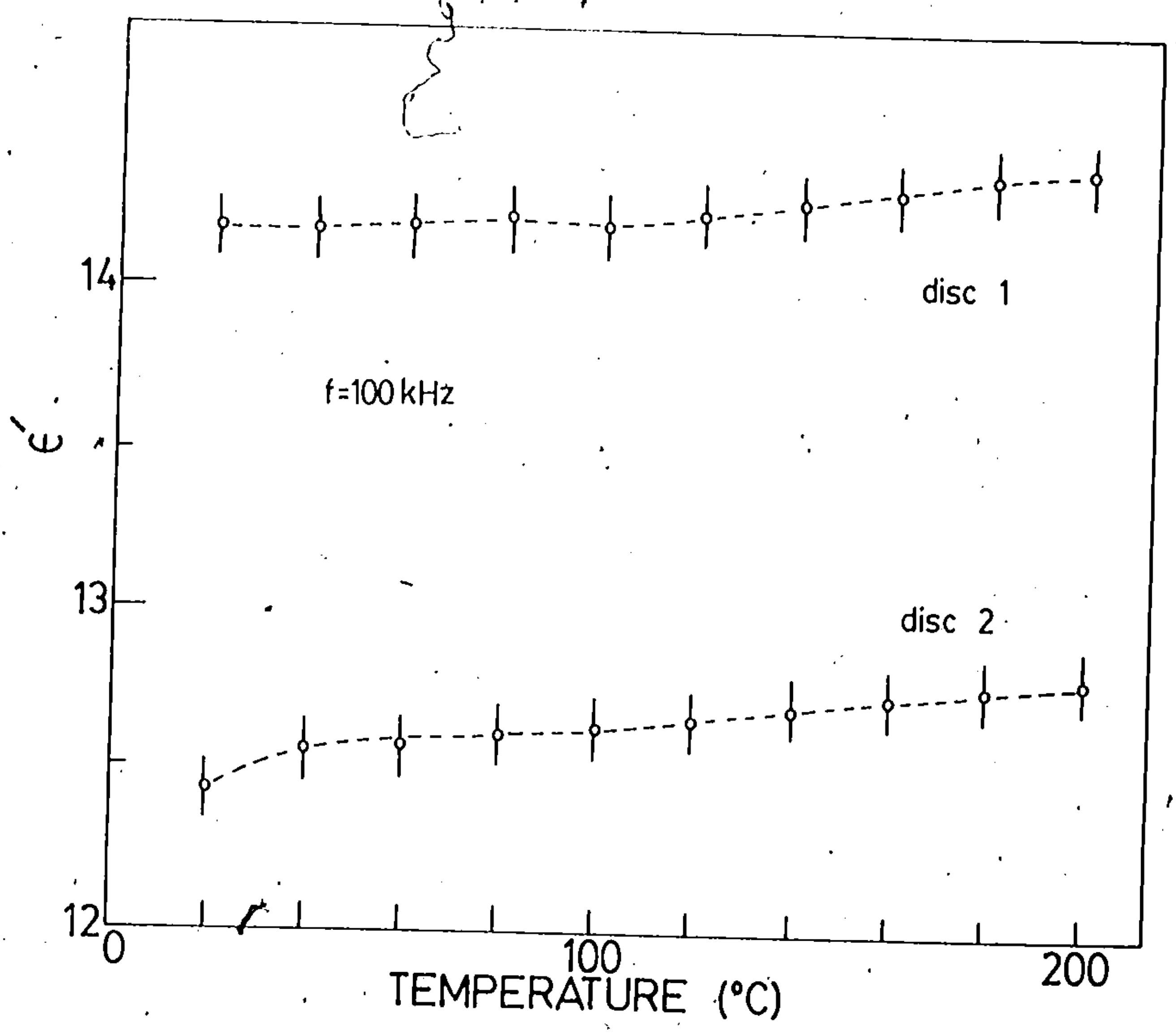

Figure 23 Dielectric constant vs. temperature at 100 kHz.

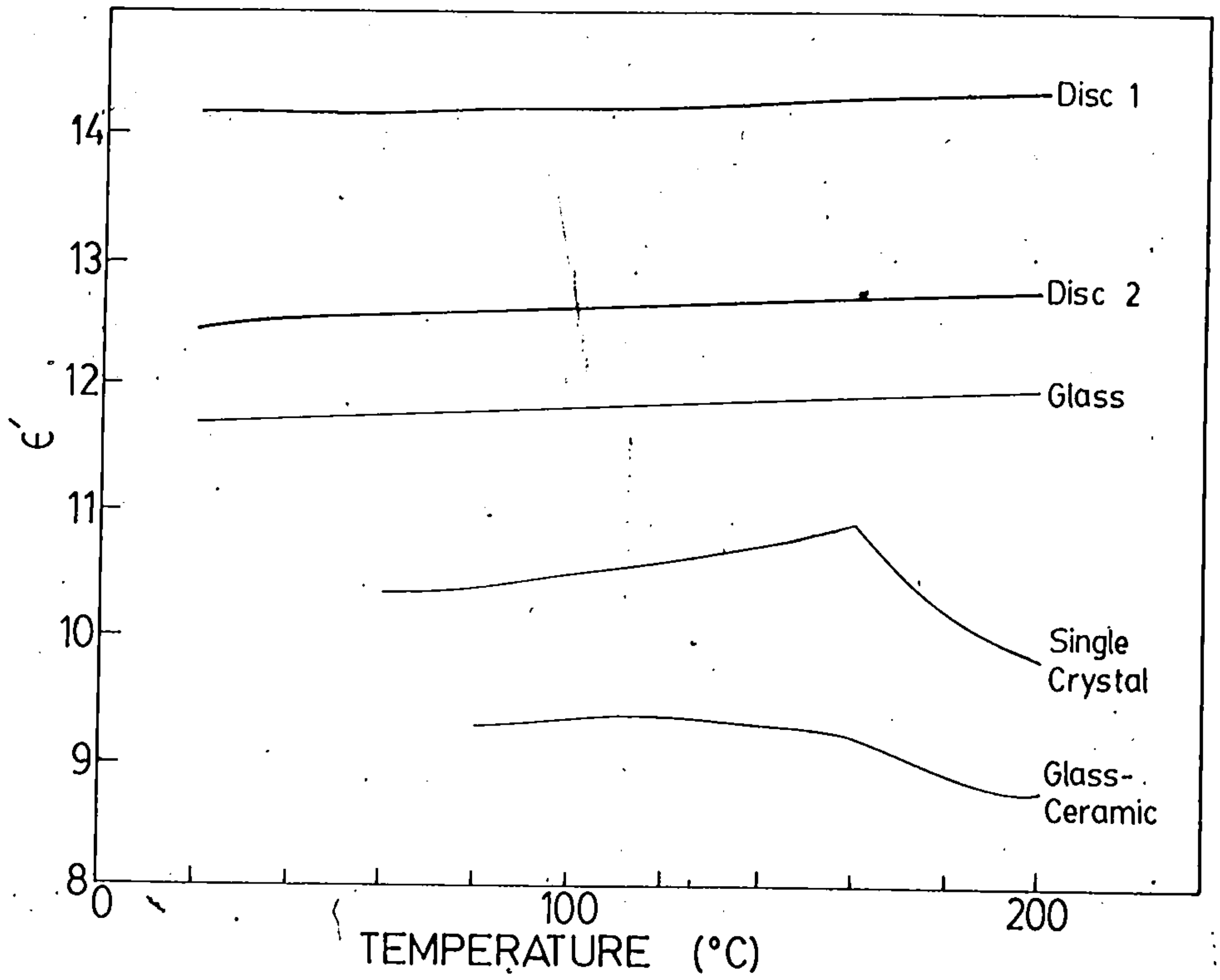

Figure 24 Dielectric constant vs. temperature at 100 kHz for different fresnoite materials [14,(1985)].

fresnoite glass-ceramic rises slightly up to a temperature of 120°C and then it decreases. The reason for this peak is probably the same as for the single crystal. The peak is shifted and its magnitude is decreased due to the non-stoichiometry of the glass-ceramic. Figure 24 also shows that the dielectric constant of both the fresnoite discs and the fresnoite glass rise slightly with temperature.

The magnitude of the dielectric constants of fresnoite at 20°C are [7,(1977)]:

$$\varepsilon'_{11} = 15.0$$

$$\varepsilon'_{33} = 11.0$$

Since the measurements were performed on multigrain ceramics with no preferred orientation, symmetry considerations [18, (1979)] leads to the following prediction for the dielectric constant of these ceramics:

$$\varepsilon' = \frac{2x\varepsilon'_{11}+\varepsilon'_{33}}{3} \simeq 13.7 \qquad (6)$$

Table 8 shows that the dielectric constant of disc 1 varied between 14.0 and 14.4. This is quite close to the value calculated above. Table 9 shows that ε' of disc 2 varied from 12.4 to 13.1, which is slightly smaller than predicted above. The actual value of ε' could also depend on factors such as the porosity and grain size - however, since both discs were fabricated from the same powder, pressed under the same pressure, and sintered at the same temperature, it was expected that these discs would yield values of ε' much closer to each other. The discrepancy between these values is discussed in detail in section 4.1.3.

The important result of Figure 24 is that the dielectric constant of the fresnoite discs and glass rises slightly with temperature. Classical dielectric theory [64,(1954)] predicts the following relationship between the dielectric constant and temperature:

$$\frac{\varepsilon'-1}{\varepsilon'+2} \doteq A + \frac{B}{T} \qquad (7)$$

where, $A = \frac{N\alpha}{3\varepsilon_o}$, $B = \frac{N\mu^2}{9\varepsilon_o kT}$

and, N is the number of molecules per unit volume;
α is the polarizability per molecule;
μ is the permanent dipole moment of a molecule;
k is Boltzmann's constant;
T is the absolute temperature.

This relation is based on the assumption that the local electric field which acts on an atom is given by the Lorentz field - a field due to polarization charges on the surface of a spherical cavity inside a uniformly polarized dielectric [65,(1976)]. All short range (or non-polar) interactions were neglected in the derivation of this relation, thus it is best satisfied by dipolar gases. Equation (7) shows that a plot of $\frac{\varepsilon'-1}{\varepsilon'+2}$ vs. $\frac{1}{T}$ for a given frequency should yield a straight line, with a slope of B and an intercept of A. The values of the slope and intercept for the function $\frac{\varepsilon'+1}{\varepsilon'+2}$ vs. $\frac{1}{T}$ for both fresnoite discs are shown in Table 10. These values were calculated from simple linear regression.

Figure 25 is a plot of $\frac{\varepsilon'-1}{\varepsilon'+2}$ vs. $\frac{1}{T}$ for both fresnoite discs at a frequency of 100 kHz. This curve shows that the function $\frac{\varepsilon'-1}{\varepsilon'+2}$ decreases with $\frac{1}{T}$. In fact, Table 10 shows that

TABLE 10

Values of the Slope and y-Intercept for the Function $\frac{\varepsilon'-1}{\varepsilon'+2}$ vs. $\frac{1}{T}$ for Fresnoite Discs 1 and 2

Frequency	Disc 1		Disc 2	
	Slope (k)	y-Intercept	Slope (k)	y-Intercept
10 KHz	-1.9	0.82	-3.5	0.80
20 KHz	-1.8	0.82	-3.5	0.80
40 KHz	-1.7	0.82	-3.4	0.80
100 KHz	-1.4	0.82	-3.4	0.80
200 KHz	-1.6	0.82	-3.4	0.80
400 KHz	-1.6	0.82	-3.2	0.80
1 MHz	-1.6	0.82	-3.1	0.80
2 MHz	-1.6	0.82	-3.0	0.80
4 MHz	-1.6	0.82	-3.1	0.81
10 MHz	-1.9	0.82	-2.6	0.81

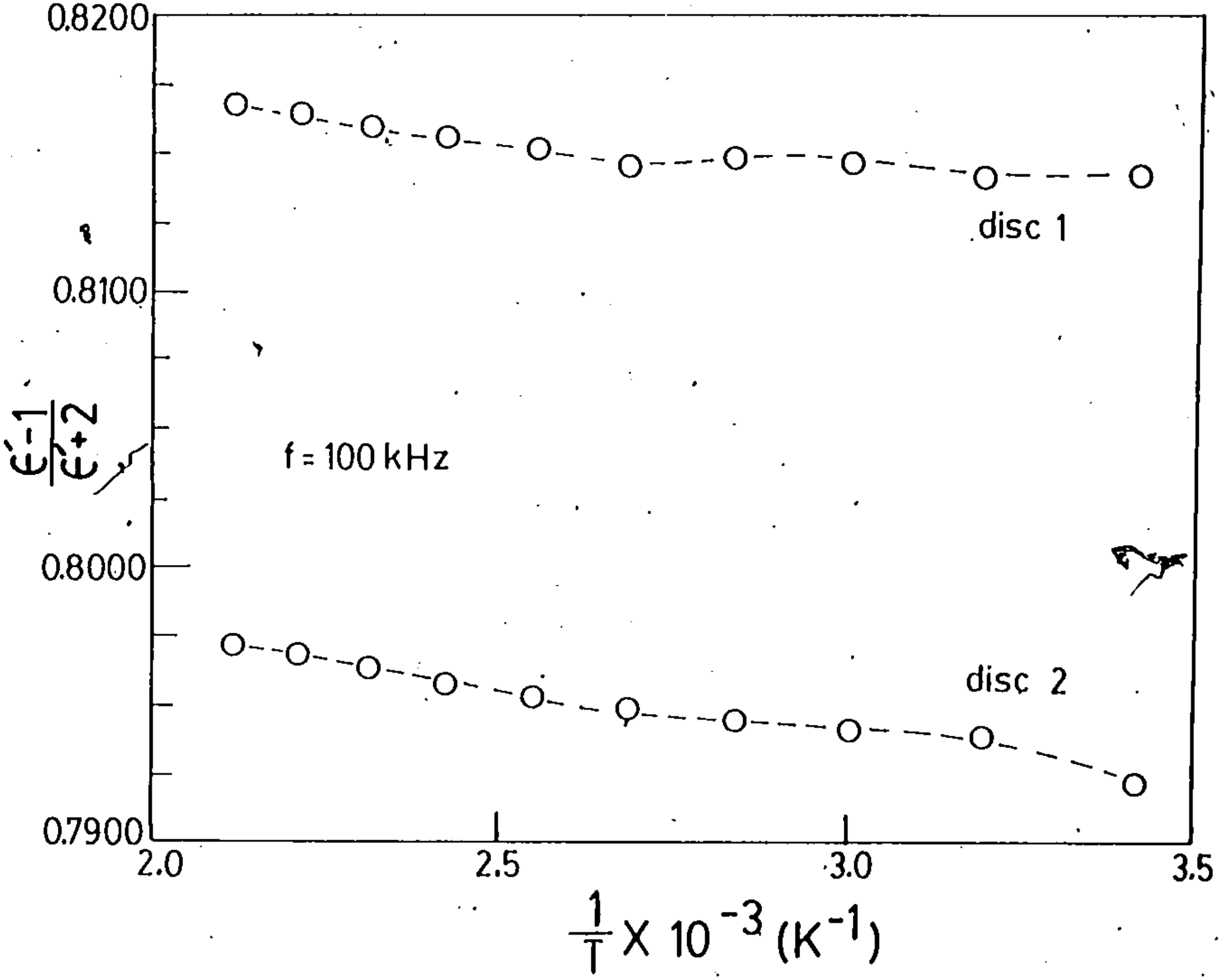

Figure 25 $(\frac{\varepsilon'-1}{\varepsilon'+2})$ vs. $(\frac{1}{T})$ at 100 kHz.

the value of the slope, B, is negative for both discs at each frequency considered. Since the slope was defined as $N\alpha^2/9\varepsilon_o kT$, it is easily seen that a negative slope is not permissible. Thus it has been shown that fresnoite does not conform to the theory developed for dipolar substances.

Due to the extreme complications encountered when short-range interactions are considered, a quantitative theory beyond the scope of the classical theory already discussed is not available. However, there should be some parameter which can quantitatively explain the increase in the dielectric constant with temperature. The temperature coefficient of the dielectric constant is defined as:

$$T\varepsilon' \equiv \frac{1}{\varepsilon}\frac{\Delta\varepsilon'}{\Delta T} \qquad (8)$$

Figure 26 shows this quantity plotted vs. temperature for: fresnoite discs 1 and 2, a fresnoite single crystal, a fresnoite glass, and a fresnoite glass-ceramic. The values for the single crystal, glass, and glass-ceramic were calculated from the data of Halliyal et al [14,(1985)]. Also shown in this figure are the values of $T\varepsilon^S_{11}$ and $T\varepsilon^S_{33}$ measured at 20°C [66,(1978)]. It is not known if these values are constant with temperature, but they can be used as a standard to compare the other curves to.

Figure 26 shows that the values of $T\varepsilon'$ for both the single crystal and the glass-ceramic fluctuate widely with temperature, while for both of the discs and the glass, $T\varepsilon'$ is fairly constant. This difference may be due to the fact that both the single crystal and glass-ceramic are polar in

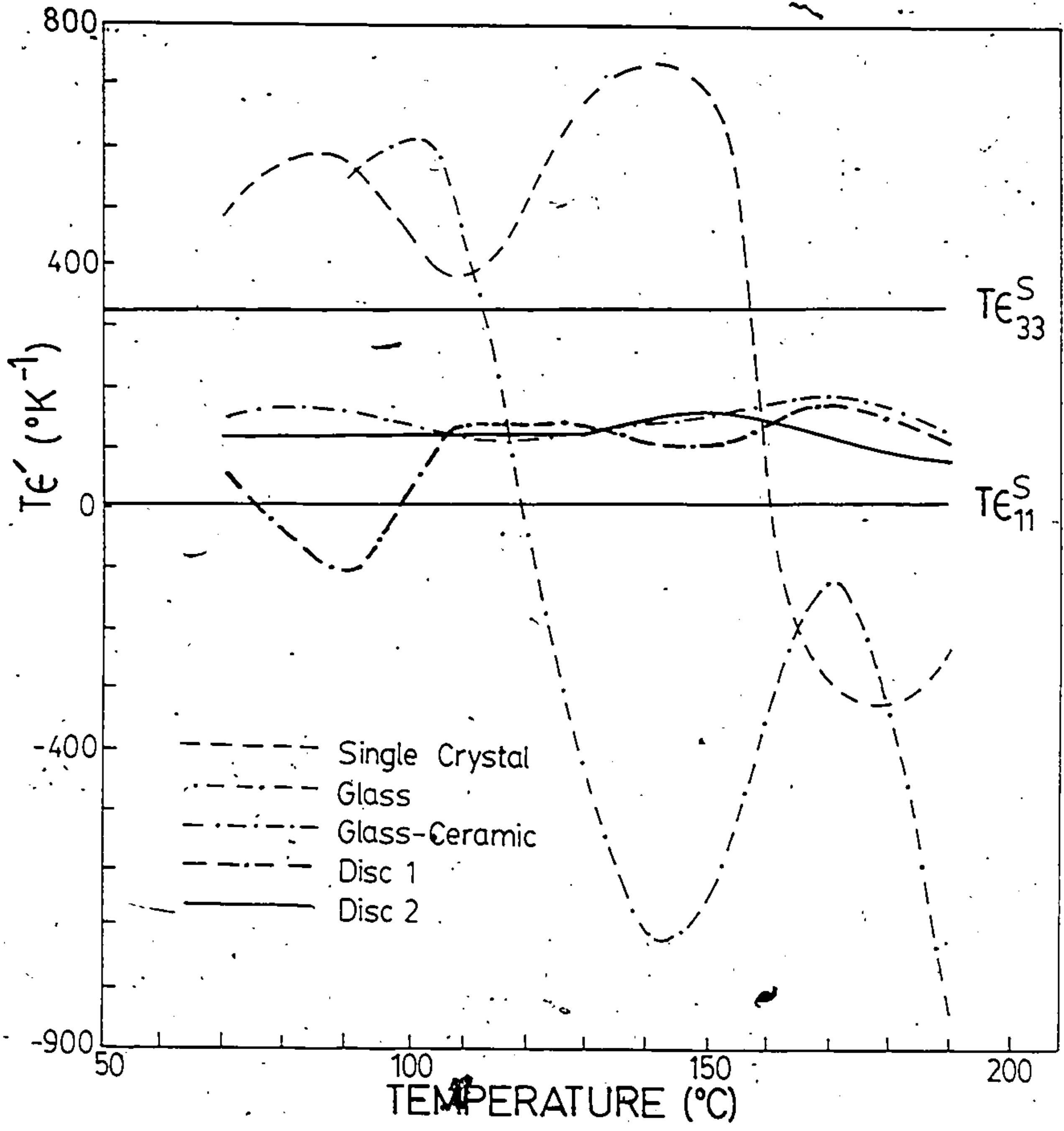

Figure 26 Temperature coefficient of the dielectric constant vs. temperature at 100 kHz for different fresnoite materials. The values of $T_{\varepsilon}{}^{S}_{11}$ and $T_{\varepsilon}{}^{S}_{33}$ were measured at 20°C.

nature, while the other materials are not.

If the low-temperature dip in the curve of $T\varepsilon'$ for disc 1 is discounted, it is seen that the values of $T\varepsilon'$ for the discs and the glass is approximately $100\text{-}120 \times 10^{-6} K^{-1}$. If a weighted average of $T\varepsilon^{S}_{11}$ and $T\varepsilon^{S}_{33}$ is taken, i.e.,

$$T\varepsilon^{S} = \frac{2 \times T\varepsilon^{S}_{11} + T\varepsilon^{S}_{33}}{3} = 110 \times 10^{-6} K^{-1} ,$$

it is seen that this lies in the range of the values obtained for the discs and the glass. Figure 26 also shows that at 200°C, $T\varepsilon'$ for both the discs and the glass is decreasing and possibly approaching zero. If this is true, it means that the dielectric constant, ε', approaches a constant value. Thus, the dielectric constant of these materials could rise slightly with temperature up to some maximum value at a temperature above 200°C.

So far, the reason for the increase in the dielectric constant with temperature has not been discussed. The dielectric constant decreases with temperature for dipolar material at low pressures (i.e., those substances for which Eq. (7) is valid) because the increase in temperature results in an increase in the vibration of the dipoles, which in turn lowers the effective length of the dipole.

Since fresnoite is a pyroelectric material, it does possess a permanent dipole. However, it is not a dipole in the simple sense of a dipolar molecule. Due to its symmetry in the x and y planes, the permanent dipole of a fresnoite unit cell can be thought of as: a centre of positive charge and a centre of negative charge which do not coincide in the z plane. The increase in the dielectric constant with temperature means that the length of the permanent dipole (i.e., the distance between the lines of positive and negative charge in the z plane) must increase slightly with temperature. This increase could be related to the thermal expansion of fresnoite, that is, the increase in temperature causes the unit cell to expand slightly, which causes the dipole length to increase. However, if the ceramics truly consisted of randomly oriented grains, this effect would cancel out and not be reflected in the measurements. Thus the ceramic targets must be slightly oriented for this discussion to be valid. This slight orientation could have occurred during the pressing and sintering process.

Figures 27 and 28 show, respectively, the dielectric constant of an alumina porcelain (95%Al_2O_3-4%talc-1%BaF_2) and a steatite ceramic (84%talc-10%BaF_2-3% Ball Claly-3% bentorite) vs. temperature for the frequency range 100 Hz to 10^6 Hz [68,(1954)]. These figures show that the dielectric constant of these ceramics rises with temperature - especially for the lower frequencies. These ceramics (like most ceramics) contain more than one phase - crystalline bulk phase(s) and a small amount of a glass or amorphous phase.

The amorphous phase gives rise to an interfacial or space charge polarization [64], which is a consequence of the difference in the electrical conductivities of the phases. At room temperature, this type of polarization is

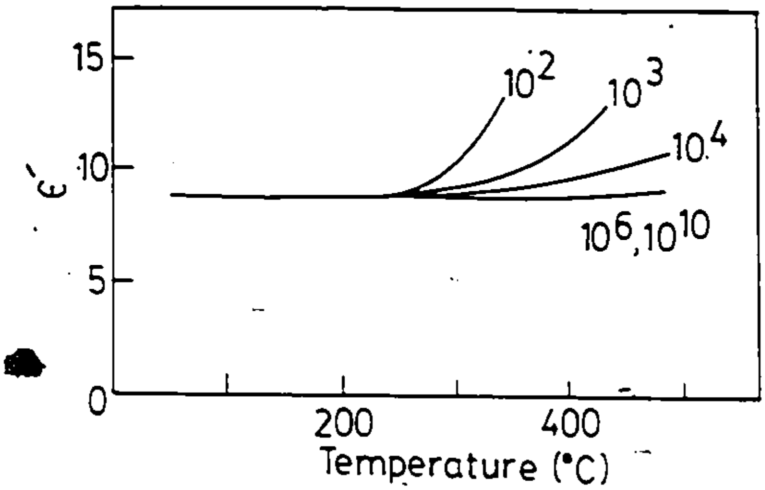

Figure 27 Dielectric constant vs. temperature of an alumina porcelain for a range of frequencies [68,(1976)].

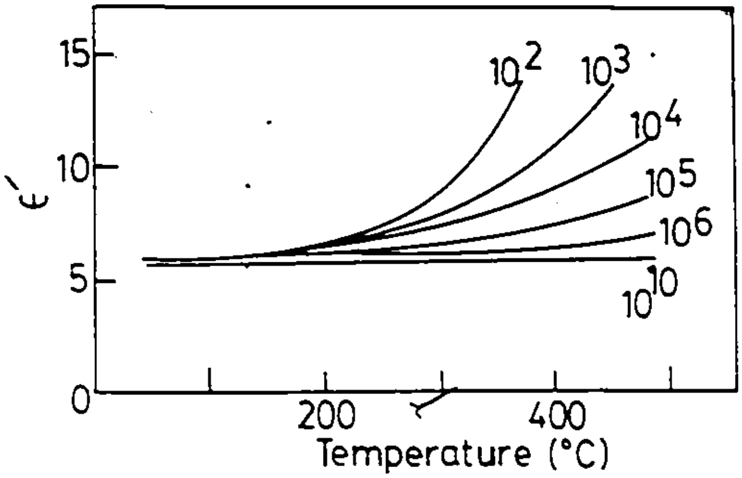

Figure 28 Dielectric constant vs. temperature of a steatite ceramic for a range of frequencies [68,(1976)].

usually negligible even at low frequencies [68,(1976)]. As the temperature is raised, the conductivity increases, which increases the number of charges which are impeded at the interfaces or grain boundaries, and thus the polarization also increases. This effect is only significant at low frequencies due to the low conductivity of the dielectric phases (i.e., at high frequencies the ions cannot move as fast as the field switches).

73

Figures 27 and 28 show that the dielectric constant rises with temperature from 50 to 200°C in a manner which is very similar to that of the fresnoite discs and glass (Figure 24). This effect cannot be separated from the thermal expansion effect discussed previously, and it is likely that the rise in the dielectric constant of the fresnoite discs and glass is due to a combination of these two factors.

Figure 29 shows a plot of ε' vs. frequency at 160°C for both fresnoite discs. This figure shows that in the frequency range 10 KHz to 2 MHz, the dielectric constant for both discs is fairly constant. However, in the frequency range 2 to 10 MHz, the dielectric constant of disc 2 increases, while for disc 1 it decreases and then increases slightly. This increase in ε' with frequency was not expected.

A schematic illustration of the general behaviour of the total polarizability (and hence the dielectric constant) with frequency is shown in Figure 30. The frequency range of 2 to 10 MHz corresponds to the UHF to microwave frequency range shown in Figure 30. The dipolar polarizability becomes negligible in this frequency because the permanent dipoles do not have enough time to re-orient themselves at

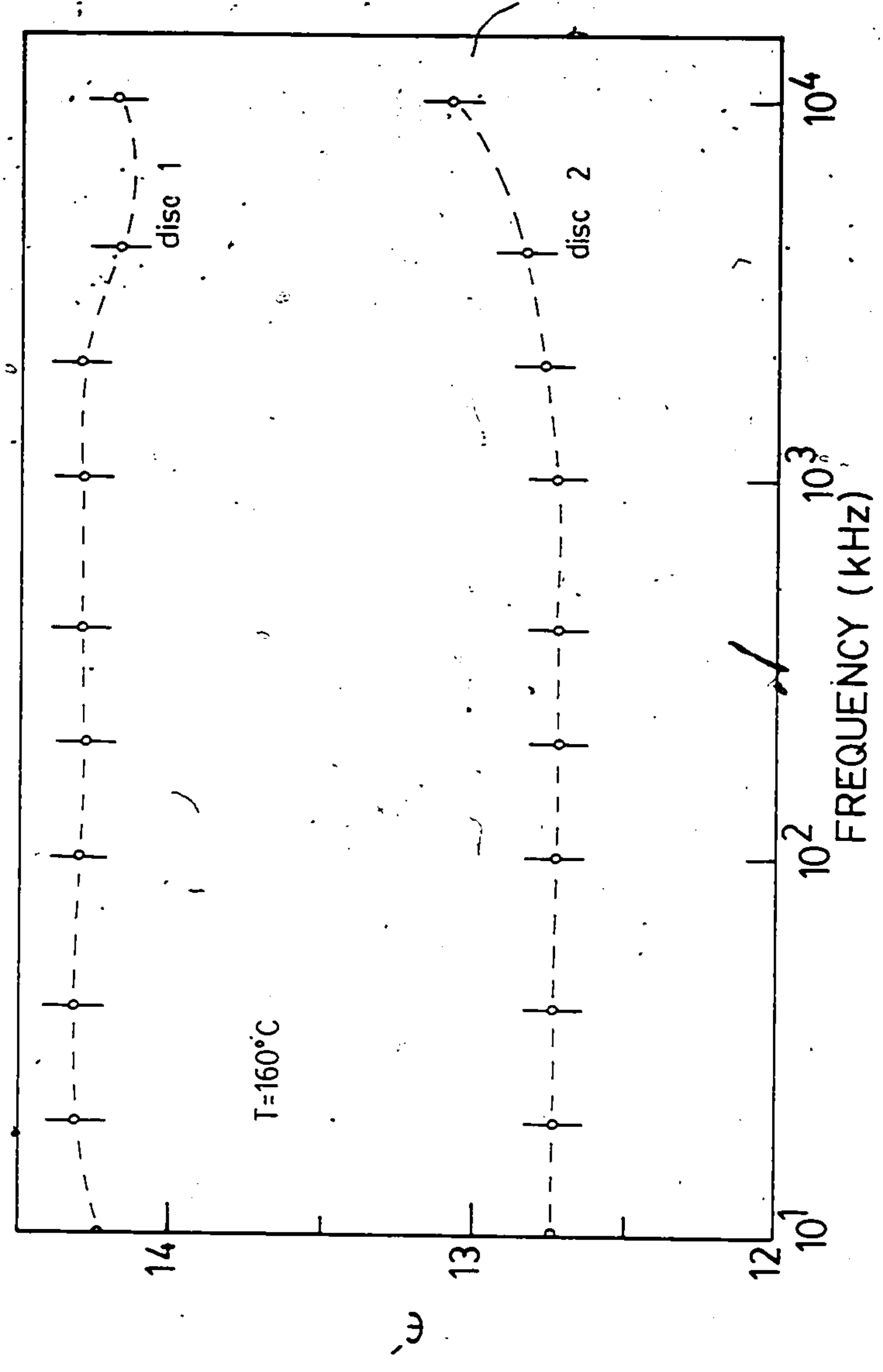

Figure 29 Dielectric constant vs. frequency at 160°C.

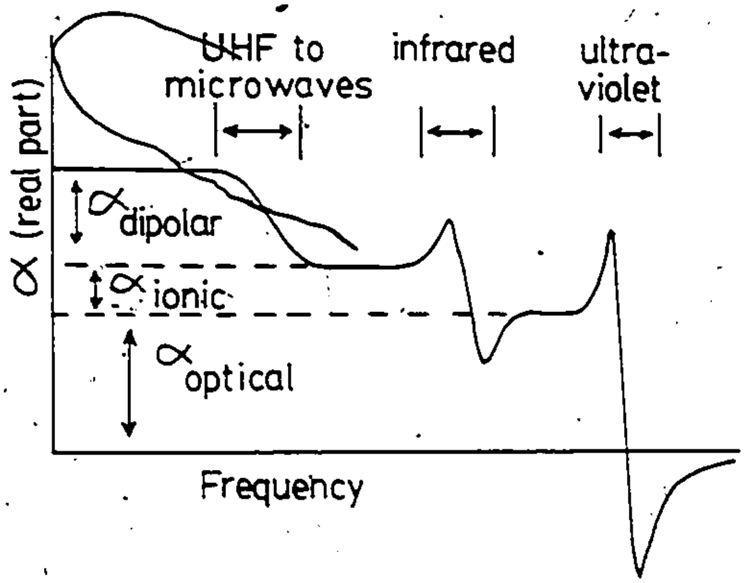

Figure 30 Schematic illustration of the behaviour of the total polarizability vs. frequency for a dielectric material [65,(1976)].

these frequencies. Since the permanent dipoles are restricted in the fresnoite discs (i.e., are not free to rotate in the field), the contribution of the dipolar polarizability to the total polarizability was expected to be small, and thus it was anticipated that the dielectric constant would slightly decrease with frequency. The increase in ε' with frequency in the range of 2-10 MHz may have been due to one of the experimental factors discussed henceforth.

Figure 30 also shows that the variation of the dielectric constant with frequency is quite complicated. Debye, proposed the following relationship between the dielectric constant and frequency [(69), 1979]:

$$\varepsilon' = \varepsilon_\infty + \frac{\varepsilon_s - \varepsilon_\infty}{1 + \omega^2\theta^2} \qquad (9)$$

where, ε_s is the static permittivity (dielectric constant in a d.c. field-constant);

ε_∞ is the permittivity at an infinite frequency-constant:

ω is the frequency of the field;

θ is the time lag between the application of the field and the establishment of equilibrium - it is inversely proportional to temperature and typically $\sim 10^{-13}$ sec.

This relation describes the relaxation spectrum of a dielectric material. That is, when the frequency ω is much greater than the reciprocal of the time it takes a molecule to align itself with the field, ε' will equal ε_∞. When the frequency is much less than this value, ε' will equal ε_s.

The Debye equation is very useful when a wide frequency range is considered. However, examination of the time lag constant, θ, leads to useful information regarding the behaviour of ε' vs. temperature.

The following relationship exists between the time lag constant and temperature [16,(1971)]:

$$\theta \propto \frac{1}{T} \qquad (10)$$

There are two conditions which should be considered. At low frequencies or high temperatures ($\omega\theta << 1$), it is seen that $\varepsilon' \sim \varepsilon_s$ and it is temperature invariant. When $\omega\theta \sim 1$, it is seen that according to equations (9) and (10), ε' should increase with temperature.

The relationship between θ and temperature is very complicated due to the fact that it would include such microscopic variables as the interfacial polarization and lattice expansion discussed previously. In general, since mechanisms such as conduction are temperature enhanced, ε' will increase with temperature up to some maximum value and then decrease with increasing temperature. The temperature at which this maximum occurs will increase with frequency. This is shown schematically in Figure 31, where $\omega_2 > \omega_1$. With reference to Figure 24, it is seen that the maximum of ε' for the fresnoite ceramics and the fresnoite glass will occur at a temperature of $T > 200^{\circ}C$.

4.1.2 Discussion of the Dielectric Losses

It is conventional to plot ε'' vs. frequency (at a constant temperature) and tan δ vs. temperature (at a constant frequency) when analyzing dielectric losses. The

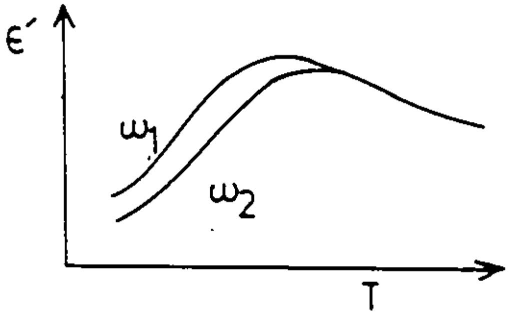

Figure 31 Temperature dependence of the dielectric constant for a dielectric material which undergoes dielectric relaxation (satisfies the Debye relation) [16,(1971)]. Note that $\omega_2 > \omega_1$.

values of ε'' were calculated from eq. (5). All of the curves plotted at a constant frequency or at a constant temperature were very similar (as they were in the case of ε'). Figure 32 is a plot of tan δ vs. temperature at 100 kHz, and Figure 35 is a plot of ε'' vs. frequency at 160°C. The other curves are located in Appendix II.

If fresnoite is assumed to have a low conductivity (i.e., it is a good insulator), the loss tangent can be approximated by [16,(1971)]:

$$\tan \delta \approx \frac{\omega\theta(\varepsilon_s - \varepsilon_\infty)}{\varepsilon_s + \varepsilon_\infty\omega^2\theta^2} \qquad (11)$$

where the quantities ω, θ, ε_s, and ε_∞ are defined by eq. (9).

At low frequencies ($\omega\theta << 1$), tan δ will increase with frequency. When the frequency is increased such that $\omega\theta >> 1$, tan δ will decrease with increasing frequency. The maximum frequency, ω_m, is given by:

$$\omega_m = \frac{1}{\theta}\sqrt{\frac{\varepsilon_s}{\varepsilon_\infty}} \qquad (12)$$

Figure 33 shows the general relationship of tan δ vs. temperature for a low conductivity dielectric as described by Eq. (11). In the range of $\omega\theta < 1$, tan δ is seen to rise with temperature up to a maximum at $T = T_m$: and in the range $\omega\theta > 1$, tan δ decreases with temperature. After this point, tan δ increases due to conduction losses. In Figure 34, the temperatures T_{1m} and T_{2m} represent maxima in tan δ at two frequencies ω_1 and ω_2 where $\omega_2 > \omega_1$. This relationship stems from eq. (12), since θ is inversely proportional to temperature. Since the frequency range investigated (10 kHz - 10 MHz) was both relatively low and narrow, it is reasonable to

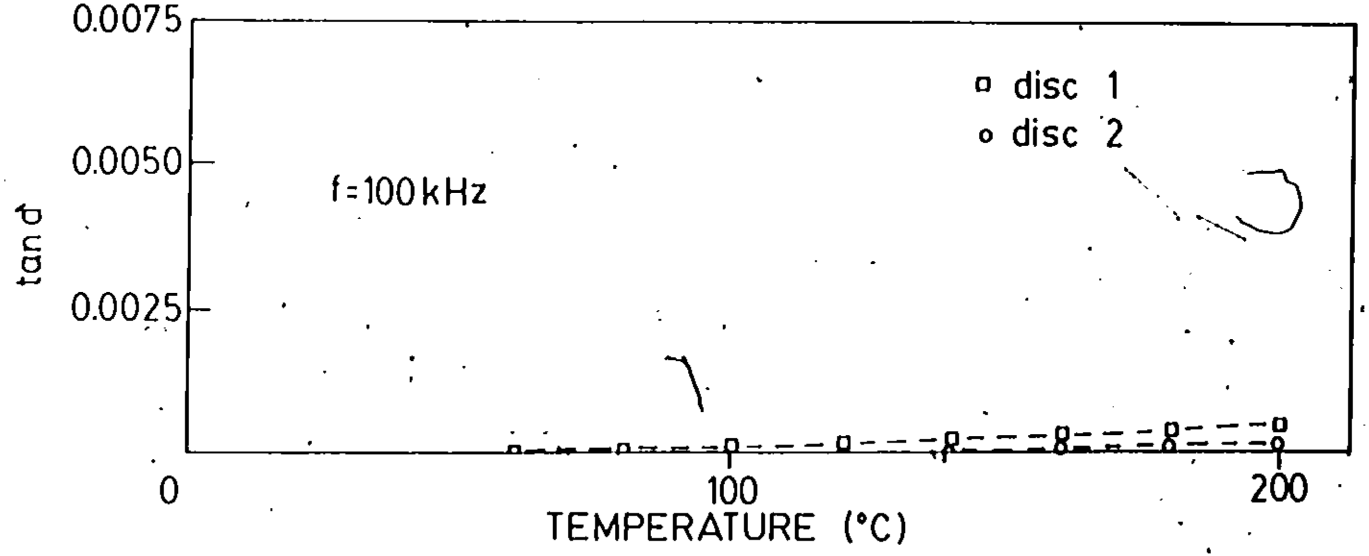

Figure 32 Tan δ vs. temperature at 100 kHz for the fresnoite discs.

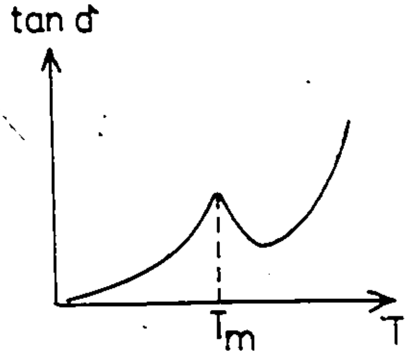

Figure 33 General relationship of tan δ vs. temperature for a low conductivity dielectric [16(1971)]. The rise in tan δ at $T > T_m$ is due to increased conduction losses.

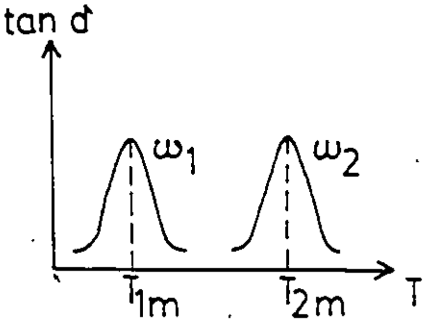

Figure 34 The effect of increasing the frequency on the temperature dependence of tan [16,(1971)]. Note that $\omega_2 > \omega_1$.

assume that in this range $\omega\theta << 1$, and tan δ should increase with temperature for both discs as shown in Figure 32.

The frequency dependence of the losses is slightly more difficult to discuss. Figure 35 shows that the losses for both discs are quite similar at low frequencies (10 kHz - 100 kHz), but in the range 100 kHz - 10 MHz the losses of disc 2 are quite significant, while the losses for disc 1 are very small. At a frequency of 400 kHz, there is a sharp maximum in the losses of disc 2, while the losses of disc 1 are negligible. If the frequency of 400 kHz corresponded to ω_m, it is expected that the losses would also be substantial for disc 1.

The losses were analyzed in terms of the possible resonance spectra, since at resonant frequencies the losses will be maximum [67,(1980)]. Since there can be motion both across and through the disc, two forms of resonance were considered: the transverse mode of resonance which accounts for the wave motion through the disc, and the radial mode of resonance which accounts for the wave motion across the disc.

Before the resonance spectra of the ceramic discs could be analyzed, Poisson's ratio, σ, had to be estimated. A simple average of tetragonal crystals in an isotropic polygrain ceramic leads to the following relations for Lame's constants, λ and μ:

$$\lambda = \frac{C_{12}^{E} + 2C_{13}^{E}}{3} \qquad (13)$$

$$\mu = \frac{2C_{44}^{E} + C_{66}^{E}}{3} \qquad (14)$$

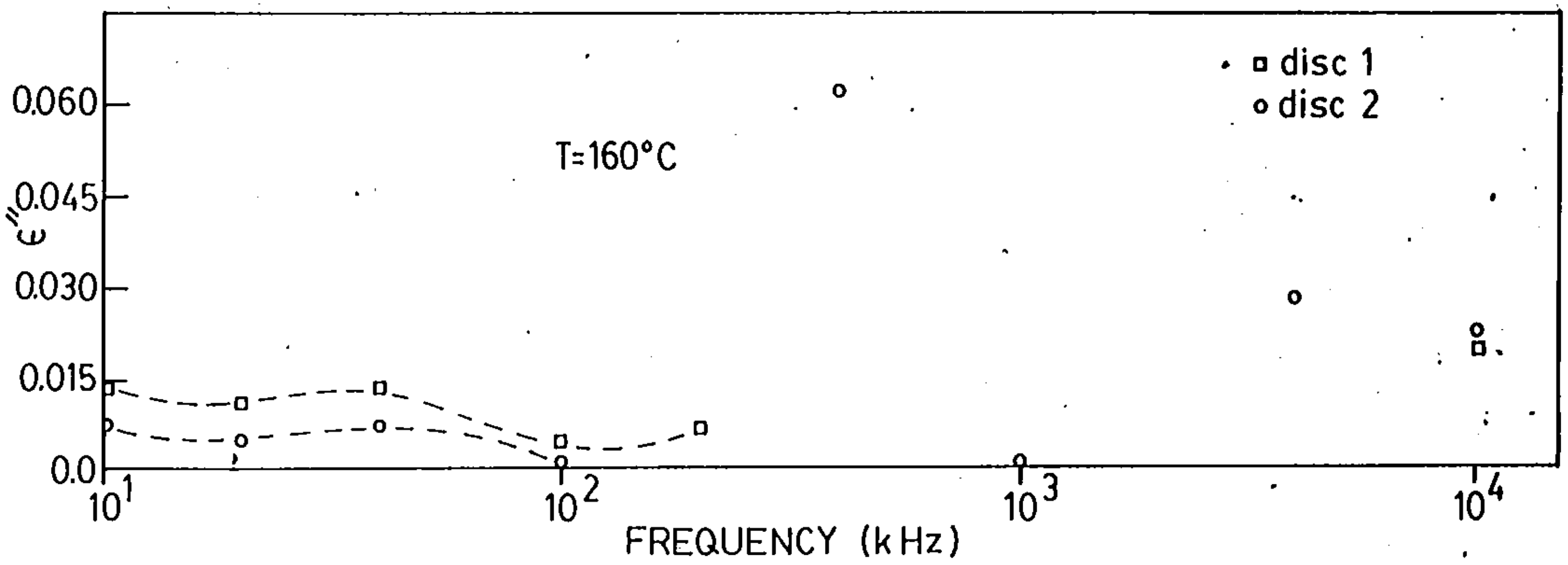

Figure 35 ε" vs. frequency at 160°C for the fresnoite discs.

where C^E_{ij} is the elastic stiffness for the fresnoite tetragonal crystal when the external electric field E is kept constant. Poisson's ratio, σ, is given by:

$$\sigma = \frac{\lambda}{2(\mu+\lambda)} \qquad (15)$$

The elastic stiffness of the fresnoite single crystal may be taken from Kimura [7,(1977)]. Substitution of these values into the above relations yielded:

$$\sigma = 0.20$$

The boundary condition for the thickness mode of resonance was both ends mechanically clamped, which should give rise to half wave-length resonance [70,(1964)]. The resonant frequency in the thickness direction (transverse mode) is given by [71,(1979)]:

$$f_{R_{(t)}} = \frac{1}{d}\left(\frac{1-\sigma}{(1-2\sigma)(1+\sigma)}\right)^{\frac{1}{2}}\left(\frac{\bar{C}^E_{33}}{\rho}\right)^{\frac{1}{2}} \qquad (16)$$

where: d is the disc thickness: disc 1→d = 0.00265m;
disc 2→d = 0.00147m

σ is Poisson's ratio (=0.20)

$\bar{C}^E_{33} = \frac{1}{3}(C^E_{33} + 2C^E_{11})$

ρ is the density = 4450 $kg \cdot m^{-3}$.

Substitution of the appropriate elastic constants and dimensions yields:

$$f_{R_{(t)}} \sim 2.1 \text{ MHz (disc 1)}$$

$$f_{R_{(t)}} \sim 3.7 \text{ MHz (disc 2)}$$

The boundary conditions for the radial mode of resonance corresponded to both ends being mechanically free, which should also give rise to half wave-length resonance. The resonant frequency in the radial direction is given by [71,(1979)]:

$$f_{R_{(r)}} = \frac{1}{r}\,\frac{n}{2\pi}\,\left(\frac{\bar{C}^E_{11}}{(1-\sigma^2)\rho}\right)^{\frac{1}{2}} \qquad (17)$$

where, r is the radius of the discs, which is 0.01155m

n is a shape factor which is also a function of Poisson's ratio, and is equal to 2.05 (for σ~0.3)

$\bar{C}^E_{11} = \frac{1}{3}(2C^E_{11} + C^E_{33})$

ρ is the density = 4450 $\mathrm{kg \cdot m^{-3}}$.

Substitution of the appropriate elastic constants yields:

$$f_{R_{(r)}} \sim 150\ \mathrm{kHz}$$

Examination of Figure 35 reveals that there is a maximum in ε'' for disc 2 at 4MHz, which is close to the value of $f_{R_{(t)}}$ calculated for it. However, since there is no maximum for disc 1 at ~2MHz, which is the calculated value of $f_{R_{(t)}}$, it is reasonable to assume that the losses at 4MHz for disc 2 are not due to a transverse mode of resonance. The large peak in the losses at 400 kHz for disc 2 and the small maximum at 200 kHz for disc 2 are fairly close to the calculated value of $f_{R_{(r)}}$. Thus, these ceramic discs could have undergone resonance in the radial direction, but not in the thickness direction. The cause of the high losses for both discs in the 4-10 MHz range is not clearly known.

4.1.3 Possible Experimental Errors in the Dielectric Measurements

Although fresnoite discs 1 and 2 were prepared in the same manner, they yielded slightly different results. The possible causes for this discrepancy are discussed below.

When the fresnoite discs were polished, 1.0μ Al_2O_3 powder suspended in water was used as the abrasive agent. This may have resulted in the formation of disturbed regions or layers near the polished surfaces. If such regions were formed, they would alter the capacitance of the disc, since there would now be more than one capacitor connected in series. Aluminum was evaporated on the discs to improve the contact between the brass electrodes and the ceramic. This resulted in some Al_2O_3 formation on the disc surfaces and would have the same effect as discussed above. These two effects cannot really be separated from each other and they will henceforth be referred to as the surface-layer effect.

The dielectric constant calculated from Eq. (5) is theoretically accurate, but a better method would have been to first measure the capacitance of a standard whose dielectric constant was known and was stable over the whole temperature and frequency range. The dielectric constant would have then been calculated from (provided the discs possessed the same diameter):

$$\varepsilon_{fresnoite} = \frac{C_f d_f \varepsilon_s}{C_s d_s} \qquad (18)$$

where, ε_s is the dielectric constant of the standard

C_s is the measured capacitance of the standard

d_s is the thickness of the standard

C_f is the measured capacitance of the fresnoite disc

d_f is the thickness of the fresnoite disc.

Teflon was chosen to be used as a standard material. A teflon disc of the same diameter as the fresnoite discs was fabricated and coated with aluminum. The dielectric constant calculated from the capacitance measurements was quite different from the known value. This difference could have resulted from Al_2O_3 formation on the faces of the disc and a small air gap due to slightly non-parallel disc faces. An attempt to compensate for the surface-layer effect is detailed in Section 4.1.4.

The difference in the dielectric constant of the two discs could have resulted from the fabrication method used. High purity paraffin was used as a binder, and ideally, it should have completely evaporated during the sintering process. However, quantitative compositional analysis of different fresnoite discs indicated that there was carbon present inside the discs, which means that some of the paraffin (which is carbon based material) did not completely evaporate. The compositional analysis is detailed in section 4.3.2.1.

It is reasonable to assume that a larger percentage of residual carbon would be left in the thicker disc (disc 1), since gases yielded from the paraffin would have a greater distance to diffuse through the disc. The residual carbon left in the discs should be present at the grain boundaries, and it could have a large effect on the interfacial polarization discussed in section 4.1.2. Thus, if there is more carbon present in disc 1, the interfacial component of the polarization would be larger for disc 1 than for disc 2, which would account for the increased dielectric constant of disc 1 over disc 2. Quantitative compositional measurements should be performed on the fracture surfaces of discs of different thicknesses to support this hypothesis.

4.1.4 Compensation of the Surface-Layer Effect

One reason proposed for the discrepancy between the measured values of the dielectric constant for the fresnoite discs was the surface-layer effect discussed previously. The measured values for the capacitance and dielectric loss of the discs are combined below to compensate for this effect.

Figure 36 is a schematic representation of the geometry of this situation. There are two fresnoite discs and each disc possesses modified surface layers as shown. For this analysis, it had to be assumed that each modified layer is of the same thickness. The measured capacitance and dielectric loss can be written as:

$$\left.\frac{1}{C_t}\right]_i = \left.\frac{1}{C_m}\right]_i + \left.\frac{1}{C_f}\right]_i \quad ; \; i = 1,2 \qquad (19)$$

where, the numbers 1 and 2 denote fresnoite discs 1 and 2 respectively,

the subscript t denotes the total measured value,

the subscript m denotes the modified layer,

the subscript f denotes true fresnoite.

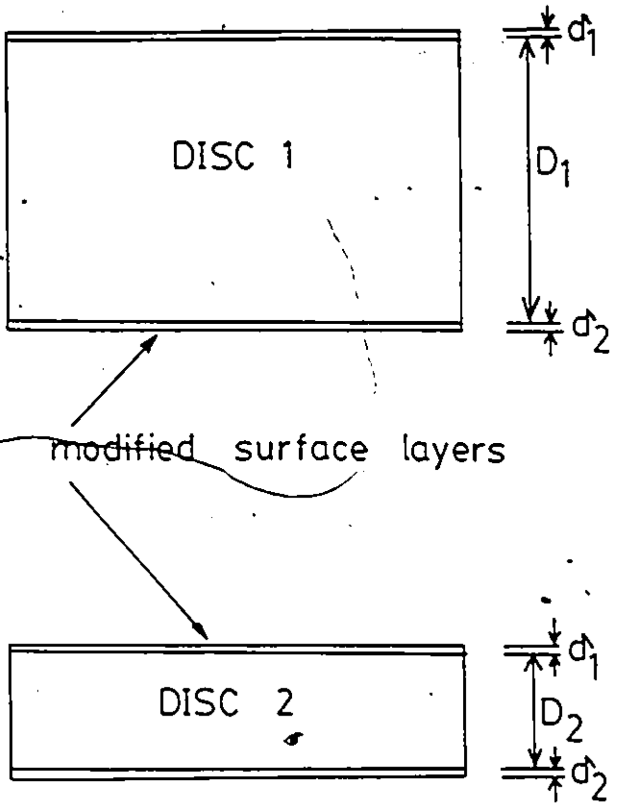

Figure 36 Schematic representation of the surface layer effect. The relative thickness of the modified layers has been exaggerated for clarity. For this calculation, $D_1 \neq D_2$, but it must be assumed that $\delta_1 = \delta_2$ for both discs.

Since, $C_f = \frac{A\varepsilon_o\varepsilon_f}{d}$, the previous expressions can be written as,

$$\left.\frac{1}{C_t}\right]_i = \left.\frac{1}{C_m}\right]_i + \frac{d_i}{A\varepsilon_o}\cdot\frac{1}{\varepsilon_f}\ ;\ i = 1,2 \tag{20}$$

The modified surface layers are assumed to possess the same thickness, i.e.,

$$\left[\frac{1}{C_m}\right]_1 = \left[\frac{1}{C_m}\right]_2$$

Thus, Eqs. (19) yield:

$$\left[\frac{1}{C_t}\right]_1 - \left[\frac{1}{C_t}\right]_2 = \frac{1}{A\varepsilon_o}\left[\frac{\Delta}{\varepsilon_f}\right] \tag{21}$$

where $\Delta \equiv d_1 - d_2$.

Consideration of the real components of Eq. (21) yields:

$$\left[\frac{1}{C'_t(1+\tan^2\delta)}\right]_1 - \left[\frac{1}{C'_t(1+\tan^2\delta)}\right]_2 = \frac{d}{A\varepsilon_o}\left[\frac{1}{\varepsilon'_f(1+\tan^2\delta)}\right] \tag{22}$$

where, the prime refers to the real part of the measured parameter, i.e., $C = C' + iC''$.

Tables 6 and 7 show that $\tan^2\delta << 1$. Therefore,

$$\left[\frac{1}{C'_t}\right]_1 - \left[\frac{1}{C'_t}\right]_2 \simeq \frac{d}{A\varepsilon_o}\left[\frac{1}{\varepsilon'_f}\right] \tag{23}$$

Similarly, consideration of the imaginary components of Eq. (21) yields:

$$\left[\frac{1}{C''_t}\right]_1 - \left[\frac{1}{C''_t}\right]_2 = \frac{d}{A\varepsilon_o}\left[\frac{1}{\varepsilon''_f}\right] \tag{24}$$

This expression can be rearranged to give:

$$\frac{C''_{t2}\cdot C''_{t1}}{C''_{t1} - C''_{t2}} = \frac{A\varepsilon_o}{\Delta}\cdot\varepsilon''_f \tag{25}$$

Thus, whenever the measured value of either tan δ_1 or tan δ_2 is zero, the compensated values of ε'' will be zero. Tables 11 and 12 list the values of ε_f' and ε_f'' calculated from Eqs. (23) and (25) and the data in Tables 6 and 7. Figure 37 is a plot of the compensated values of ε' vs. temperature for the frequency of 100 Hz.

Figure 37 shows that the compensated values are much larger than expected. This probably means that the assumption that each modified layer possessed the same thickness (which was necessary for the above calculations) was not correct. It may also be concluded that the surface-layer effect was not the sole reason for the difference in the dielectric constant for the two discs. That is, the contribution of the residual carbon to the interfacial polarization could be more of a factor than the surface-layer effect.

4.2 Determination of the Optimum Sintering Temperature of the Ceramics

Ceramic powders of two compositions were studied. These compositions were: $Ba_2Si_2TiO_8$ (fresnoite) and $Ba_{2.99}Si_2Ti_{0.8}O_{8.59}$. The second composition was chosen on the basis of preliminary ESCA results of thin films sputtered from fresnoite targets. The DTA results for fresnoite are shown in Figure 38. The results of this figure are summarized in Table 13. The DTA results for the composition $Ba_{2.99}Si_2Ti_{0.8}O_{8.59}$ were very similar to fresnoite and are also included in this table.

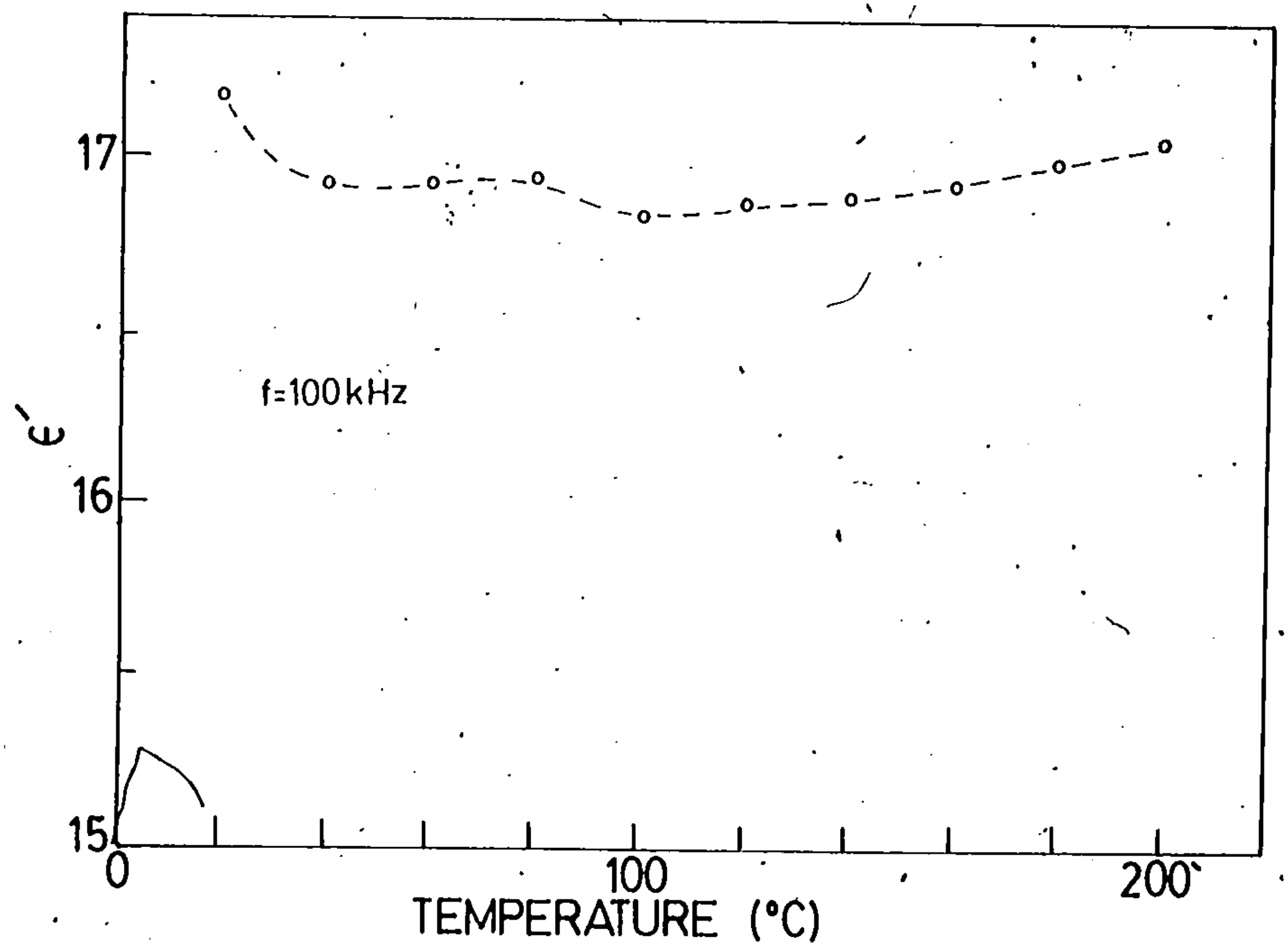

Figure 37 Modified dielectric constant vs. temperature at 100 kHz.

TABLE 11

Modified Values of the Dielectric Constant for Both Fresnoite Discs. The Discs Were Assumed to Have Modified Surface Layers of the Same Thickness

T	Frequency									
(^{o}C)	10 KHz	20 KHz	40 KHz	100 KHz	200 KHz	400 KHz	1 MHz	2 MHz	4 MHz	10 MHz
20	17.18	17.16	17.18	17.18	17.12	17.10	17.12	17.04	16.37	15.84
40	16.94	16.91	16.92	16.91	16.83	16.88	16.88	16.81	16.29	15.77
60	16.96	16.93	16.93	16.91	16.84	16.87	16.88	16.82	16.30	15.81
80	16.98	16.95	16.95	16.93	16.86	16.87	16.89	16.82	16.30	15.83
100	16.86	16.83	16.83	16.81	16.72	16.78	16.76	16.69	16.15	15.71
120	16.95	16.87	16.87	16.84	16.77	16.82	16.81	16.74	16.19	15.76
140	16.91	16.88	16.89	16.87	16.80	16.86	16.85	16.77	16.23	15.80
160	16.95	16.92	16.93	16.91	16.84	16.91	16.89	16.81	16.27	15.85
180	17.02	16.99	16.99	16.97	16.90	16.97	16.95	16.88	16.32	15.91
200	17.08	17.05	17.05	17.02	16.95	17.02	17.00	16.92	16.37	15.97

TABLE 12

Modified Values of ε" for Both Fresnoite Discs. The Discs Were Assumed to Have Modified Surface Layers of the Same Thickness. Blank Values Correspond to ε" = 0.0.

T	Frequency									
(°C)	10 KHz	20 KHz	40 KHz	100 KHz	200 KHz	400 KHz	1 MHz	2 MHz	4 MHz	10 MHz
20									-0.044	-0.256
40										-0.168
60										-0.175
80										-0.171
100										-0.175
120										-0.183
140	0.160	0.106	0.489	-0.003						-0.193
160	-2.823	0.516	1.115	0.024						-0.200
180	-3.078	0.799	6.200	0.023						-0.403
200	4.417	0.797	2.402	0.042	-0.006					-0.507

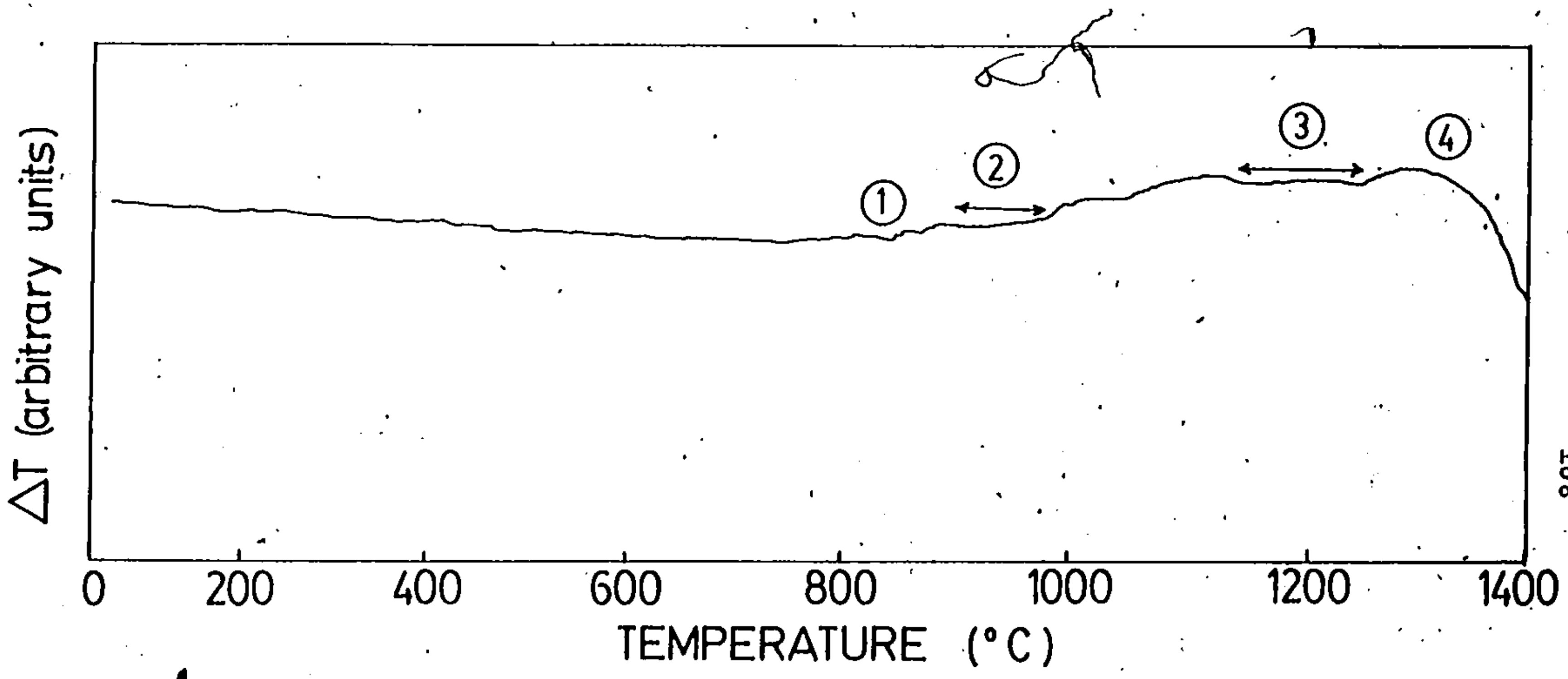

Figure 38 DTA of fresnoite. The indicated reactions are detailed in Table 12.

TABLE 13

Summary of the DTA Results for the Two Ceramic Powders. The Reaction Number Corresponds to the Reaction Shown In Figure 38

Reaction Number	Explanation	Temperature Range	
		$Ba_2Si_2TiO_8$	$Ba_{2.99}Si_2Ti_{0.8}O_{8.59}$
1	Anatase to Rutile transformation of TiO_2 [72, (1976)]. The TiO_2 powder used was found to consist of both forms of TiO_2.	830-850°C	800-820°C
2	Calcination, i.e., $BaCO_3 \quad BaO + CO_2$	920-980°C	950-980°C
3	Ceramic formation. For fresnoite this consisted of: $2BaO+2SiO_2+TiO_2 \quad Ba_2Si_2TiO_8$ For the composition, $Ba_{2.99}Si_2Ti_{0.8}O_{8.59}$ this as well as other reactions occurred due to the non-stoichiometry of the powder.	1140-1240°C	1120-1160°C
4	Softening or melting of the ceramic begins.	1300°C	1250°C

With reference to Table 13, the proper sintering temperature is located between the ceramic formation temperature and the softening temperature. This temperature range is about 1240-1300°C for the fresnoite powder, and 1160-1250°C for the $Ba_{2.99}Si_2Ti_{0.8}O_{8.59}$ powder.

Fresnoite discs were fabricated and sintered in five degree intervals from 1250-1300°C. SEM[11] micrographs and x-ray diffraction[12] patterns were obtained for each disc. The samples were coated with carbon to prevent electrical-charge build-up on them during the SEM analysis. All x-ray diffraction analyses were performed under the following conditions. A Cu x-ray tube operated at 40 kV and 20 mA was used to generate monochromatic CuK_α x-rays of wavelength 0.1542 nm. The diffracted x-rays were detected by a counter connected to a chart recorder with a feed rate of 2°/min.

Figure 39(a)-(c) shows SEM micrographs of the fresnoite discs sintered at 1250 and 1300°C, as well as the disc sintered at 1275°C. Figure 39(a) shows that at 1250°C, rectangular grains were not yet formed which indicates that sintering was not complete. Figures 39(b) and (c) show that at 1275 and 1300°C, rectangular grains were formed and the ceramics were well sintered. The temperature of 1275°C was judged to be the best sintering temperature for fresnoite. At temperatures higher than this, the discs had a tendency to warp which made them unsuitable for sputtering targets.

---

[11] Nanolab 7 SEMCO.

[12] Philips Model PW1011/60.

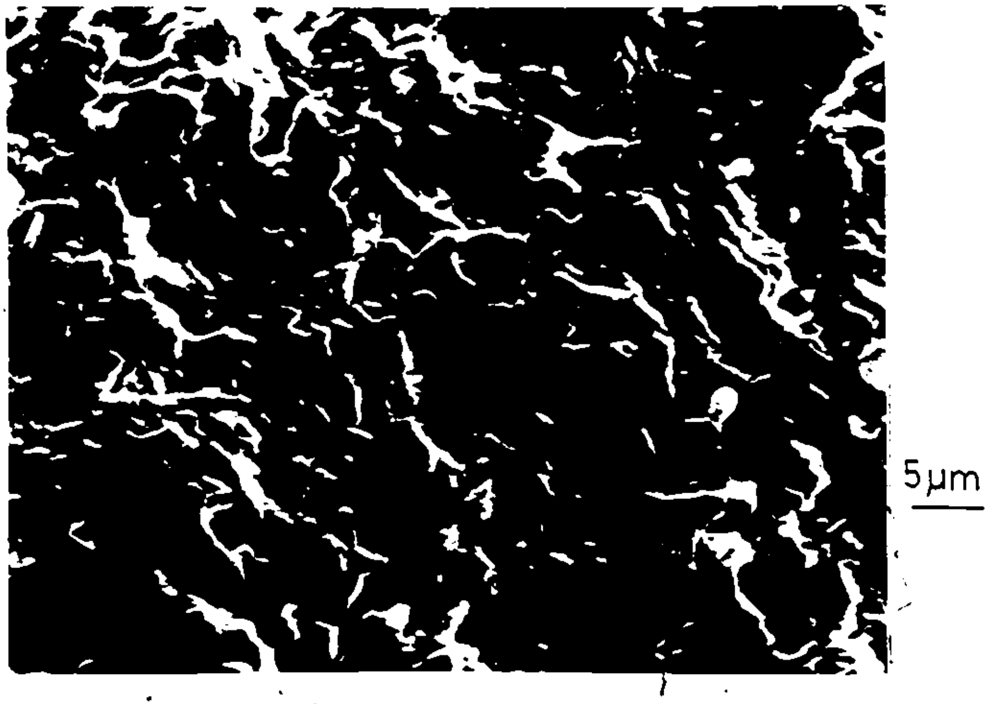

Figure 39(a) SEM micrograph of the fresnoite ceramic sintered at 1250°C.

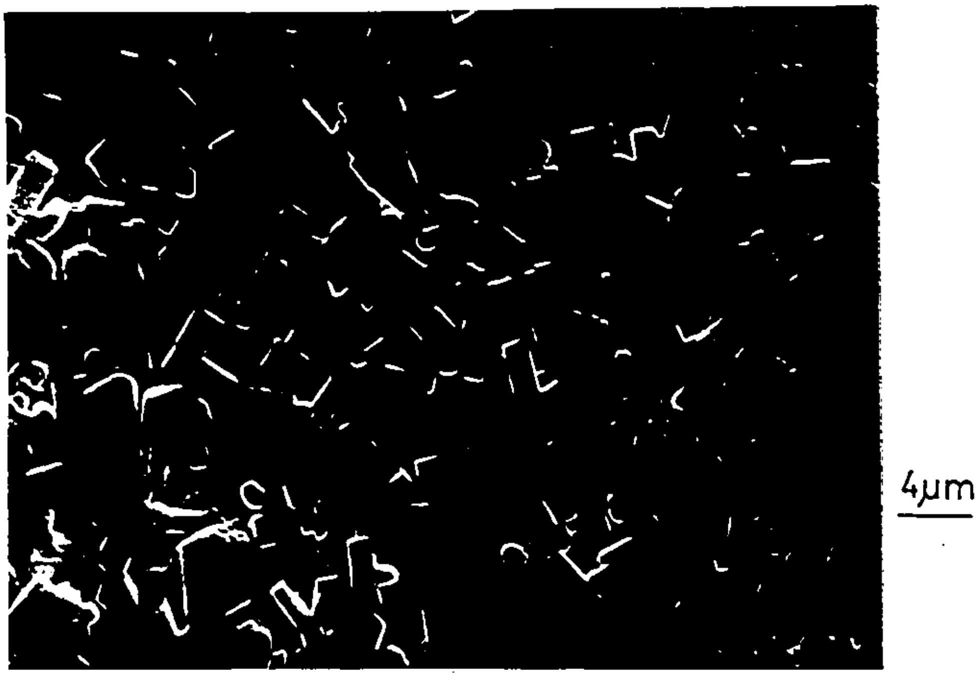

Figure 39(b) SEM micrograph of the fresnoite ceramic sintered at 1275°C.

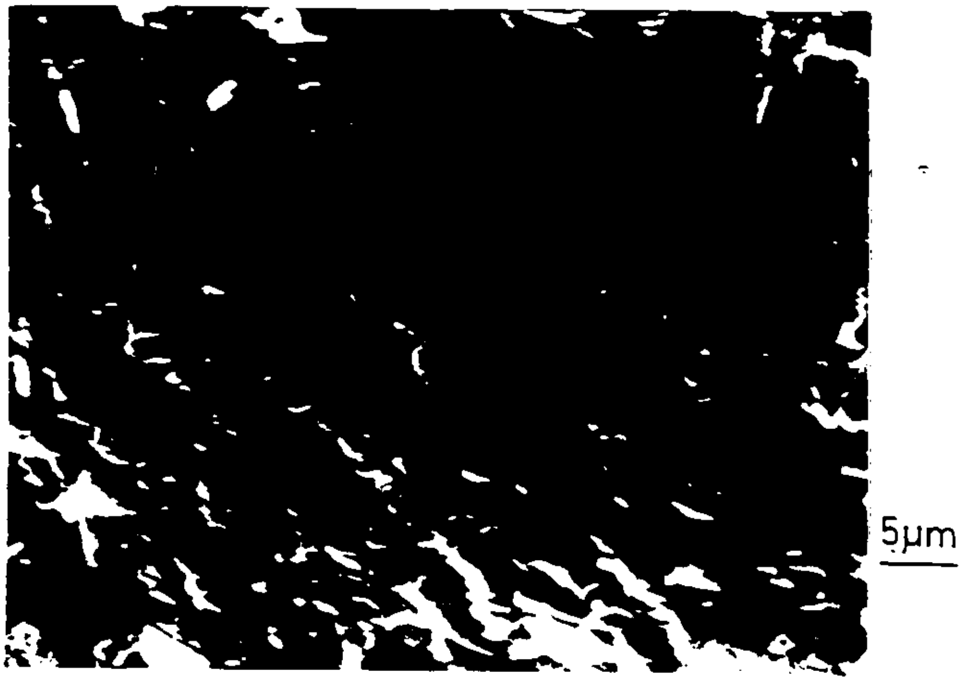

Figure 39(c) SEM micrograph of the fresnoite ceramic sintered at 1300°C.

The x-ray diffraction pattern obtained from the disc sintered at 1275°C is shown in Figure 40. All of the fresnoite diffraction peaks predicted by the JCPDS powder diffraction file are present in this pattern, and these peaks are labelled. The origin of the few peaks which are not indexed are discussed in detail in section 4.3.2.1.

Discs of the composition $Ba_{2.99}Si_2Ti_{0.8}O_{8.59}$ were pressed and sintered at temperatures 1160-1250°C. These discs all cracked and warped during the sintering process, and thus sputtering targets of this composition could not be fabricated. However, the possibility remained that a mixture of this powder and fresnoite powder could yield ceramics of sufficient quality to be used as sputtering targets. Small amounts of these powders were mixed, and discs were pressed and sintered. It was finally found that the composition:

$$\tfrac{1}{2}Ba_2Si_2TiO_8 + \tfrac{1}{2}Ba_{2.99}Si_2Ti_{0.8}O_{8.59}$$

sintered at 1245°C resulted in ceramics of the minimum desired quality. This composition will henceforth be referred to as "mod-BST". Figure 41 is an SEM micrograph of this ceramic. It shows that the grains are not very distinct, especially when compared to Figure 39(b). However, this was the best ceramic which could be produced from the $Ba_{2.99}Si_2Ti_{0.8}O_{8.59}$ powder. The x-ray diffraction pattern for the mod-BST ceramic is shown in Figure 42. In this figure, the fresnoite diffraction peaks are labelled. The intensity of the secondary phase peaks is much greater for mod-BST than for fresnoite, which indicates that these

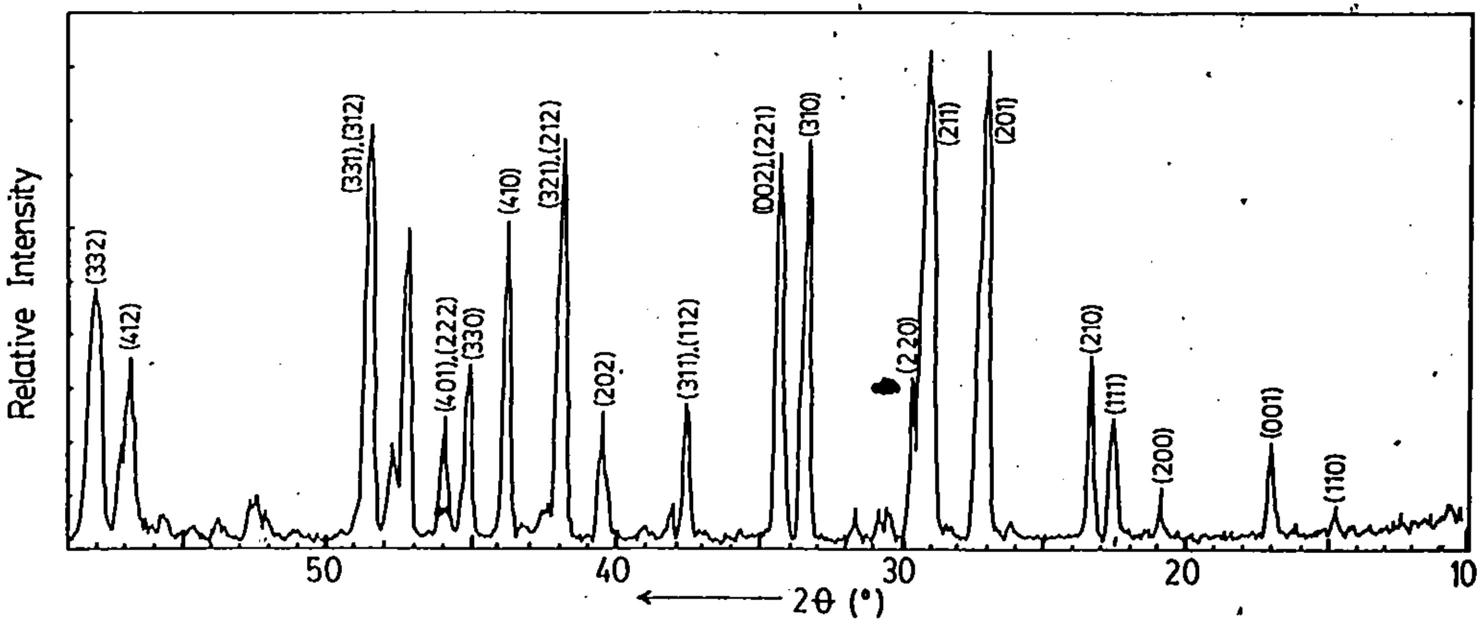

Figure 40 X-ray diffraction pattern of the fresnoite ceramic. The fresnoite diffraction peaks are indexed.

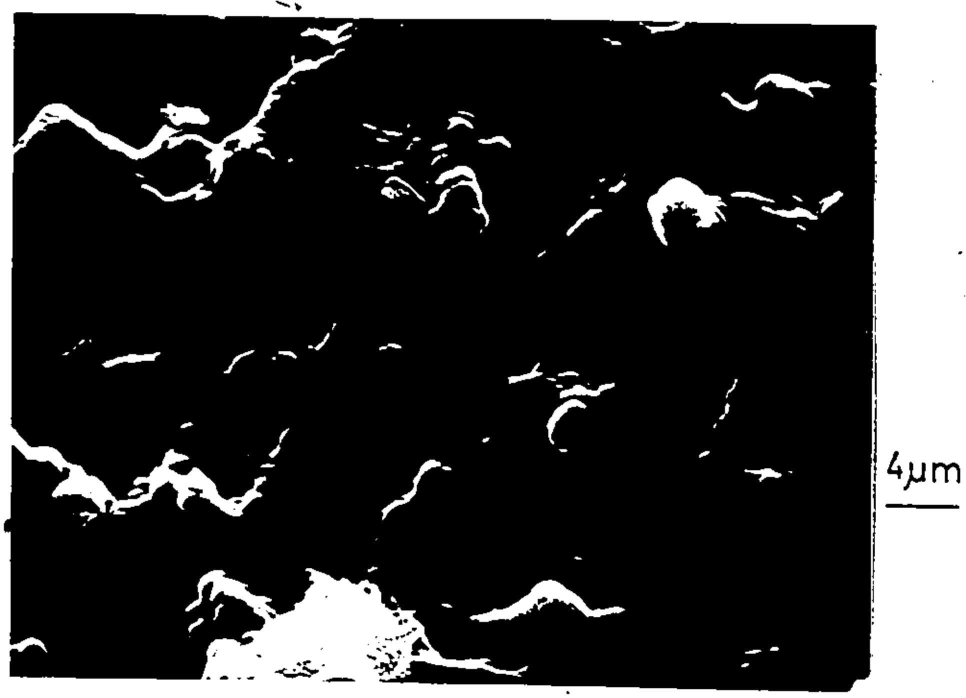

Figure 41 SEM micrograph of the mod-BST ceramic sintered at 1245°C.

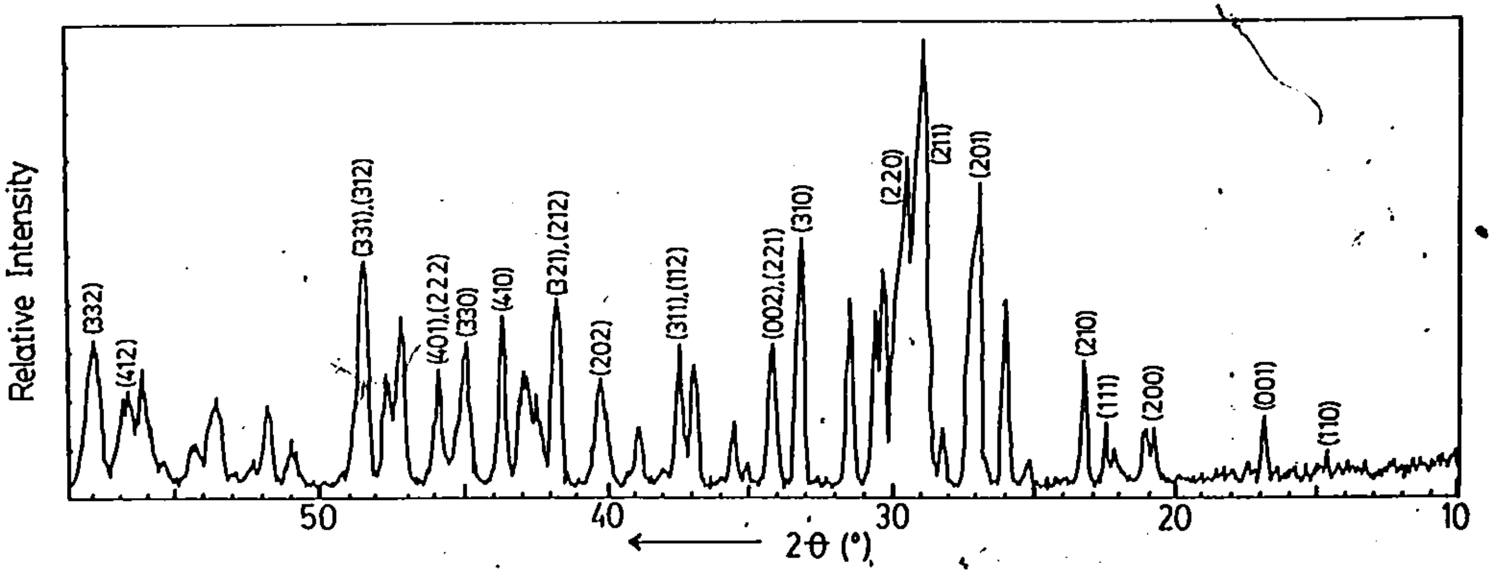

Figure 42 X-ray diffraction pattern of the mod-BST ceramic. The fresnoite peaks are indexed.

ceramics contained a much higher amount of secondary phases than the fresnoite ceramics. The diffraction peaks which are not indexed are discussed in detail in section 4.3.2.2.

4.3 Thin Film Analysis

4.3.1 Influence of the Deposition Parameters

Thin films can possess different morphologies: amorphous, polycrystalline, and epitaxial (or preferentially oriented). While there are many factors in the sputtering process which can influence the morphology of a film, the two variables which exert the greatest influence are: the substrate temperature, and the substrate itself. It is well known that the nature of the substrate can greatly affect the properties of the film which is deposited on it. Single crystal substrates such as NaCl, MgO, Si, Ge, and mica are commonly used for the production of polycrystalline and epitaxial thin films.

Amorphous films are usually formed at low substrate temperatures. At these low temperatures, the incident atoms have a low surface mobility so that a disordered (i.e., amorphous) state is "frozen" in before the atoms can reach their most preferable energetic sites which corresponds to the crystallographic structure of the material [73,(1977)].

One well known empirical relationship observed for metallic thin films is that crystalline films are usually formed if [74,(1979)]:

$$T_s > \frac{1}{3} T_m$$

where T_s is the substrate temperature (K), and T_m is the melting point of the bulk target (K).

The above relationship indicates that metallic thin films do not require much thermal energy to gain enough surface mobility to form crystalline thin films. This arises from the fact that metals crystallize into close-packed structures which do not differ that much from the random arrangement of the amorphous structure.

Ceramics can contain significant amounts of covalent bonding and consequently these materials are characterized by a relatively low coordination number. Thus, for the formation of a crystalline thin film, it is expected that the substrate temperature might have to be much greater than for the case of metallic thin films and it could even be required to approach the melting point of the film (~2/3 T_m). This is a consequence of the low coordination number, since it requires that the atoms be displaced relatively large distances if they are to occupy positions which correspond to the crystal structure.

Table 14 lists the different substrate materials and substrate temperatures investigated in the course of this work. The other sputtering variables were held constant and are summarized in Table 15.

It was found that 75W represented the maximum RF power which could be applied to the ceramic target. If the applied RF was any higher than this, the target would crack and sputtering would cease. Thickness measurements indicated that for an RF power of 75W (which corresponds to a power density of ~18 W/cm^2), the deposition rate

TABLE 14

Range of Deposition Parameters which were Varied in This Investigation. In all Cases, the Target Material was A $Ba_2Si_2TiO_8$ Ceramic - Except * Which Was A Mod-BST Target

Substrate Material	Substrate Temperature (^oC)	Applied R.F. Power (W)	Time (Hrs.)
NaCl (100)	170	50,75	10
	260	75	10
Mica (001)	170	50	8.5
	225	65	7
	365	50	10
	375	50	10
Si (100) and (111)	80	75	9.5
	170	75	9.5
	275	75	10
	340	75	8
	480	75	10
	650	75	9.5
	*80	75	10

TABLE 15

Summary of the Deposition Parameters Not Included in Table 14. These Parameters Were Held Constant Throughout This Work

Target Diameter		2.31 cm
Target to Substrate Distance		3.1 cm
Reflected R.F. Power		<5% of the incident R.F. power
Pressure		~90m Torr
Flow Rate	Ar	15 scc/min
	O_2	0.1 scc/min

was approximately 20 Å/min.

The substrate was placed as close to the target as possible without it being inside of the plasma. This helped minimize any radial losses of the sputtered material while avoiding any problems associated with the re-sputtering of the substrate and film.

The films prepared under the conditions detailed in Tables 14 and 15 were analyzed by x-ray diffraction and were found to be generally amorphous. Ayukawa [13,(1983)] reported that a thin film of fresnoite oriented in the (001) direction was formed by sputtering a fresnoite target onto an NaCl substrate heated at 170°C. His result, however, was not reproducible.

Figure 43 is an SEM micrograph of a thin film deposited onto an NaCl substrate. This figure shows the film to be peeled and cracked. Even though the film was cooled very slowly (<20°C/hr.), the film condition was most likely due to a difference of the thermal expansion coefficients between the film and NaCl combined with the surface roughness of the cleaved NaCl crystal.

Figure 44 is an SEM micrograph of a thin film sputtered onto a mica substrate. This figure is indicative of the condition of all the films deposited onto mica and Si substrates - the films were continuous and showed no evidence of being flawed.

Figure 43 SEM micrograph of a fresnoite film deposited onto an NaCl substrate.

Figure 44 SEM micrograph of a fresnoite film deposited onto a mica substrate.

4.3.2 Compositional Analysis

4.3.2.1 Fresnoite Ceramics and Thin Films Sputtered From Fresnoite Ceramic Targets

A quantitative compositional study was carried out to determine if any components (i.e., Ba, Si, Ti, or O) were lost during the sintering process of the ceramic sputtering targets or during the sputtering process for the formation of thin films. The facilities for such a detailed compositional analysis are not available at the University of Windsor; except for an x-ray energy dispersion analyser (EDS). Below is listed the techniques and locations where the specific work was performed.

1) Electron Spectroscopy for Chemical Analysis (ESCA) - Surface Science Western (SSW), University of Western Ontario, London, Ont.

2) Wavelength Dispersive Spectroscopy (WDS), Electron Spectroscopy for Chemical Analysis (ESCA), Auger Electron Spectroscopy (AES) - Energy Conversion Devices Inc. (ECD), Troy, Michigan, U.S.A.

3) Rutherford Backscattering Spectroscopy (RBS), Dept. of Physics, Queen's University, Kingston, Ont.

The bulk of the analyses was done by ESCA at the University of Western Ontario. A small number of samples were analysed at ECD and Queen's University.

Figure 45 shows a typical printout from an ESCA analysis of a fresnoite ceramic. The elements were identified from the energy of the ejected secondary electrons.

Figure 46 shows the display obtained during an EDS analysis of a fresnoite ceramic. Figure 46 and Table 16

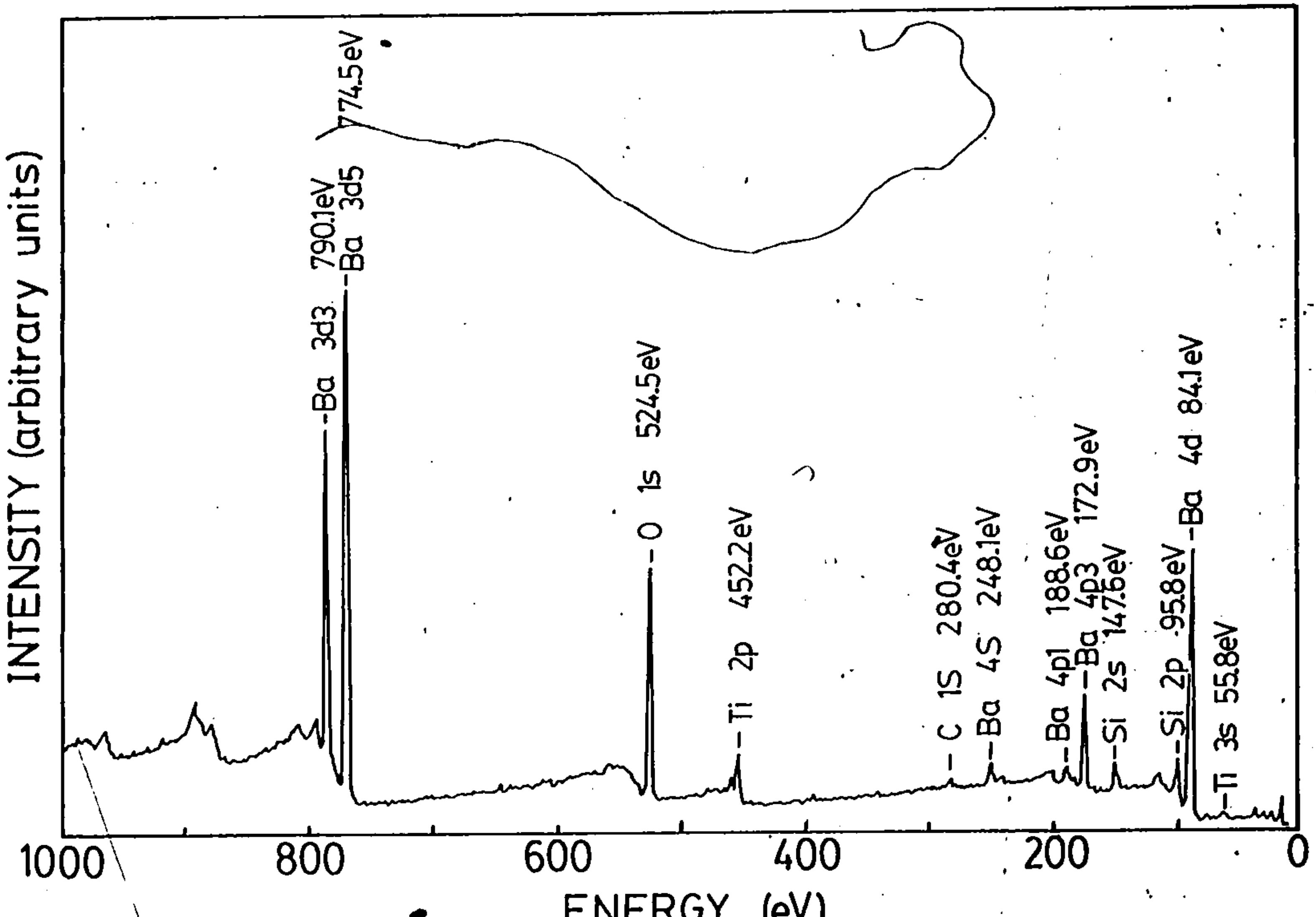

Figure 45 ESCA results for a fresnoite ceramic. The binding energy of the emitted electrons is indicated.

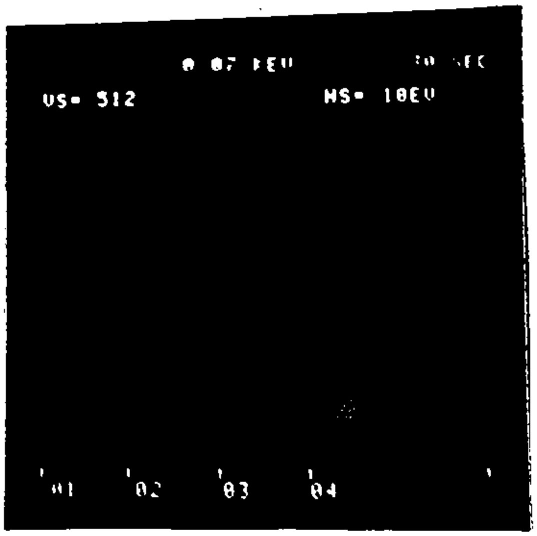

Figure 46 EDS display for a fresnoite ceramic. The emitted energy spectra of barium and titanium almost perfectly overlap for the peaks in the 4.5 and 4.9 keV energy ranges. Table 16 defines the specific transitions and actual emitted energy. The overlap which occurs is too severe to allow the peaks to be de-convoluted and thus an accurate quantitative analysis is very difficult for this material.

TABLE 16

Emitted X-Ray Energy of Barium and Titanium in the 4.5 and 4.9 keV Energy Ranges [75, (1978)]. These Emissions Overlap Too Severely to Allow a Precise Quantitative Analysis by the EDS* Technique (See Figure 46)

Element	Energy (keV)	Designation	
Ba	4.3309	$nL_{II}M_{I}$	Overlap for the Energy Peak in the 4.5keV Range
	4.45090	$\alpha_2L_{III}M_{IV}$	
	4.46626	$\alpha_1L_{III}M_{V}$	
Ti	4.50486	α_2KL_{II}	
	4.51084	α_1KL_{III}	
Ba	4.82753	$\beta_1L_{II}M_{IV}$	Overlap for the Energy Peak in the 4.9keV Range
	4.8519	$\beta_4L_{I}M_{II}$	
	4.9269	$\beta_3L_{I}M_{III}$	
	4.9939	$\beta_6L_{III}N_{I}$	
Ti	4.93181	$\beta_{1,3}KM_{II,III}$	
	4.9623	$\beta_5KM_{IV,V}$	

* EDS - energy dispersive spectroscopy

show that the emitted energy spectra of barium and titanium overlap, so a precise quantitative analysis can only be done if these energy peaks are de-convoluted - which is difficult to do. The results obtained by WDS are in principal very similar; however, since the resolution of this technique is much greater than for EDS, this problem was not encountered.

Figure 47 is a printout obtained from an RBS analysis of a fresnoite ceramic. Also shown is a simulated pattern for the exact composition of fresnoite. The possible reasons for the difference between these patterns are discussed henceforth.

Table 17 lists the compositional data obtained from the fresnoite ceramics analysed by the different techniques. The compositional data obtained for the films sputtered from fresnoite targets is shown in Table 18. The data presented in both tables is in terms of atomic per cent (at.%). The last column of each table, $(\Sigma+)/2$, is one-half of the summation of the product of the valence and the amount (at.%) of the cations (Ba, Si, and Ti) present in the sample. Electroneutrality considerations leads to the condition that this parameter should equal the amount of oxygen in the sample.

The ESCA results for the targets and films indicated that there was a significant amount of carbon present in them. This carbon may have been left over from the paraffin binder.

The samples analysed by ESCA were usually sputtered with Ar+ ions in-situ for 3 min. before they were examined. This removed a few monolayers of material and helped ensure

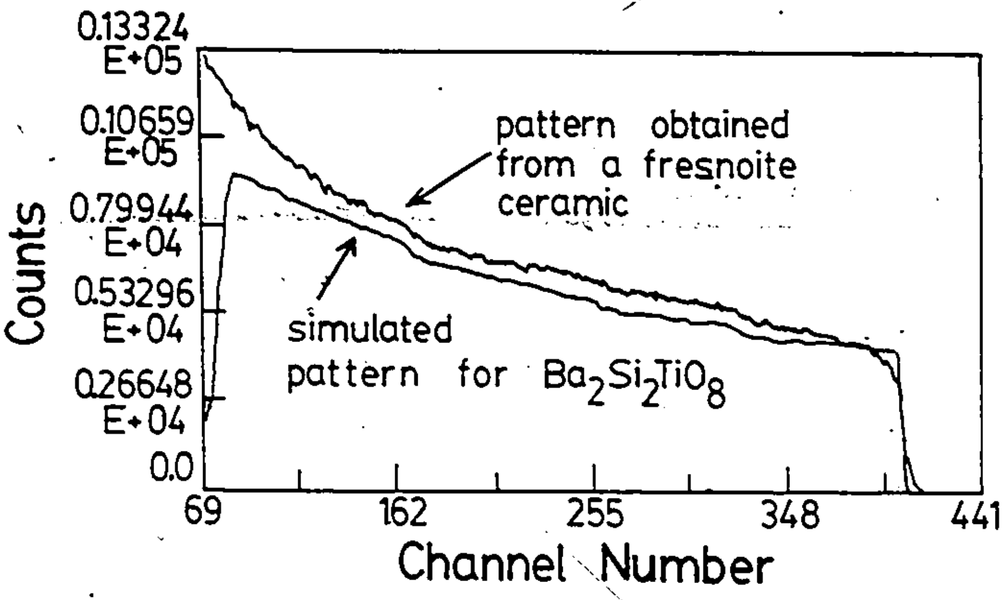

Figure 47 Printout obtained from an RBS analysis of a fresnoite ceramic. Also shown is the simulated pattern for the composition $Ba_2Si_2TiO_8$.

TABLE 17

Composition of the Fresnoite Ceramic Sputtering Target (at.%) Determined by the Different Techniques. (Σ+/2) is One-Half the Summation of the Product of the Valence and the Amount (at.%) of the Cations Present. Electroneutrality Consideration Leads to the Requirement that this Parameter Should Equal the Amount (at.%) of Oxygen Present

Technique	Ba	Ti	Si	O	(Σ+)/2
Ideal Composition of Fresnoite	15.38	7.69	15.38	61.54	61.52
WDS	15.8	7.9	14.0	62.3	59.6
ESCA (ECD)	15	3	15	67	51
ESCA (SSW)	13.7	6.7	24.9	54.6	76.9
RBS	10.84	7.25	22.22	59.69	69.78

WDS - Wavelength dispersive spectroscopy

ESCA - Electron Spectroscopy

RBS - Rutherford backscattering spectroscopy

TABLE 18

Composition of the Thin Films Sputtered From the Fresnoite Ceramics (at.%) Determined by the Different Techniques. The Film Number Indicates the Specific Films Which Were Measured By More than One Technique

Technique	Film No.	Ba	Ti	Si	O	(Σ+)/2
WDS	1	9.9	12.9	13.2	64.1	62.1
ESCA(ECD)	1	10	5	14	71	48
ESCA(SSW)	2	8.7	8.0	24.4	51.5	73.5
	3	8.4	8.9	28.0	54.6	82.2
	4	9.0	8.5	28.0	53.6	82
	5	8.9	7.8	27.1	56.3	78.7
RBS	4	7.60	10.48	11.22	70.70	51
	5	7.44	9.83	13.22	69.52	50.84

WDS - Wavelength dispersive spectroscopy

ESCA - Electron spectroscopy for chemical analysis

RBS - Rutherford backscattering spectroscopy.

that a "clean" surface was analysed. Two of the thin films were analysed before and after they were sputtered, and it was found that this decreased the carbon content from 33.8 to 4.17at.% and 28.18 to 10.39at.%. This leads to the conclusion that most of the carbon present in the films was due to atmospheric contamination, and the ceramics and films were assumed to be composed entirely of Ba, Si, Ti, and O.

Examination of Table 17 reveals that there is a wide fluctuation in the measured compositions of the fresnoite ceramics. Since the ceramics were all fabricated from the same batch of powder and were sintered under the same conditions, it was expected that these measurements would yield more consistent results.

The composition determined by the WDS methods was very close to the actual composition of fresnoite, and it satisfield the electro-neutrality condition to within 5%. An external calibration standard of single crystal benitoite, $BaSi_3TiO_9$ (13) was employed for this technique. The atomic correction factors (i.e., fluorescence, absorption, etc.) which are necessary for an accurate quantitative analysis are dependent on the chemical environment, and since benitoite is very similar to fresnoite, it yielded very accurate results when it is used as a calibration standard for fresnoite. Thus, the WDS technique was judged to be the most accurate of the techniques used.

The ESCA results were not based on external calibration.

---

(13) Tousimis Research Co., cat. #8045-83.

Instead, elemental sensitivity factors were used, and these are not as accurate as the correction factors derived from a suitable calibration standard. The difference in the ESCA results from ECD and SSW arose from the different correction factors used.

Since the RBS technique relies on kinetic processes only, it should have yielded the most accurate results. However, the RBS results shown in Table 17 and Figure 47 are very much different than the actual composition of fresnoite. Discussion with Queen's University indicated that the ceramic was not sputtered or fractured before it was analysed. Thus, processes such as surface segregation could have resulted in the outer surface not being representative of the interior or bulk of the ceramic.

If the composition determined by WDS is taken to be the true composition of the ceramic, the secondary phases present in the ceramic (as indicated in Figure 40) can be discussed in terms of the deviation of the actual composition (that determined by WDS) from the ideal composition of fresnoite. Table 19 lists the secondary phase diffraction peaks from a fresnoite ceramic. These peaks were taken from Figure 40 and are listed in terms of the increasing detector angle, 2θ. The interplanar spacing (d-spacing) was calculated from Bragg's law with the assumption that only first order diffraction peaks were present. A search through the JCPDS powder diffraction file produced the possible sources of these peaks, which are also shown in this table. It should be noted that the diffraction peaks listed in Table 19 are, for the most

TABLE 19

Secondary Phase Diffraction Peaks for a Fresnoite Ceramic. These Peaks Were Taken from Figure 40

$2\theta_{CuK_\alpha}$ (°)	d (nm)	Possible Sources
26.15	0.341	Ba_2SiO_4, $Ba_2Ti_9O_{20}$
28.4	0.314	Ba_2SiO_4, $Ba_2Ti_9O_{20}$
30.5	0.293	Ba_2SiO_4, Ba_3SiO_5
30.75	0.291	Ba_2SiO_4
31.6	0.283	(101), (110) $BaTiO_3$
38.0	0.237	?
39.0	0.231	(111) $BaTiO_3$, Ba_2SiO_4
42.3	0.214	Ba_2SiO_4
47.3	0.192	(302), (411) $BaSiTiO_5$
47.75	0.191	(420) $BaSiTiO_5$, Ba_2SiO_4
52.1	0.176	Ba_2SiO_4
52.4	0.175	Ba_3SiO_5
53.7	0.171	Ba_2SiO_4
54.5	0.168	Ba_2SiO_4, $Ba_2Ti_9O_{20}$
55.6	0.165	Ba_2SiO_4

part, very small when compared to the fresnoite diffraction peaks in Figure 40. The other major diffraction indices of the materials listed in Table 19 overlap those of fresnoite.

Table 19 shows that Ba_2SiO_4 accounts for most of the secondary phase diffraction peaks. Also, there may be small amounts of Ba_3SiO_5, $Ba_2Ti_9O_{20}$, and $BaTiO_3$. While there are only two diffraction peaks listed for barium titanate in Table 19, these peaks are the highest intensity peaks according to the JCPDS file. The other strong diffraction peaks of this material overlap those of fresnoite. Barium titanate possesses an extremely high dielectric constant [76,(1978)] and its presence is interesting because it may explain the difference in the measured dielectric constant of the two fresnoite discs. The disc with the higher dielectric constant (disc 1) could have possessed a slightly larger amount of $BaTiO_3$ than the other disc.

The other phase that might be present in the ceramic was $BaSiTiO_5$. In terms of its lattice structure, this material is almost identical to fresnoite. It is tetragonal, and its lattice constants are: a = 0:8525 nm and c = 0.522 nm (compared to a = 0.852 nm and c = 0.521 nm for fresnoite). According to the JCPDS powder diffraction index, the only difference between these two materials is: the material $BaSiTiO_5$ does not possess the (110) diffraction peak of fresnoite ($@2\theta_{Cu_{K_\alpha}} = 14.76°$), and $BaSiTiO_5$ possess two diffraction peaks which are not intrinsic to fresnoite - (302) or (411) and (420) which corresponds to values of $2\theta_{Cu_{K_\alpha}}$ equal to 47.3° and 47.72°, respectively.

This means that there could have possibly been a large amount of $BaSiTiO_5$ present in the ceramic. However, the composition measured by the WDS technique was very close to the actual composition of fresnoite. If there had been a large amount of $BaSiTiO_5$ formed, the intensity of the secondary phase peaks should have been much greater than they were in Figure 40 to compensate for the shift in composition from $Ba_2Si_2TiO_8$ to $BaSiTiO_5$. Thus, it was concluded that the fresnoite ceramic sputtering targets were polycrystalline in nature with fresnoite as the dominant phase with small amounts of $BaTiSiO_5$, Ba_2SiO_4, Ba_3SiO_5, $Ba_2Ti_9O_{20}$, and $BaTiO_3$ also present.

Table 17 shows that the different techniques used gave very inconsistent results for the composition of the fresnoite ceramics. This inconsistency is also expected to be present in Table 18 - the composition of the thin films. Thus, before the composition of the sputtered thin films can be discussed, these results must be adjusted in such a manner that they are not a function of the measurement technique.

The WDS technique was judged to yield the most accurate results. The differences between the results obtained from the WDS and other techniques for the composition of the fresnoite ceramics can be used to generate atomic correction factors which should improve the compositional results for the thin films. These correction factors are based on the ratio of the WDS results (actual amount) to the results obtained from the other techniques (nominal amount) for each element. For example, the atomic correction factors (η) for the ESCA (ECD) thin film results are defined below:

$$\eta_{Ba} = \frac{15.8}{15}$$

$$\eta_{Ti} = \frac{7.9}{3}$$

$$\eta_{Si} = \frac{14.0}{15}$$

$$\eta_{O} = \frac{62.3}{67}$$

In each case, the numerator is the elemental fraction (at.%) determined by the WDS method for a fresnoite ceramic, and the denominator is the elemental fraction (at.%) determined by ESCA (ECD) for a fresnoite ceramic. Table 20 shows the correction factors for each analysis technique derived from Table 17. Table 21 lists the corrected compositions for the thin films shown in Table 18.

Table 21 shows that the ESCA results (both ECD and SSW) are very similar to the WDS results after the correction factors were applied. This is not true for the RBS results. Even after they were compensated, they are still quite different from the WDS results. This probably arises from the fact that the ceramic was not pre-sputtered for the RBS analysis, while it was for the other analysis techniques. Processes such as surface segregation could have altered the outer 1-2 monolayers of the ceramic. Thus, the ceramic surface analysed by RBS could have been very much different than that analysed by WDS and ESCA, and a comparison between the two sets of results for the purpose of obtaining atomic

TABLE 20

Correction Factors for the Thin Film Compositional Results. These Factors are Based on the Differences in the Compositional Results for the Fresnoite Ceramics

Technique	Ba	Ti	Si	O
WDS	1.00	1.00	1.00	1.00
ESCA(ECD)	1.05	2.63	0.933	0.930
ESCA(SSW)	1.15	1.18	0.562	1.14
RBS	1.46	1.09	0.630	1.04

TABLE 21

Corrected Thin Film Compositions (at.%). These Values Were Obtained by Applying the Correction Factors in Table 20 to the Thin Film Compositions in Table 18

Technique	Film No.	Ba	Ti	Si	O	$(\Sigma+)/2$
Ideal Composition of Fresnoite		15.38	7.69	15.38	61.54	61.52
WDS	1	9.9	12.9	13.2	64.1	62.1
ESCA(ECD)	1	10.5	13.2	13.1	66.0	63.1
ESCA(SSW)	2	10.3	9.4	13.7	58.8	56.5
	3	9.7	10.5	15.7	62.3	62.1
	4	10.4	10.0	15.7	61.2	61.8
	5	10.3	9.2	15.2	64.2	59.1
RBS	4	11.1	11.4	7.1	73.8	48.1
	5	10.8	10.7	8.3	72.6	48.8

correction factors may not be valid. Since the same films (no. 4 and 5 from Tables 18 and 21) were analysed by both RBS and ESCA (SSW), the adjusted ESCA results must be assumed to be more accurate than the adjusted RBS results. This is supported by consideration of the electro-neutrality condition - the adjusted ESCA results satisfy this requirement very well, while the opposite is true for the adjusted RBS results.

If the WDS and adjusted ESCA results shown in Table 21 are assumed to be the actual composition of the thin films, it is seen that the composition of the sputtered thin films are very much different from that of the fresnoite ceramics. The thin films are deficient in Ba and possess an excess of Ti. The amounts of Si and O present in the films are approximately the same as those amounts present in the ceramic targets. This compositional shift from the ceramic targets (WDS determination) to the sputtered thin films (adjusted results) is shown in Figure 48. The film number from Table 21 is enclosed in parentheses and the measurement technique is also given. All of the stable compounds for the BaO-SiO_2-TiO_2 system listed in the JCPDS file are also indicated on this figure. Since there is no ternary phase diagram available for this system, the phase boundaries could not be shown.

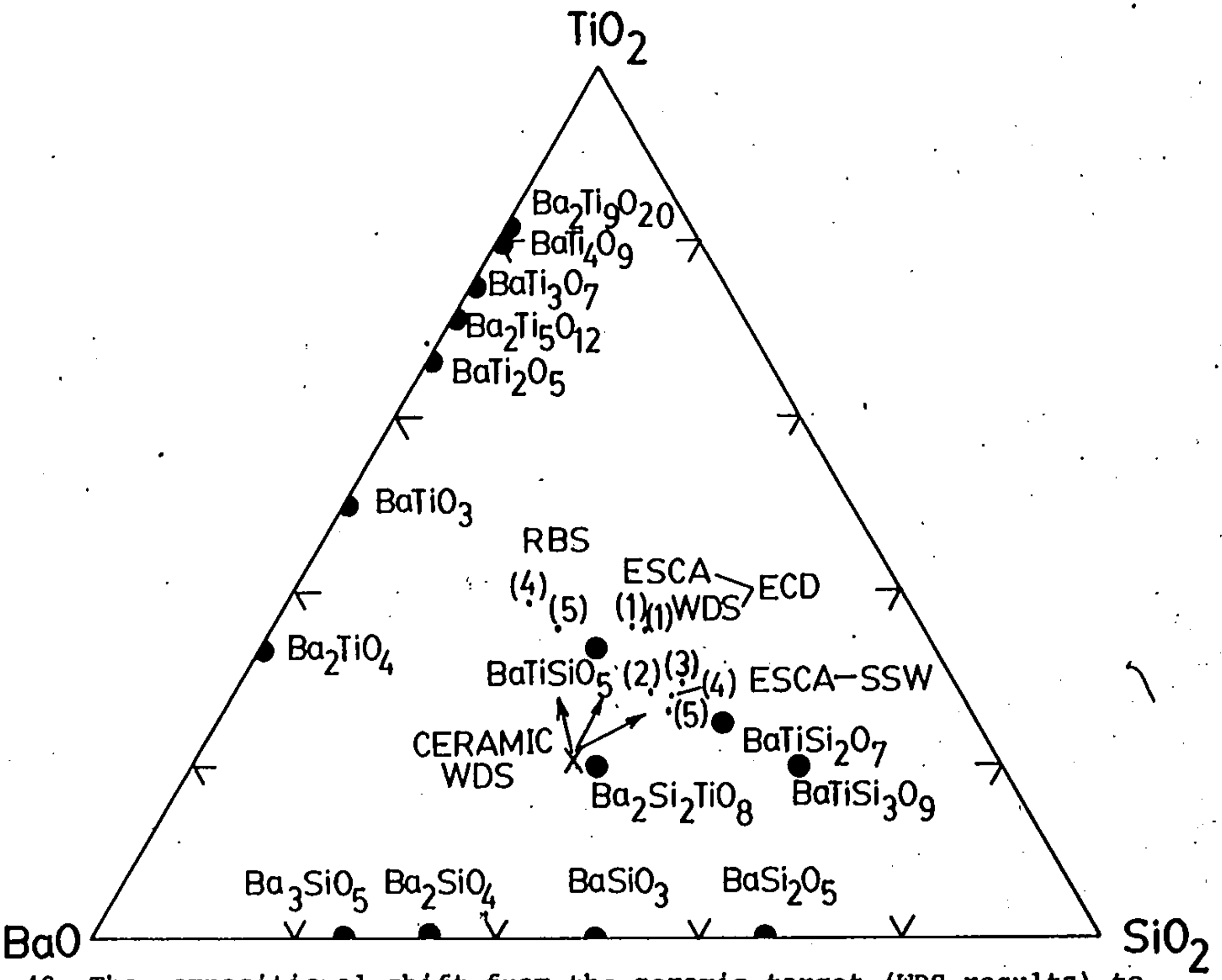

Figure 48 The compositional shift from the ceramic target (WDS results) to the sputtered thin films (adjusted results). The film number from Table 21 is enclosed by parentheses. The stable compounds for the $BaO-SiO_2-TiO_2$ system listed in the JCPDS file are also shown.

Figure 48 shows that the compositional shift from the target to the film is almost parallel to the $BaO-TiO_2$ edge line for the WDS and adjusted ESCA results. This compositional shift is an example of preferential sputtering. That is, Ba, Si, Ti, and O were not sputtered in proportion to their target concentrations. Figure 48 shows that, in general, Ti is preferentially sputtered while Ba has the lowest sputtering yield. McClure and Crowe [77,(1979)] and Panitz and Hu [78,(1980)] r.f. sputtered stoichiometric polycrystalline $BaTiO_3$ targets and obtained stoichiometric $BaTiO_3$ thin films. Thus the preferential sputtering which has been observed in the sputtering of fresnoite may not be a factor for the sputter deposition of barium titanate thin films. On the other hand, a compositional shift similar to that observed for fresnoite has been reported in the sputtering of both $Pb(Zr,Ti)O_3$ [79,(1978)] and $(Pb,La)(Zr,Ti)O_3$ [80,(1977)]. In order to obtain stoichiometric thin films, a few excess wt% (~10) of PbO was added to the target. However, PbO is a very volatile material and the observed losses of it were probably a consequence of target heating rather than the sputtering process itself [81,(1983)].

During the sputtering process, the ejected particles usually consist of neutral atoms, although molecules have been observed [50,(1982)]. Due to the complexity of the sputtering process, there are no comprehensive formulae available to determine the sputtering yields of the different elements in a multicomponent system. However, there have been models proposed which predict the sputtering yields for a binary or two-component system. Kelly [82,(1983)] derived the following expression for the component sputtering yield ratio of a binary (AB) compound:

$$\frac{Y_A^{\,c}}{Y_B^{\,c}} = \frac{C_A+C_B\gamma}{C_B+C_A\gamma}\,\frac{U_B}{U_A}\,. \tag{26}$$

where, $Y_A^{\,c}$ and $Y_B^{\,c}$ are the component sputtering yields of components A and B respectively, and the component sputtering yield is the average number of sputtered atoms of component i per incident ion divided by the equilibrium surface concentration C_i^s of component i, i.e., $Y_i^c = Y^i/C_i^s$. C_A and C_B are the relative amounts (at.%) of elements A and B respectively. U_A and U_B are the surface binding energies of elements A and B respectively, and $\gamma \equiv (4M_AM_B)/(M_A+M_B)$ with M_A and M_B being the atomic masses of elements A and B respectively.

This equation assumes that the sputtering yield depends only on the mass and surface binding energy of the ejected atoms.

Thus, if the surface binding energy of the atoms in fresnoite were known, the relative sputtering yields of these elements could be estimated from eq. (26). For the purpose of this calculation, the surface binding energy of the cations in fresnoite was assumed to be related to the number of bonds which have to be broken to liberate them. Figure 1 shows that to free one Si atom, four Si-O bonds must be broken, and to free one Ti atom, five Ti-O bonds must be broken. Each Ba atom is coordinated to six O atoms [3, (1967)] and thus six Ba-O bonds must be broken to free one Ba atom. The distances between all the cations and their oxygen nearest neighbours were calculated from their published atomic locations [4,(1967)]. These distances were found to be equal to the sum of the ionic radii of the two atoms [83,(1976)], which means that in fresnoite, all of the cations are adjacent to their nearest neighbour oxygen ions. This enabled the bond energy to be approximated by those values published by Kerr and Trotman-Dickenson [84,(1978)]. These values are listed in Table 22 and were measured at 25°C from diatomic molecules.

The component sputtering yields calculated from eq. (26) with the surface binding energies from Table 22 are listed in Table 23. The values of the ratios shown in Table 23 are all very close to unity (within ~10%). Since this calculation involved the adaptation of a formula developed for a binary system to a ternary system, the relative uncertainty is probably much greater than this amount. Thus, Table 23 shows that:

$$Y_{Ba} \sim Y_{Si} \sim Y_{Ti}$$

This result is much different from the experimental observation, which was:

$$Y_{Ti} > Y_{Si} > Y_{Ba}$$

Another reason for this difference between these two sets of results arises from the values of the bond energies used. The bond energies used were measured at 25°C at 1 atm. pressure, and the conditions present during the sputtering operation were much different than this. Thus, this model is much too "simple" to accurately estimate the sputtering yields from a multicomponent target.

One final compositional analysis was performed: a thin film sputtered from a fresnoite ceramic target was analyzed by Auger electron spectroscopy (AES). As it was examined, the film was sputtered at a rate of 1.9 nm/min until about 200 nm (or about one-fifth the thickness of the film) had been analyzed. The results are shown in Figure 49. Due to the nature of the Auger process (sec. 2.4.1) and the fact that an external calibration standard was not utilized, it is not surprising that the elemental compositions indicated in Figure 49 do not match these results shown in Table 21. However, Figure 49 does establish that the sputtered thin films do possess a uniform composition vs. depth.

4.3.2.2 Mod-BST Ceramics and Thin Films Sputtered From a Mod-BST Ceramic Target

A mod-BST ceramic was sputtered under the same conditions as the fresnoite ceramics. The resultant thin film was analyzed by ESCA at SSW. Table 27 summarizes the results

TABLE 23

Component Sputtering Yields of the Cations Present in Fresnoite. These Values were Calculated From Eq. (26) With the Surface Binding Energies Listed in Table 22

A	B	$\gamma \equiv \frac{4M_AM_B}{(M_A+M_B)^2}$	$\frac{Y_A^c}{Y_B^c}$
Ba	Ti	0.77	1.09
Si	Ti	0.93	1.08
Ba	Si	0.56	0.94

much too "simple" to accurately estimate the sputtering yields from a multicomponent target.

One final compositional analysis was performed: a thin film sputtered from a fresnoite ceramic target was analyzed by Auger electron spectroscopy (AES). As it was examined, the film was sputtered at a rate of 1.9 nm/min until about 200 nm (or about one-fifth the thickness of the film) had been analyzed. The results are shown in Figure 49. Due to the nature of the Auger process (sec. 2.4.1) and the fact that an external calibration standard was not utilized, it is not surprising that the elemental compositions indicated in Figure 49 do not match these results shown in Table 21. However, Figure 49 does establish that the sputtered thin films do possess a uniform composition vs. depth.

4.3.2.2 Mod-BST Ceramics and Thin Films Sputtered From a Mod-BST Ceramic Target

A mod-BST ceramic was sputtered under the same conditions as the fresnoite ceramics. The resultant thin film was analyzed by ESCA at SSW. Table 24 summarizes the results

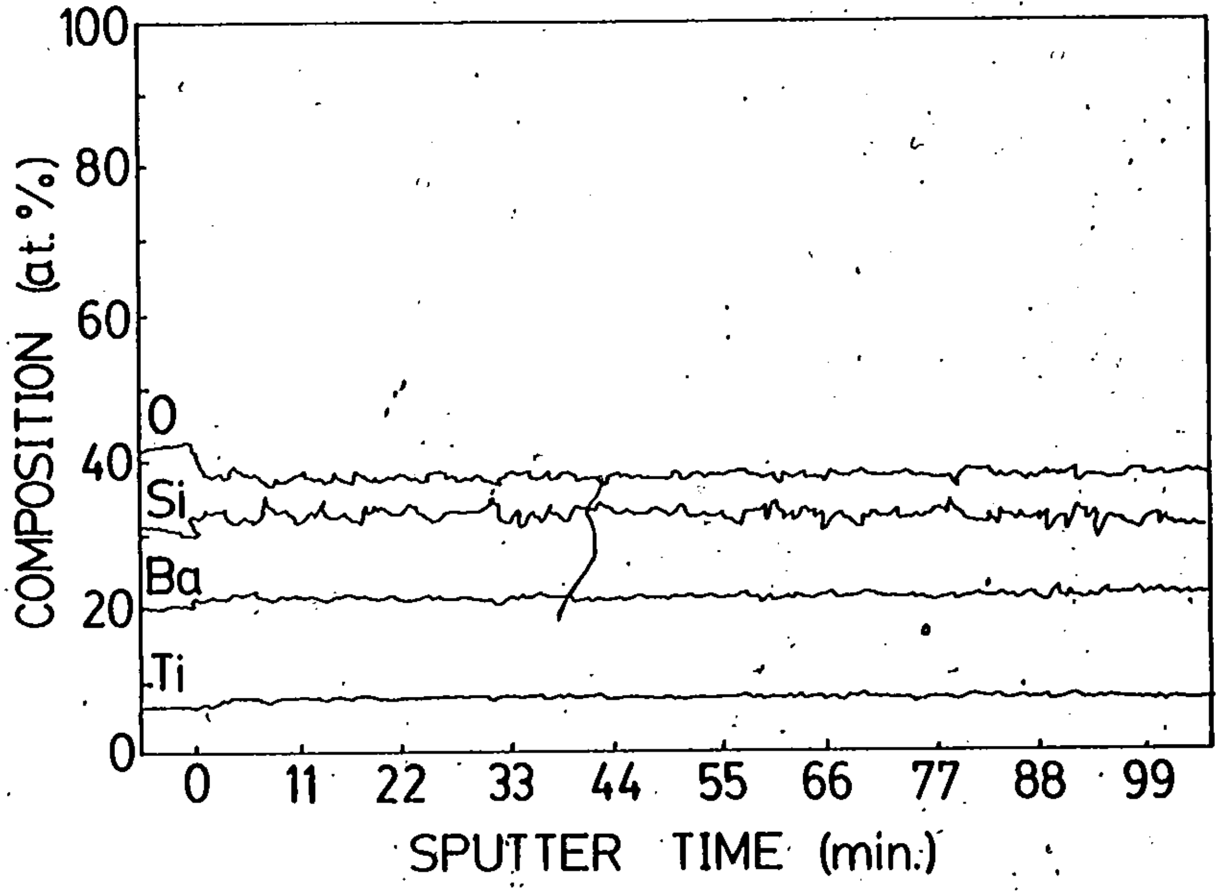

Figure 49 AES depth profile of a film sputtered from a fresnoite ceramic target. The film was sputtered at speed of 1.9 nm/min to a depth of 200 nm. These results indicate that the films possessed a uniform composition vs. depth.

TABLE 24

ESCA(SSW) Results (at.%) for a Mod-BST Ceramic and a Thin Film Sputtered From a Mod-BST Ceramic

	Ba	Ti	Si	O	(Σ+)/2
Ideal Composition of mod-BST	18.09	6.63	14.65	60.64	60.65
Ceramic	14.79	4.40	21.05	59.76	65.69
Film	7.66	6.41	30.14	55.80	80.76

obtained from this analysis. Table 24 shows that the measured composition of the mod-BST ceramic differed significantly from the expected or ideal composition of mod-BST.

The correction factors for ESCA(SSW) from Table 20 were applied to these results and the adjusted compositions are shown in Table 25. This table shows that the adjusted composition of the mod-BST ceramic is much closer to the ideal composition of mod-BST. Since the correction factors used were derived from measurements based on fresnoite ceramics and not mod-BST ceramics, these results may not be as reliable as those of the fresnoite ceramics and their films. This is reflected in the electroneutrality conditions; the adjusted mod-BST compositions in Table 25 do not satisfy this requirement as well as the adjusted fresnoite compositions. However, since these adjusted compositions seem to be much more reasonable than the measured completions in Table 24, they are assumed to be the actual composition of the ceramic and thin film.

Just as they were for the fresnoite ceramics, the secondary phases present in the mod-BST ceramic can now be discussed in terms of the adjusted ESCA(SSW) composition in Table 25. The secondary or non-fresnoite diffraction peaks for the mod-BST ceramic are listed in Table 26. These peaks were taken from Figure 42 and are listed in terms of increasing detector angle, 2θ. This table also shows the interplanar spacing (or d-spacing) calculated from Bragg's law with the assumption that only first order diffraction

TABLE 25

Adjusted ESCA(SSW) Results (at.%) for a Mod-BST Ceramic and a Thin Film Sputtered from a Mod-BST Ceramic. The Correction Factors Used Were the ESCA(SSW) Factors Listed in Table 20

	Ba	Ti	Si	O	(Σ+)/2
Ideal Composition of Mod-BST	18.09	6.63	14.65	60.64	60.65
Ceramic	17.01	5.19	11.83	68.13	51.05
Film	8.81	7.56	16.94	63.61	57.81

TABLE 26

Secondary Phase Diffraction Peaks for the Mod-BST Ceramic. These Peaks Were Taken from Figure 42

2 Cu_{K_α} (°)	d(nm)	Possible Sources
22.2	0.401	(100)$BaTiO_3$
25.2	0.353	$Ba_2Ti_9O_{20}$
26.0	0.343	Ba_2SiO_4, $Ba_2Ti_9O_{20}$
28.4	0.314	Ba_2SiO_4, $Ba_2Ti_9O_{20}$
30.4	0.294	Ba_2SiO_4, $Ba_2Ti_9O_{20}$
30.6	0.292	Ba_2SiO_4
31.5	0.284	(101),(110) $BaTiO_3$
35.1	0.256	Ba_2SiO_4
35.5	0.253	Ba_2SiO_4
36.9	0.244	Ba_2SiO_4
38.9	0.232	(111)$BaTiO_3$, Ba_2SiO_4
42.5	0.213	Ba_2SiO_4
43.0	0.210	Ba_2SiO_4
47.2	0.193	(302),(411) $BaSiTiO_5$
47.7	0.191	(420) $BaSiTiO_5$,Ba_2SiO_4
51.0	0.179	Ba_2SiO_4
51.8	0.177	Ba_2SiO_4
52.3	0.175	Ba_3SiO_5
53.5	0.171	Ba_2SiO_4
54.2	0.169	Ba_2SiO_4
56.2	0.164	?

was present, as well as the possible sources of these peaks.

Comparison of Figures 40 and 42 reveals that for the most part, the same secondary peaks are present in each ceramic, although the intensity of the secondary peaks in mod-BST is much greater than those of fresnoite. However, there are more of the lower intensity Ba_2SiO_4 diffraction peaks present in the mod-BST ceramic than in the fresnoite ceramic, which means that there is probably much more Ba_2SiO_4 present in the mod-BST ceramic. The presence of a large amount of Ba_2SiO_4 may explain the difficulty in sintering a powder of the mod-BST composition into a ceramic with the necessary shape integrity (low porosity and no warpage or cracking) required for a sputtering target. That is, if the sintering temperature of Ba_2SiO_4 is much different than that of fresnoite, then the cracking and warping which was observed in most of the mod-BST ceramics was most likely due to the presence of a large amount of this phase.

The adjusted ESCA(SSW) compositions of the mod-BST ceramic and sputtered thin film from Table 25 were plotted in Figure 50 to highlight the compositional shift which occurred during the sputtering process. Also shown in this figure are the stable compounds for the $BaO-SiO_2-TiO_2$ system listed in the JCPDS file. Figure 50 shows that the composition of the mod-BST ceramic is located almost halfway between Ba_2SiO_4 and fresnoite, so there should be much more Ba_2SiO_4 present in the mod-BST ceramic than in the fresnoite ceramic.

Based on the two compositional shifts detailed in Figures 48 and 50, it is possible to estimate the target composition

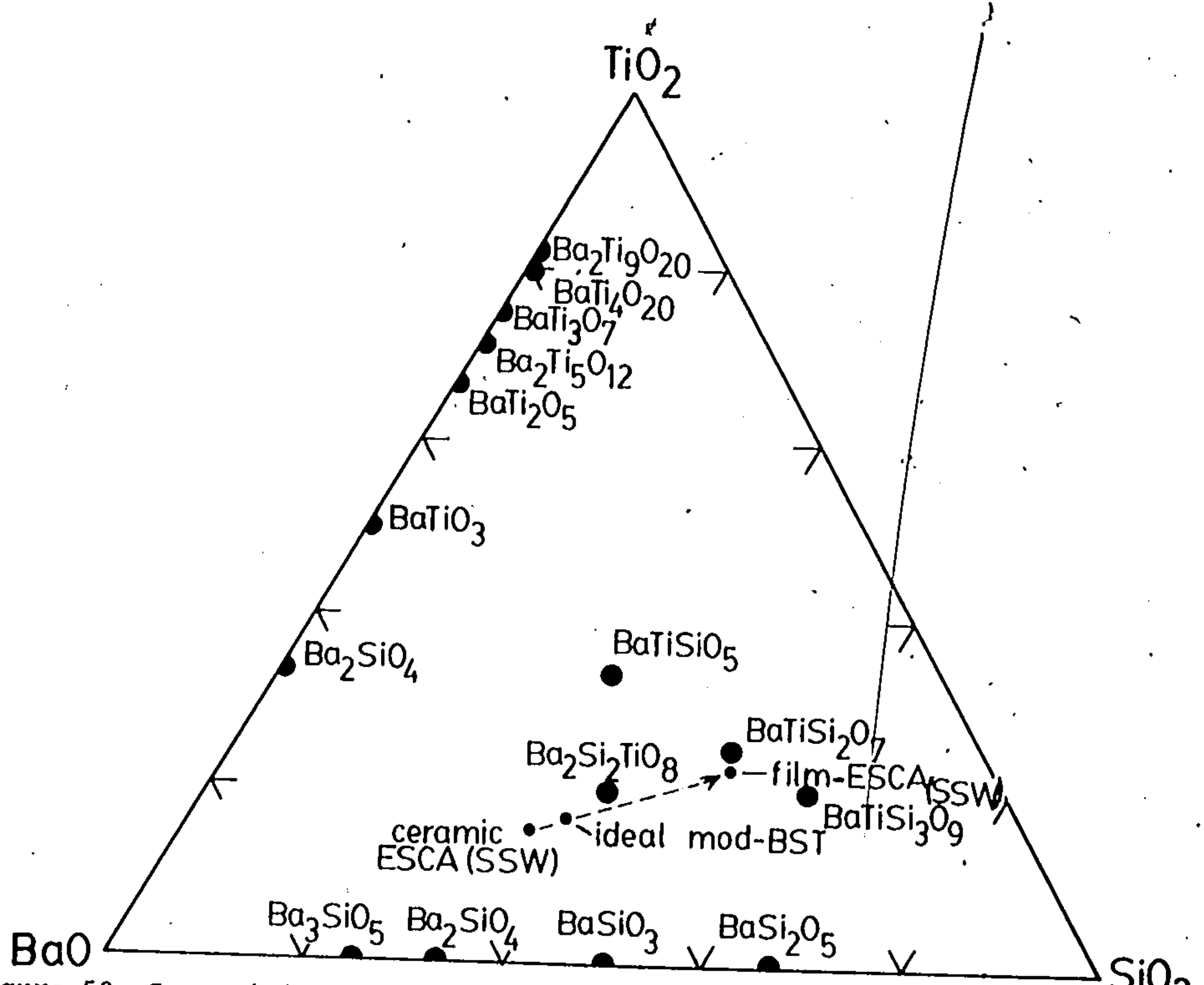

Figure 50 Compositional shift from the mod-BST ceramic target to the sputtered thin film. The ideal composition of mod-BST is also indicated, as well as the stable compounds for the $BaO-SiO_2-TiO_2$ system listed in the JCPDS file.

which upon sputtering will yield a thin film of the composition $Ba_2Si_2TiO_8$. This target composition and the predicted compositional shift between it and the sputtered thin film are shown in figure 51. In this figure, it is assumed that the compositions will be determined by ESCA (SSW), and they will be adjusted with the appropriate correction factors from Table 20. The indicated target composition is approximately $Ba_{3.5}Si_2TiO_{9.5}$. Since it was found that a ceramic sputtering target of composition $Ba_{2.99}Si_2Ti_{0.8}O_{8.59}$ could not be successfully sintered, an alternate method of target fabrication might have to be employed to produce a ceramic target of composition $Ba_{3.5}Si_2TiO_{9.5}$. One alternate method would be to sinter some powder of this composition into a solid form, then crush the ceramic into a fine powder, and finally, hot-press the crushed ceramic into the desired target shape.

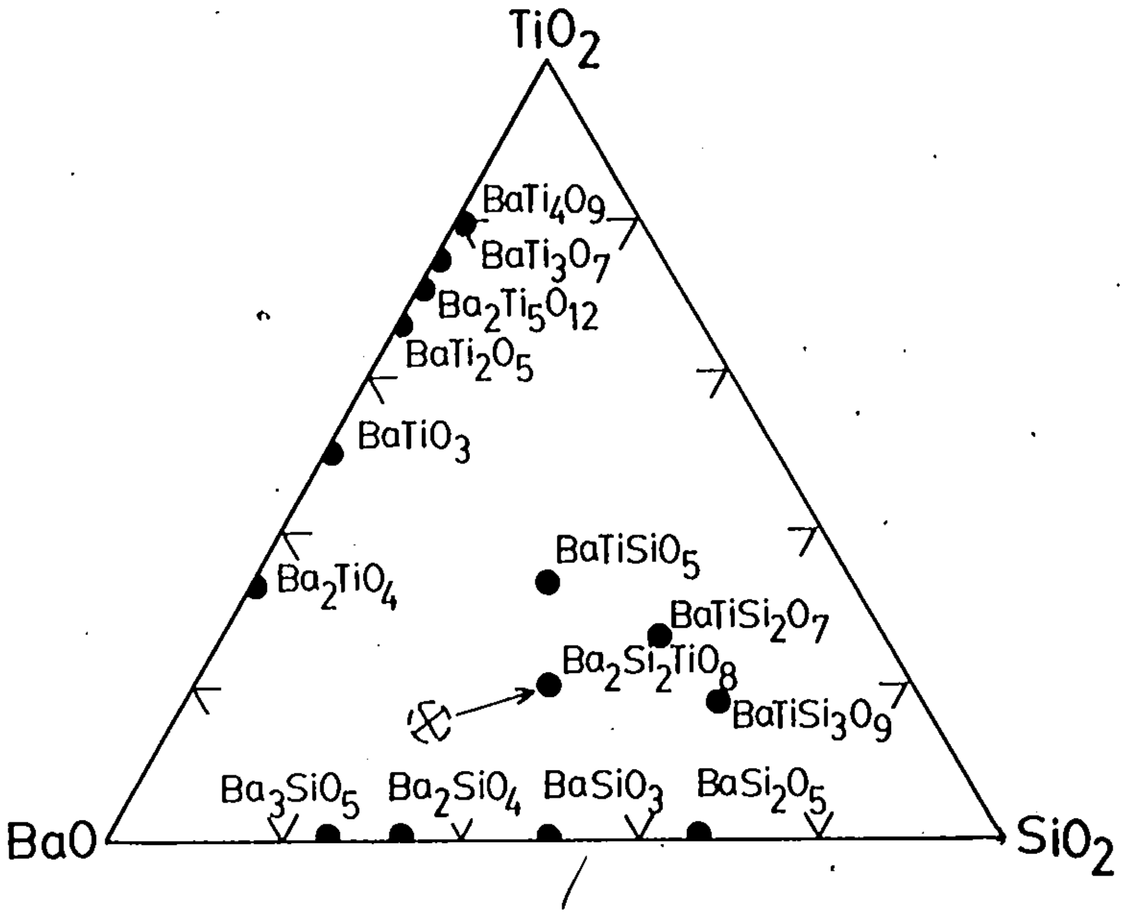

Figure 51 Estimated target composition required for the production of a fresnoite film via r.f.-sputtering. This composition is approximately $Ba_{3.5}Si_2TiO_{9.5}$.

4.3.3 Structure of the Annealed Thin Films

4.3.3.1 X-ray Diffraction Analysis

Over the course of this work, the thin films were deposited on a variety of substrates which were heated over the range of 80 to 650°C. The only film which exhibited any indication of partial crystallinity in the as-deposited state was the film which was deposited with a substrate temperature of 650°C. This film was deposited on (100)Si, and the x-ray diffraction pattern of this film is shown in Figure 52. The amorphous halo is located in the range $22° < 2\theta < 32°$. The broad peak centred at about $2\theta = 34°$ may be the result of weakly defined (210) and/or (311) reflections from either $Ba_2Si_2TiO_8$ or $BaTiSiO_5$ or both - probably caused by a preferential orientational growth of crystalline grains. A separate diffraction experiment confirmed that this peak did not arise from the silicon substrate - the (400)Si peak due to the 2nd harmonic of CuK_α ($\lambda = 0.0771$ nm) radiation was observed to be very narrow in shape and occurred at $2\theta = 33°$. The thickness of this film (~1.2μ) is the most probable reason that this peak was not observed in Figure 52.

Based on the results of Ayukawa [13,(1983)], the thin films were annealed at 700, 725, 750, 775, and 800°C for 10 hours, and the amorphous to crystalline transition of these films was characterized by both x-ray and electron diffraction techniques. All of the annealed thin films which were examined by x-ray diffraction possessed (100)Si substrates. In order to inhibit the oxidation of the substrate (i.e., the formation of SiO_2) during the annealing process, the films

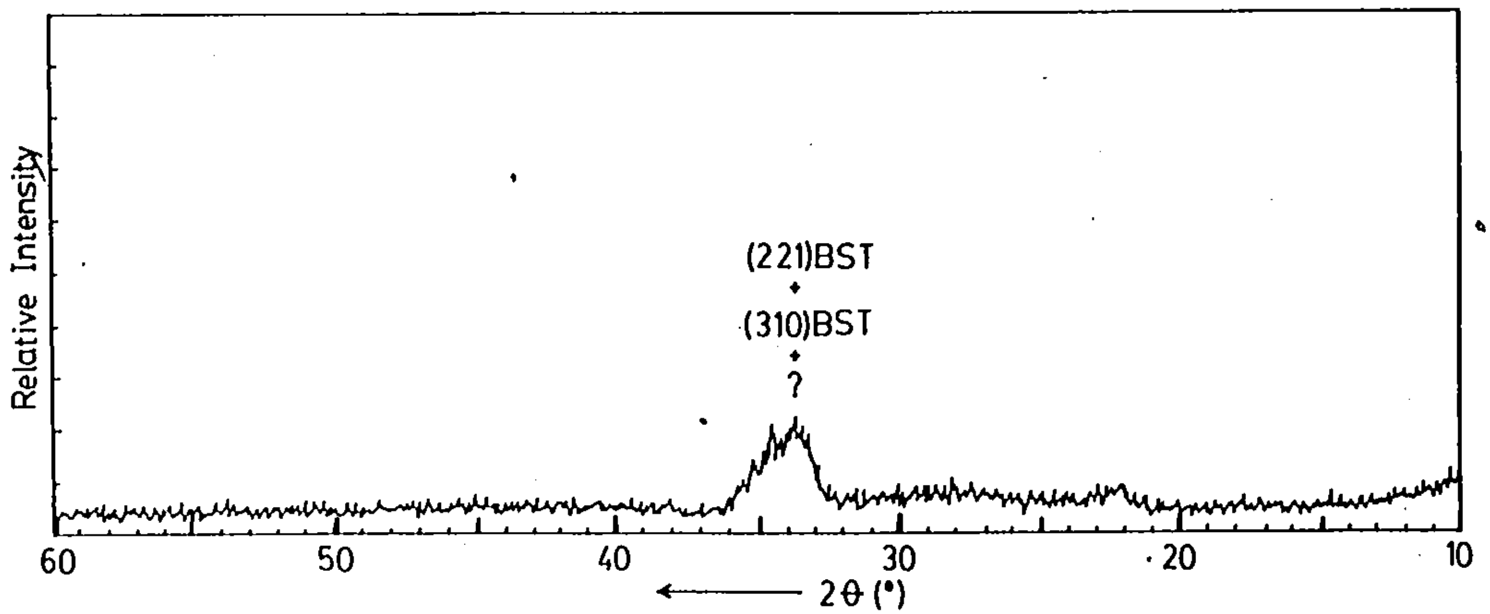

Figure 52 X-ray diffraction pattern of a thin film sputtered from a fresnoite ceramic. The substrate temperature was 650°C, and this sample was the only one which gave any indication of partial crystallinity in the as-deposited state.

were encapsulated in fused quartz cylinders which were evacuated to a pressure of 5 x 10^{-2} torr prior to the heat treatment.

Figures 53, 54, and 55 are x-ray diffraction patterns for thin films sputtered from fresnoite ceramics annealed at temperatures of 700, 725, and 800°C. The substrate temperatures of these films were 650, 480, and 275°C respectively. The labelled diffraction peaks were indexed according to the JCPDS file, and the unlabelled peaks can be attributed to the formation of some type of SiO_2 (most likely tridymite) during the annealing process. The towering peak at $2\theta=33°$ in Figures 53 and 54 is due to the (400)Si peak for the 2nd CuK_α harmonic. As mentioned previously, the following criteria are the only means by which $Ba_2Si_2TiO_8$ can be distinguished from $BaTiSiO_5$ by diffraction techniques:

1. $Ba_2Si_2TiO_8$ possesses the (110) and (220) reflections at values of $2\theta_{CuK_\alpha}$ equal to 14.76° and 29.68° respectively. These reflections are not present in $BaTiSiO_5$.

2. $BaTiSiO_5$ possesses the (302) or (411) and (420) reflections at values of $2\theta_{CuK_\alpha}$ equal to 47.3° and 47.7° respectively. The reflections are not present in fresnoite. Thus, the diffraction peaks labelled BST on Figures 53, 54, and 55 can be attributed to both $BaTiSiO_5$ and $Ba_2Si_2TiO_8$, and the diffraction peaks which are inherent to only one of these materials ((110) and (220) for $Ba_2Si_2TiO_8$; (302) or (411) and (420) for $BaTiSiO_5$) are labelled accordingly.

Since the (110) reflection of $Ba_2Si_2TiO_8$ is not present in the diffraction pattern of the film annealed at 700°C

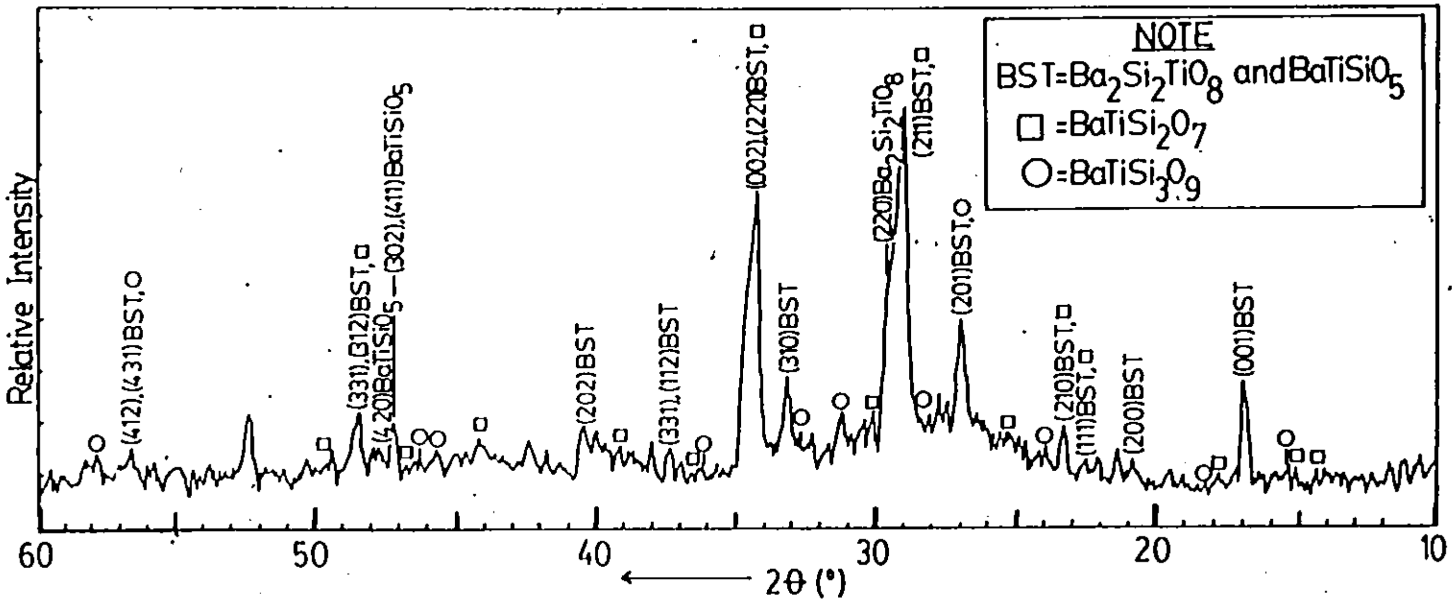

Figure 53 X-ray diffraction pattern of a thin film sputtered from a fresnoite ceramic and annealed at 700°C. The substrate temperature of this film was 650°C.

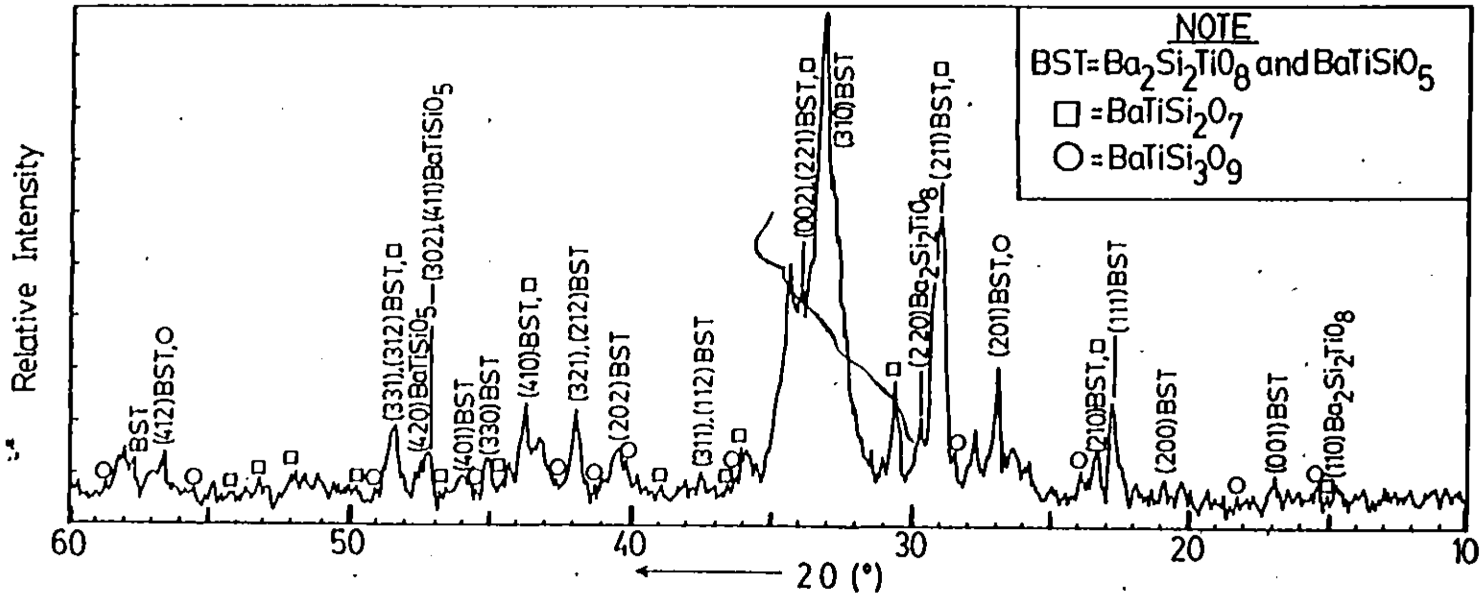

Figure 54 X-ray diffraction pattern of a thin film sputtered from a fresnoite ceramic and annealed at 725°C. The substrate temperature of this film was 480°C.

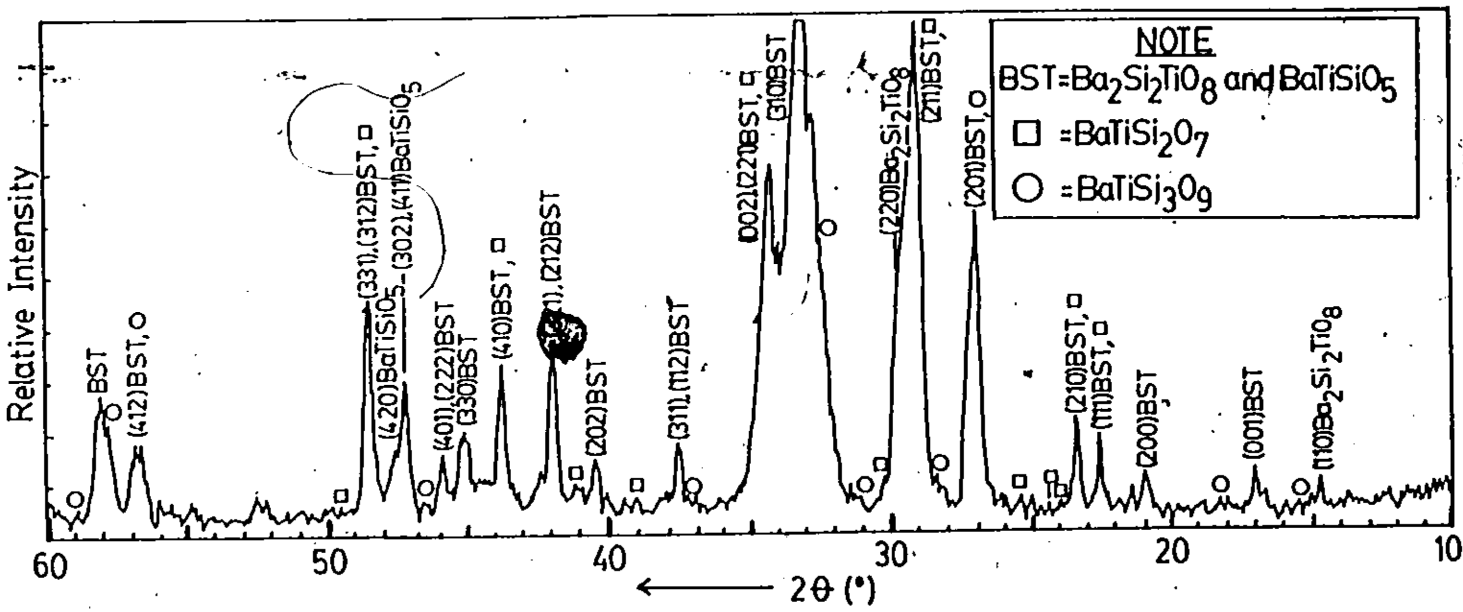

Figure 55 X-ray diffraction pattern of a thin film sputtered from a fresnoite ceramic and annealed at 800°C. The substrate temperature of this film was 275°C.

(Fig. 53) and is present in the diffraction pattern of the films annealed at 725 and 800°C (Figs. 54 and 55), it seems that fresnoite was not formed at an annealing temperature of 700°C, but it was formed at annealing temperatures of 725 and 800°C. However, the (110) diffraction peak has a very low intensity, and thus it also is possible that it could be absent from the diffraction pattern, even though fresnoite is present in the film. Figure 55 shows that the (220) diffraction peak of fresnoite (which occurs at a value of $2\theta_{Cu}$ of 29.7°) is not present as a distinct peak, but rather as a shoulder on the very intense (211) BST diffraction peak (@ $2\theta_{CuK_\alpha} = 29°$). Since the (211) BST diffraction peak of Figure 53 exhibits the same type of shoulder, it can be proposed that the (220) diffraction peak of fresnoite is present in this diffraction pattern, which means that fresnoite was formed when the film was annealed at 700°C, even though the (110) diffraction peak was not clearly distinguishable.

Figures 53, 54, and 55 show that the annealed thin films crystallized into four distinct phases - $Ba_2Si_2TiO_8$, $BaTiSiO_5$, $BaTiSi_2O_7$, and $BaTiSi_3O_9$. These figures also show that the intensity of the diffraction peaks of $BaTiSi_2O_7$ and $BaTiSi_3O_9$ are very much less than those of $Ba_2Si_2TiO_8$ and $BaTiSiO_5$, which indicates that the amounts of $BaTiSi_2O_7$ and $BaTiSi_3O_9$ formed in the crystallized films are very small compared to that of $Ba_2Si_2TiO_8$ and $BaTiSiO_5$. Since $Ba_2Si_2TiO_8$ and $BaTiSiO_5$ are ~~so~~ very similar in terms of their diffraction characteristics, it is difficult to estimate the relative amounts of these two phases present in the annealed thin films from the diffraction patterns shown in figures 53, 54, and 55. However, the compositions of these films are shown in figure 48, where films numbered (5), (3) and (2) correspond to the films annealed at 700, 725, and 800°C respectively. The indicated compositions of these films suggest that they contain more $BaTiSiO_5$ than $Ba_2Si_2TiO_8$, although the presence of $BaTiSi_2O_7$ and $BaTiSi_3O_9$ may have increased the amount of $Ba_2Si_2TiO_8$ relative to $BaTiSiO_5$.

Figure 53 shows that the film annealed at 700°C was not completely crystallized since the amorphous halo is present. However, the fact that an annealing temperature of 700°C was sufficient to crystallize the thin films is contrary to the results of Ayukawa [13,(1983)]. He found that thin films sputtered from fresnoite ceramic targets did not crystallize to any degree when annealed at 700°C. The difference between his results and those presented in figure 53 can be attributed to the substrates used - the films studied by Ayukawa were deposited on amorphous fused quartz cylinders, while these films were deposited on (100)Si wafers.

Comparison of figures 54 and 55 (the diffraction patterns for the thin films annealed at 725 and 800°C) with figure 40 (the x-ray diffraction pattern of a randomly oriented multigrain fresnoite target ceramic) leads to the conclusion that no particular preferential orientational growth of the crystalline grains occurred in these films. If these diffraction patterns are compared to figure 53 (the diffraction pattern for the thin film annealed at 700°C), it is seen that the (001) BST diffraction peak is relatively much greater for the film annealed at 700°C than for the other annealed films and the target ceramic. This result is especially important for the fabrication of piezoelectric fresnoite thin films, since these films would require a strong (001) preferential growth [10,(1979)]. Dielectric measurements would have to be made to confirm that this film is indeed piezoelectric (i.e., there was some degree of preferential (001) orientation in this film). However, if this sample did possess any amount of preferred (001) orientation, it was probably a consequence of the higher substrate temperature (650°C) used for this film compared to the other films (480 and 275°C). That is, the formation of epitaxial small crystallite embryos on the (100) Si surface could have resulted from an increased mobility of the incident ions on the silicon surface due to the higher substrate temperature of this film.

Figures 56 and 57 are x-ray diffraction patterns of thin films sputtered from a mod-BST ceramic and annealed at 700 and 800°C respectively. The substrate temperature of these films was 80°C. These figures show that the films sputtered from mod-BST targets crystallized into the same phases ($Ba_2Si_2TiO_8$, $BaTiSiO_5$, $BaTiSi_2O_7$, and $BaTiSi_3O_9$) as the films sputtered from fresnoite ceramics. However, the intensity of the $BaTiSi_2O_7$ and $BaTiSi_3O_9$ diffraction peaks are greater for these films than for the films sputtered from fresnoite ceramics, which indicates that more $BaTiSi_2O_7$ and $BaTiSi_3O_9$ were formed in the films sputtered from mod-BST ceramics than those sputtered from fresnoite ceramics. This inference is supported by consideration of figure 50,

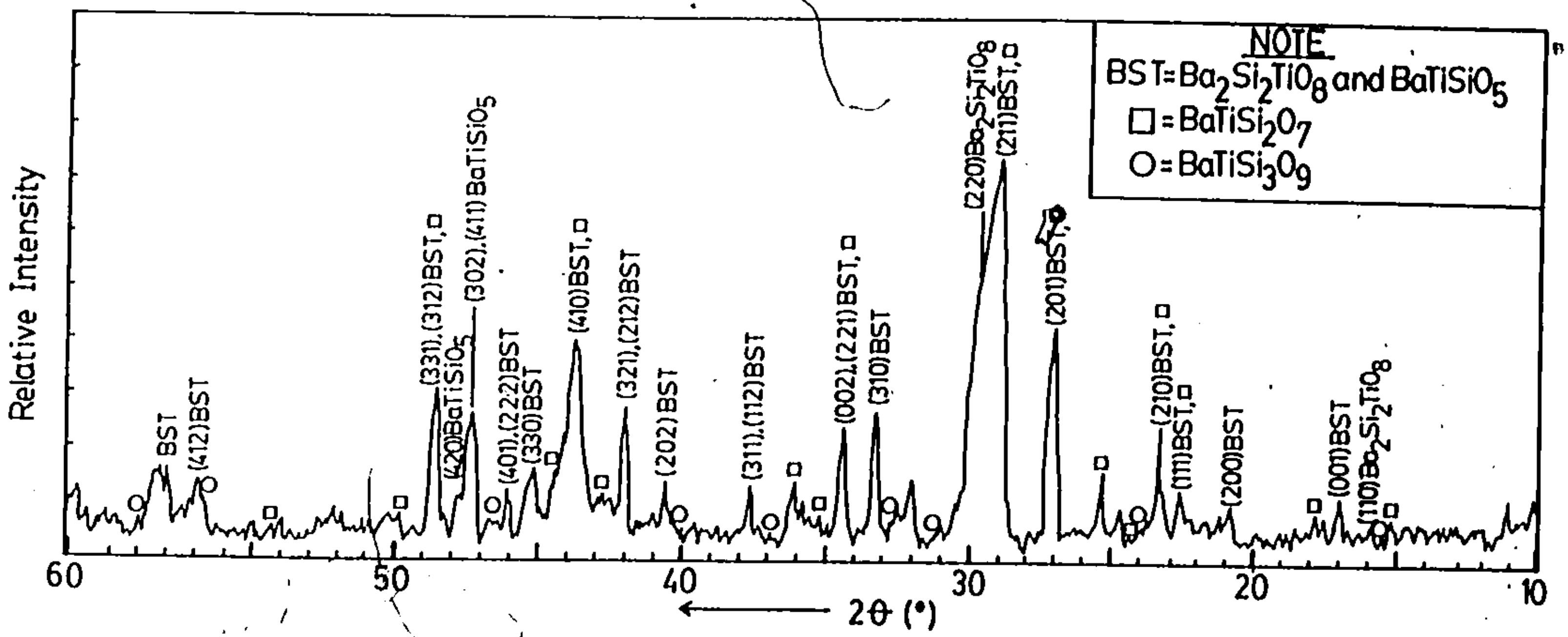

Figure 56 X-ray diffraction pattern of a thin film sputtered from a mod-BST ceramic and annealed at 700°C. The substrate temperature of this film was 80°C.

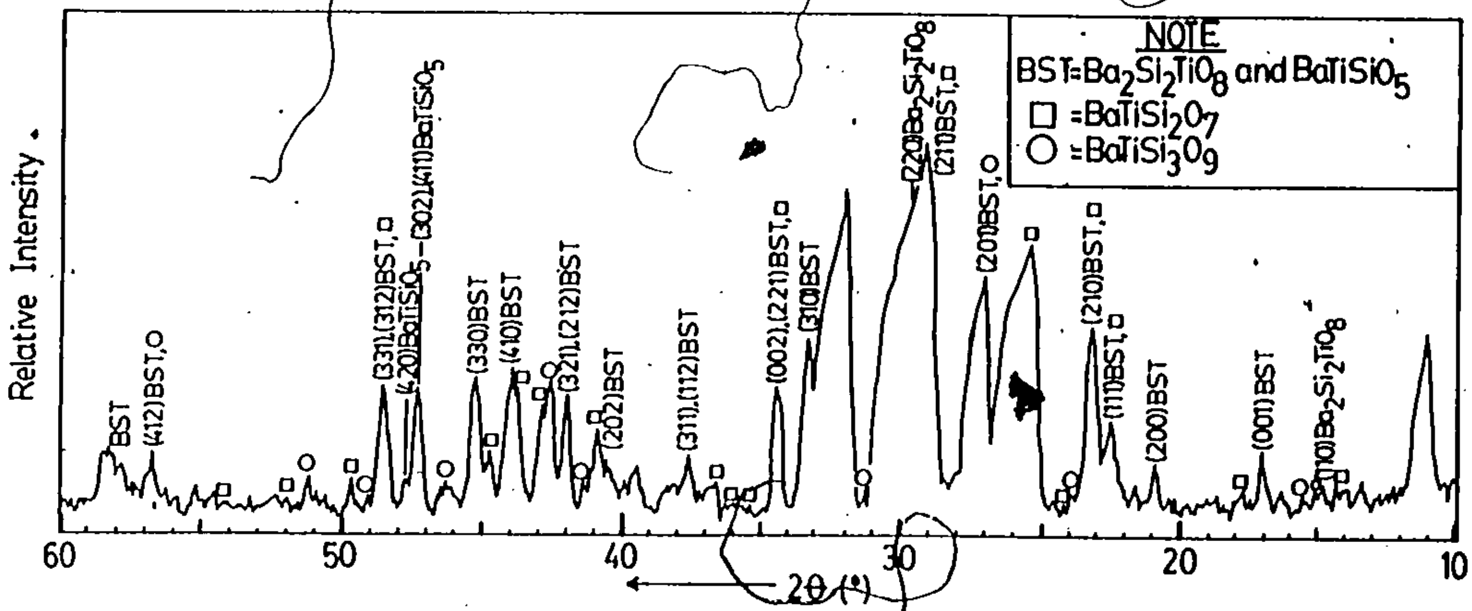

Figure 57 X-ray diffraction pattern of a thin film sputtered from a mod-BST ceramic and annealed at 800°C. The substrate temperature of this film was 80°C.

the composition of a film sputtered from a mod-BST ceramic, which shows that the composition of these films is much closer to $BaTiSi_2O_7$ and $BaTiSi_3O_9$ than the films sputtered from fresnoite ceramics (figure 48). Comparison of figures 56 and 57 with figure 42 (the x-ray diffraction pattern of a mod-BST ceramic) leads to the conclusion that these films did not crystallize with any type of preferred orientation. Since these films were deposited with a substrate temperature of only 80°C, this result is in agreement with that obtained from the annealed thin films sputtered from fresnoite ceramic targets - that if all other parameters are held constant, the formation of oriented thin films is dependent on the substrate temperature of the films and not the annealing temperature.

4.3.3.2 Electron Diffraction Analysis

In order to verify the x-ray diffraction results, it was desired to analyze the thin films by electron diffraction. Thus, it was necessary to separate the thin film from the substrate so that it could be examined in a transmission electron microscope.[14] The following procedure was developed to obtain samples for TEM analysis:

1. Fabricate a thin film on an NaCl crystal and immerse it in a steam bath.

2. Gently place the specimen in water (@ room temperature) with the film side facing up.

---

[14] JEOL CX 100.

3. With the film at about water level, slowly move the specimen in the water - the thin film should float off. If it doesn't, repeat step 1.

4. Catch a fragment of the thin films on a 3 mm copper grid.

A large number of samples was prepared by this technique. Most of them were encapsulated in fused quartz cylinders which were evacuated to a pressure of 5×10^{-2} torr, and annealed at temperatures between 700 and 800°C. Examination of the annealed specimens revealed that all the thin film fragments except for one had disintegrated during the heat treatment.

Figures 58 and 59 are the electron diffraction pattern and corresponding bright field image for a thin film which was not annealed. The substrate temperature of this film was 175°C. The electron diffraction pattern consists of very broad rings which are characteristic of amorphous structures. The bright field image shows that the grains are homogeneous, continuous, indistinguishable in shape, and are all very small in size, with a diameter of about 50 nm.

Figures 60 and 61 are the electron diffraction pattern and corresponding bright field image for the thin film specimen annealed at 750°C for 10 hours. The substrate temperature of this film was also 175°C. The spot pattern reveals that the film had crystallized. The interplanar (or d) spacing of these planes was calculated from the relation:

$$\frac{1}{d_{hk\ell}} = \frac{1}{\lambda L} R \qquad (28)$$

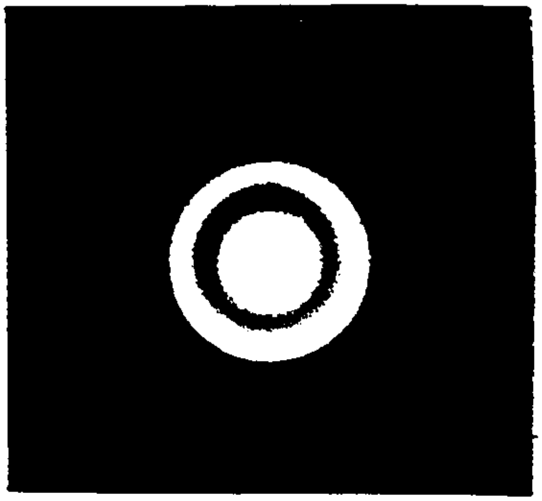

Figure 58 Electron diffraction pattern for a thin film fragment which was not annealed. The substrate temperature of this film was 175°C. The diffraction pattern indicates that the film possessed an amorphous structure.

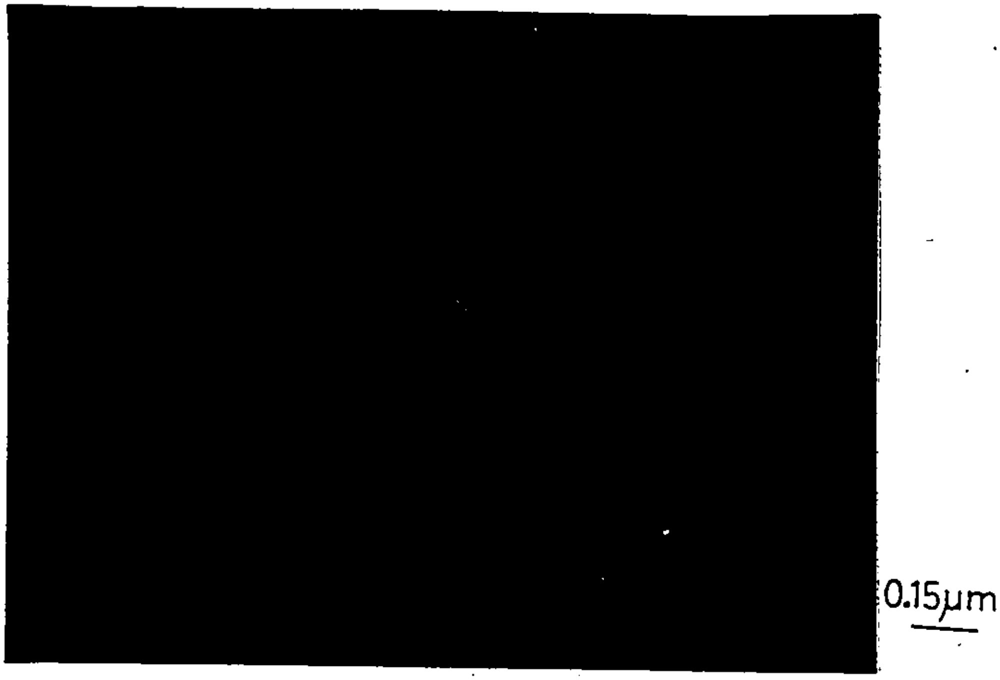

Figure 59 Bright field image of the film area which gave rise to the electron diffraction pattern shown in Figure 58.

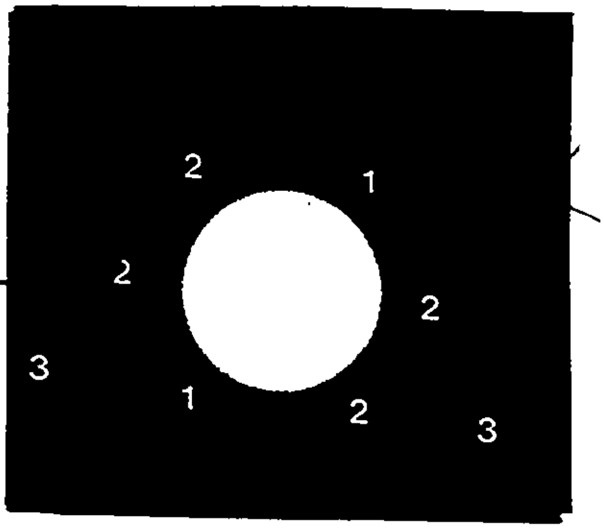

Figure 60 Electron diffraction pattern for a thin film fragment which was annealed at 750°C. The substrate temperature of this film was 175°C. The spots are labelled in terms of their respective d-spacing, which is listed in Table 30.

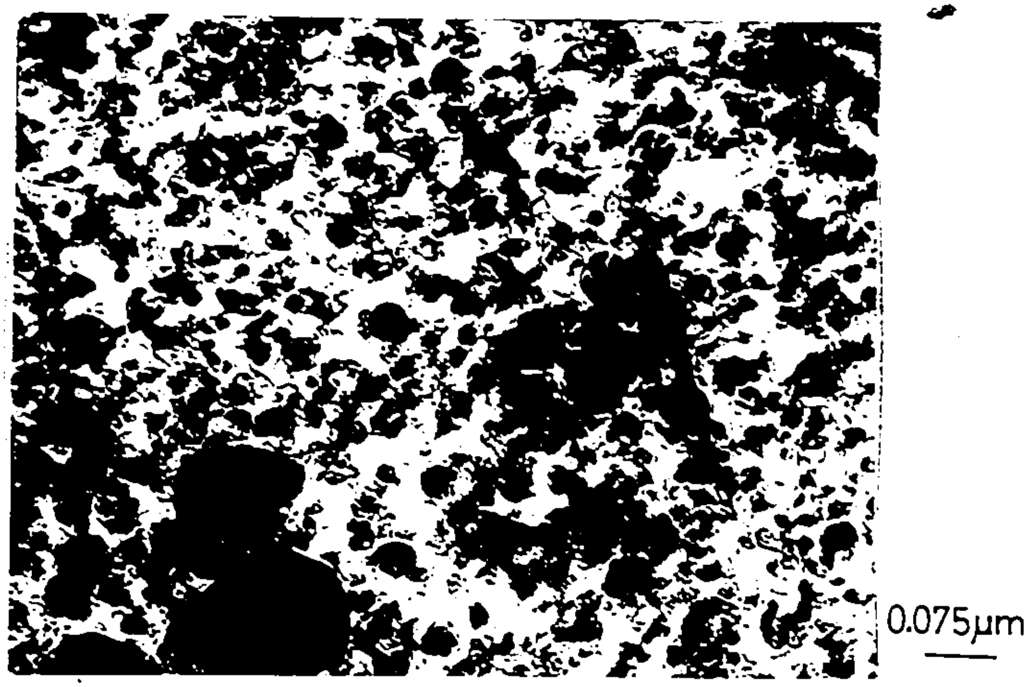

Figure 61. Bright field image of the film area which gave rise to the electron diffraction pattern shown in Figure 60.

where, λL is the camera constant (calculated from a high purity aluminum standard);

R is the radius of spot in cm (measured from the negative).

On figure 60, the spots are labelled in terms of their respective d-spacings. These d-spacings are shown in Table 27, along with the d-spacings of $Ba_2Si_2TiO_8$, $BaTiSiO_5$, $BaTiSi_2O_7$ and $BaTiSi_3O_9$, which were the phases identified in the films annealed on silicon substrates. The d-spacing of the outer spots was found to be 0.129 nm. This was not included in Table 27 due to the fact that the d-spacings listed in the JCPDS files of $Ba_2Si_2TiO_8$, $BaTiSiO_5$, $BaTiSi_2O_7$, and $BaTiSi_3O_9$ do not go this low.

The angle between the spots labelled (2) and the spots labelled (1) was measured to be 60°±2°. If this diffraction pattern had resulted from one single crystal, this angle should correspond to the angle between the two diffraction planes which give rise to these spots. The four spots labelled (2) on figure 60 were assumed to be the result of electron diffraction by the (202) family of planes from either $Ba_2Si_2TiO_8$ and/or $BaTiSiO_5$. Various permitted combinations of the (311) and (112) families of tetragonal indices were then used to calculate the angle between these diffraction planes, according to equation (29) below, which is valid for tetragonal systems [87,(1965)]:

$$\cos \phi = \frac{\dfrac{h_1h_2 + k_1k_2}{a^2} + \dfrac{\ell_1\ell_2}{c^2}}{\left[\left(\dfrac{h_1^2+k_1^2}{a^2} + \dfrac{\ell_1^2}{c^2}\right)\left(\dfrac{h_2^2+k_2^2}{a^2} + \dfrac{\ell_2^2}{c^2}\right)\right]^{1/2}} \qquad (29)$$

TABLE 30

Possible Sources of the Spots Labelled (1) and (2) on Figure 60. The d-Spacing and (hkℓ) Values for These Materials Was Taken from the JCPDS File

Spot (1) - d = 0.238 nm			Spot (2) - d = 0.226 nm		
d(nm)	(hkℓ)	Material	d(nm)	(hkℓ)	Material
0.2392	(311),(112)	$Ba_2Si_2TiO_8$	0.222	(202)	$Ba_2Si_2TiO_8$
0.2394	(311),(112)	$BaTiSiO_5$	0.222	(202)	$BaTiSiO_5$
0.2466	?	$BaTiSi_2O_7$	0.2216	?	$BaTiSi_2O_7$
0.2438	(004)	$BaTiSi_3O_9$	0.2245	(104)	$BaTiSi_3O_9$

where, ϕ = the angle between the two planes (°);

$(h_1k_1\ell_1)$ = (202)

$(h_2k_2\ell_2)$ = various allowed combinations of the (311) and (112) families of tetragonal indices;

a = 0.852 nm, c = 0.521 nm .

It was found that a value of $(h_2k_2\ell_2) = (1\bar{3}1)$ yielded a value of $\theta = 57°$, which was very close to the measured angle. This calculation was also performed using the unit cell parameters of $BaTiSi_3O_9$, $(h_1k_1\ell_1) = (104)$, and $(h_2k_2\ell_2) = (004)$ and $(00\bar{4})$, but the resultant angle was not close to the measured one.

The incident beam direction (direction of the incoming electrons with respect to the crystal lattice) was calculated from the following relation [87,(1965)]:

$$[uvw] \equiv \left[\begin{vmatrix} k_1 & \ell_1 \\ k_2 & \ell_2 \end{vmatrix}, \begin{vmatrix} \ell_1 & h_1 \\ \ell_2 & h_2 \end{vmatrix}, \begin{vmatrix} h_1 & k_1 \\ h_2 & k_2 \end{vmatrix} \right] \qquad (30)$$

$$= [k_1\ell_2 - \ell_1k_2,\ \ell_1h_2 - h_1\ell_2,\ h_1k_2 - k_1h_2]$$

The beam direction calculated by considering only the (202) family of planes was [uvw] = [010]. However, when both the $(1\bar{3}1)$ and (202) families of planes were considered, it was found that different values of [uvw] resulted, depending on which particular indices were used. This meant either that the indexing was completely wrong, or that the diffraction pattern did not result from a single-crystal, since this would require that the calculated value of [uvw] be independent of the particular indices considered.

Examination of figure 60 reveals that some of the spots seem to be slightly blurred, and that there is a ring present in the vicinity of the spots labelled (1) and (2). These are indications that this diffraction pattern did not originate from one single crystal. Figure 61 shows that the grain size after annealing was about 50 nm. Since the diameter of the incident electron beam was about 0.5-1μm, it can be concluded that the diffraction pattern shown in figure 60 did arise from a group of crystals, and it was just a coincidence that the measured co-planar angle satisfied the single crystal diffraction requirements (i.e., the measured angle equaled the calculated angle for the indexed planes). However, the diffraction indices (202) and (1$\bar{3}$1) which were assigned to these diffraction spots are probably correct, simply because based on the d-spacing of these spots, there are not any more likely choices in the barium titanium silicate family of materials.

The large dark areas present on figure 61 could indicate areas where grain growth occurred during the annealing process. The different intensity of colour of the grains in this figure suggests that the crystallized grains are randomly oriented.

CHAPTER 5

SUMMARY AND CONCLUSIONS

5.1 Ceramic Sputtering Targets

The optimum sintering temperatures were found to be 1275 and 1245°C for the fresnoite and mod-BST ceramics, respectively.

The dielectric constant of the fresnoite ceramics was measured over a frequency range of 10kHz to 10 MHz, and a temperature range of 20 to 200°C. It was found to vary from 12.42 to 14.41. The dielectric constant also depended on the ceramic disc thickness.

When sintered, both types of ceramics formed at least three distinct phases: $Ba_2Si_2TiO_8$, $BaTiSiO_5$, and Ba_2SiO_4. A small number of other very low intensity diffraction peaks which could have been the result of the formation of extremely small amounts of compounds such as $BaTiO_3$ were also observed in the x-ray diffraction pattern.

The composition of the sintered fresnoite ceramic was determined to be slightly shifted from the stoichiometric formula of fresnoite by wavelength-dispersive-x-ray spectroscopy. From this analysis, correction factors for Ba, Si, Ti, and O were derived and successfully applied to the ESCA results for the compositions of sputtered thin films.

5.2 R.F.-Sputtered Thin Films

The compositions of thin films r.f.-sputtered from both types of ceramics were found to be significantly different from that of the base target compositions. Quantitative compositional analysis of these films and targets confirmed that the films were deficient in barium and possessed an excess of titanium.

All the films were completely amorphous in their as-deposited condition, except one which was deposited on (100) Si heated to 650°C. When annealed at temperatures between 700 and 8-0°C, the films crystallized into four phases: $Ba_2Si_2TiO_8$, $BaTiSiO_5$, $BaTiSi_2O_7$, and $BaTiSi_3O_9$. The only film which gave some indication of the desired [001] orientation of the $Ba_2Si_2TiO_8$ and $BaTiSiO_5$ phases when annealed, was a film deposited on (100)Si at a substrate temperature of 650°C.

CHAPTER 6

RECOMMENDATIONS FOR FUTURE RESEARCH

1. Ceramics of the approximate composition $Ba_{3.5}Si_2TiO_{9.5}$ should be fabricated and r.f.-sputtered. If the compositional shift observed in the r.f.-sputtered fresnoite and mod-BST ceramics is maintained, these thin films should have an approximate composition of stoichiometric fresnoite.
2. Ceramic sputtering targets should be fabricated without the use of a paraffin binder. This would ensure that any carbon detected in the ceramics is the result of environmental contamination.
3. All sputtering should be done with the substrate temperatures higher than 650°C, so that a crystalline thin film, possibly oriented in the (001) direction may be obtained.

REFERENCES

1. J.T. Alfors, M.C. Stinson, R.A. Matthews, A. Pabst, "Seven New Barium Minerals From Eastern Fresno County California," Amer. Min., 50, 314-340 (1965).

2. D.E. Rase, R. Roy, "Phase Equilibria in the System $BaTiO_3$-SiO_2," J. Amer. Cer. Soc., 38, No. 11, 389-395 (1955).

3. P.B. Moore, J. Louisnathan, "Fresnoite: Unusual Titanium Coordination," Science, 156, 1361-1362 (1967).

4. L.D. Calvert, J. Trotter, "Fresnoite," Structure Reports, 32A, 442-443 (1967).

5. M. Kimura, Y, Fujino, T. Kawamura, "New Piezoelectric Crystal: Synthetic Fresnoite ($Ba_2Si_2TiO_8$)," Appl. Phys. Lett., 29, 227-228 (1976).

6. S. Haussuhl, J. Eckstein, K. Recker, F. Wallrafen, "Growth and Physical Properties of Fresnoite $Ba_2TiSi_2O_8$," J. of Crys. Gr., 40, 200-204 (1977).

7. M. Kimura, "Elastic and Piezoelectric Properties of $Ba_2Si_2TiO_8$," J. Appl. Phys., 48, 2850-2856 (1977).

8. J. Melngailis, J.F. Vetelino, A. Jhunjhunwala, J.B. Reed, R.E. Fahey, E. Stern, "Surface Acoustic Wave Properties of Fresnoite, $Ba_2Si_2TiO_8$," App. Phys. Lett., 32, No. 4, 203-205 (1978).

9. H. Yamauchi, "Surface-Acoustic-Wave Characteristics on Fresnoite ($Ba_2Si_2TiO_8$) Single Crystal," J. Appl. Phys., 49, 6162-6164 (1978)

10. H. Yamauchi, K. Yamashita, H. Takeuchi, "$Ba_2Si_2TiO_8$ For Surface-Acoustic-Wave Devices," J. Appl. Phys., 50, 3160-2167 (1979).

11. A. Halliyal, A.S. Bhalla, R.E. Newnham, L.E. Cross, "$Ba_2TiGe_2O_8$ and $Ba_2TiSi_2O_8$ Pyroelectric Glass-Ceramics," J. Mat. Sc., 16, 1023-1028.

12. A. Halliyal, A. Safari, A.S. Bhalla, R.E. Newnham, L.E. Cross, "Grain-Oriented Glass Ceramics for Piezoelectric Devices," J. Amer. Cer. Soc., 67, 331-335 (1984).

13. M. Ayukawa, "$Ba_2Si_2TiO_8$ Thin Films," M.A.Sc. Thesis, The University of Windsor, 1983.

14. A. Halliyal, A.S. Bhalla, S.A. Markgraf, L.E. Cross, R.E. Newnham, "Unusual Pyroelectric and Piezoelectric Properties of Fresnoite ($Ba_2TiSi_2O_8$) Single Crystal and Polar Glass-Ceramics," Ferroelectrics (1985), To be published.

15. S.A. Markgraf, A. Halliyal, A.S. Bhalla, R.E. Newnham, "X-ray Structure Refinement and Pyroelectric Investigation of Fresnoite, $Ba_2TiSi_2O_8$," Ferroelectrics (1985). To be published.

16. I.S. Zheludev, "Physics of Crystalline Dielectrics, Vol. 2,", Plenum Press, New York, pp. 533-620 (1971).

17. J.C. Anderson, "Dielectrics," Reinhold Publishing Co., New York, pp. 121-142 (1964).

18. J.F. Nye, "Physical Properties of Crystals, 8th Ed., Oxford University Press, Oxford, pp. 110-130 (1979).

19. M.E. Lines, A.M. Glass, "Principles and Applications of Ferroelectrics and Related Materials," Claredon Press, Oxford, pp.

20. Y. Konishi, T. Tsuji, "Electro-Ceramics Bases and Applications," Ohm Publishing Co., Tokyo, pp. 77-120 (1978) (in Japanese).

21. D.A. Berlincourt, D.R. Curran, H. Jaffe, "Piezoelectric and Paramagnetic Materials and Their Function in Transducers," in Physical Acoustics, Vol. 1 - Part A, Ed. by W.P. Mason, Academic Press, New York, pp. 169-270 (1964).

22. T. Tanaka, "Piezoelectric Devices in Japan," Ferroelectrics, 40, 167-187 (1982).

23. R.M. White, "High Frequency Ultrasonic Devices," in Topics In Solid State and Quantum Electronics, ed. by W.D. Hershberger, John Wiley and Sons Ltd., New York, 187-223 (1972).

24. G.S. Kino, J. Shaw, "Acoustic Surface Waves," Scientific American, 227, No. 4, 50-68 (1972).

25. J.J. Campbell, W.R. Jones, "A Method for Estimating Optimal Crystal Cuts and Propagation Directions for Excitation of Piezoelectric Surface Waves," IEEE trans. Sonics and Ultrasonics, SU-15, No. 4, 209-214 (1968).

26. M.B. Schulz, J.H. Matsinger, "Rayleigh-Wave Electromechanical Coupling Constants," Appl. Phys. Lett., 20, No. 9, 367-369 (1972).

27. M.B. Schulz, B.J. Matsinger, M.G. Holland, "Temperature Dependence of Surface Acoustic Wave Velocity on α Quartz," J. Appl. Phys., 41, No. 7, 2755-2765 (1970).

28. T.L. Szabo, A.J. Slobodnik, Jr., "The Effect of Diffraction on the Design of Acoustic Surface Wave Devices," IEEE trans. Sonics and Ultrasonics, SU-20, No. 3, 240-251 (1973).

29. R.M. O'Connell, "Cuts of Lead Potassium Niobate, $Pb_2KNb_5O_{15}$, For Surface Acoustic Wave (SAW) Applications," J. Appl. Phys., 49, 3324-3327 (1978).

30. J. Henaff, M. Feldmann, M.A. Kirov, "Piezoelectric Crystals for Surface Acoustic Waves (Quartz, $LiNbO_3$, $LiTaO_3$, Tl_3VS_4, Tl_3TaSe_4, $AlPO_4$, GaAs," Ferroelectrics, 42, 161-185 (1982).

31. A.W. Warner, D.A. Pinnow, "Piezoelectric and Photoelastic Properties of Lithium Iodate," J. Acoustical Soc. of Amer., 47, No. 3, 791-794 (1970).

32. H. Takeuchi, K. Yamashita, "Surface Acoustic Wave Characteristics of CuCl," J. Appl. Phys., 52, 7448-7449 (1981).

33. C.S. Hartmann, D.T. Bell, R.C. Rosenfeld, "Impulse Model of Acoustic Surface-Wave Filters," IEEE trans. on Microwave Theory and Techniques, MTT-21, No. 4, 162-175 (1973).

34. R.M. O'Connell, "High Piezoelectric Coupling Temperature-Compensated Cuts of Berlinite ($AlPO_4$) for SAW Applications," IEEE trans. Sonics and Ultrasonics, SU-24, No. 6, 376-384 (1977).

35. A. Jhunjhunwala, J.F. Vetelino, J.C. Field, "Temperature Compensated Cuts with Zero Power Flow in Tl_3VS_4 and Tl_3Se_4," Electronics Lett., 12, No. 25, (1976).

36. R.W. Whatmore, N.M. Shorrocks, C. O'Hara, F.W. Ainger, I.M. Young, "Lithium Tetraborate: A New Temperature Compensated SAW Substrate Material," Electronics Lett., 17, No. 1, 11-12 (1981).

37. Y. Ito, H. Takeuchi, S. Jyomura, K. Nagatsuma, S. Ashida, "Temperature-Compensated $PbTiO_3$ Ceramics for Surface Acoustic Wave Applications," Appl. Phys. Lett., 35, No. 8, 595-597 (1978).

38. M. Kodama, H. Egami, S. Yoshida, "Fabrication of Temperature Stabilized Piezoelectric Ceramic For Surface Wave Applications," Jap. J. Appl. Phys. 14, No. 11, 1847-1848 (1975).

39. M. Tamura, M. Yonezawa, "Temperature-Stabilized Piezoelectric Ceramics for Acoustic Surface-Wave Filters," Proc. IEEE, 62, 416 (1974).

40. A.J. Slobodnik, Jr., USAF Report No. AFCRL-72-0082 (1981) (unpublished).

41. T. Mitsuyu, O. Yamazaki, K. Ohji, K. Wasa, "Piezoelectric Thin Films of Zinc Oxide for SAW Devices," Ferroelectrics, 42, 233-240 (1982).

42. K. Tsubouchi, N. Mikoshiba, "Zero Temperature Coefficient SAW Delay Line On AIN Epitaxial Films," 1983 IEEE Ultrasonics Symp. Proc., IEEE, New York, 299-310 (1983).

43. E. Dieulesaint, D. Royer, "Properties of Piezoelectric Selenium And Selenium Layers," Ferroelectrics, 42, 187-195 (1982).

44. L.E. Kinsler, A.R. Frey, "Fundamentals of Acoustics, 2nd Ed., John Wiley and Sons Inc., New York, 333-378 (1962).

45. G.J. Deboo, C.N. Burous, "Integrated Circuits and Semi-Conductor Devices," McGraw-Hill Inc., New York, 95-146 (1971).

46. S.J. Martin, S.S. Schwartz, R.L. Gunshor, R.F. Pierret, "Surface Acoustic Wave Resonators on a ZnO-on-Si Layered Medium," J. Appl. Phys., 54, 561-569 (1983).

47. L. Maissel, "Application of Sputtering to the Deposition of Films," in Handbook of Thin Film Technology, ed. by L. Maissel and R. Glang, McGraw-Hill Book Co., New York, 4-1 - 4-44 (1970).

48. J.A. Thornton, "Sputter Coating - Its Principles and Potential," SAE trans., 82, 1787-1805 (1974).

49. W.D. Westwood, "Glow Discharge Sputtering," Progress in Surface Sci., 7, 71-111 (1976).

50. J.A. Thornton, "Coating Deposition by Sputtering," in Deposition Technologies for Films and Coatings," ed. by R.F. Bunshah, Noyes Publications Inc., New Jersey, 170-243, (1982).

51. G.S. Anderson, W.N. Mayer, G.K. Whener, "Sputtering of Dilectrics by High Frequency Fields," J. Appl. Phys., 33, No. 10, 2991-2992 (1962).

52. R.V. Stuart, "Vacuum Technology, Thin Films and Sputtering," Academic Press, New York, 123-130 (1983).

53. J.M. Morabito, "Selected Area and In-Depth Auger Analysis of Thin Films," Thin Solid Films, 19, 21-41 (1973).

54. K. Siegbahn, "ESCA: Atomic, Molecular and Solid State Structure Studied by Means of Electron Spectroscopy," Nova Acta Regiae Societatis Scientiarum Upsaliensis Ser. IV, Vol. 20, Uppsula, 7-36 (1967).

55. C.A. Evans, Jr., "Ion Probe Mass Spectroscopy: Overview", Thin Solid Films, 19, 11-19 (1973).

56. W.K. Chu, J.W. Mayer, M.A. Nicolet, T.M. Buck, G. Amsel, F. Eisen, "Principles and Applications of Ion Beam Techniques for the Analysis of Solids and Thin Films," Thin Solid Films, 17, 1-41 (1973).

57. M-A. Nicolet, J.W. Mayer, I.V. Mitchell, "Microanalysis of Materials by Backscattering Spectrometry," Sci., 177, No. 4052, 841-849 (1972).

58. G.A. Hutchins, "Electron Probe Microanalysis," in Characterization of Solid Surfaces, ed. by P.F. Kane and G.B. Larrabee, Plenum Press, New York, 441-484 (1974).

59. J.V. Gilfrich, "X-ray Fluorescence Analysis," in Characterization of Solid Surfaces, ed. by P.F. Kane and G.B. Larrabee, Plenum Press, New York, 275-306 (1974).

60. E.P. Bertin, "Introduction to X-ray Spectrometric Analysis," Plenum Press, New York, 83-119 (1978).

61. J.W. Coburn, "Sputtering in the Surface Analysis of Solids: A Discussion of some Problems," J. Vac. Sci. Tech. 13, No. 5, 1037-1044 (1976).

62. P.H. Holloway, G.E. McGuire, "Chemical Characterization of Coatings by Analytical Techniques Sensitive to the Surface and Near-Surface," Thin Solid Films, 53, 3-18 (1978).

63. M.G. Lagally, "Surface Analysis Techniques," in Advanced Techniques for Characterizing Microstructures, ed. by F.W. Wiffen and J.A. Spitznagel, AIME, New York, 213-237 (1982).

64. A.R. Von Hipple, "Dielectrics and Waves," John Wiley and Sons Ltd., New York, p. 1-5 (1954).

65. C. Kittel, "Introduction to Solid State Physics," 5th ed., John Wiley and Sons Ltd., New York, 399-412 (1976).

66. H. Yamauchi, "Surface-Acoustic-Wave Characteristics on Fresnoite ($Ba_2Si_2TiO_8$) Single Crystal," J. Appl. Phys., 59, 6162-6164 (1978); and M. Kimura (private communication).

67. K.J. Pascoe, "Properties of Materials for Electrical Engineers," John Wiley and Sons Ltd., New York, p. 173-186 (1980).

68. W.D. Kingery, H.K. Bowen, D.R. Uhlmann, "Introduction to Ceramics," 2nd ed., John Wiley and Sons Ltd., New York, pp. 913-974 (1976).

69. L. Solymar, D. Walsh, "Lectures on the Electrical Properties of Materials," 2nd ed., Oxford University Press, New York, pp. 259-260 (1979).

70. J. Blitz, "Elements of Acoustics," Butterworth and Co. Ltd., London, pp. 39-41 (1964).

71. K. Okazaki, "Exercise on Electrical Engineering Materials," Gakken-Sha, Tokyo, p. 232 (1979) (in Japanese).

72. K.G. Geraghty, L.F. Donaghey, "Kinetics of the Reactive Sputter Deposition of Titanium Oxides," J. Electrochemical Soc., 123, No. 8, 1201-1207 (1976).

73. L. Eckertova, "Physics of Thin Films," Plenum Press, Czechoslovakia, pp. 102-105 (1977).

74. K.L. Chopra, "Thin Film Phenomena," Robert E. Krieger Pub. Co., Reprint ed., Huntington, New York, p. 198 (1979).

75. R.C. Weast, ed., "CRC Handbook of Chemistry and Physics," 59th ed-, CRC Press Inc., West Palm Beach, Florida, p. E-145, E-149 (1978).

76. K. Okazaki, "Ceramic Engineering for Dielectrics," (Rev. Ed.), Gakken-sha Pub. Co. Ltd., Tokyo, Japan, p. 165 (1978), (in Japanese).

77. D.J. McClure, J.R. Crowe, "Characterization of Amorphous Barium Titanate Films Prepared by RF Sputtering," J. Vac. Sci. Tech., 16, 311-314 (1979).

78. J. Panitz, C. Hu, "RF-Sputtered Ferroelectric Barium Titanate Films on Silicon," Ferroelectrics, 27, 161-164 (1980).

79. A. Okada, "Electrical Properties of Lead-Zirconate-Lead-Titanate Ferroelectric Thin Films and Their Composition Analysis by Auger Electron Spectroscopy," J. Appl. Phys., 49, 4495-4499 (1978).

80. M. Ishida, H. Matsunami, T. Tanaka, "Preparation Properties of Ferroelectric PLZT Thin Films by RF Sputtering," J. Appl. Phys., 48, 951-953 (1977).

81. S.B. Krupanidhi, N. Maffei, M. Sayer, K. El-Assal, "RF Planar Magnetron Sputtering and Characterization of Ferroelectric Pb(Zr,Ti)O_3 Films," J. Appl. Phys., 54, 6601-6609 (1983).

82. G. Betz, G.K. Wehner, "Sputtering of Multicomponent Materials," in Sputtering by Particle Bombardment II, ed. by R. Behrisch, Springer-Verlag, Berlin, p. 29 (1983).

83. C. Kittel, "Introduction to Solid State Physics," 5th ed., John Wiley and Sons Ltd., New York, p. 100 (1976).

84. R.C. Weast, ed., "CRC Handbook of Chemistry and Physics," 58th ed., CRC Press Inc., West Palm Beach, Florida, p. F219-F225 (1978).

85. W.D. Kingery, H.K. Bowen, D.R. Uhlmann, "Introduction to Ceramics," 2nd ed., John Wiley and Sons Ltd., New York, pp. 58-59 (1976).

86. R.C. Weast, ec., "CRC Handbook of Chemistry and Physics," 58th ed., CRC Press Inc., West Palm Beach, Florida, pp. D61-D66 (1978).

87. P.B. Hirch et al, "Electron Microscopy of Thin Crystals," Butterworths Pub. Co., London, pp. 538 (1965).

88. G.E. Muilenberg, ed., "Handbook of X-ray Photoelectron Spectroscopy," Perkin-Elmer Co., Minnesota, pg. 9 (1979).

APPENDIX I

Plots of Dielectric Constant vs. Temperature and Frequency For the Two Fresnoite Ceramic Discs

This Appendix contains the plots of dielectric constant vs. temperature, and dielectric constant vs. frequency for the two fresnoite ceramic discs. The values of the dielectric constant for the two discs were taken from Tables 8 and 9.

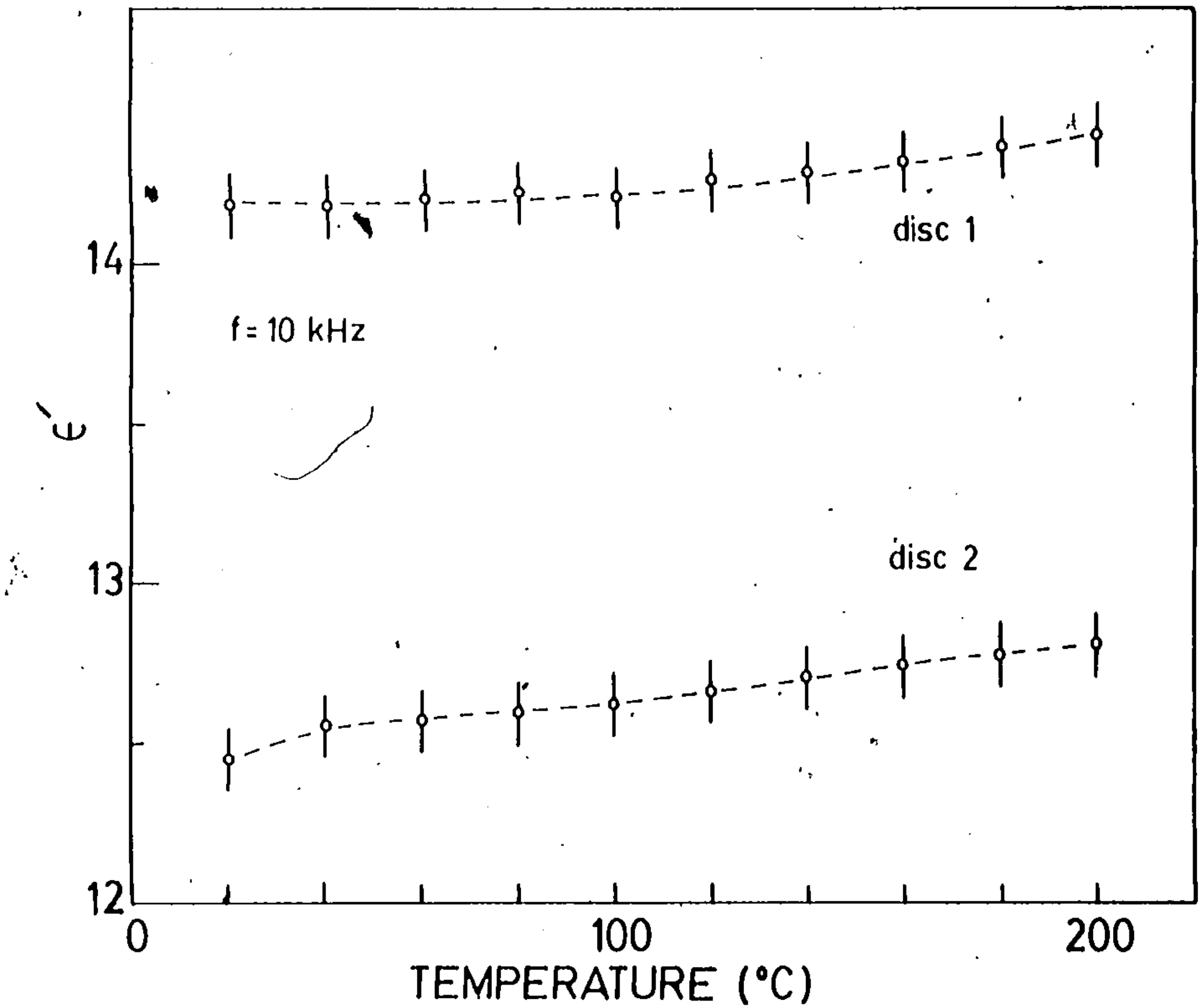

Figure A1.1 Dielectric constant vs. temperature at 10 kHz.

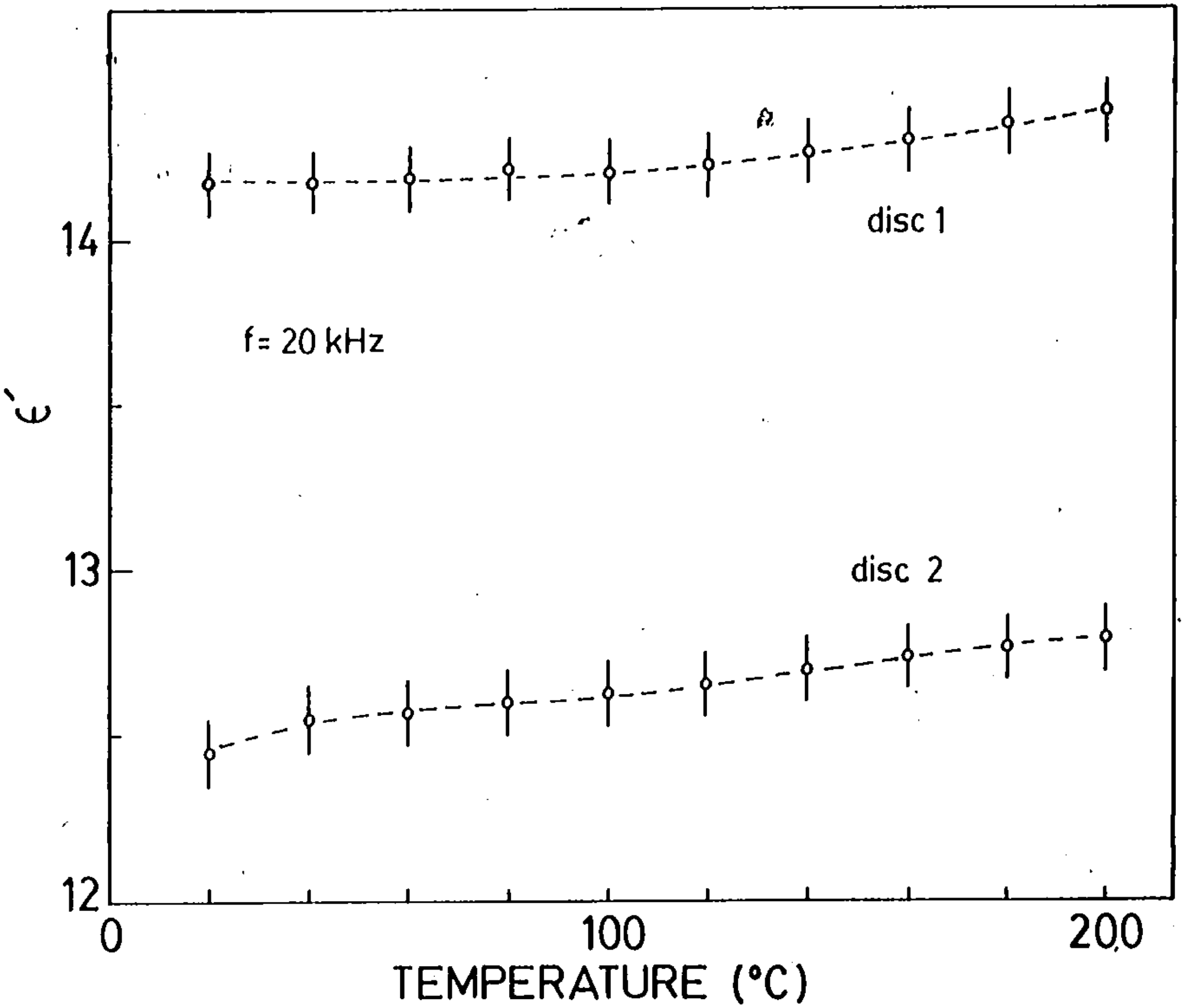

Figure A1.2 Dielectric constant vs. temperature at 20 kHz.

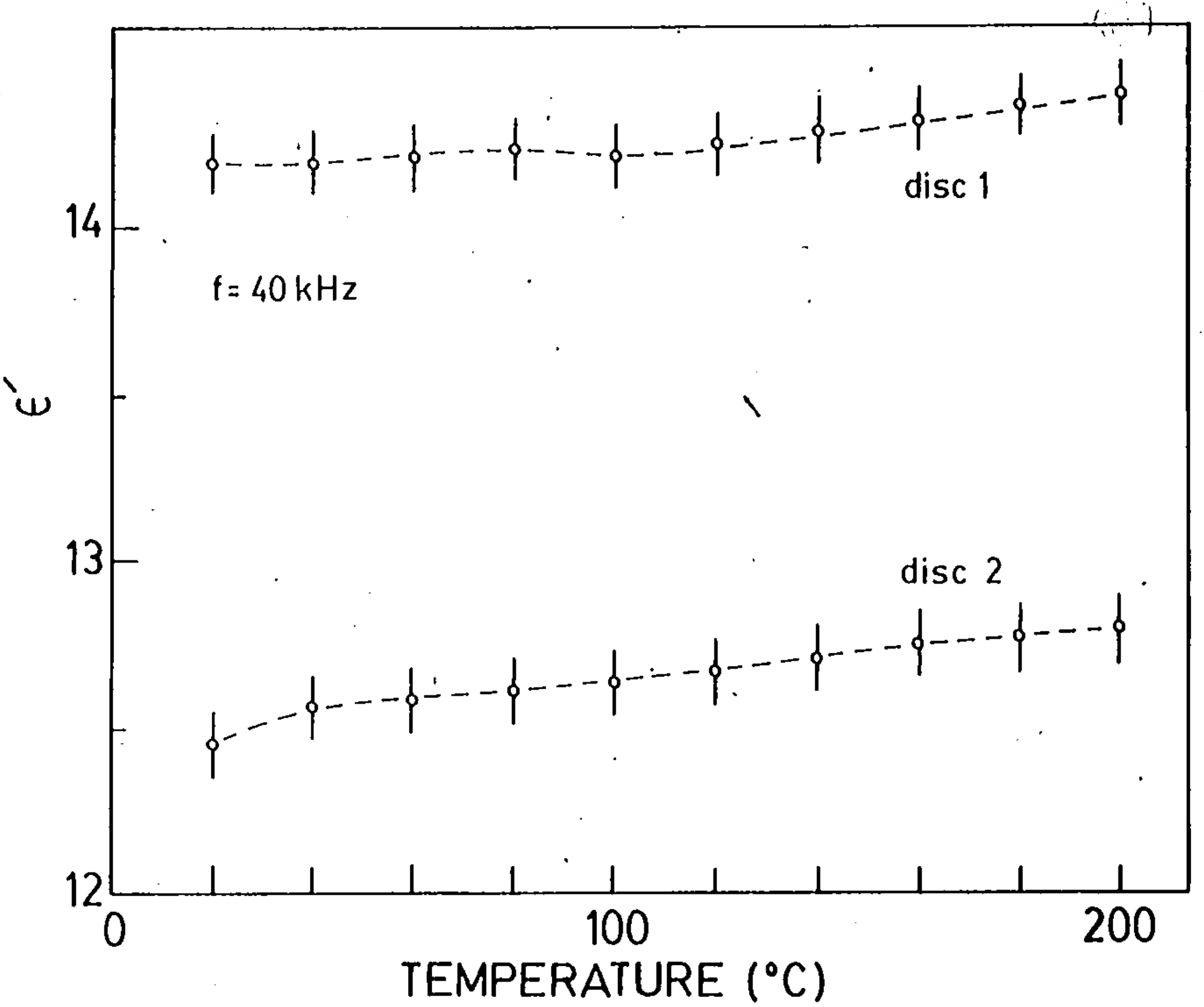

Figure A1.3 Dielectric constant vs. temperature at 40 kHz.

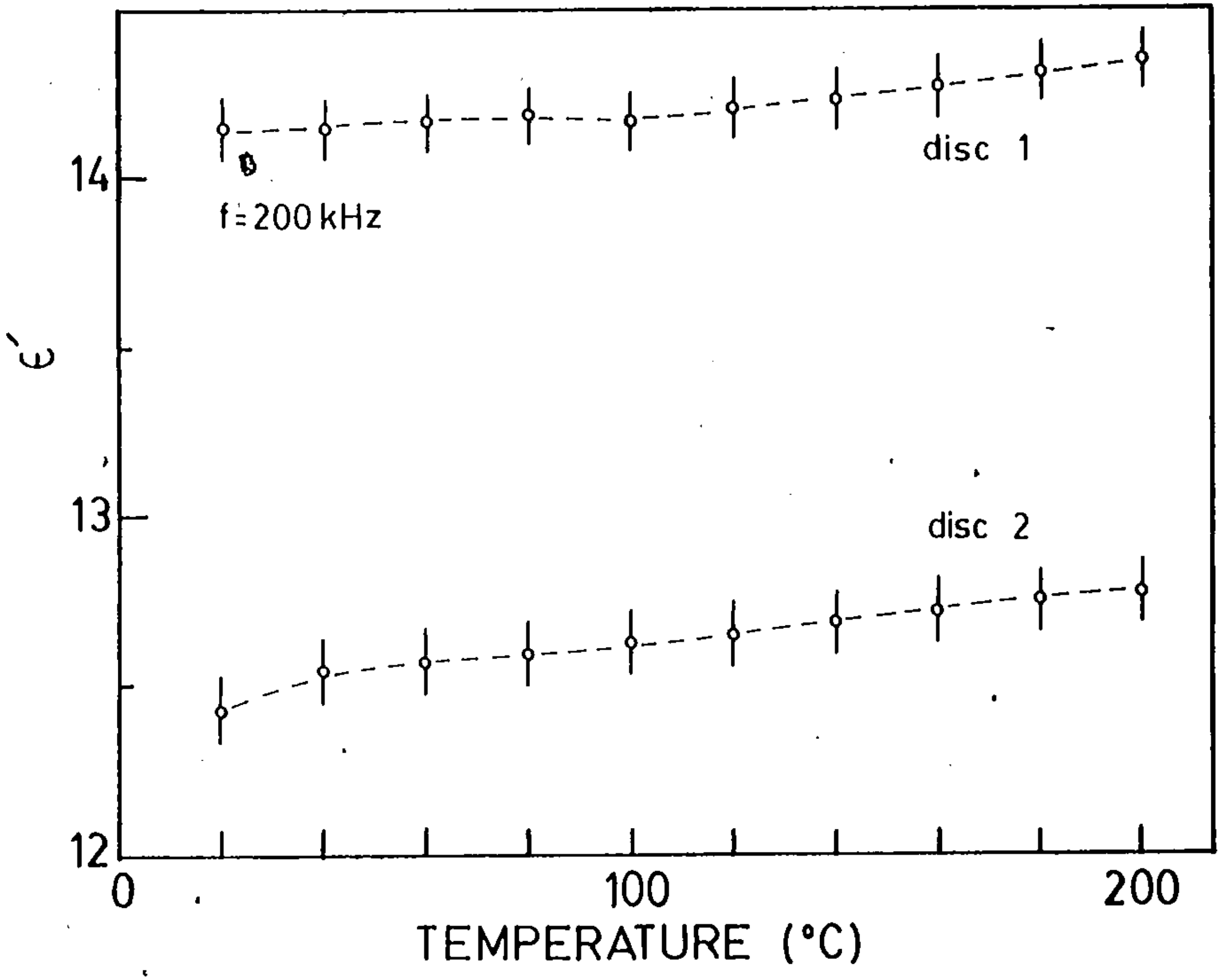

Figure A1.4 Dielectric constant vs. temperature at 200 kHz.

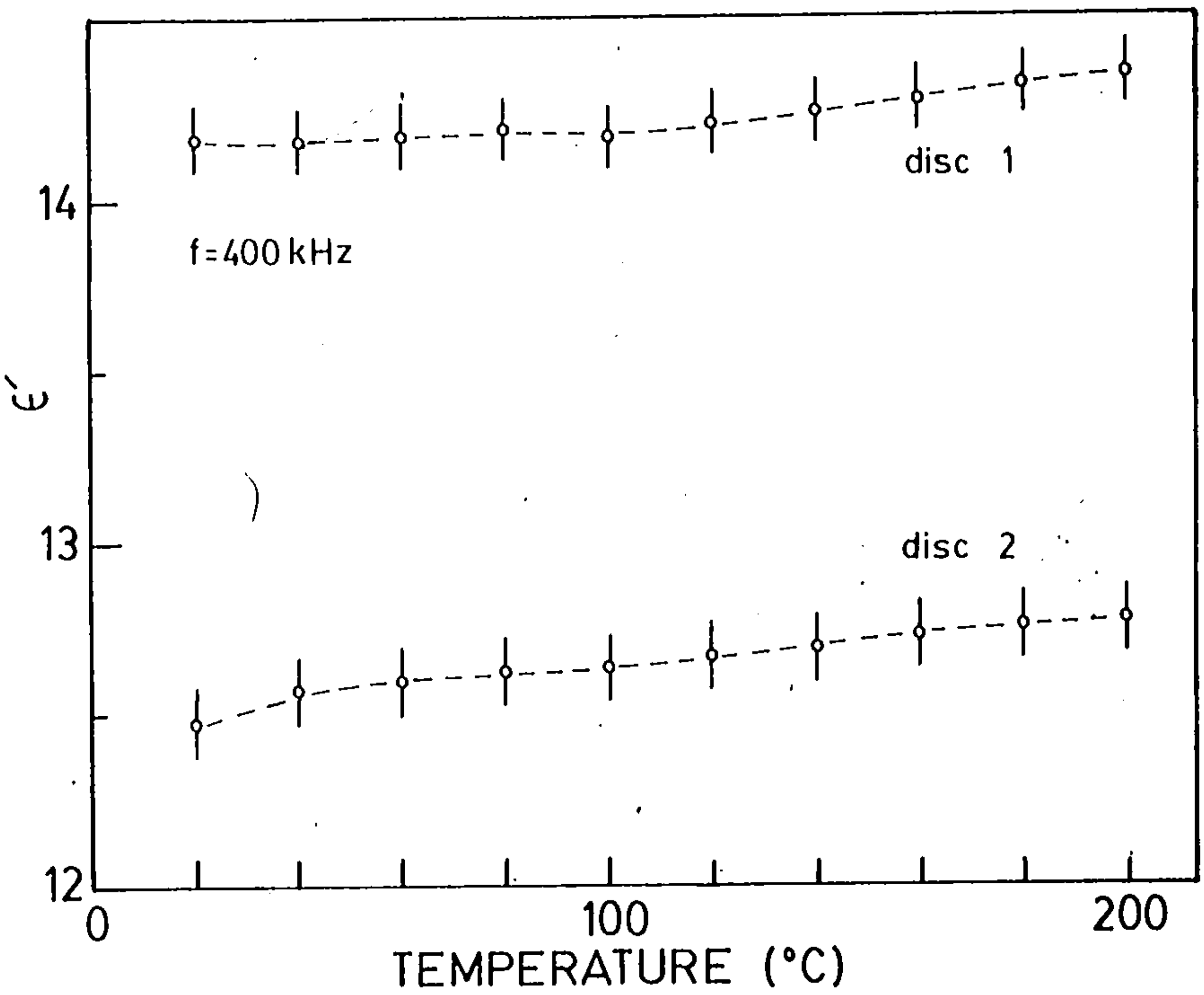

Figure A1.5 Dielectric constant vs. temperature at 400 Hz.

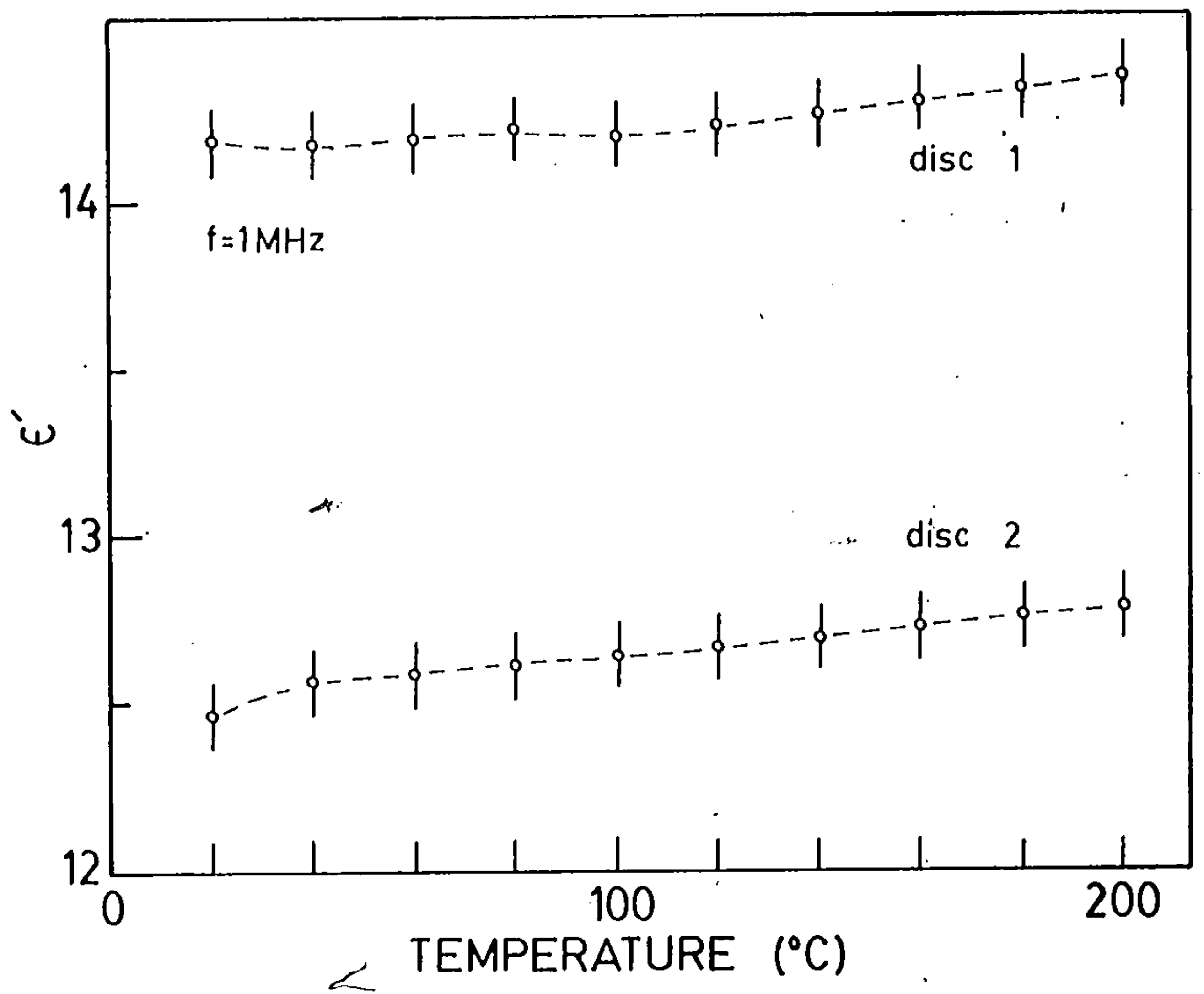

Figure A1.6 Dielectric constant vs. temperature at 1 MHz.

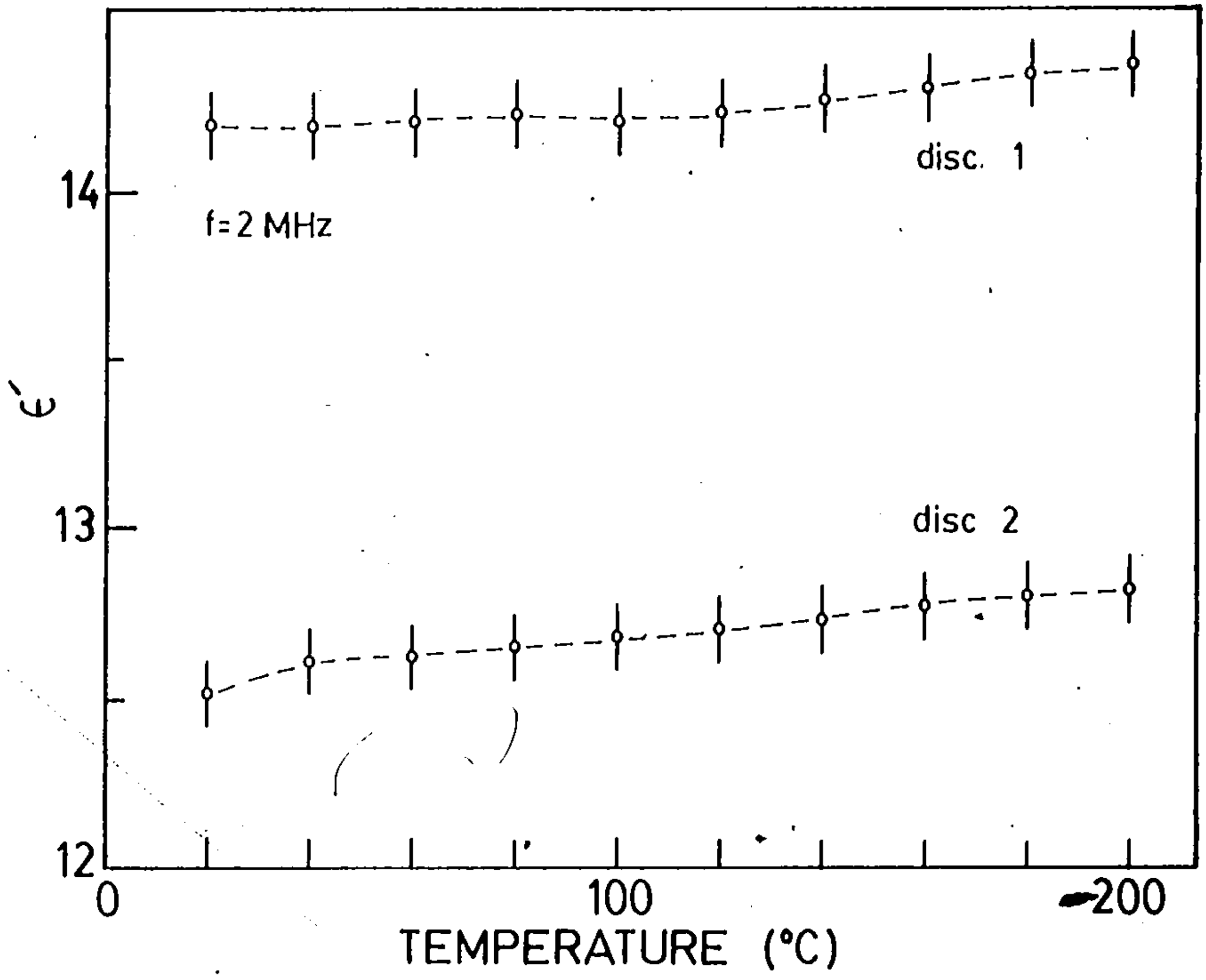

Figure A1.7 Dielectric constant vs. temperature at 2 MHz.

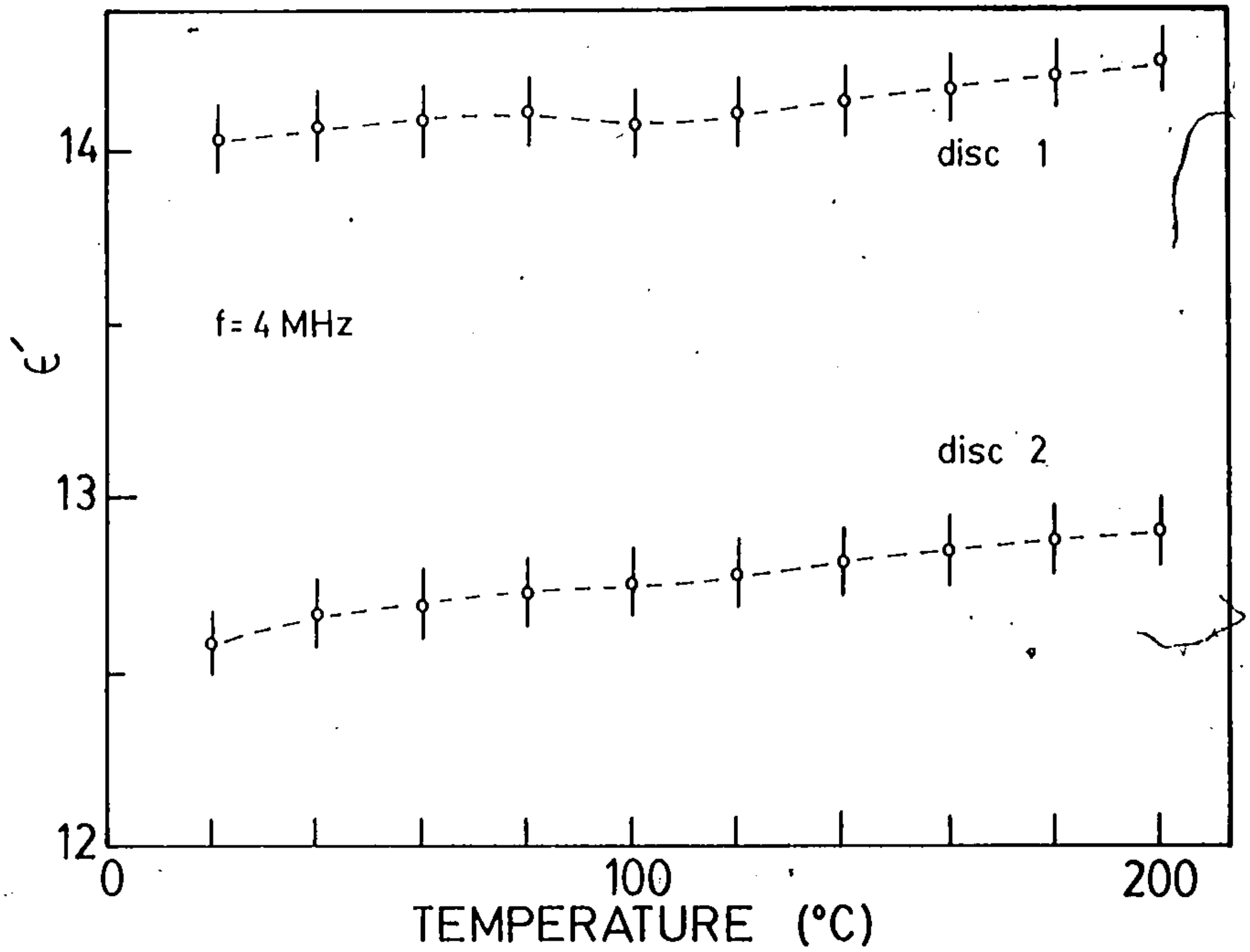

Figure A1.8 Dielectric constant vs. temperature at 4 MHz.

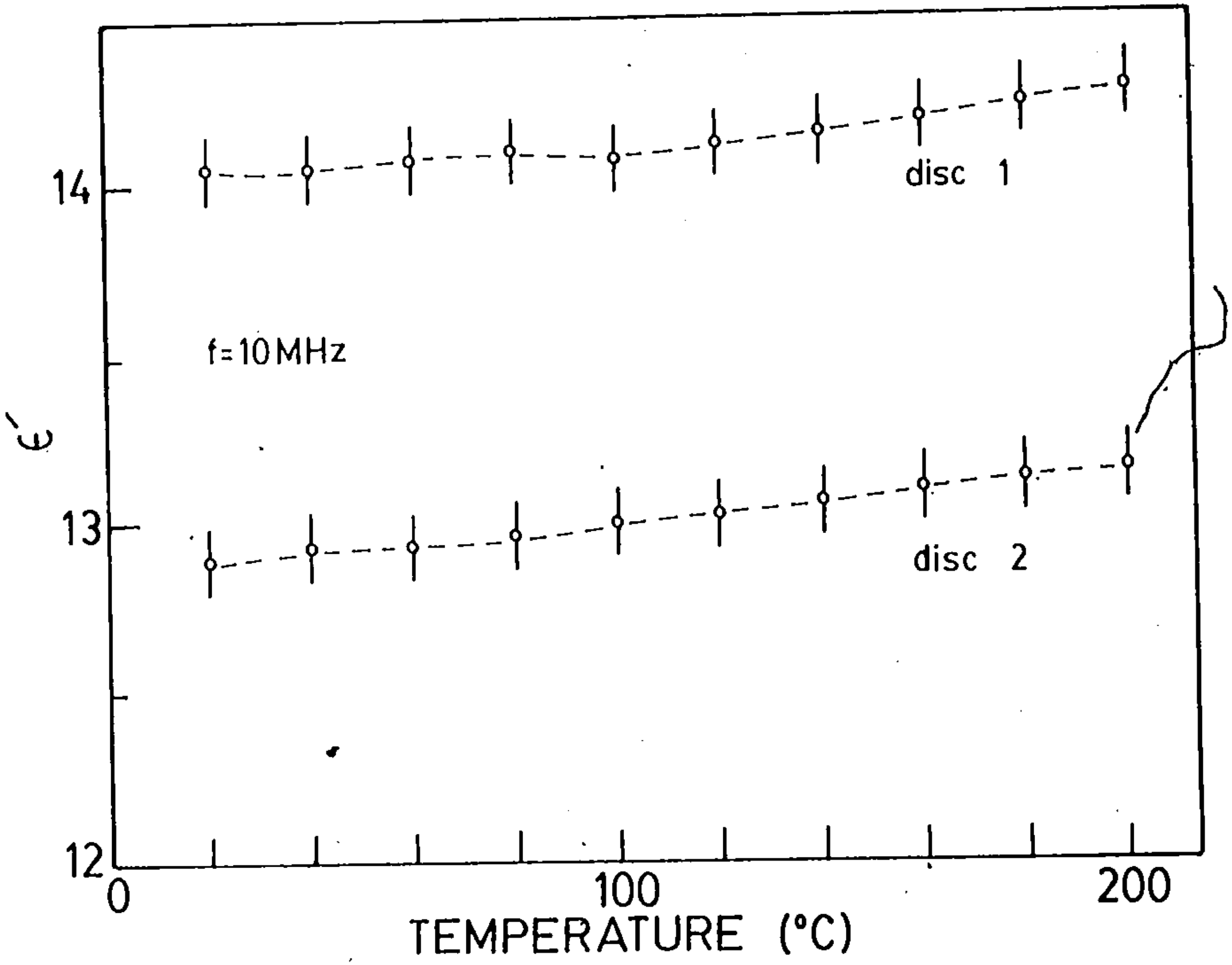

Figure A1.9 Dielectric constant vs. temperature at 10 MHz.

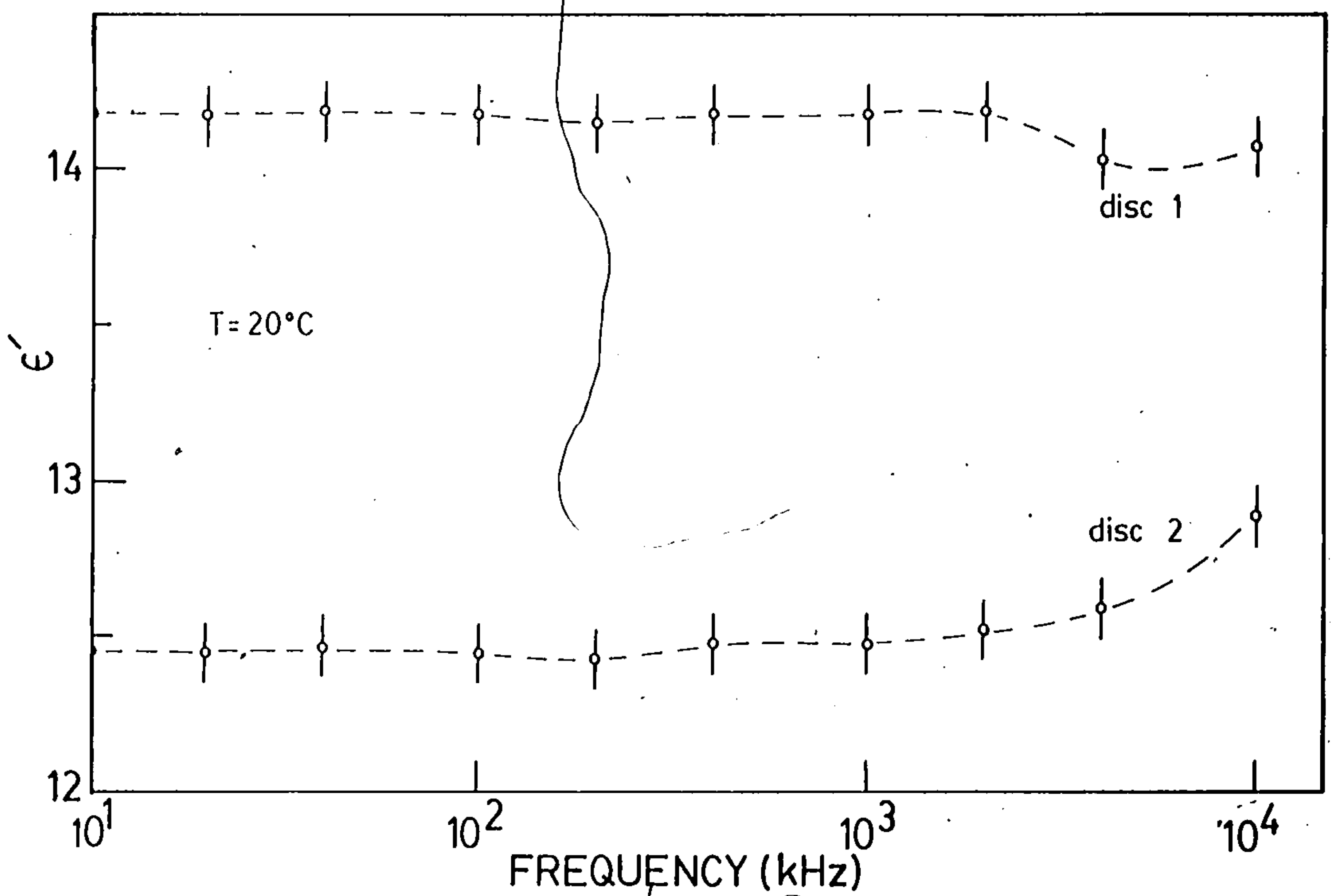

Figure A1.10 Dielectric constant vs. frequency at 20°C.

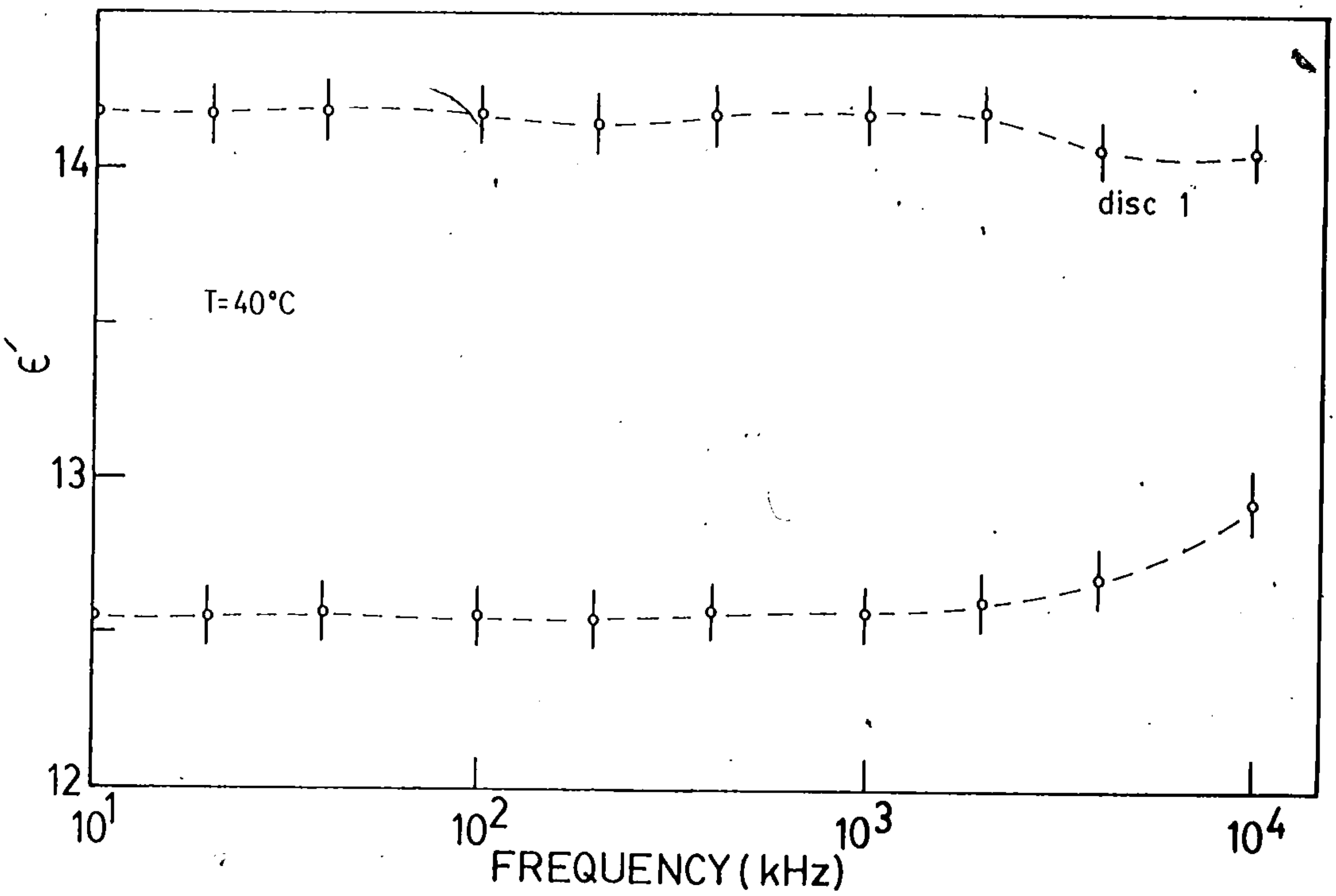

Figure A1.11 Dielectric constant vs. frequency at 40°C.

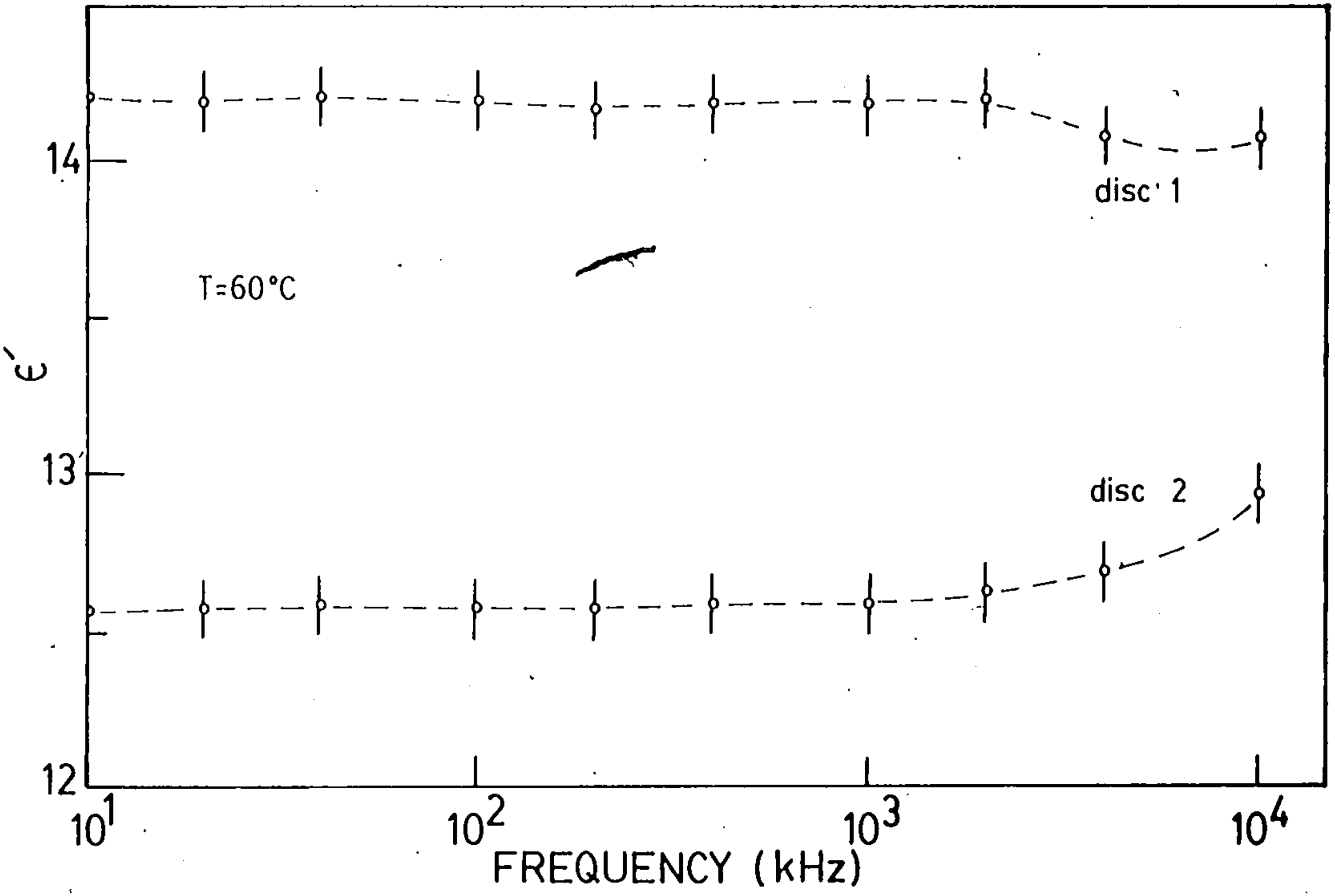

Figure A1.12 Dielectric constant vs. frequency at 60°C.

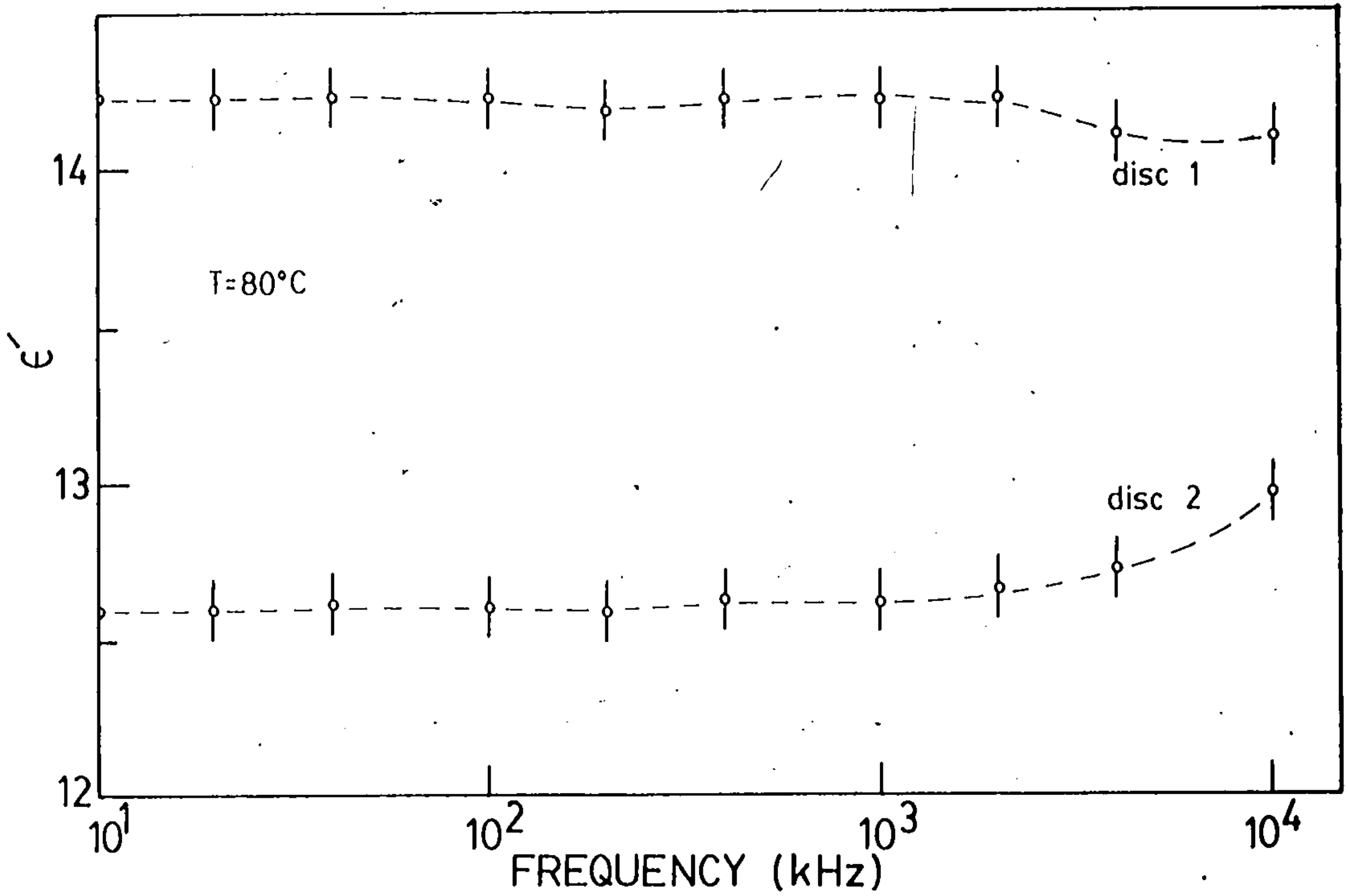

Figure A1.13 Dielectric constant vs. frequency at 80°C.

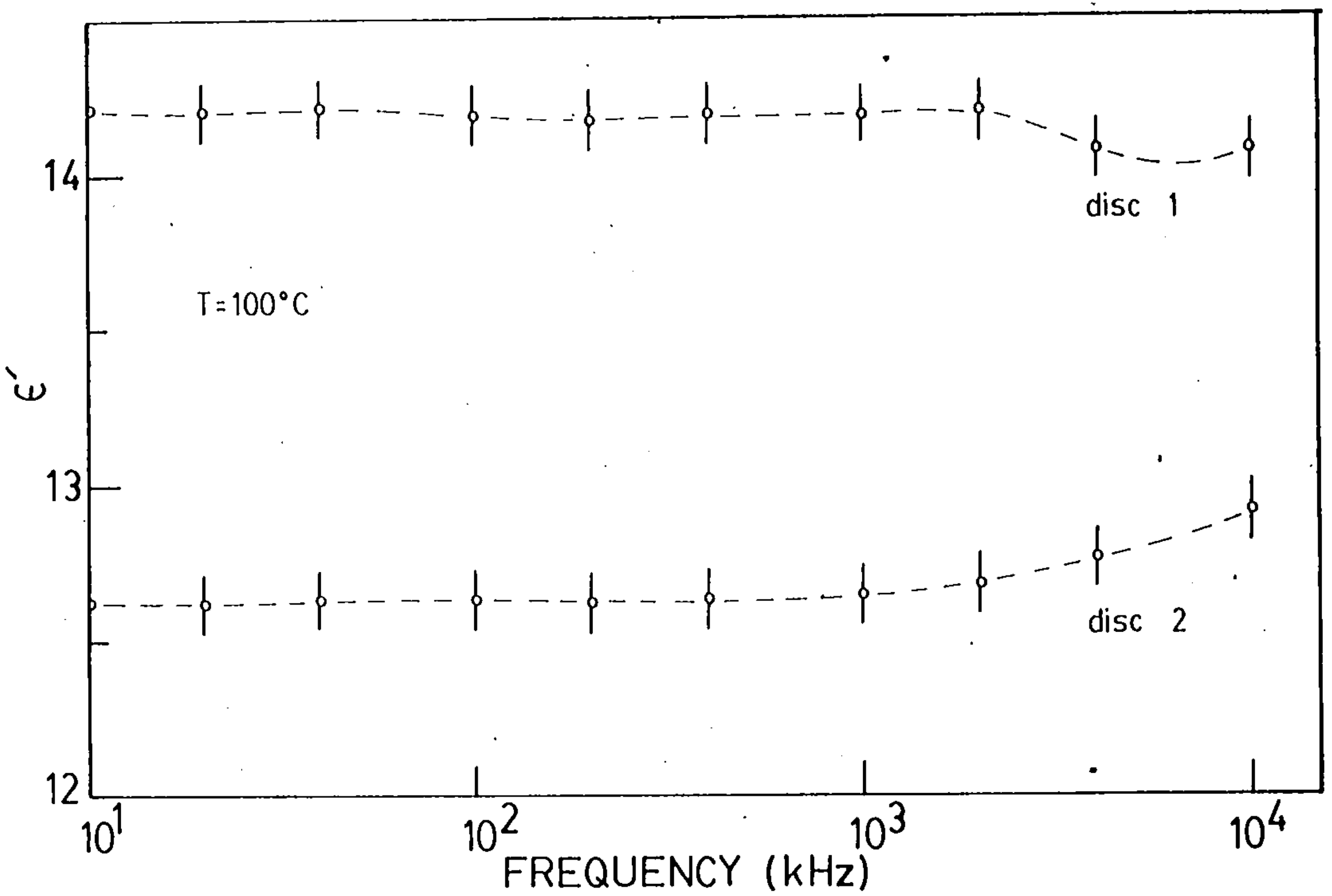

Figure A1.14 Dielectric constant vs. frequency at 100°C.

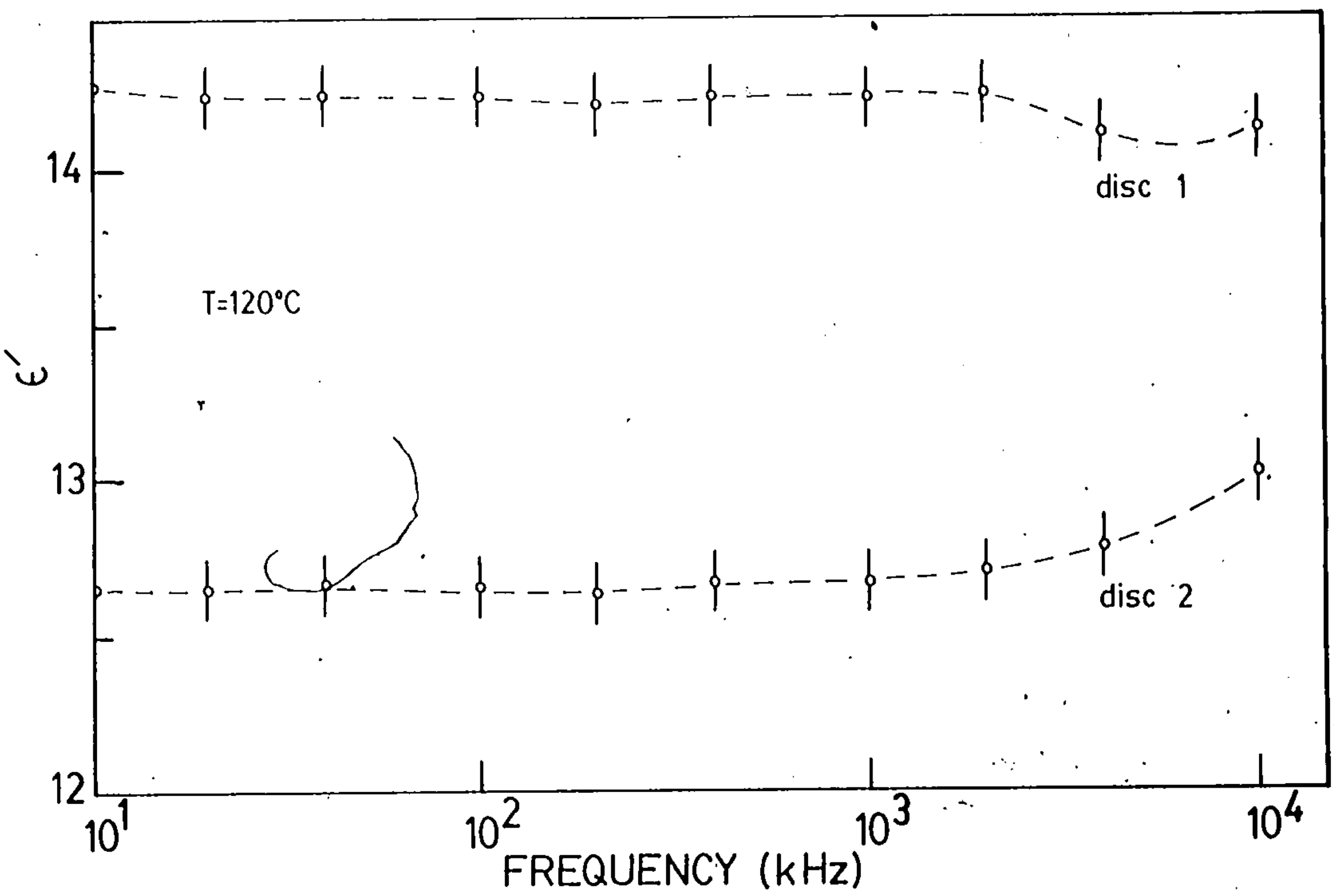

Figure A1.15 Dielectric constant vs. frequency at 120°C.

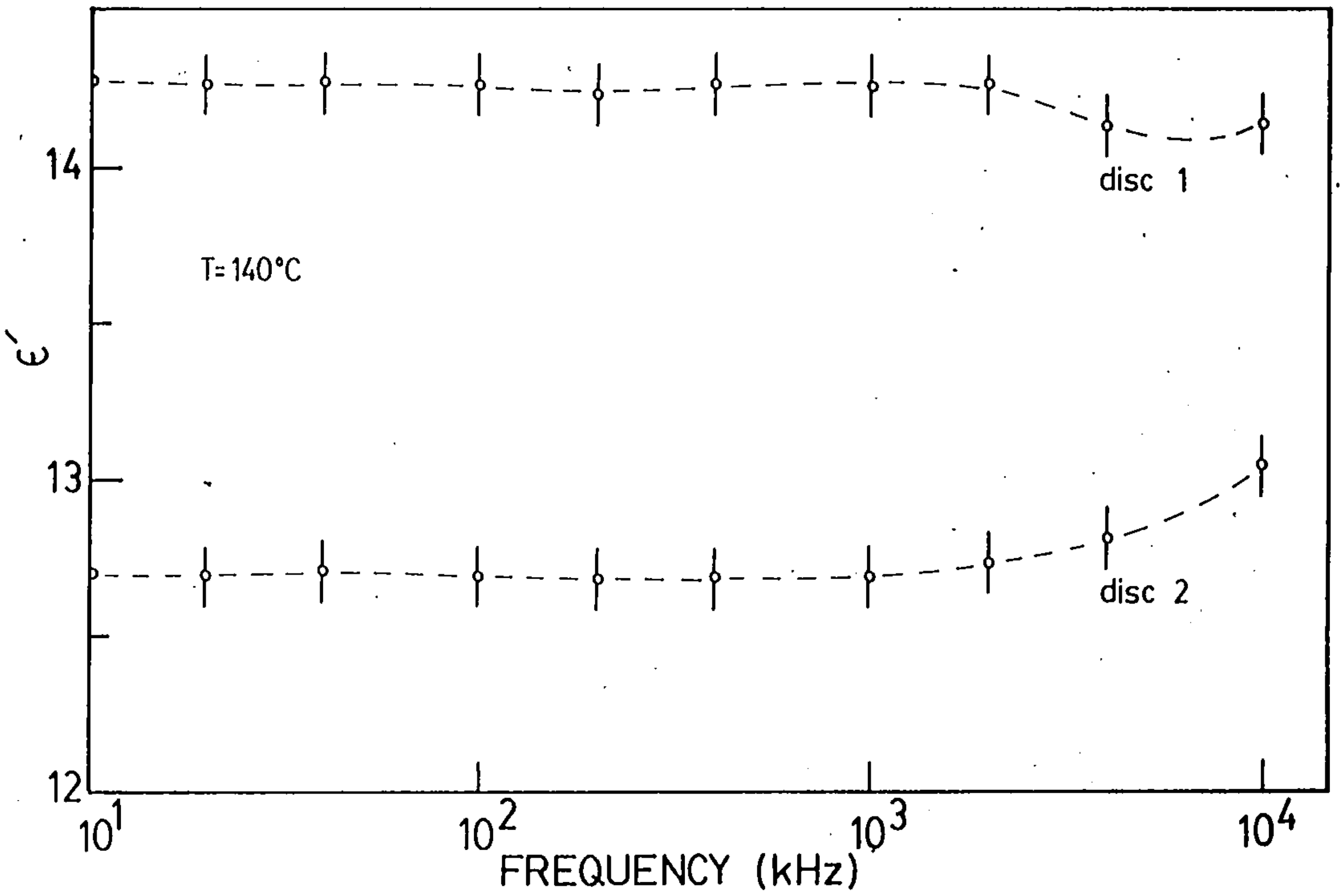

Figure A1.16 Dielectric constant vs. frequency at 140°C.

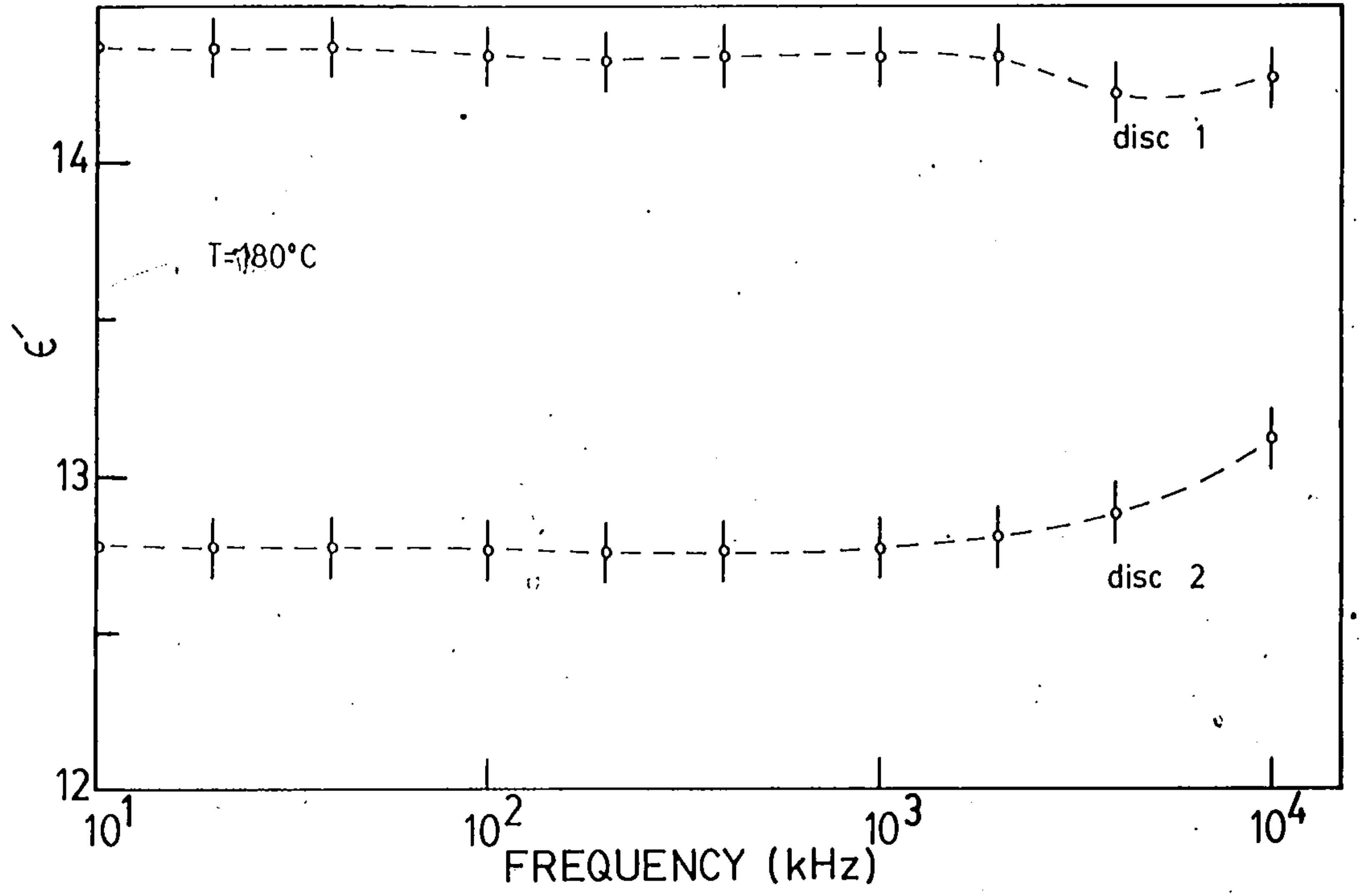

Figure A1.17 Dielectric constant vs. frequency at 180°C.

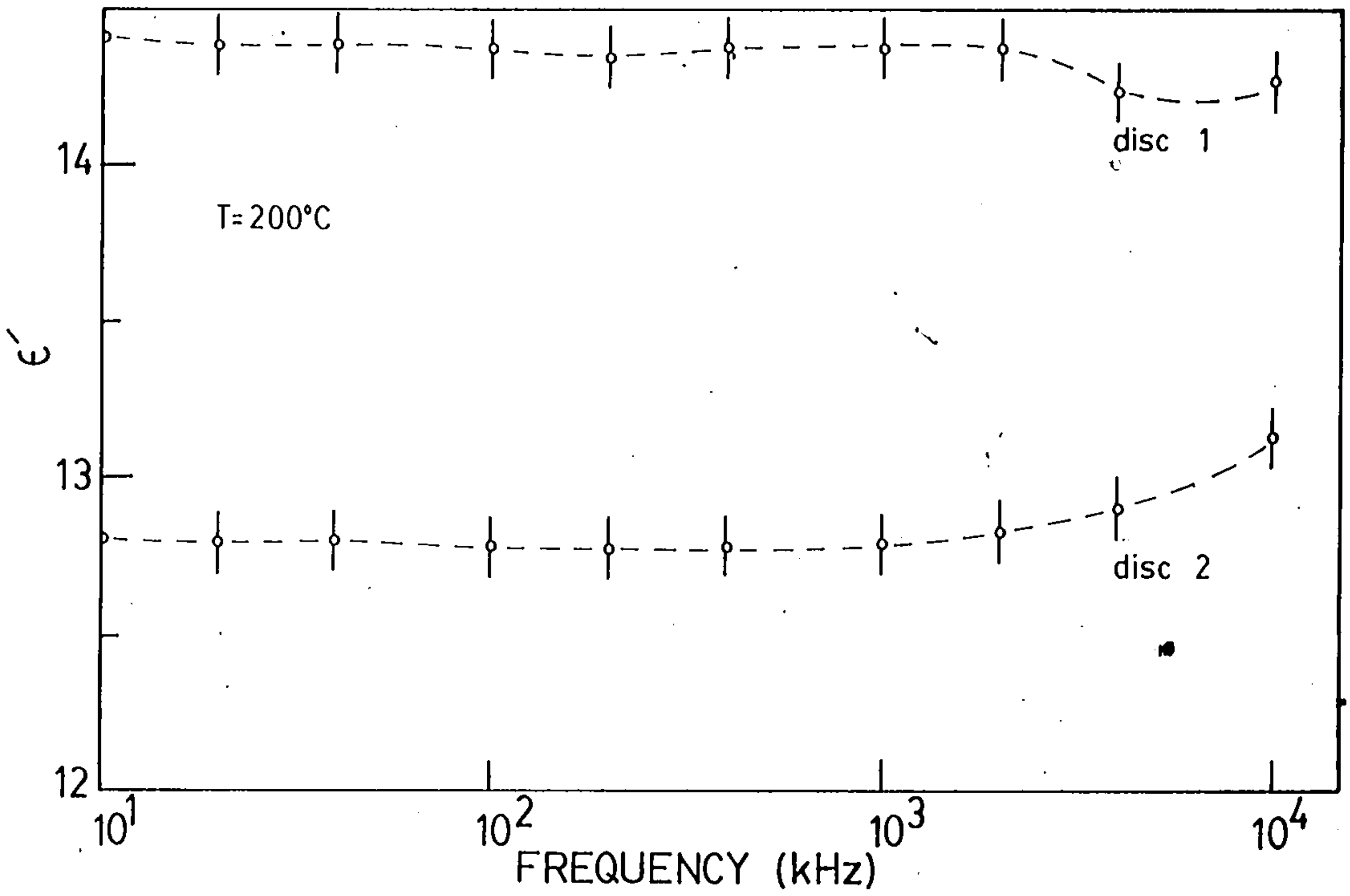

Figure A1.18 Dielectric constant vs. frequency at 200°C.

APPENDIX II

Plots of tan δ vs. Temperature and ε" vs. Frequency For the Two Fresnoite Ceramic Discs

This Appendix contains the plots of tan δ vs. temperature, and ε' vs. frequency for the two fresnoite ceramic discs. The values of tan δ were taken from tables 6 and 7, and the values of ε" were calculated from the relation:

$$\varepsilon'' = \tan\delta \cdot \varepsilon'$$

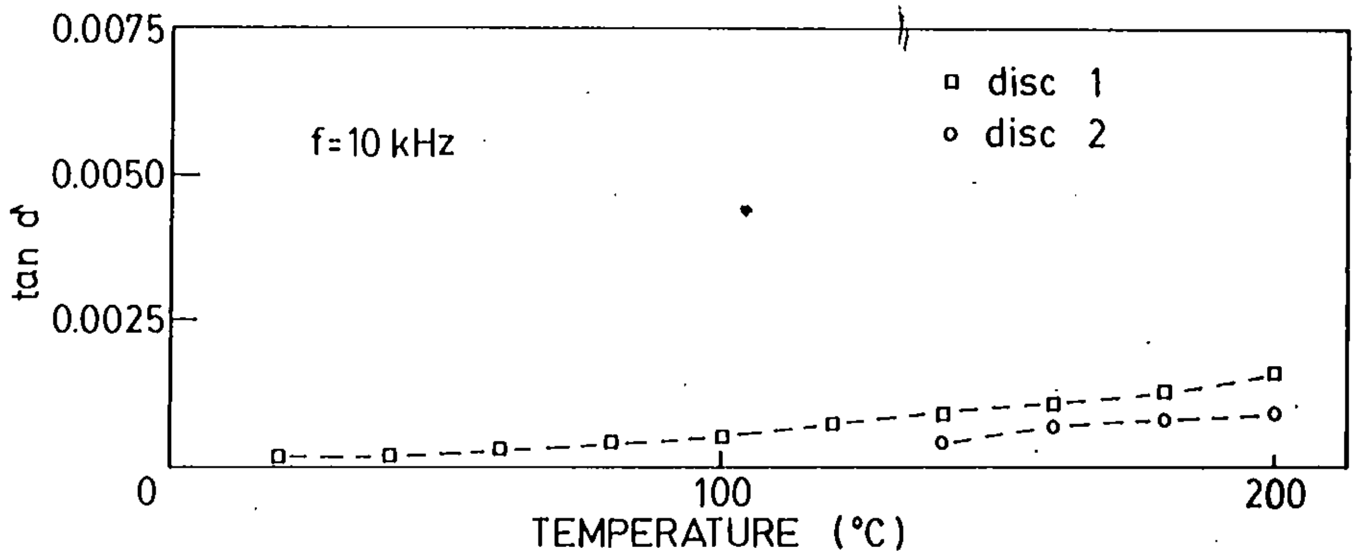

Figure A2.1 tan δ vs. temperature at 10 kHz.

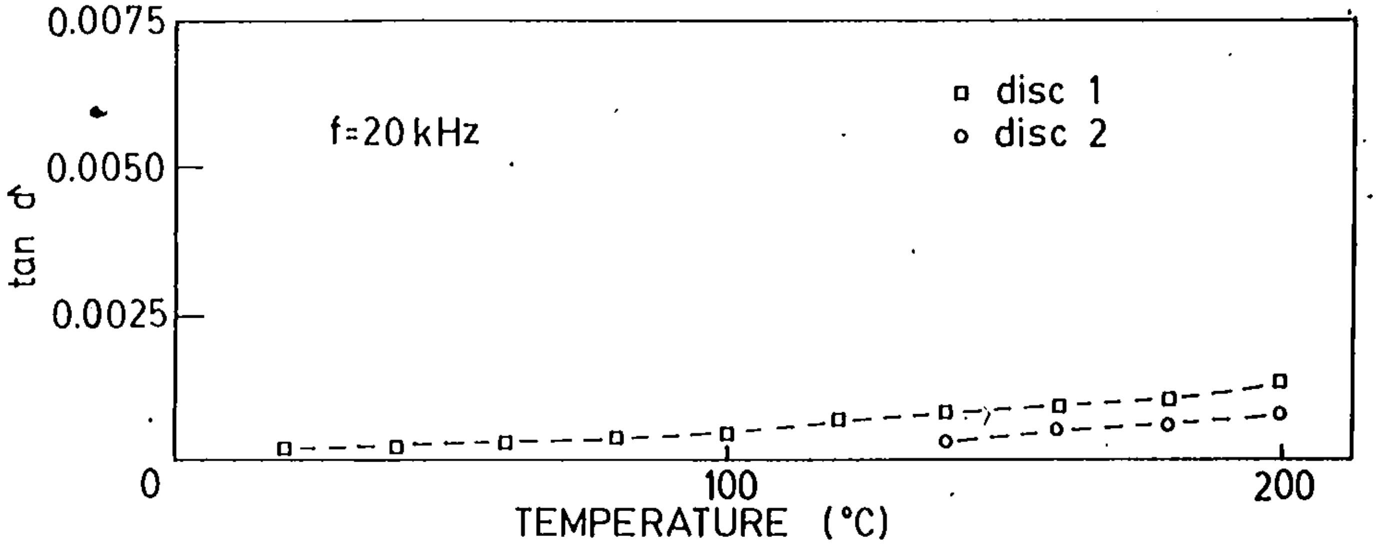

Figure A2.2 tan δ vs. temperature at 20 kHz.

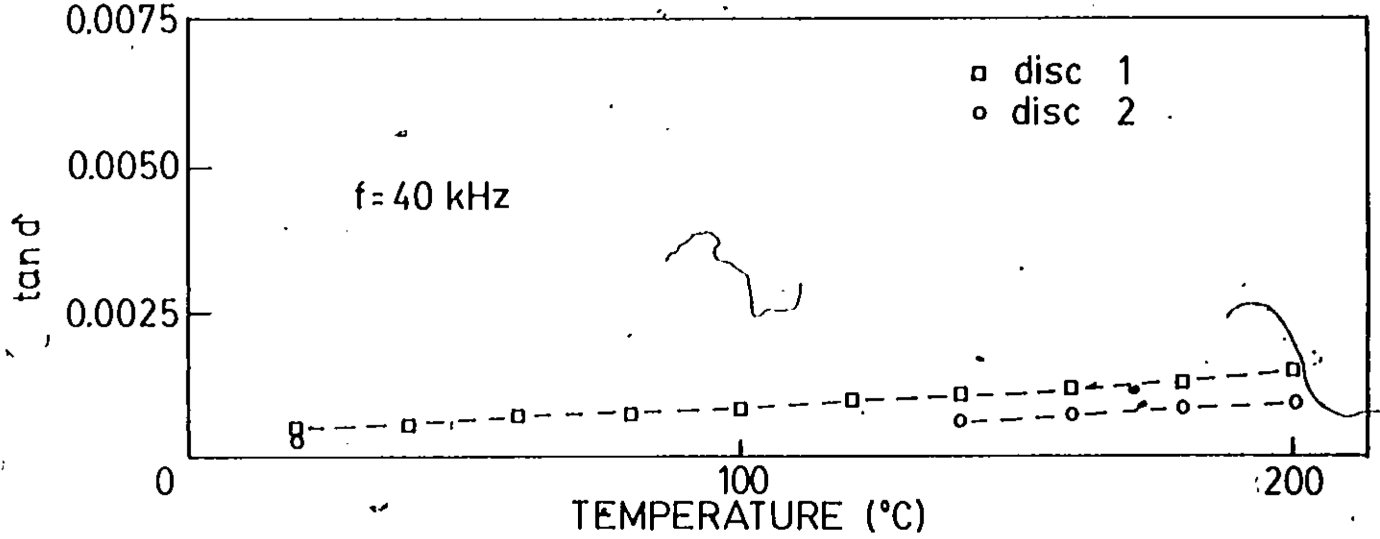

Figure A2.3 tan δ vs. temperature at 40 kHz.

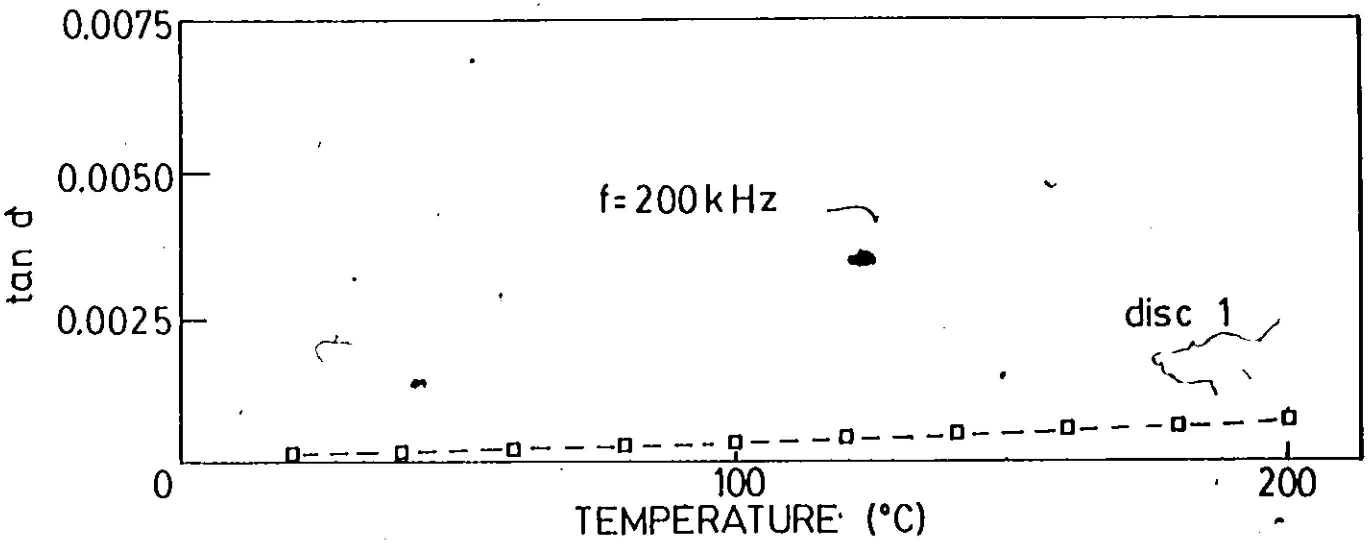

Figure A2.4 tan δ vs. temperature at 200 kHz.

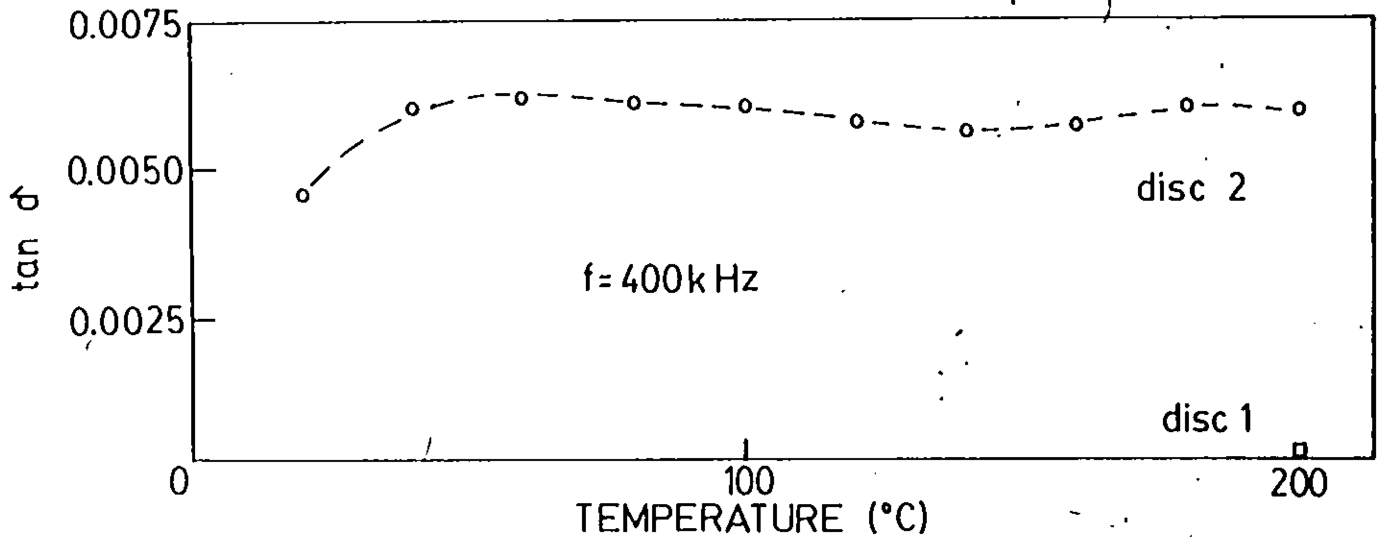

Figure A2.5 tan δ vs. temperature at 400 kHz.

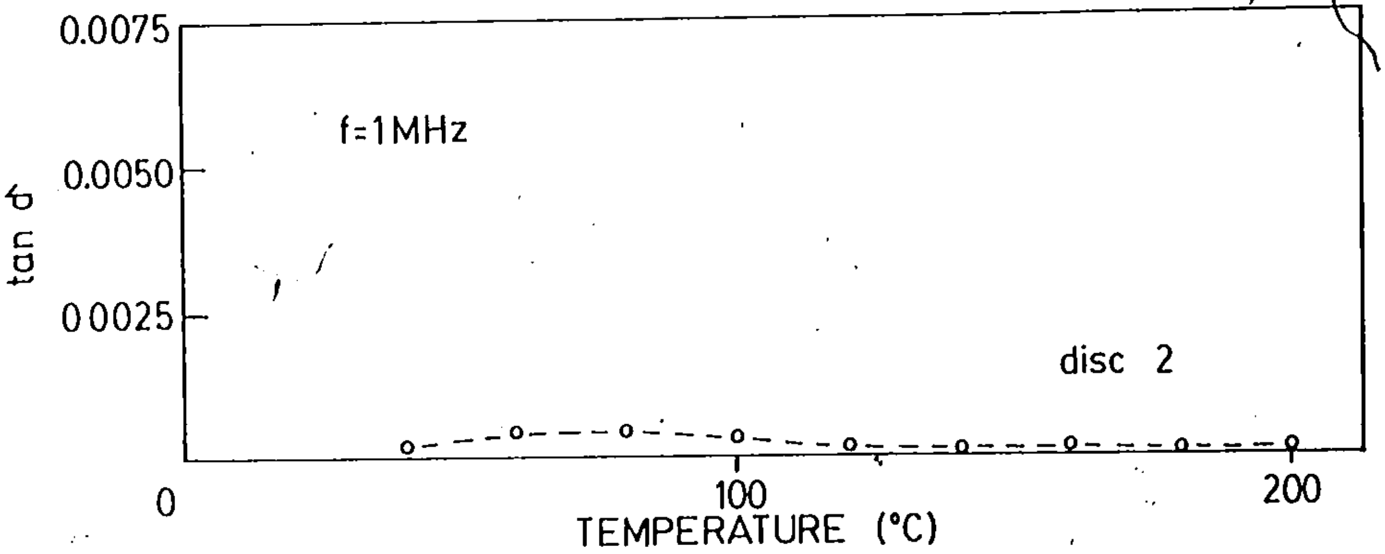

Figure A2.6 tan δ vs. temperature at 1 MHz.

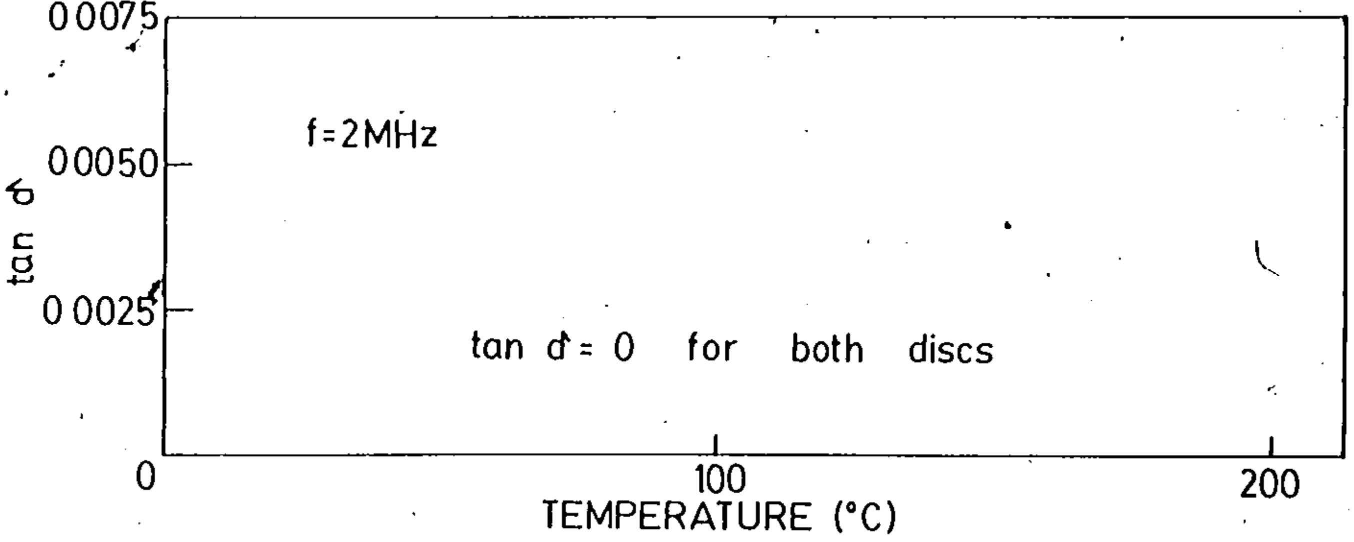

Figure A2.7 tan δ vs. temperature at 2 MHz.

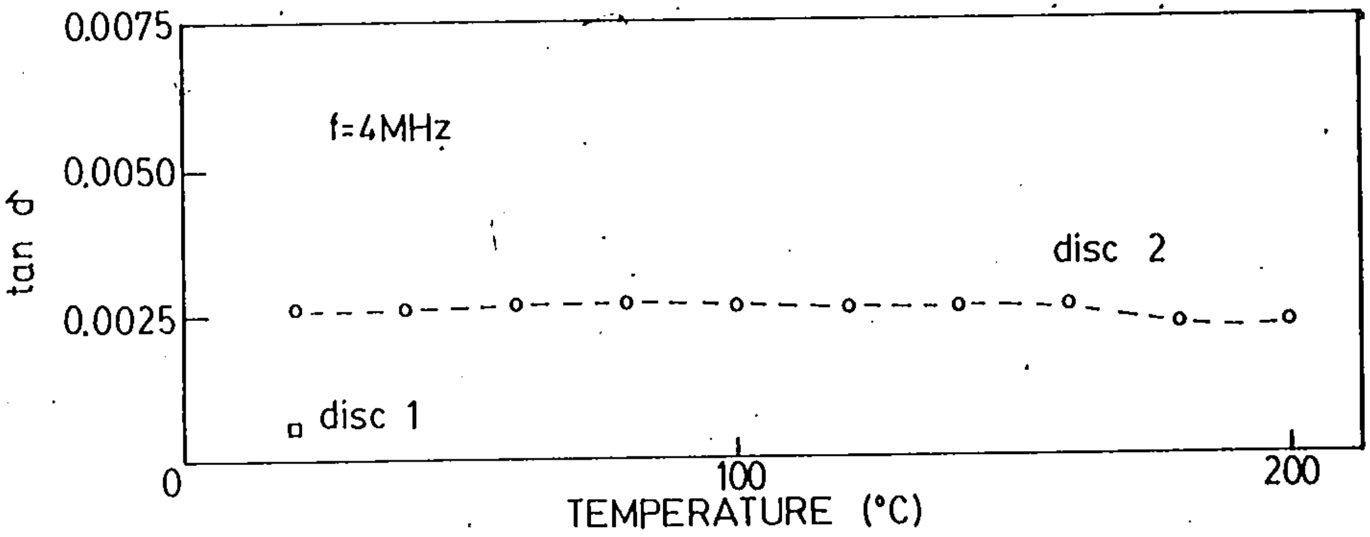

Figure A2.8 tan δ vs. temperature at 4 MHz.

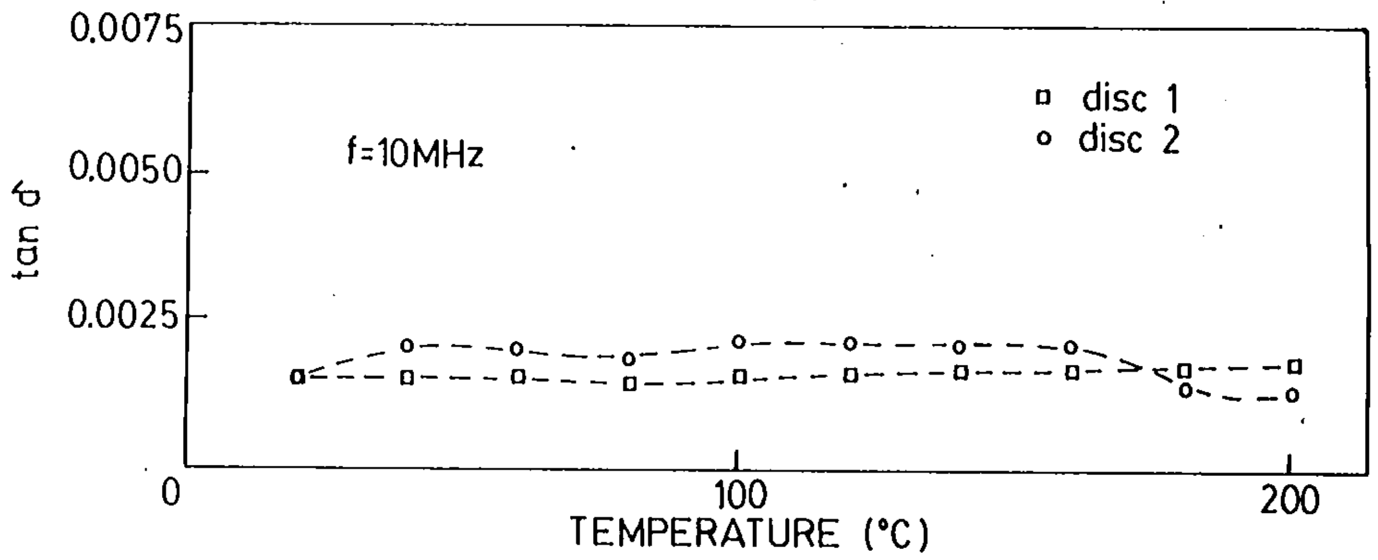

Figure A2.9 tan δ vs. temperature at 10 MHz.

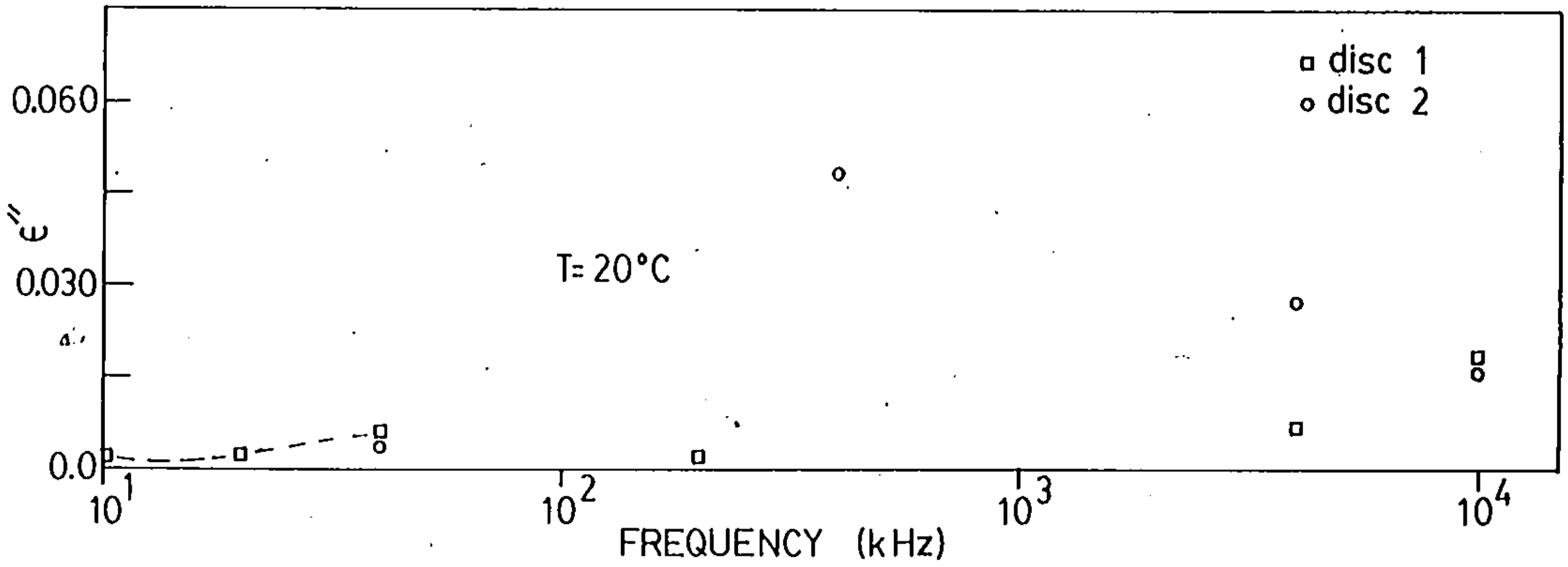

Figure A2.10 ε" vs. frequency at 20°C.

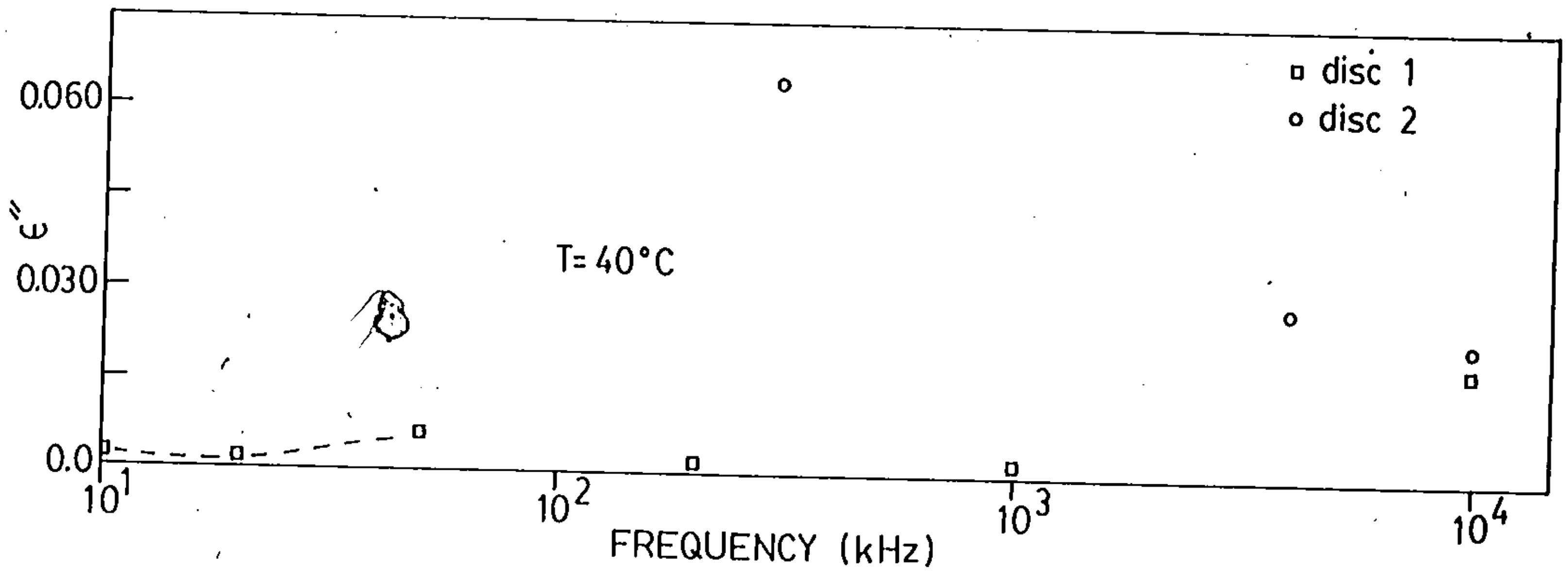

Figure A2.11 ε" vs. frequency at 40°C.

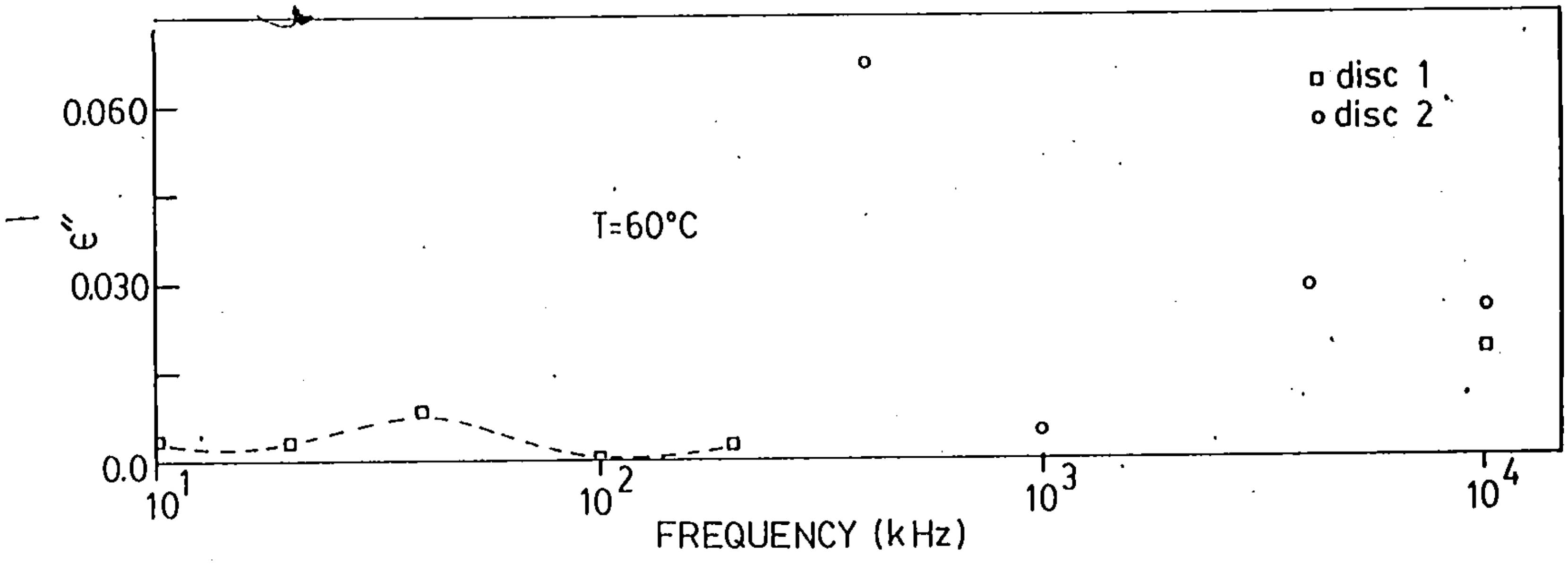

Figure A2.12 ε" vs. frequency at 60°C.

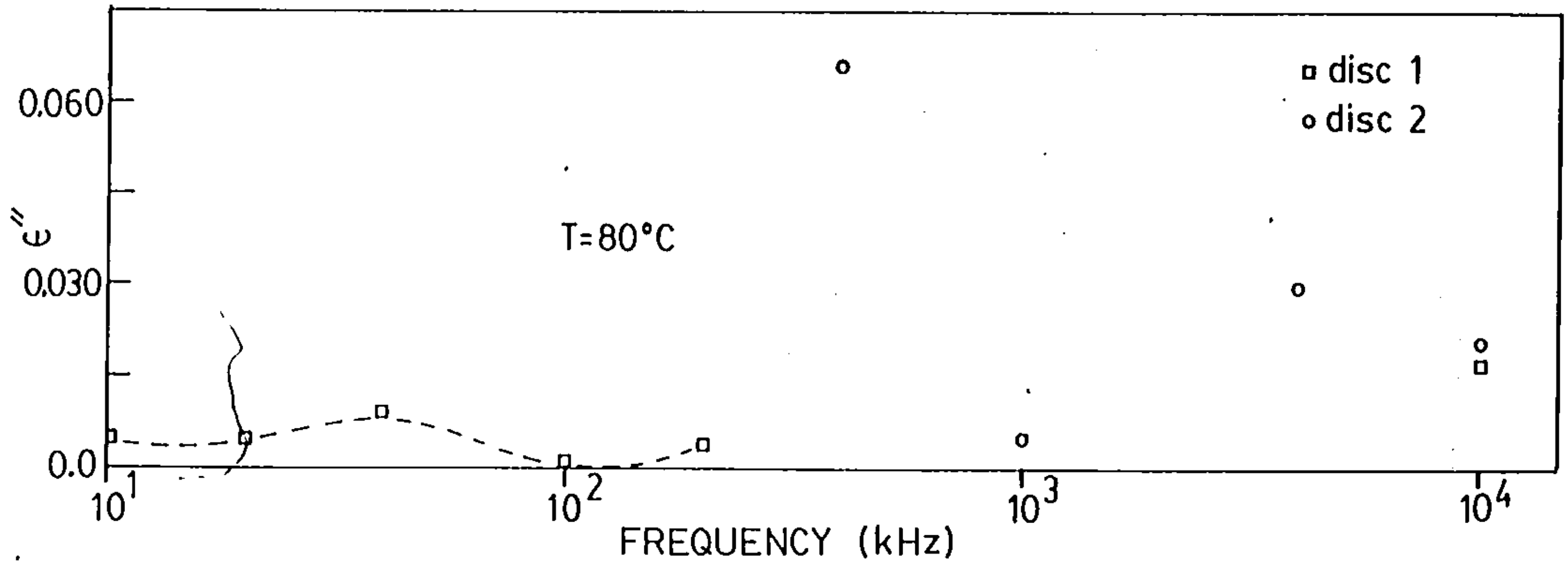

Figure A2.13 ε" vs. frequency at 80°C.

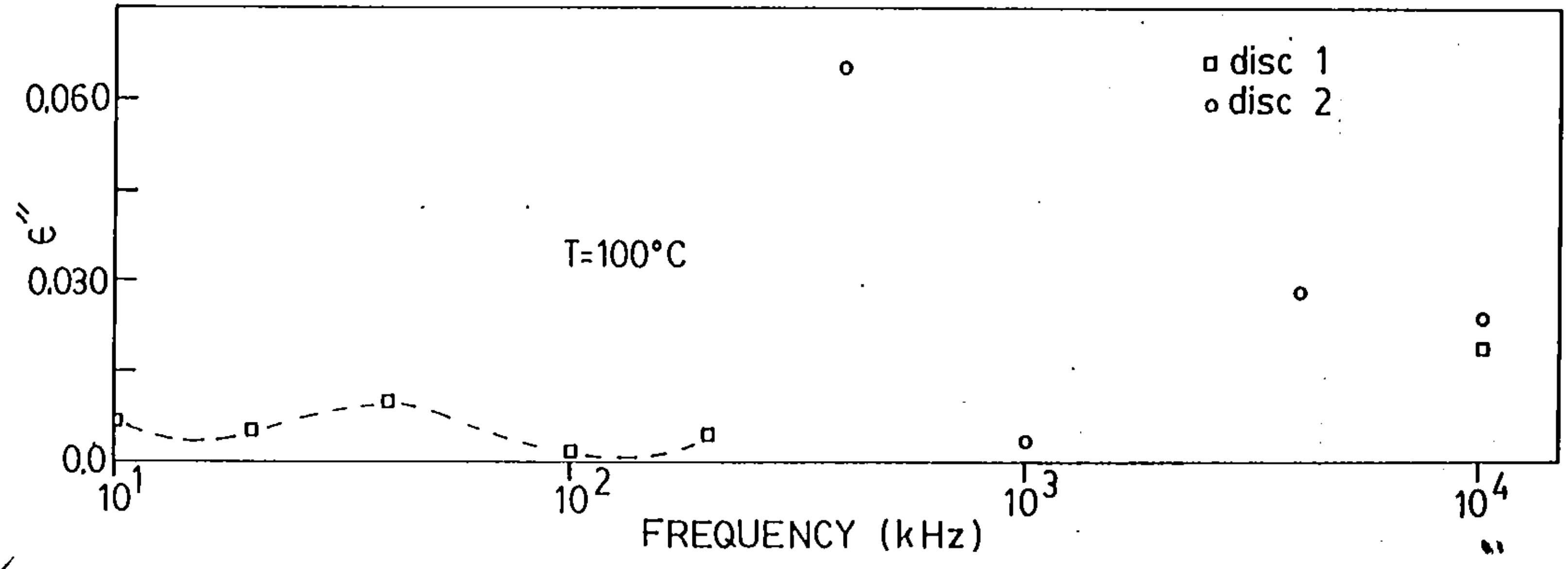

Figure A2.14 ε" vs. frequency at 100°C.

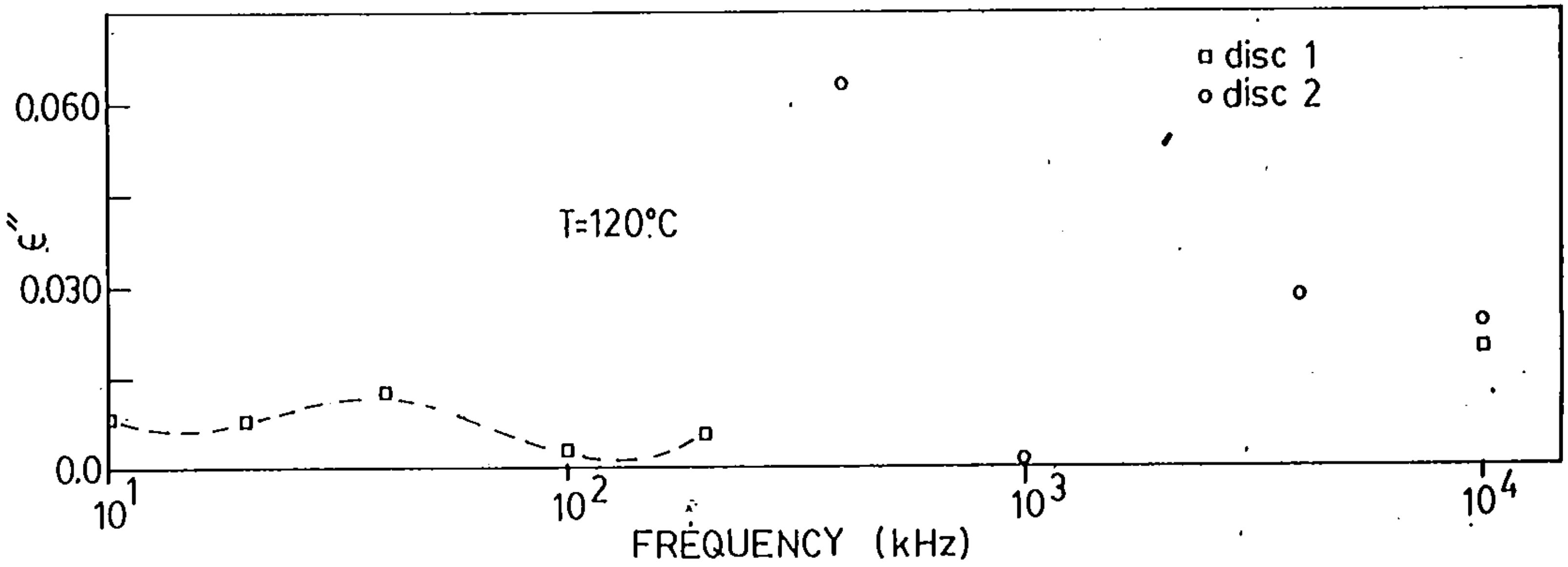

Figure A2.15 ε" vs. frequency at 120°C.

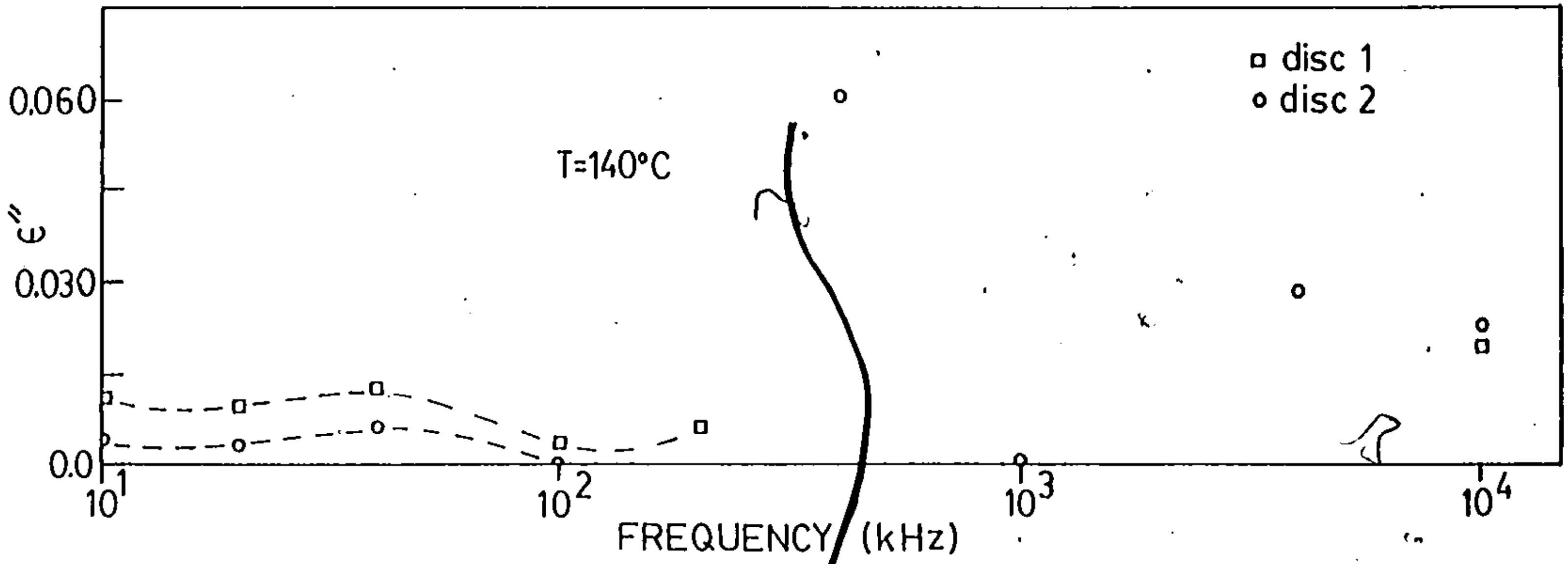

Figure A2.16 ε" vs. frequency at 140°C.

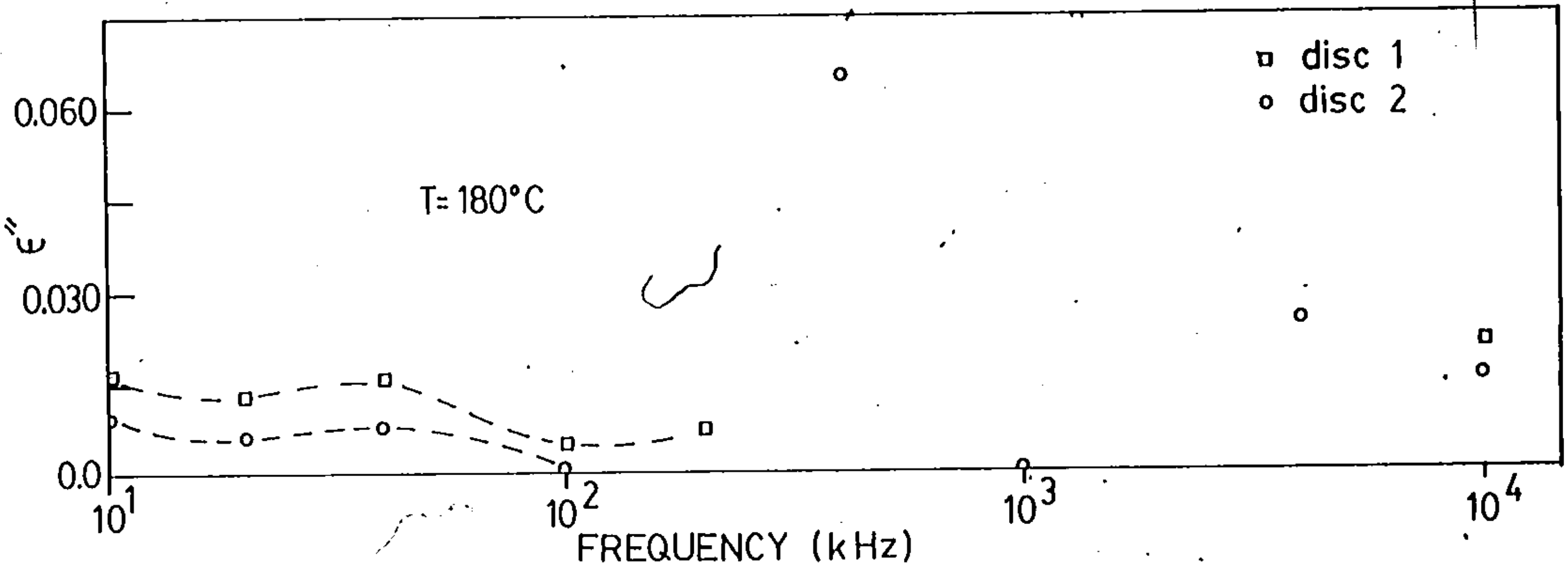

Figure A2.17 ε" vs. frequency at 180°C.

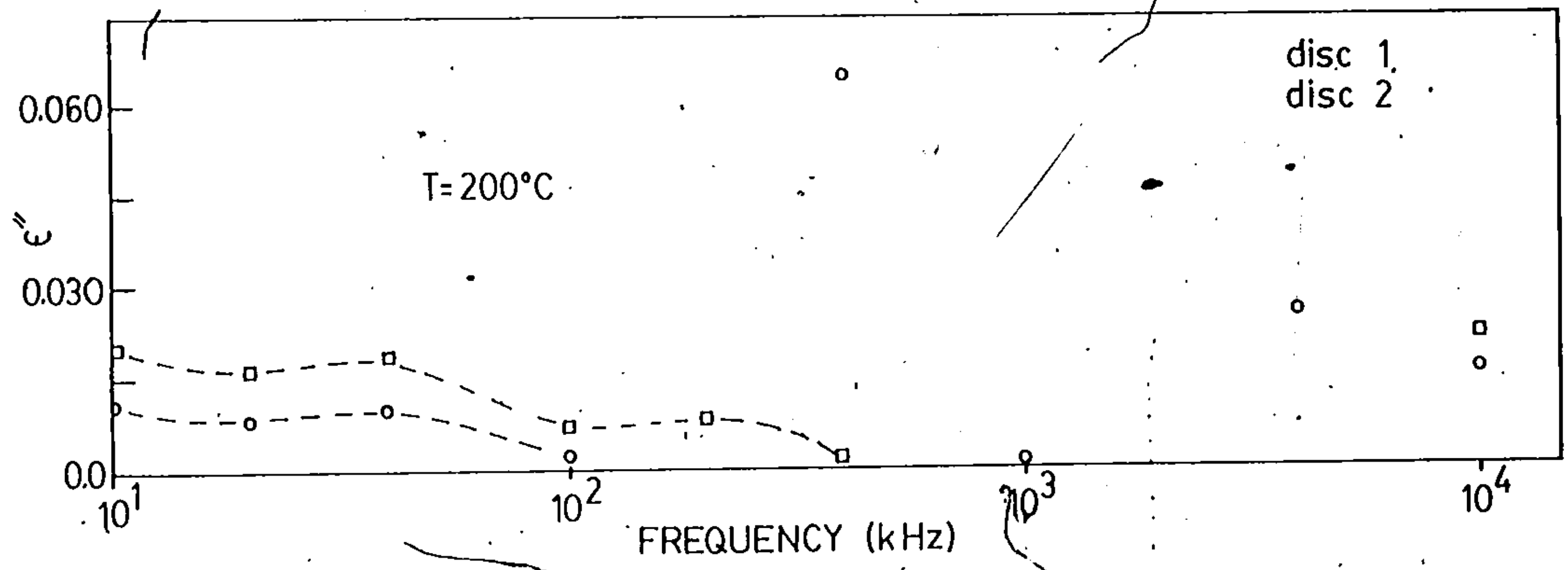

Figure A2.18 ε" vs. frequency at 200°C.

VITA AUCTORIS

The author was born in Windsor, Ontario, Canada on October 12, 1960.

Education:	Secondary School Diploma, Level IV, obtained at Centennial Secondary School, Windsor, Ontario, 1978.
	Secondary School Diploma, Level V, obtained at Centennial Secondary School, Windsor, Ontario, 1979.
	B.A.Sc. in Engineering Materials, obtained at the University of Windsor, Windsor, Ontario, 1983.

Publication derived from this thesis:

R.J. White, M. Ayukawa, G. DeMaggio, J.W. Robinson, and H. Yamauchi, "Thin Films RF Sputtered From $Ba_2Si_2TiO_8$ Ceramic Targets," to be published in the Proceedings of the World Congress of High Tech Ceramics, Milan, Italy, June 23-28, 1986.